Towards enhanced radiative emission for optical read-out of donor spins in silicon

Salahuddin Nur

A dissertation submitted in partial fulfillment

of the requirements for the degree of

Doctor of Philosophy

of

University College London.

Department of Electronic and Electrical Engineering

University College London

September 10, 2018

I, Salahuddin Nur, confirm that the work presented in this report is my own. Where information has been derived from other sources, I confirm that this has been indicated in the work.

Abstract

Silicon has several features that make it an attractive platform for implementing quantum information processing (QIP). The unique combination of a mature fabrication technology, extraordinarily long coherence times and high control fidelities of donor spins in isotopically purified silicon have made them good candidates for realising spin based quantum bits. Increased spin-photon coupling has the potential to add additional benefits including efficient optical readout of individual donor spins and even a route to generating entanglement. Efficient optical detection of the donor spin state could provide the missing piece of puzzle to realise long-range qubit couplings and construct quantum networks, however, achieving this in silicon is challenging due to its indirect bandgap. Photonic structures such as solid immersion lenses (SILs), circular Bragg resonators (CBRs), photonic crystal (PhC) cavities etc. can enhance radiative emission and/or its collection up to several orders of magnitude, potentially allowing it to compete with non-radiative processes such as Auger recombination. In this thesis, we report our first steps towards fabricating and characterizing such photonic structures, designed to enhance radiative emission and optical collection from ^{31}P donor bound excitons (D^0Xs) in silicon. We have fabricated silicon SILs using a neon focussed ion beam milling system. A bilayer resist based fabrication recipe has also been optimised using relatively inexpensive process materials, which efficiently produces CBRs and PhC cavities with desired optical properties on undoped silicon-on-insulator wafers. The optical properties of the fabricated devices are investigated using cavity reflection measurements. We have measured an absorption limited cavity quality factor (Q) of $\sim 5,000$ around ^{31}P D^0X emission wavelengths ($\sim$ 1078 nm) for silicon PhC cavities at room temperature. Silicon PhC cavities with such a quality factor ($\sim 5,000$) and enhanced collection can permit for optically accessing spins at a single or at least few donors level.

Impact Statement

We experimentally explore the potential of building an efficient spin-photon interface in silicon. Silicon provides a low-noise, fabrication and integration friendly platform for implementing spin qubits. In recent years, the research and development of silicon based quantum information systems have gained significant attention in both academia and industry. Our study towards an efficient spin-photon interface in the optical domain for silicon is a pioneering endeavour to combine the exception spin coherence times of donors in silicon with optical access. The knowledge acquired will benefit the researchers, both from academia and industry, pursuing efficient multi-qubit coupling, large-scale quantum information processing (QIP) system and network nodes in Si and/or SiC based platforms.

Through this work we started a direction of research in photonic crystal cavities that was new both to the group and the institute — the London Centre for Nanotechnology (LCN). We have collaborated with several groups from different universities in UK, bringing to the LCN the knowledge and skills to incorporate, activate and characterize emitters in SOI substrates and to develop new process recipes for fabricating nanophotonic structures. The experimental set-ups and fabrication recipes built up during this project can also be used by different groups in the LCN: for example, several groups from UCL and Imperial College are now using all or part of the optimized fabrication recipe for fabricating silicon based nanostructures in the LCN cleanroom. The knowledge developed in this project around ion implantation for donor incorporation and activation in Si/SOI substrates has been found useful for others in the group pursuing donor spin based QIP systems.

Acknowledgements

I thought writing the acknowledgement part would be the easiest so I left it for the last. However, when started, I have found that it is one of the most difficult part to write, specially within limited pages. During the four years of PhD, so many people have contributed to my work and life in so many different ways that it is not easy to acknowledge them all properly.

First of all, I would like to express my deepest gratitude to my supervisor, John Morton, for giving me the opportunity to join the Quantum Spin Dynamics (QSD) group, his unconditional support and guidance. Thank you, John, for everything, and specially for granting me the freedom to pursue a 'brave' project. I totally enjoyed the challenges.

Thanks to EPSRC and UCL Faculty of Engineering Sciences, for the financial support to carry out the research.

I am very grateful to my second supervisor, Jeroen Elzerman, for the access to the optics lab, for the magical optics setup and for everything!

I would like to thank Thomas Krauss, for providing us the Cz-SOI wafer with which I made all the photonic cavities; Christopher Reardon, for showing the tricks of fabricating photonic crystal cavities at York JEOL Nanocentre.

I would also like to thank Mete Atature for allowing access to QINM lab at Cambridge and Clemens Matthiesen for the initiation to optics and PL measurements.

The list of people I need to, want to thank at London Centre for Nanotechnology is almost exhaustive. The super postdocs in QSD, the cleanroom staff, Guy Matmon, Olliver Tedder, many friends/colleagues from several other labs — without your help and support, I could not have managed to carry out my experiments. Hee-Jin Lim, thanks very much for all of your efforts, guidance and time you managed for me during and after the experiments. Our friendship and collaboration have just started and it will

go far beyond this PhD. Christoph Zollitsch, having a friend and colleague like you is a privilege! Thanks for always being there when we needed you, be it in the lab or in a pub, and also for proofreading the draft of this thesis! Thanks must go to many other people with whom I worked in the LCN cleanroom, all the frustrations and rare bit of successes we shared while fabricating devices are unique.

For last four years, QSD has been my second family. The stress of the PhD life, late night experiments, working weekends became rather very enjoyable because of you guys! Thanks for tolerating my crude humour, irrational arguments about anything, everything!

Finally, I would like to thank my parents and my sisters for all the support they have provided me through out my life.

Last, but my no means least, I would like to thank my wife, Mahjabin, for her perpetual patience, love and support.

List of Publications

The work described in this dissertation has been published in the following articles and presented at the following conferences.

Journal Articles

- S Nur, H-J Lim, G Matmon, J Elzerman, J J L Morton. Silicon photonic crystal cavities at near band-edge wavelengths. *Manuscript in preparation*.

Conference Contributions/Presentations

- S Nur, J J L Morton. Cavity quantum electrodynamics for optical manipulation of spin qubits in silicon. *Summer School Silicon Photonics 2014*, University of Ghent, Ghent, Belgium, June 2014.

- S Nur, C C Lo, J J L Morton. Cavity quantum electrodynamics for optical manipulation of spin qubits in silicon. *Silicon Quantum Information Processing (SiQIP 2014)*, UCL, London, UK, September 2014.

- S Nur, C C Lo, J J L Morton. Towards cavity enhanced light-matter interaction in silicon for optical readout of spin qubits. *IoP Topical Research Meeting on Hybrid Quantum Systems 2014*, University of Nottingham, Nottingham, UK, December 2014.

- S Nur, C C Lo, C Matthiesen, C Reardon, J Sagar, J Mansir, P A Warburton, T F Krauss, M Atature, J J L Morton. Fabrication of photonic structures for optical detection of donor spin states in silicon. *Silicon Quantum Information Processing 2015: Scaling up (SiQIP2015)*, University of Cambridge, Cambridge, UK, September 2015.

- S Nur, C C Lo, C Matthiesen, C Reardon, J Sagar, J Mansir, P A Warburton, T F Krauss, M Atature, J J L Morton. Design and fabrication of photonic structures for enhanced emission and optical detection of donor spin states in silicon. *SOLID STATE QUANTUM PHOTONICS 2016*, University of Sheffield, Sheffield, UK, March 2016.

- S Nur, H Lim, C Reardon, O Tedder, C C Lo, C Matthiesen, G Matmon, J Sagar, P A Warburton, M Atature, T F Krauss, J Elzerman, J J L Morton. Fabrication and characterisation of photonic structures for enhanced radiative emission in silicon. *The 12th International Symposium on Photonic and Electromagnetic Crystal Structures (PECS-XII)*, University of York, York, UK, July 2016.

- S Nur, H Lim, C Reardon, O Tedder, C C Lo, C Matthiesen, G Matmon, J Sagar, P A Warburton, M Atature, T F Krauss, J Elzerman, J J L Morton. Fabrication and characterization of photonic crystal cavities for optical detection of donor spin states in silicon. *Silicon Quantum Information Processing 2016: Towards hybrid quantum circuits*, University of Cambridge, Cambridge, UK, September 2016.

Contents

List of Figures

List of Tables

Chapter 1

Introduction

1.1 Quantum information processing (QIP)

Processing information stored in quantum systems utilising quantum mechanical phenomena such as superposition and entanglement can give a significant boost to computational power for particular tasks. The potential of quantum information processing significantly attracted physicists' attention in latter part of twentieth century. Since then a lot of interest and effort have been committed to this fascinating field of research [1–4]. It has already been proved theoretically that quantum information processing (QIP) systems or quantum computers (QCs) will be superior than conventional classical computers for certain complex problems and specific tasks [3–5] such as simulating quantum systems [6], factoring integers and finding discrete logarithms [7], polynomial speed up in data search [8], solving large systems of linear equations[5], secure communication [9–11] and high-precision metrology [12, 13]. These improvements have dramatic consequences on computing ability and information processing. For example, an estimated time for an ideal quantum computer to factor a 1000 digit number using Shor's algorithm is 100 seconds whereas classical computers with number field sieve algorithm would take more than 100 years for the same task [14, 15]. As the technology is still in its infancy, the potential of quantum information processing has not been explored/exposed completely. Even at present, in addition to the scientific interest/research, the unique technique and unprecedented computing power of QIP systems show tremendous prospects in many practical/commercial applications such as the development of new medicines and materials [16, 17], machine learning & artificial intelligence [18, 19], financial services, supply chain & logistics, software ver-

ification & validation [17], numerical weather prediction [20], image processing [21], cybersecurity [11, 22] etc.

However, the realisation of quantum computers with practical quantum systems is quite challenging. First of all, the system has to be strongly isolated from the environment to retain coherent quantum states/information and then, on the other hand, efficient control over the system is necessary to initialise, manipulate, measure quantum states for processing information [3, 4]. To experimentally implement such a platform for QIP fulfilling the self-opposing criteria, researchers are investigating various physical systems and introducing new technologies for efficiently implementing and manipulating qubits - the basic unit of information in a quantum computer. There are numerous physical systems which, in principle, can represent a quantum two level system for a qubit implementation. Platforms based on optical modes of a photon, electronic states of ions/atoms suspended electromagnetically in vacuum, flux and charge states of superconducting circuits, spins of molecules in liquid solution, spin and charge states of impurities and artificial atoms in solid-state systems are examples of the most investigated ones [3, 4, 15, 23]. Each type of system has its own merits and weakness in satisfying DiVincenzo criteria - the standard requirements for realising QIP systems [24, 25] and it is still too early to choose any particular candidate as the best one for quantum computing. Among all the candidates, solid state systems are inherently more promising in terms of scalability and ease of integration with complementary electronics.

1.2 Silicon based qubits

In the last 6 decades, the microelectronics industry has revolutionised the modern world and our everyday life with a variety of electronic devices and information processing systems. Silicon has been used as the primary material platform for making conventional electronic and information processing devices in microelectronics industry since the invention of the integrated circuits in late 1950s. Technically, silicon is the most researched element among all elements known to us. A trillion-dollar microelectronics industry has developed and standardised silicon growth techniques, fabrication and integration processes. Until now, ease of design, scalability and low power consumption have allowed to continuously reduce the dimensions of silicon based transistors and

increase device density for more powerful yet smaller processing units. But with this continuous size reduction, the device dimensions would reach the order of few atoms within the next few years. Atomic-scale classical devices are extremely challenging to fabricate with current technology and their functionality/reliability will be affected by quantum mechanical effects at these ultra-scaled device dimensions. Thus further scaling of classical information processing systems to realise more powerful computers demands a novel device and/or information processing approach. Quantum information processing (QIP) can be considered as an attractive alternative to overcome this bottleneck as QIP exploits the same laws of quantum mechanics that limits the further improvement of classical/conventional electronics. In addition, QIP systems built on a silicon platform will inherently experience the benefits of the matured technology and well-developed fabrication processes.

To this end, spins confined in shallow impurities and artificial atoms (quantum dots) in silicon and silicon based materials can provide suitable two-level quantum systems for implementing quantum bits [27–35]. Figure 1.1 shows two example candidates/architectures for qubit implementation in silicon. Due to the cubic symmetry of the crystal structure, pure silicon has six degenerate valleys in its conduction band. In the case of nanoscale silicon devices with quantum dots and/or dopant impurities, this valley degeneracy is broken by the influence of several factors such as strain, spatial/electrostatic confinement, electric field etc. The manifestation of the valley splitting for quantum dot and impurity donors have been shown in the top energy diagrams of Figure 1.1 a &b [26] Thus, at sufficiently low temperatures, only the lowest-energy, non-degenerate valley state gets populated in these devices. The spin of electrons localised in such non-degenerate ground states of donors or artificial quantum dots can be used for qubit implementation. In the presence of external magnetic field, the electron spin states get separated due to the Zeeman interaction. These energetically separated spin eigenstates can be used to encode $|0\rangle$ and $|1\rangle$ states of a quantum bit. The electron spins in the ^{31}P donors exhibit an additional hyperfine interaction with the ^{31}P nuclear spin, which can be further utilised for realising nuclear spin based information storage and read-out schemes. Different architectures of control gates have been proposed and implemented for the manipulation and read-out of the encoded quantum information [27]. The schematics of quantum dot and impurity donor based qubit architectures with

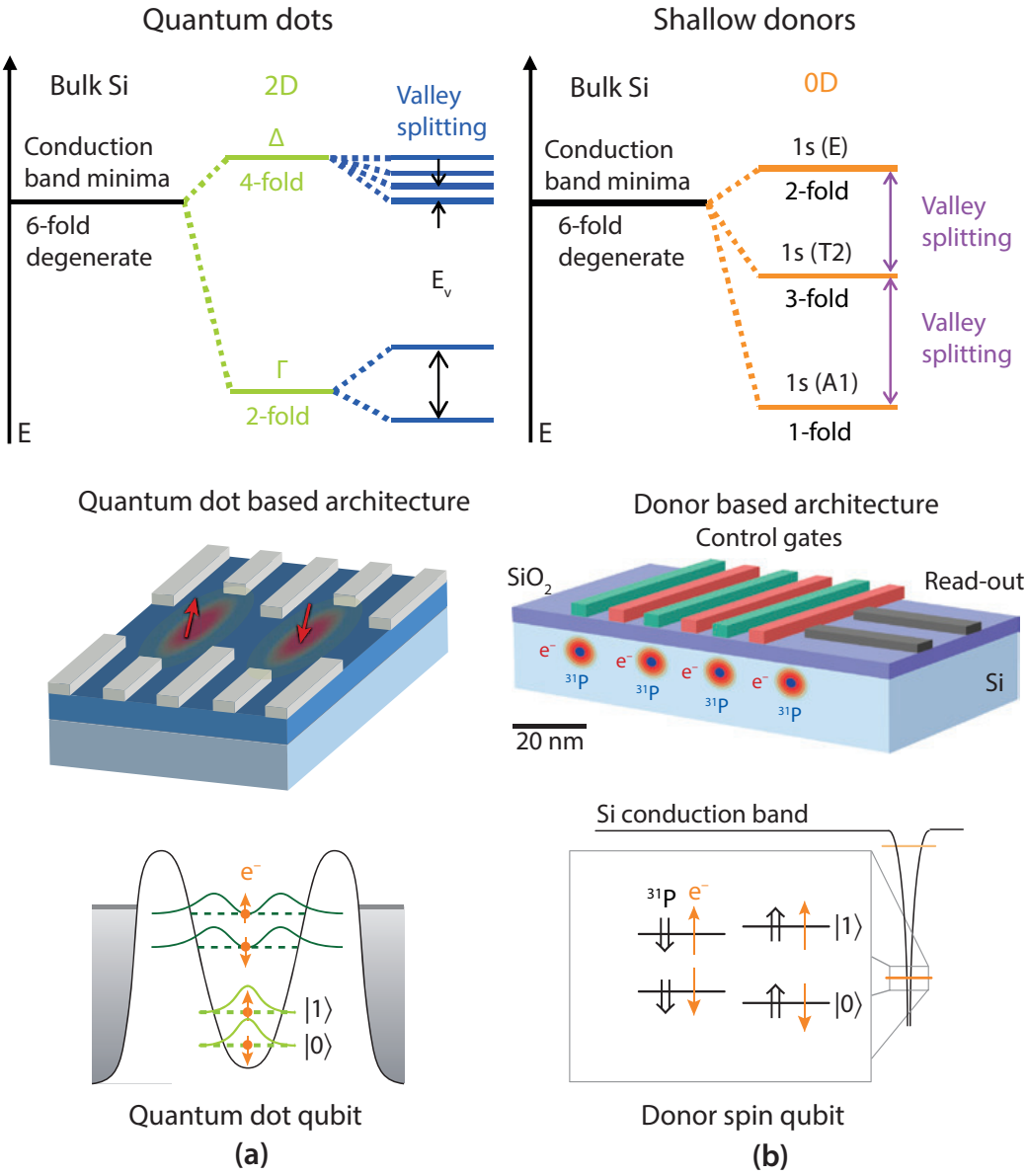

Figure 1.1: Example of silicon based qubit architectures: (a) Valley splitting of quantum dots (QDs) in silicon and QD based qubits, (b) Valley splitting of dopants/donors and donor based qubits in silicon. Images reproduced from [26, 27]

corresponding energy levels have shown in the bottom of Figure 1.1a & b, respectively [27].

In general, quantum information stored in spins is very sensitive to any kind of magnetic fluctuation/noise present in the system. So, most of the solid-state QIP candidates, in spite of the potential of scalability and ease of qubit manipulation, suffer significantly from background noise; their information storing/processing capabilities are severely limited by the noise emanating from nuclear magnetic moments of host material. But silicon as a host material suffers much less from background magnetic

noise. In natural silicon, the fraction of ^{29}Si nuclei with magnetic spin is only $\sim 5\%$. So, even in natural silicon, an electron spin coherence time of $\sim 200\,\mu$s and nuclear spin coherence time of ~ 60 ms for phosphorus donors have been observed [29, 36]. By isotopic purification of natural silicon, the concentration of the magnetic nucleus carrying ^{29}Si isotopes can be reduced [37–39]. With only the nuclear spin free ^{28}Si isotope left, an almost noise free background can be obtained in the silicon substrate for preserving and processing quantum information. For example, at low temperature, the bound electron and nuclear spin of a phosphorus atom embedded in a ^{28}Si matrix can store spin quantum information in the order of seconds and minutes, respectively; for quantum dots this time scale is several milliseconds [31, 34, 40–43]. Typical gate manipulation times with microwave pulses are $\sim 10-100$ ns for electron spins and $\sim 10\,\mu$s for nuclear spins [44]. In the case of ^{31}P donor spins, control error rates as small as 10^{-4} has been reported [45, 46]. With these spin coherence and gate control fidelity/timescales, a reasonably high coherence time to gate operation time ratio can be obtained which is, according to DiVincenzo [3, 25], a necessary criteria (coherence time to gate operation time ratio $> 10^4$ [3, 25, 47]) for fault tolerant quantum computation.

There are two dominant ways through which a quantum state can get corrupted. The first one is called the spin-lattice relaxation or population relaxation. The population relaxation involves a transition between two different spin states due to fluctuation of the energy of the system and is characterised by the population relaxation time, T_1. The second process, the spin-spin relaxation, involves transitions between states within the same energy due to spin-spin couplings, which randomly change the state of an observed spin. While this process is energy conserving, it destroys the quantum information stored in its spin state. Such processes are characterised by the coherence time, T_2. The coherence time (T_2) bounded by the population relaxation time (T_1), gives us a measure for how quickly the quantum information stored in a spin system gets corrupted. From literature, we find that electron spins of donors in silicon and also of silicon-based quantum dots have above millisecond coherence times (T_2) [27, 31, 33, 40, 41, 43]. Each candidate has certain promises for a spin qubit implementation. For example, phosphorus donors in ^{28}Si platform have very long electron and nuclear spin coherence time - $\gtrsim 1$ second and ≈ 3 minutes, respectively [40, 41, 48]. These long coherence times make phosphorus donor spins suitable for both processing

and storage qubits. A scanning tunnelling microscopy (STM) technique can be used to incorporate individual phosphorus donors into the substrate with atomic scale precision [49–52]. This deterministic single spin positioning would allow implementing efficient qubit coupling schemes and scalable architectures. These features make phosphorus donor impurities in silicon a very attractive candidate for spin qubit implementations. Hence, in this work we focus on phosphorus donors for spin qubit implementation in silicon.

1.2.1 Donor impurities and bound excitons in silicon

When a group V shallow donor substitutes a silicon atom in the lattice structure, its extra electron is only loosely bound to the nucleus as the Coulomb attraction is screened by core electrons. Thus, the substitutional donor effectively behaves like a hydrogen atom embedded in a silicon matrix, as shown in Figure 1.2a. These hydrogen like donor impurities have their ground states just below the silicon conduction band minimum (Figure 1.2b) which has six-fold degeneracy in k-space. This leads to a six-fold degeneracy of the 1s donor ground state, further divided into singlet, doublet and triplet states. The singlet state is formed with an even superposition/contribution from all six degenerate minima or valleys and thus, it is a member of the "A" symmetry point group. The triplets are an odd superposition of two coaxial valley ellipsoids (and are themselves threefold degenerate (of the "T2" point group), and the doublets are the two remaining antisymmetric orthogonal combinations (of the "E" point group) [26, 53, 54]. These

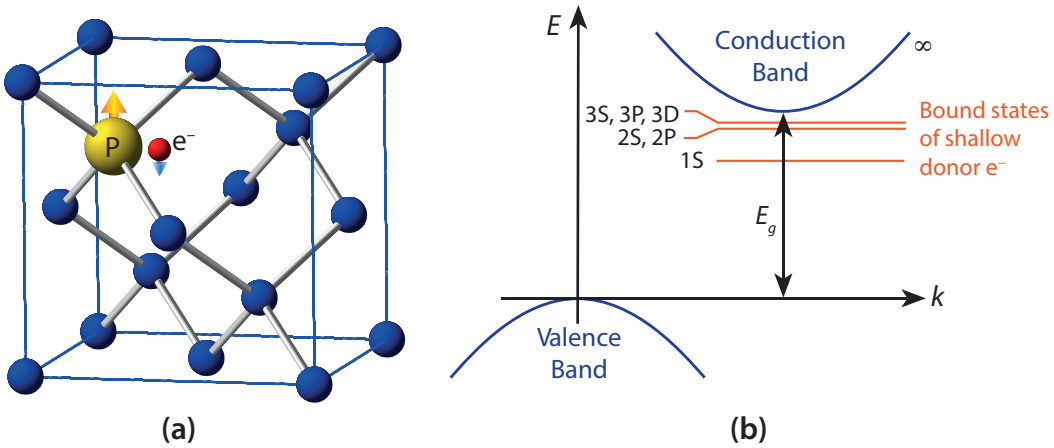

Figure 1.2: Hydrogenic donor impurity in silicon: (a) A substitutional phosphorus (^{31}P) donor in silicon lattice, (b) bound states of a shallow donor electron, image reproduced from [53]

valley splitting of dopants in silicon has been shown in the top energy diagram of Figure 1.1b. Low-lying donor ground states can be utilised for a spin qubit. For example, in case of phosphorus donors in silicon, the magnetic field split orbital singlet (1s:A) states can be used efficiently as spin qubit [26, 53, 54].

An electron and hole can form a weak bond due to the Coulomb attraction and exist as a quasi-particle which is known as an exciton. In semiconductors, an electron and hole forming exciton are usually separated over several lattice constants. The pair has a delocalised wavefunction and can move freely inside the crystal. This type of electron-hole pair is termed as a free-exciton. The electron-hole pair of a free exciton recombine through the emission of a photon with characteristic energy. In the case of indirect bandgap semiconductors, the recombination takes places through phonon assisted channels [55]. In silicon, impurities such as phosphorus can attract free excitons via the van der Waals interaction and trap them when the temperature is sufficiently low. As the bound states have lower energy, neutral donors in silicon trap free excitons quite efficiently and form donor bound excitons (D^0Xs) [56, 57]. Figure 1.3a shows the schematics of the hydrogen like neutral donor and donor bound exciton in silicon.

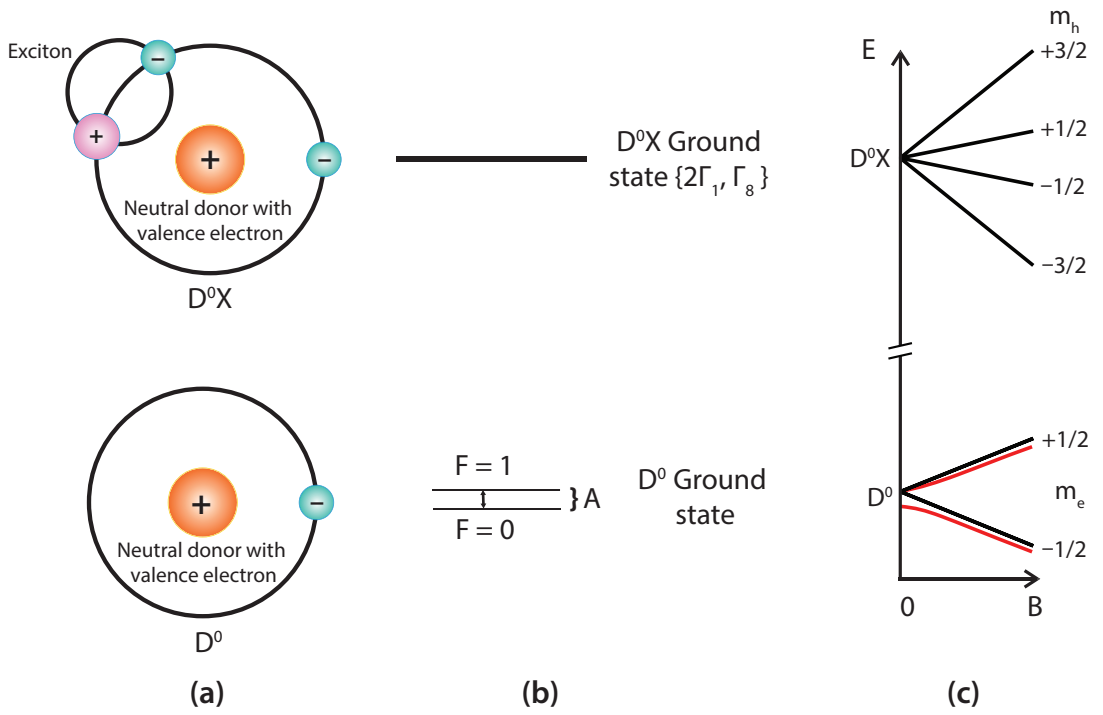

Figure 1.3: Ground energy states of (D^0) and (D^0X) in silicon: (a) Schematics of neutral donor and donor bound exciton. Ground state energy levels of D^0 and D^0X in silicon without (b) and with (c) the presence of any magnetic field [53, 54].

Without a magnetic field, a ^{31}P donor in silicon forms a triplet state of total spin $F = 1$ and a singlet state corresponding to spin $F = 0$. These triplet and singlet states are separated by an energy equal to hyperfine constant A (0.486 μeV) [58], as shown in Figure 1.3b. The degeneracy of the triplet state can be lifted by applying an external magnetic field (Figure 1.3c). A ^{31}P D^0X consists of two interacting electrons and one hole, as well as the fixed $^{31}P^+$ ion. In the (D^0X) ground state, two electrons occupy the lowest valley-orbit state and form a spin singlet. These electrons do not have any paramagnetic contribution to the energy levels. The hole wave function belongs to the four-fold degenerate state (Figure 1.3b) and the spin- 3/2 hole splits the energy levels of the bound exciton under a magnetic field (Figure 1.3c) [54, 59].

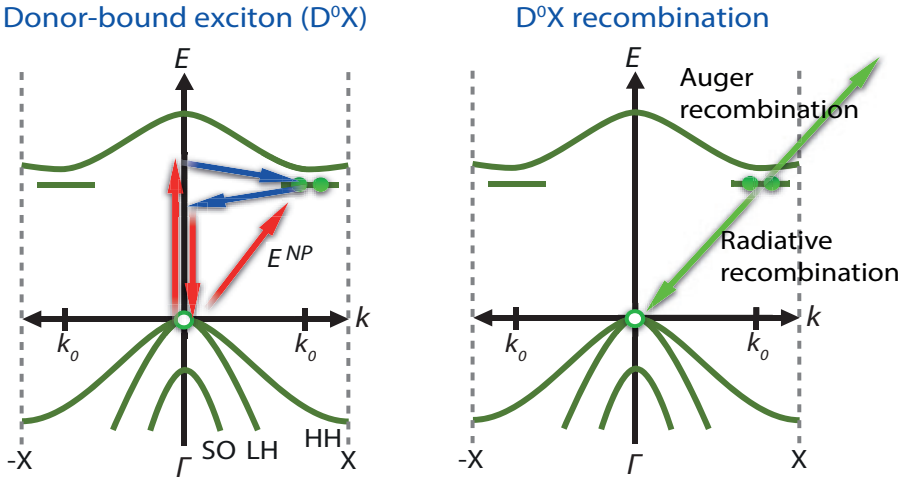

Figure 1.4: Recombination mechanisms of donor-bound exciton (D^0X) in silicon.

Photoluminescence spectra emanating from a donor-bound exciton (D^0X) recombination can be used to characterise impurity types and determine their concentration in silicon [60]. Figure 1.4 schematically shows the recombination mechanisms of donor-bound exciton (D^0X) in silicon. The dominating mechanism for recombination for D^0Xs in silicon involves a wave vector conserving process in addition to photon emission. This phonon assisted recombination takes place, as mentioned above, due to silicon's indirect bandgap nature. Typically, however, there is also a sharp no-phonon transition that occurs due to the electron scattering from the central cell potential [53, 61].

The most interesting feature of the no-phonon transitions from the D^0X ground state to the donor ground state has been observed in isotopically purified silicon. Under external magnetic magnetic field, spin selective transitions from Zeeman-split D^0X

ground states to D^0 ground states can reveal donor spin states.

1.2.2 Optical read-out of spin states in silicon

The ultimate goal of quantum information science is to build information processing systems with effectively coupled qubits and communication networks using efficient entanglements of distributed quantum memories. An efficient way to construct such a system/network is to couple/connect stationary qubits and quantum memory nodes using flying photons in a fully quantum way. Spin coupled quantum emitters in solids are promising candidates for realising spin-photon interfaces which can connect the quantum states of photons to internal states of quantum emitters (stationary qubit or memory). A suitable emitter-solid system should retain long spin coherence time, favourable optical properties such as fast radiative emission rate, high quantum efficiency (QE) etc. and allow robust fabrication of quantum photonic systems. Quantum dots (QDs) in III-V materials, defect/colour centres in wide-badgap semiconductors etc. [62–65] are examples of widely studied emitter-solid systems for realising efficient spin-photon interfaces. However, none of the candidate emitter-solid systems has all the desired optical properties and fulfils the quantum memory performance. For example, short radiative lifetime ($\sim$ 1 ns), near unity quantum efficiency, matured fabrication/integration techniques etc. make self-assembled III-V semiconductor QDs an attractive photonic system; but limited spin coherence time ($\sim$ 1 µs), large inhomogeneous broadening of a QD ensemble (typically at the level of THz compared to the sub-GHz homogenous linewidth of a QD), difficulties in forming local qubit clusters seriously hinder coupling of multiple qubits and practical implementation of scalable spin-photon interfaces with QDs [62, 63, 66, 67] . Colour centres such as nitrogen-vacancies (NVs), silicon-vacancies (SiVs) in diamond also have certain promising properties for implementing spin-photon interfaces. NV centres allow very long ($\sim$ 1 s) spin coherence time even at room temperature, all optical spin control, proof-of-concept demonstration of several quantum information/communication applications; however, dominant broad phonon sideband, spectral broadening, yet-to-be matured fabrication processes make multi NV coupling, multi-node quantum network, scalable integration etc. challenging [63, 65]. SiV centres, on the other hand, provides better optical properties, photostability than NV centres but with a poor quantum memory performance ($\sim$ 100 ns) [63, 68]. Thus,

the search for new material systems with good optical, memory and fabrication-friendly properties for the implementation of a efficient spin-photon interface is an active field of research [63, 64, 69, 70]. Thus, investigating the potential of efficient spin-photon coupling and optical read-out of impurity spins in silicon is an important and interesting field of research. In Table 1.1, the optical and memory properties of ^{31}P donor spins in silicon are presented along with those of other promising quantum systems such as III-V QDs, colour centres in diamond etc.

Table 1.1: Properties of solid-state quantum systems for qubit implementation

Candidate system	III-V QD [62, 63, 66, 67]	^{31}P D^0X in Si [48, 71–73]	Diamond NV [63, 74–76]	Diamond SiV [63, 68, 77, 78]
No-phonon emission wavelength (nm)	$900-1550$	1078	637	737
Radiative lifetime	~ 1 ns	~ 2 ms	~ 12 ns	~ 1 ns
Radiative quantum efficiency	~ 1	10^{-4}	~ 0.8	~ 0.1
Oscillator strength	$\sim 10-100$	7.1×10^{-6}	0.006	N/A
Ensemble linewidth	$20-30$ nm	150 fm	$\lesssim 1$ nm	~ 20 pm
Homogeneous/ single emitter linewidth	~ 1 pm	~ 10 fm	~ 20 fm	~ 200 fm
Coherence time	~ 1 µs	~ 1 s	~ 1 s	~ 100 ns

Experimental studies validate the prospect for realising and manipulating individual qubits in silicon with substitutional donors such as phosphorus or bismuth [29, 79]. Spin qubits in silicon benefit from long coherence time (Table 1.1) and matured fabrica-

tion technologies, as discussed in Section 1.2. However, in silicon platform, the challenges come in when we consider fast control of individual spins and coupling them for information processing. The issue of long-distance coupling and realising quantum networks could be tackled efficiently if we can devise a system to couple static donor spin qubits to flying qubits [65, 80–83]. The implementation of a such a spin-photon interface in silicon demands optical control/read-out of donor spin states. Picosecond optical control and sub-microsecond optical readout schemes have already been been demonstrated for spin qubits implemented with quantum dots in direct bandgap materials and colour centres in diamond [84–87]. Compared to these optical techniques, microwave control and electrical readout schemes for donor spin qubits in silicon are considerably slower; they are in the order of sub-microseconds and milliseconds, respectively. So, devising optical control/read-out schemes could allow, in addition to efficient coupling, faster and more localised manipulation of donor spin qubits.

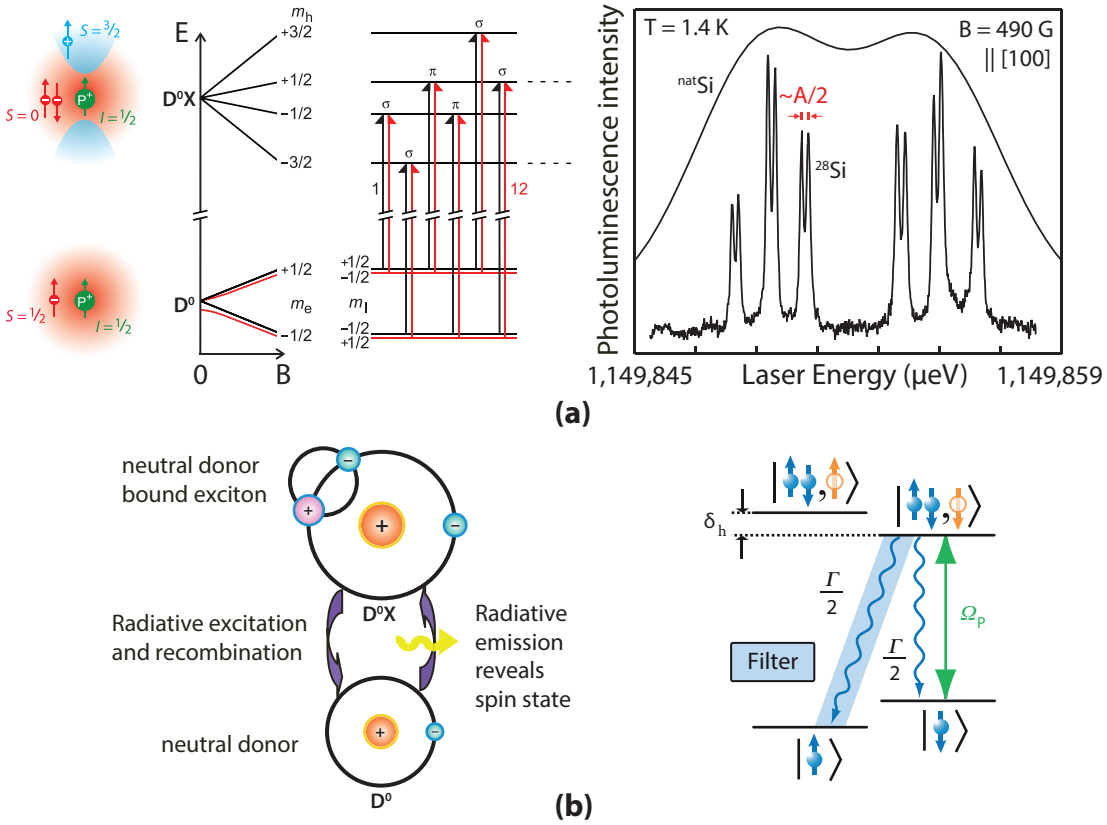

Figure 1.5: Optical detection schemes for donor spins in silicon: (a) Under external magnetic field spin selective transitions from D^0X to D^0 states can reveal nuclear spin states, image reproduced from [54, 88]. (b) An electron spin states can be manipulated by exploiting the 3-state Λ system, reproduced from [80].

Figure 1.5a shows the magnetic field separated energy levels responsible for the

D^0X hyperfine transitions and the photoluminescence excitation (PLE) spectrum of the transitions. The unique properties of D^0X's hyperfine transitions in isotopically purified ^{28}Si already open a door to manipulate donor spin states. Subsecond hyperpolarization of the nuclear and electron spins (70% and 90% respectively) of ^{31}P donors in ^{28}Si allows us to efficiently initialise qubit/memory states. Moreover, the ultra-narrow linewidths of D^0X transitions ($\sim$ 150 neV), narrower than D^0 hyperfine splittings ($\sim$ 486.1 neV), are suitable for optical detection/manipulation of donor spin states [88–90]. For magnetic fields greater than the hyperfine splitting ($\gg$ 0.005 T), all ^{31}P $D^0X \rightarrow D^0$ transition energies can be separately addressed, so, we can readily populate/polarise certain nuclear/electronic spin states through selective optical pumping [54, 91, 92]. Furthermore, dipole allowed ^{31}P $D^0X \rightarrow D^0$ transitions can be used to reveal/detect the nuclear/electron spin state of the donor, as illutrated in Figure 1.5. The D^0X system is also promising for optical spin control schemes such as spin rotation using stimulated Raman transitions [84, 85, 93].

The main challenge of realising these optical spin read-out/control schemes in a silicon platform is silicon's indirect bandgap nature. The D^0X transition in silicon has a very low quantum efficiency ($\sim 10^{-4}$) and weak oscillator strength (7.1×10^{-6}) for no-phonon emission which are several orders of magnitude smaller than those of optically active candidates such as III-V QDs and colour centres in diamond, as listed in Table 1.1. The low quantum efficiency/oscillator strength makes the realisation of any optical scheme difficult. However, if we can sufficiently enhance and detect no-phonon/radiative emission from $D^0X \rightarrow D^0$ transitions in silicon, in principle, it would allow us to implement optical spin control/read-out techniques.

1.3 Enhancement of radiative emission in silicon

Detection of photons from an emitter located in a high refractive index material substrate depends on factors such as the quantum efficiency of the emitter, extraction of the emitted photons from the high-index host material and guiding the extracted photons to the collection objective [94]. Hence, the total radiative emission efficiency can be expressed as

$$\eta_{\text{total}} = \eta_{\text{emission}} \times \eta_{\text{extraction}} \times \eta_{\text{collection}}$$

In the case of silicon, both the emission and extraction efficiency are very low (quantum efficiency $\sim 10^{-4}$ and extraction efficiency $\sim 1\%$). So, to enhance the total emission efficiency of an emitter in silicon, all three constituting components have to be optimised carefully. In this Section, we briefly discuss potential candidates for enhancing the total emission in silicon.

1.3.1 Nanostructures

Silicon nanostructures such as nanowires, nanocrystals or quantum dots are good candidates for enhancing and tuning visible, near-infrared photoluminescence (PL) emission. A bandgap modification due to wave function overlap is possible by utilising several techniques such as quantum confinement effect, strain engineering, suitable surface termination/passivation, carrier confinement etc. [98–100]. Employing any one or a combination of these techniques, it is possible to change the indirect bandgap nature of bulk silicon material and make it behave like a direct bandgap or quasi-direct bandgap material in the nanoscale regime. Favourable bandgap tuning would even allow emission at room or elevated temperatures. Experimental studies well validate the theoretical predictions for different kinds of nanostructures - nanocrystals [95, 101] quantum dots [102–104], nanowires [96, 97, 105]. Examples of enhanced no-phonon emissions with the size/quantum confinement dependent bandgap tuning from silicon nanocrystals [95]

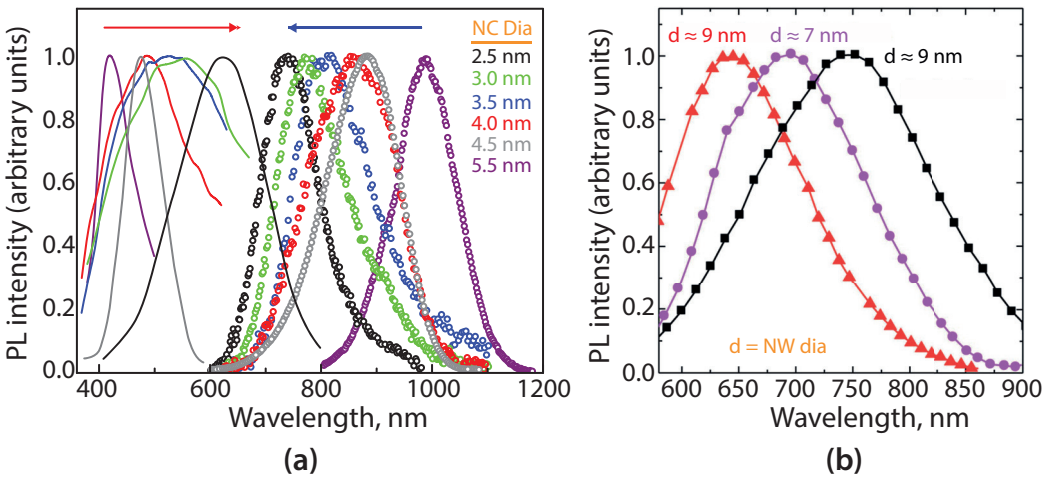

Figure 1.6: Room temperature PL emission in silicon nanostructures: (a) Normalised hot PL (continuous curves in the visible wavelength range) and excitonic PL emission (curves with circles in the long/infrared wavelength side) from Si nanocrystals [95]. The excitonic PL spectra show a blueshift and the hot PL spectra show a redshift for smaller nanocrystal sizes [95]. (b) Size dependent PL emission (normalised) from Si Nanowires [96, 97] which shows a blueshift for decreasing nanowire diameters.

and nanowires [96, 97] have been shown in Figure 1.6a & b, respectively.

Recently, it has been theoretically predicted and experimentally demonstrated that properly surface capped/strained nanostructures can enhance photon emission rate in silicon by four orders of magnitude [101, 106]. Based on these results, silicon nanostructures seem to be very attractive platforms for optically manipulating/controlling single donor spin qubits at elevated temperatures and a model has already been proposed for such a system [107]. But several critical challenges complicate the issue when it comes to realisation. First of all, all experimental results show that significant enhancement of radiative emission takes place only in nanostructures with sub-10 nm dimensions. In this regime, it is extremely challenging to deterministically fabricate desired structures and incorporate/localise a single donor at a precise position. Moreover, for sub-10 nm structures, incorporated donors show a tendency to segregate towards the interface, especially if the surface is oxide passivated [108]. Finally, the transition to direct bandgap is not always achieved through a quantum confinement effect alone; suitable surface passivation/strain engineering is also an additional requirement for achieving a direct bandgap. However, surface properties such as interface defects, type of terminating material, interface-donor distance etc. seriously affects the coherence time for donor spins. Hence, in spite of the fact that silicon nanostructures are attractive for emission enhancement and light emitting device realisation, several critical issues affecting spin coherence make them challenging platform for implementing a spin-photon coupling system.

1.3.2 Solid immersion lenses

Emitters inside indirect bandgap silicon have very low quantum efficiency, for example, the ^{31}P D^0X in silicon has a quantum efficiency around 10^{-4} (This means out of $\sim 10^4$ recombinations only one takes place through a radiative channel releasing a characteristic photon). The high refractive index of silicon ($n_{\mathrm{Si}} \approx 3.5$) adds further difficulties to the outcoupling of emitted photons. The high refractive index property gives rise to considerable amount of total internal reflection (TIR) and traps most of the emitted photons back inside the silicon substrate when they try to escape to the lower density medium, as shown in Figure 1.7a. So, the photon extraction efficiency of silicon is very poor and even a high numerical aperture (NA) objective does not help much for col-

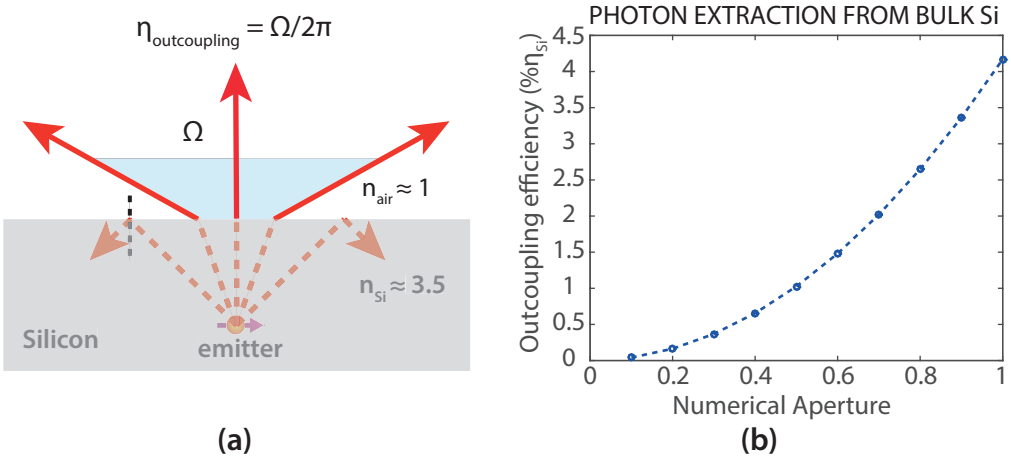

Figure 1.7: Photon extraction from bulk Si: (a) An emitter inside a silicon slab; most of the emitted photons get trapped inside the high refractive index silicon medium due to strong total internal reflection (TIR). (b) The efficiency of outcoupling to collection objective with varying NA.

lecting detectable photons from a point source inside silicon. The maximum $\eta_{\text{outcoupling}}$ ($= \eta_{\text{extraction}} \times \eta_{\text{collection}}$) obtainable to a high NA objective from bulk silicon is around 5-6% only, as illustrated in Figure 1.7(b).

Solid immersion lenses (SILs) can be used to outcouple emitted photons efficiently to the collection objective. SILs are designed to have spherical surfaces which reduce photon trapping due to total internal reflection. They also use the idea of filling the objective space with high refractive index materials which in turn increase the numerical aperture of the collection system to $NA = n_{\text{SIL}} \sin\theta$, where θ is the angular semi-

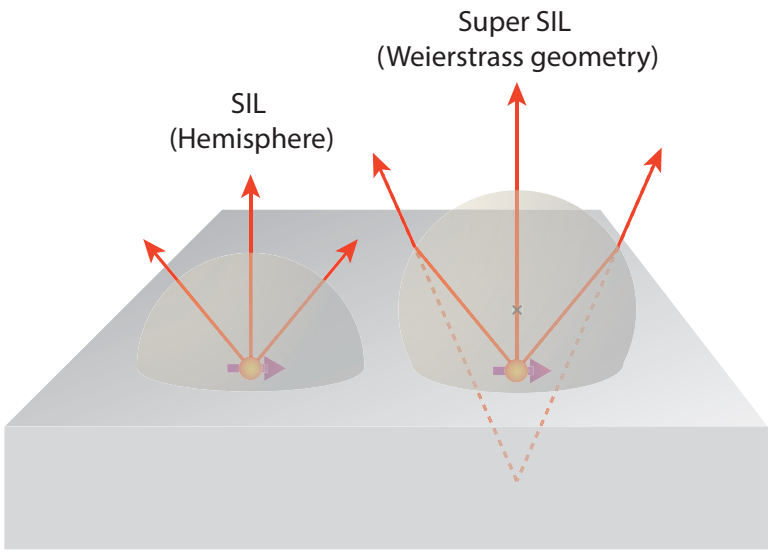

Figure 1.8: Solid Immersion Lens (SIL): The schematics of (a) a simple SIL and (b) a Super-SIL.

aperture in the objective space [109–111]. SILs cannot modify the quantum efficiency of the emitters, but they help extracting photons from the high refractive index host material and focus the photons to the collection objective. Thus, they can enhance detection of emission by improving extraction and collection efficiency.

Geometrically, spherical structures in a high refractive index material have two focal points - one at the centre of the sphere and another below the centre. For realising SILs either a simple hemisphere or a supersphere (*Weierstrass*) geometry can be used, as illustrated in Figure 1.8. A simple hemispherical SIL increases both lateral magnification & *NA* by n_{SIL} and reduces the focal spot by a factor of $1/n_{\mathrm{SIL}}$ compared to the vacuum case. The ideal magnification factor for super-hemispherical SILs is n_{SIL}^2 (but in practice the *NA* is enhanced by a factor of n_{SIL}) while the spot size reduction factor is $1/n_{\mathrm{SIL}}^2$. Careful implementation of Super-SILs can increase the photon outcoupling by an order of magnitude compared to the case without SILs [112–115].

1.3.3 Cavity QED

In the early twentieth century, the spontaneous emission was thought to be a fundamental property of an excited atom/emitter which is necessary to achieve a thermal equilibrium with the surroundings. In 1946, E. M. Purcell has shown in his seminal paper [116] that spontaneous emission is a function of the emitter?s environment. Thus, the rate of spontaneous emission can be controlled with careful modification of the local environment of the emitter, for example, by placing it in a cavity.

Cavity quantum electrodynamics (QED) investigates the interaction of a single emitter with resonant structures, i.e., cavities. Cavity QED opens the door to control/enhance light matter interaction exploiting suitable cavity structures. As our main goal is to enhance radiative or spontaneous emission of a single emitter, tuning light-matter interaction with cavities can provide us one effective way to do that [117, 118].

In the early twentieth century, the spontaneous emission was thought to be a fundamental property of an excited atom/emitter which is necessary to achieve a thermal equilibrium with the surroundings. In 1946, E. M. Purcell has shown in his seminal paper [116] that spontaneous emission is a function of the emitter?s environment. Spontaneous emission can be considered as a property of an atom-vacuum system. The probability of such an emission depends on the availabilty of vacuum states for the ra-

diated photons. With suitable modification of these states, significant control over the spontaneous emission rate can be achieved [117, 118]. Thus, the rate of spontaneous emission can be controlled with careful modification of the local environment of the emitter, for example, by placing it in a cavity.

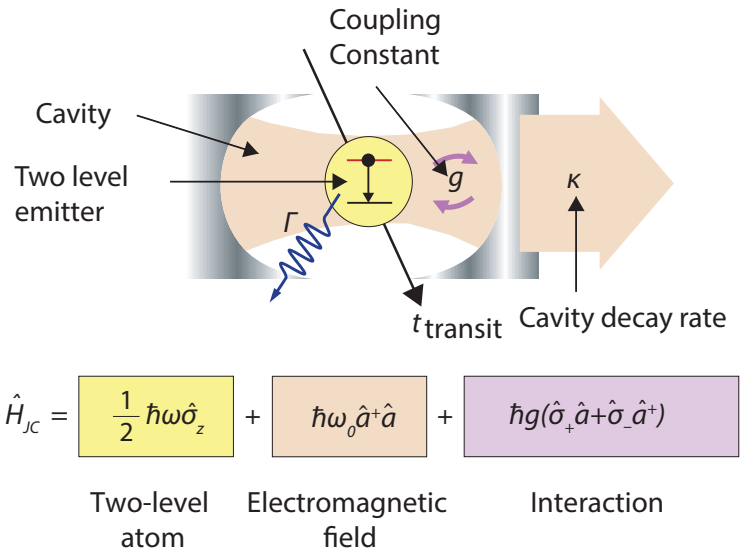

Figure 1.9: Atom-photon interaction in a cavity and and Jaynes-Cummings Hamiltonian [119].

Electromagnetic fields get quantized when confined in a small space comparable to their wavelengths. The light-matter interaction in a cavity can be treated as an interaction between a single/quantized electromagnetic field mode and a two level system. The Jaynes-Cummings (JC) Hamiltonian can easily characterise this type of single atom, single cavity mode interaction, as illustrated in Figure 1.9. The first term of the JC Hamiltonian describes the energy of the two-level atom, the second term is the energy of the electromagnetic field neglecting the constant zero-point energy, and the third term is the interaction between atom and electromagnetic field. Without the influence of a cavity, the direct coupling of an emitter to its environment causes a decay of its excited state amplitude through spontaneous emission (Γ). Incorporation of a cavity creates a modified radiation continuum, where the new radiation modes includes the effect of the cavity. When the cavity mode gets coupled to an output radiation continuum, the field amplitude inside the cavity also starts to decay i.e. photons leak out of the cavity (κ). The interaction coefficient g in the JC Hamiltonian is known as the coupling constant which determines the strength of coupling between the emitter and a single photon in the cavity mode.

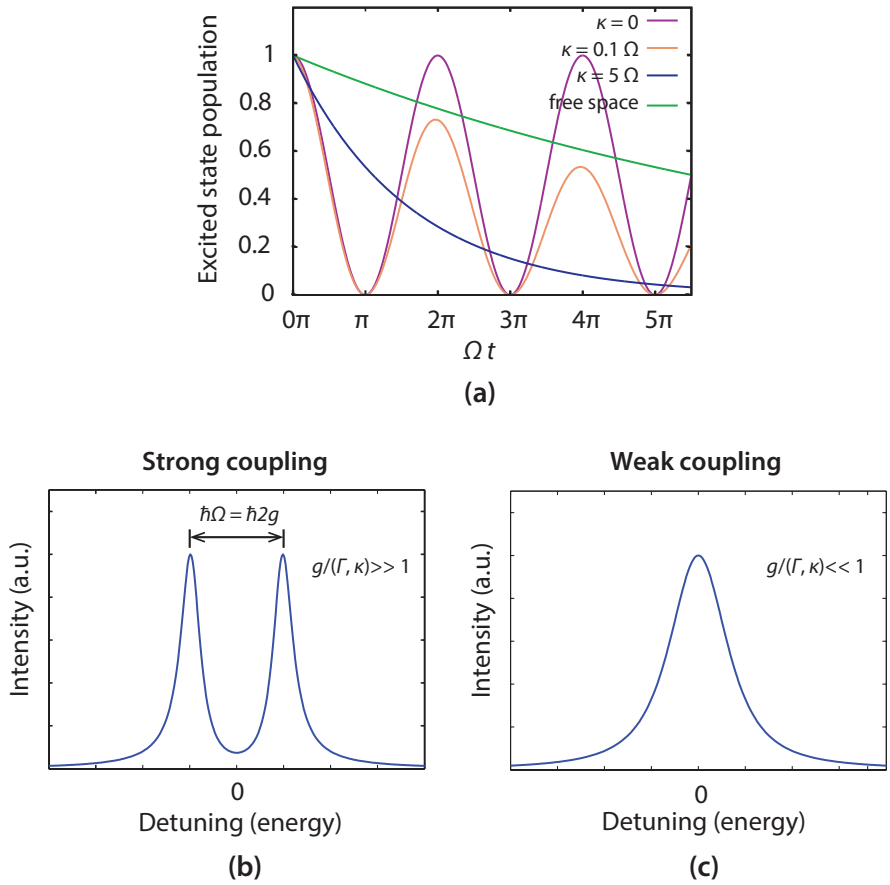

Figure 1.10: [Population dynamics and emission spectra of an emitter-cavity coupled system: (a) The excited state population is plotted as a function of time for different cavity damping rates κ, given in units of $\Omega = 2g$ (the vacuum Rabi frequency). Without cavity damping ($\kappa = 0$), the population oscillates between excited and ground states. With damping, populations get lost to an output radiation continuum and the oscillation completely dies down after certain time (damped oscillations). For $\kappa > \Omega$, the excited state population is damped faster than in free space and no oscillation occurs in this case (the Purcell effect). (b) and (c) Emission spectrum for strong and weakly coupled systems, respectively, as a function of the detuning of the emitter with respect to the cavity resonance. Images are adapted from [120–122].

The dynamics of the cavity mediated atom-photon interaction can be categorised in two limiting regimes - strong coupling regime and weak coupling regime. The strong coupling regime is defined as the situation when the coupling strength g is greater than the individual radiative loss rates Γ and κ from the emitter and the cavity, respectively [120, 121]. Thus, the strong coupling condition is described as $g/(\Gamma, \kappa) \gg 1$, where, $g =$ the coupling constant, $\kappa =$ the cavity damping rate or photon loss rate from the cavity and $\Gamma =$ the spontaneous emission rate. In this regime, the emitter-cavity system shows a strong oscillatory behaviour. An energy quantum coherently oscillates

between the emitter and the cavity several times at a rate $\Omega = 2g$ (the vacuum Rabi frequency) before the energy is lost to the environment due to the cavity damping (Figure 1.10a). Strong coupling manifests itself in the spectral domain by a doublet, where the splitting between the two peaks corresponds to the Rabi frequency $\Omega = 2g$ of the oscillations, as shown in Figure 1.10b. The strong coupling regime provides an ideal platform for testing the field quantisation formalism, the resulting Jaynes-Cummings and for implementing several scalable quantum computation and networking protocols [120–122]. However, achieving strong coupling in silicon is challenging due to very weak oscillator strengths of D^0X transitions. Thus, in this thesis we aim for the systems to work in the weak coupling regime only.

The weak coupling regime is defined as the situation where the coupling strength g is smaller than the loss rates, i.e. $g/(\Gamma, \kappa) \ll 1$ and the initially excited emitter decays to the ground state with little or no oscillation. The emitter decays to the environment through the spontaneous emission of photons instead of undergoing coherent oscillations in the emitter-cavity system (as shown in Figure 1.10a for $\kappa > \Omega$). Therefore, the Vacuum Rabi splitting is not observed in the weak coupling regime and a single Lorentzian-shaped peak appears in the spectrum at the bare cavity frequency (Figure 1.10c). Finally, an emitter can experience a strong modification of its spontaneous emission in the weak coupling regime (Figure 1.10a). If the emitter is spectrally and spatially overlapping with a high-Q cavity mode, then its spontaneous emission rate can be drastically increased with respect to emission in a bulk medium. This phenomenon is known as the Purcell effect [116]. As we want to tune spontaneous emission rate, the interaction in the weak coupling regime is the focus of our interest. Weakly coupled emitter cavity systems with strong Purcell effects are also promising for improving the efficiency of indistinguishable and entangled photon sources [123, 124].

Now, in the weak coupling regime, Fermi's golden rule can describe spontaneous emission behaviour. In free space, the transition rate of an excited emitter interacting with the continuum of vacuum modes is expressed as

$$\frac{dP_{\mathrm{e}}(t)}{dt} = \left(\frac{2\pi}{\hbar^2}\right) |\langle \mu_{12} E \rangle|^2 D_{\mathrm{free}}(\omega), \tag{1.1}$$

where, $D_{\mathrm{free}}(\omega) = \frac{\omega^2 V}{\pi^2 c^3}$ = the free space density of states and μ_{12} = the dipole moment.

From equation (1.1), we can derive the free space spontaneous emission as $\Gamma_{\text{free}} = \frac{\omega_0^3 \mu_{12}^2}{3\pi\varepsilon_0\hbar c^3}$. If the emitter is located inside a cavity, the vacuum density of states, D_{free} gets modified due to the confinement. The modified vacuum density of states, D_{cav} of an emitter inside the cavity is expressed as

$$D_{\text{cav}}(\omega) = \frac{\kappa}{2\pi V} \frac{1}{(\kappa/2)^2 + (\omega_{\text{cav}} - \omega)^2}. \tag{1.2}$$

Using the transition rate of an excited emitter and the density of states for it inside the cavity, we can derive the cavity modified spontaneous emission for the emitter under consideration as following

$$\Gamma_{\text{cavity}} = \underbrace{\left(\frac{3}{4\pi^2} \cdot \frac{Q}{V/(\lambda/n)^3}\right)}_{\substack{\text{Ideal enhancement} \\ \text{factor}}} \cdot \overbrace{\frac{\kappa^2}{4(\omega - \omega_{\text{cav}})^2 + \kappa^2}}^{\text{Spectral matching}} \cdot \underbrace{\frac{\left(\vec{\mu_{12}}.\vec{E}(\vec{r})\right)^2}{|\vec{\mu_{12}}|^2 \quad \left|\vec{E}(\vec{r_{\text{M}}})\right|^2}}_{\substack{\text{Polarisation \&} \\ \text{spatial matching}}} \cdot \Gamma_{\text{free}}, \tag{1.3}$$

where the second and the third term of the right hand side of equation (1.3) define the effect of spectral matching and dipole alignment along with spatial matching, respectively. In an ideal & resonant condition, when the emitter is located at the field maxima and is dipole aligned with the field direction, the spontaneous emission enhancement factor becomes

$$F_{\text{p}} = \left(\frac{\Gamma_{\text{cavity}}}{\Gamma_{\text{free}}}\right)_{\text{ideal}} = \frac{3}{4\pi^2} \cdot \frac{Q}{V/(\lambda/n)^3}. \tag{1.4}$$

The factor F_{p} is known as *Purcell factor* that describes the enhancement of spontaneous emission in a cavity [125]. From equation (1.4) it is evident that, in the ideal case, the emission enhancement factor is directly proportional to the ratio of cavity quality factor (Q) to cavity mode volume (V). So, a carefully designed cavity in the weak coupling regime with high Q and low mode volume, under ideal spectral/spatial matching conditions, is capable of enhancing the radiative emission rate of an emitter by several orders of magnitude.

1.4 Thesis outline

This thesis describes the progresses achieved towards the enhancement of no-phonon D^0X emissions in silicon, which may, in the future, facilitate optical read-out of donor spins in silicon and long range qubit coupling. This thesis is organised in the following way:

Chapter 2 introduces the concept of photonic band gap and defect states. Photonic crystal (PhC) cavities and circular Bragg resonators (CBRs) are the main photonic structures explored in this work for enhancing radiative emission and its extraction. The theoretical framework of these cavities, their light confinement and far field emission properties are also discussed.

Chapter 3 describes photoluminescence (PL) measurements of ^{31}P $D^0X \rightarrow D^0$ transitions in various silicon and silicon-on-insulator (SOI) samples. The aim of PL measurements is to demonstrate the proof of concept for no-phonon (NP) emission from ^{31}P $D^0X \rightarrow D^0$ transitions in ion implanted silicon-on-insulator structures. We start the PL measurements with diffusion doped bulk samples, then continue the investigation through ion implanted bulk silicon samples, diffusion doped SOI samples and finally to ^{31}P implanted SOI samples of both Cz and Fz silicon. In this process, ion implantations have been carried out for deterministic donor positioning. Optimum windows for implantation and donor activation parameters have been identified, which allows the detection of ^{31}P D^0X emission from ion implanted SOI samples.

Chapter 4 discusses the design and simulation of photonic cavities for enhancing ^{31}P D^0X emission and its extraction. The Chapter starts with a brief review of the computational method (Finite-Difference Time-Domain (FDTD) approach) used for investigating the photonic structures. The light confinement and extraction properties of fundamental resonant modes around ^{31}P $D^0X \rightarrow D^0$ transitions for CBRs, 1D and planar L3 PhC cavities are simulated. The design of L3 PhC cavities is further tuned for high quality factors and improved light extraction.

Chapter 5 summarises the nanofabrication techniques developed and utilised for realising the designed photonic structures. A neon focussed ion beam (Ne-FIB) milling is implemented for making SIL structures in silicon. We attempt several fabrication approaches to realise PhC cavities. We start with a Ne-FIB milling and then also used a single layer resist based electron beam lithography (EBL) for fabricating PhC cavities.

Finally, we design and optimise a cost-effective, multilayer resist based EBL process recipe for fabricating photonic structures. Photonic cavities (PhC cavities and CBRs) are efficiently fabricated with this multilayer resist technique.

Chapter 6 presents the optical measurements/characterisations carried out on the photonic structures realised for enhancing ^{31}P D^0X emission and/or its extraction in silicon. We first describe the PL measurement carried out on SiSIL structures which have been implemented for efficient extraction of photons emitted in silicon. Photonic cavities (CBRs & PhC cavities) are capable of enhancing both emission and extraction in/from silicon. We have implemented the resonant-scattering (RS) technique with a cross-polarisation setup for optically characterising the fabricated photonic cavities. Intrinsic quality factors of CBRs and L3 PhC cavities have been extracted using RS measurements.

Finally, Chapter 7 summarises the work in this thesis and outlines future directions.

Chapter 2

Photonic cavities: Theoretical background

2.1 Photonic cavities

The study of photonic micro/nano cavities has become a prominent field of research over the last two decades. Photonic cavity devices can be physically implemented in several different geometries such as Fabry-Perot or Bragg gratings, whispering gallery resonators, photonic crystal resonators etc. Applications of these cavities are also diverse, which e.g. range from optical telecommunication, light emitting devices to cavity QED. In this work, our main goal is to enhance emission and extraction of photons from ^{31}P D^0X transitions in silicon. To this end, we investigate photonic crystal cavities and circular Bragg resonators as they are suitable for both light/photon confinement and efficient outcoupling. In the following sections, we discuss the principles governing the properties of these cavity devices.

2.2 Photonic crystals

Photonic crystals (PhCs) are periodic arrangements of dielectric media. With careful design, the propagation of the electromagnetic wave can be affected by periodic variations of the refractive index, analogous to the influence of a periodic ionic lattice on the movement of an electron. Thus, photonic crystals can provide allowed and forbidden bands for the propagation of photons with certain energies [126]. Due to this photonic bandgap property, photonic crystals are termed photonic semiconductors and can be used to confine and control light. There are various different designs and approaches

to implement photonic crystals depending on their properties and applications. The periodicity itself can be incorporated in different ways. Photonic crystals might have periodic variations in one, two or all three dimensions. Ideally three dimensional periodic structures would provide a complete bandgap, but they are very difficult to realise. So, for practical applications, 1D and 2D photonic crystals are mostly used. In the following subsections, we discuss the principles behind the emergence of photonic bandsturctures and the unique properties of photonic crystals.

2.2.1 The basic equation

In classical electromagnetism, the propagation of light in any media can be completely explained and predicted by the four macroscopic Maxwell's equations [126]. In SI units, the Maxwell's equations can be expressed as

$$\begin{aligned} \nabla \cdot \mathbf{B} &= 0, & \nabla \times \mathbf{E} + \frac{\partial \mathbf{B}}{\partial t} &= 0, \\ \nabla \cdot \mathbf{D} &= \rho, & \nabla \times \mathbf{H} - \frac{\partial \mathbf{D}}{\partial t} &= \mathbf{J}, \end{aligned} \tag{2.1}$$

where $\mathbf{E}$ and $\mathbf{H}$ are the electric and magnetic field vectors; $\mathbf{D}$ and $\mathbf{B}$ are the displacement and magnetic induction field vectors; ρ and $\mathbf{J}$ represent the densities of the free charge and current, respectively [126].

Solving the Maxwell's equations for a particular medium reveals not only the properties of light inside it but also how the propagation of light is influenced by the medium. So, the solutions to the Maxwell's equations in a periodic medium is the key to understand the unique optical properties of photonic crystals. The study of photonic crystals can be simplified by making several assumptions regarding the dielectric medium, field components, material dispersions etc. First of all, the dielectric medium is considered to be a low-loss, time-invariant one where there is no free charge, current and source of light inside the medium. So, the densities of free charges and current can be set to zero ($\rho = 0$ and $\mathbf{J} = 0$) in the Maxwell's equations (2.1). Furthermore, for a linear and isotropic medium, we can neglect the material dispersion and consider only the real and positive values of the relative permittivity. This assumption additionally simplifies the relations between the electric (magnetic) fields and the displacement (magnetic induction) fields, leading to $\mathbf{D}(\mathbf{r}) = \varepsilon_0 \varepsilon(\mathbf{r}) \mathbf{E}(\mathbf{r})$ and $\mathbf{B}(\mathbf{r}) = \mu_0 \mu(\mathbf{r}) \mathbf{H}(\mathbf{r})$,

where, $\varepsilon_0 \approx 8.854 \times 10^{-12}$ F/m is the vacuum permittivity, $\varepsilon(\mathbf{r})$ is the relative permittivity, $\mu_0 = 4\pi \times 10^{-7}$ H/m is the vacuum permeability and $\mu(\mathbf{r})$ is the relative magnetic permeability. It has been found that $\mu(\mathbf{r}) \approx 1$ for most dielectric materials of interest which reduces the relation between the magnetic field and magnetic induction to $\mathbf{B}(\mathbf{r}) = \mu_0 \mathbf{H}(\mathbf{r})$.

Putting all these assumptions together, the Maxwell's equations (2.1) can be incorporated into a Basic equation [126]

$$\nabla \times \left(\frac{1}{\varepsilon(\mathbf{r})} \nabla \times \mathbf{H}(\mathbf{r}) \right) = \left(\frac{\omega}{c} \right)^2 \mathbf{H}(\mathbf{r}), \tag{2.2}$$

where, c $(= 1/\sqrt{\varepsilon_0 \mu_0})$ is the speed of light in vacuum. The basic equation (2.2) can be solved to find the modes $\mathbf{H}(\mathbf{r})$ and their corresponding frequencies for any system with a permittivity distribution $\varepsilon(\mathbf{r})$. If the magnetic field $\mathbf{H}(\mathbf{r})$ is determined, the electric field $\mathbf{E}(\mathbf{r})$ corresponding to a solution can also be extracted from the following relation

$$\mathbf{E}(\mathbf{r}) = \frac{j}{\omega \varepsilon_0 \varepsilon(\mathbf{r})} \nabla \times \mathbf{H}(\mathbf{r}). \tag{2.3}$$

Thus, within the assumptions considered above, the solution of the basic equation (2.2) reveals all the necessary information of a photonic system and allows to determine the dispersion relation with photonic bandstructure. Hence, to investigate the photonic bandstructure of a particular photonic system such as photonic crystals, photonic crystal cavities etc., we need to solve the basic equation and extract the modes $\mathbf{H}(\mathbf{r})$ satisfying the transversality requirement for a given frequency [126].

2.2.2 Solutions and properties of the basic equation

The Basic equation (2.2) can also be treated as an eigenvalue problem. According to the definition, an eigenvector is a vector that gives back a scalar multiple of itself when operated on by any given operator. The multiplicative constant/scalar quantity is known as the eigenvalue. Thus, if the left hand side is expressed as an operator $\hat{\Theta}$ acting on the magnetic field $\mathbf{H}(\mathbf{r})$, the Basic equation can be rewritten in the form of an eigenvalue problem

$$\hat{\Theta} \mathbf{H}(\mathbf{r}) = \left(\frac{\omega}{c} \right)^2 \mathbf{H}(\mathbf{r}), \tag{2.4}$$

where the eigenvectors/eigenfunctions, $\mathbf{H}(\mathbf{r})$, are the allowed fields in the structure, i.e., the electromagnetic modes of the system. In this form, the basic equation is also known as the linear eigenvalue Helmholtz equation. The permittivity distribution, $\varepsilon(\mathbf{r})$ is constant in the case of homogeneous media. So, solving the Helmholtz equation for homogeneous media is relatively simple. The solutions can be plane wave modes or spherical waves depending on the reference frame under consideration. It can also be shown that the operator $\hat{\Theta}$ is Hermitian and all of its eigenvalues are non-negative [126]. All these properties gurantee that the solutions of the basic equation are always orthogonal and have real eigenvalues $(\omega/c)^2$. Thus, the equation $\hat{\Theta}\mathbf{H}(\mathbf{r}) = \left(\frac{\omega}{c}\right)^2 \mathbf{H}(\mathbf{r})$ can be used efficiently to treat periodic systems.

Finally, the basic equation shows yet another very interesting property of not having fundamental length scale. For example, if a scaled version of the dielectric structure $\varepsilon(\mathbf{r})$ is considered, it can be expressed by $\varepsilon'(\mathbf{r}) = \varepsilon(\mathbf{r}/s)$ for a scaling factor s. Inserting the changed variables $\mathbf{r}' = s\mathbf{r}$ and $\nabla' = \nabla/s$ into the equation (2.2) we get the following

$$s\nabla' \times \left(\frac{1}{\varepsilon(\mathbf{r}'/s)} s\nabla' \times \mathbf{H}(\mathbf{r}'/s) \right) = \left(\frac{\omega}{c}\right)^2 \mathbf{H}(\mathbf{r}'/s), \tag{2.5}$$

where we can see that $\varepsilon(\mathbf{r}'/s) = \varepsilon'(\mathbf{r}')$. So, equation 2.5 can be rewritten as

$$\nabla' \times \left(\frac{1}{\varepsilon'(\mathbf{r}')} \nabla' \times \mathbf{H}(\mathbf{r}'/s) \right) = \left(\frac{\omega}{cs}\right)^2 \mathbf{H}(\mathbf{r}'/s), \tag{2.6}$$

which is nothing but the basic equation itself. Thus, if the eigenvalues and eigenfunctions of the basic equation are determined for a structure, they can be used for any physical size or wavelength, by an appropriate scaling. This feature is very important for designing photonic structures and the bandgap engineering. The designs are size independent and when the desired properties are found, they can be fabricated in any suitable scale to perform experiments in varying wavelength ranges.

2.2.3 Photonic bandstructure

A homogeneous medium has a continuous translational symmetry in all three dimensions, because its properties remain unchanged when translated through the same distance in a certain direction e.g., $\varepsilon(\mathbf{r}) = \varepsilon(\mathbf{r} + \mathbf{d})$. The propagation of photons in a homogeneous and isotropic dielectric medium can be depicted by relating the angular

wavenumber, $|\mathbf{k}|$ (i.e. the magnitude of the wavevector) to the angular frequency, ω of the wave under consideration. Thus, the photonic bandstructure can be obtained by plotting the relationship between the wave vector $\mathbf{k}$ and the frequency ω of the light. This association between the wavenumber and frequency is known as the dispersion relation, $\omega = c\,|\mathbf{k}|\,/n$, where n is the refractive index of the dielectric medium ($n = \sqrt{\varepsilon(\mathbf{r})\mu(\mathbf{r})} \approx \sqrt{\varepsilon(\mathbf{r})}$). The relation is derived from the fact that the plane waves, $\mathbf{H}(\mathbf{r}) = \mathbf{H}_0 e^{j\mathbf{k}\cdot\mathbf{r}}$ are in effect solutions of the basic equation (2.2) with eigenvalues $(\omega/c)^2 = |\mathbf{k}|^2/\varepsilon(\mathbf{r})$. In the case of a homogenous and isotropic dielectric medium, the dispersion relation shows a linear relationship between the angular frequency (as shown in Figure 2.1b) and the ratio of the wave vector to the material refractive index. On the other hand, the dispersion relation shows a direction dependent variation for a medium in which the refractive index changes with the direction.

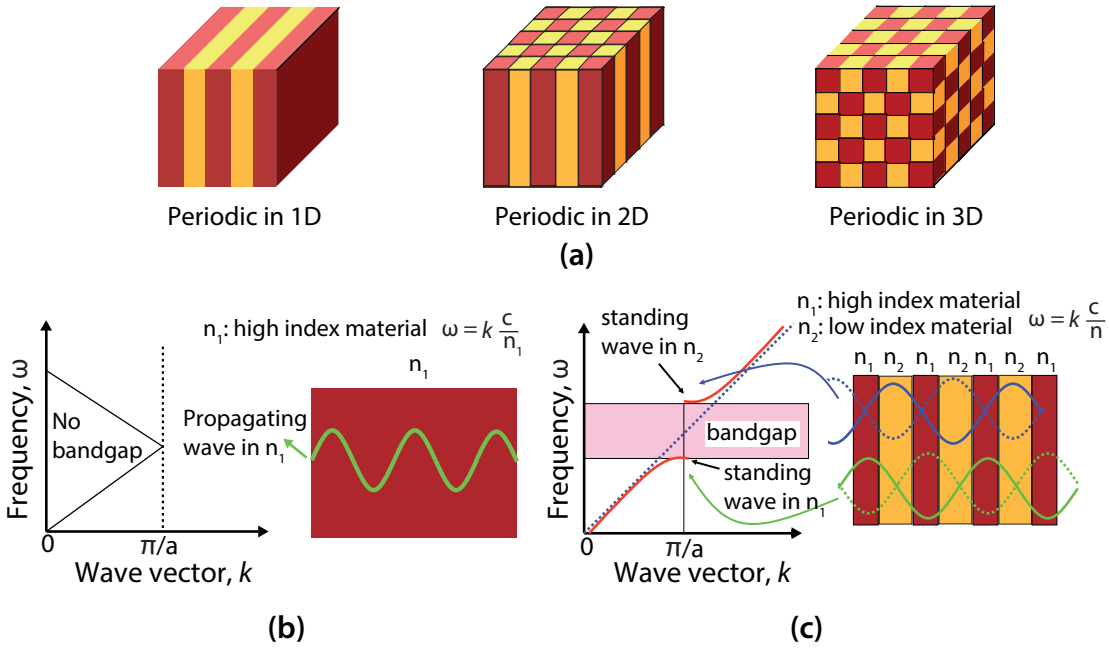

Figure 2.1: Photonic crystals and their bandgap property: (a) an example of periodic dielectric structures with different dimensionality, (b) there is no bandgap in the absence of a periodic variation of the refractive index, (c) opening of a bandgap due to the splitting of modes in case of a periodic index variation, images are adapted from [126]

In the case of a photonic crystal, the dielectric structure experiences a periodic variation of the refractive index ($n = \sqrt{\varepsilon(\mathbf{r})}$) in one, two or three dimensions, as shown in Figure 2.1a. Thus, $\varepsilon(\mathbf{r})$ can be expressed as a periodic function for multiples of a fixed step length, called the lattice constant $\mathbf{a}$. The function can be expressed as

$\varepsilon(\mathbf{r}) = \varepsilon(\mathbf{r}+\mathbf{R})$ ($\mathbf{R}$ is an integer multiple of $\mathbf{a}$) which shows discrete translational symmetry. These symmetry and periodicity properties have to be taken into account to extend the dispersion relation for the periodic structures. According to the Bloch-Floquet theorem [126, 127], for a periodic environment with discrete translational symmetry, the periodicity $\varepsilon(\mathbf{r}) = \varepsilon(\mathbf{r}+\mathbf{R})$ of the system can be translated to the solution of the basic equation (2.2) and expressed as

$$\mathbf{H}_{\mathbf{k}}(\mathbf{r}) = e^{j\mathbf{k}\cdot\mathbf{r}}\mathbf{u}_{\mathbf{k}}(\mathbf{r}), \tag{2.7}$$

where

$$\mathbf{u}_{\mathbf{k}}(\mathbf{r}) = \sum_{\mathbf{G}} \mathbf{C}_{\mathbf{G}}(\mathbf{k}) e^{j\mathbf{G}\cdot\mathbf{r}}$$

is a periodic envelop function of the real space lattice; $\mathbf{G}$ and $\mathbf{C}_{\mathbf{G}}$ are the reciprocal lattice vector and complex Fourier series coefficient, respectively. The periodic envelope function $\mathbf{u}_{\mathbf{k}}(\mathbf{r})$ retains the same periodicity and symmetries as $\varepsilon(\mathbf{r})$: $\mathbf{u}_{\mathbf{k}}(\mathbf{r}) = \mathbf{u}_{\mathbf{k}}(\mathbf{r}+\mathbf{R})$. The equation (2.7) is known as the Bloch function [126] and when inserted into the basic equation leads to an eigenvalue problem with eigenfunction, $\mathbf{u}_{\mathbf{k}}(\mathbf{r})$ and eigenvalue, $(\omega(\mathbf{k})/c)^2$. Under the periodic boundary condition, the eigenvalues become discrete $(\omega_n(\mathbf{k})/c)^2$, where, the index n gives the discrete eigenvalues. For each value of $\mathbf{k}$, there are n number of modes or solutions with discretely spaced frequencies $\omega_n(\mathbf{k})$. The behaviour of these frequency modes $\omega_n(\mathbf{k})$ as a function of $\mathbf{k}$ give rise to the photonic bands i.e., the photonic bandstructure. A photonic bandgap is defined by the range of frequencies where no solutions or allowed modes exist for any wavevector $\mathbf{k}$. For a uniform dielectric (homogeneous) medium, there exists no bandgap in the photonic bandstructure (Figure 2.1b). This becomes clear, if we artificially fold the modes at point $k = \pi/a$ (positive half of the Brillouin zone) for the case where there is no periodic variation in the refractive index. It already mentioned before that the dispersion is linear for a homogeneous medium. When the line from the negative side of the wavevector axis is folded from $\frac{2\pi}{a}$, the backward line crosses the forward line at $\frac{\pi}{a}$ and there exists no gap in between, as shown in Figure 2.1b. For a medium with periodically modulated index, a frequency gap arises between the upper and lower branches of the dispersion lines, which assures that the symmetry conditions of the systems are satisfied. The symmetry condition allows only the presence of two standing waves at

the crossing point ($k = \frac{\pi}{a}$) and they can be localised only either in the high or low index medium, as in Figure 2.1c. This gives rise to two different frequencies for these modes and ultimately results in the formation of a photonic bandgap where propagating modes are forbidden. The width of this photonic bandgap depends on the refractive index contrast in the periodically modulated dielectric structure [126, 128]

2.2.4 One-dimensional photonic crystals

As already mentioned, photonic crystals (PhCs) can be realised by implementing periodic index variation in one-, two-, or three-dimensions and are correspondingly termed as 1D, 2D and 3D PhCs. 3D PhCs are capable of providing ideal/complete bandgap properties [126]. To date, various fabrication approaches have been proposed and attempted to realise 3D PhCs with different levels of success [126, 129–136]. However, an efficient realisation of 3D PhCs in the optical and/or near infra-red regime still remains challenging [135, 137]. So, in this work, we consider and discuss 1D and 2D photonic crystals only.

The simplest possible PhC structure is the 1D PhC where the dielectric index modulation is implemented in one direction. The index variation coincides with the direction of the electromagnetic propagation and the remaining two directions are homogeneous. This structure is basically formed from multiple layers of alternating materials with different refractive index, as shown in Figure 2.2a. This multilayer stack is also known as a distributed Bragg reflector (DBR), where each interface between two materials causes a partial reflection of the incident light/wave. So, the incident light experiences multiple reflections and refractions inside the DBR structure when it passes through each layer boundary. If all the reflected light components from the interfaces interfere constructively, then there will be a very strong reflection for the wavelength range under consideration. As a result, the range of wavelengths that are reflected cannot propagate through the DBR structure and gives rise to the photonic stopband or bandgap. The width, position etc. of the bandgap depend on the refractive index contrast, angle of incident light and above all on the constructive inference conditions. When each layer of the multilayer stack has a quarter-wavelength optical thickness, the most efficient constructive interference takes place. Thus, for a quarter-wavelength stack the largest photonic bandgap is observed. In Figure 2.2b, the dispersion behaviour

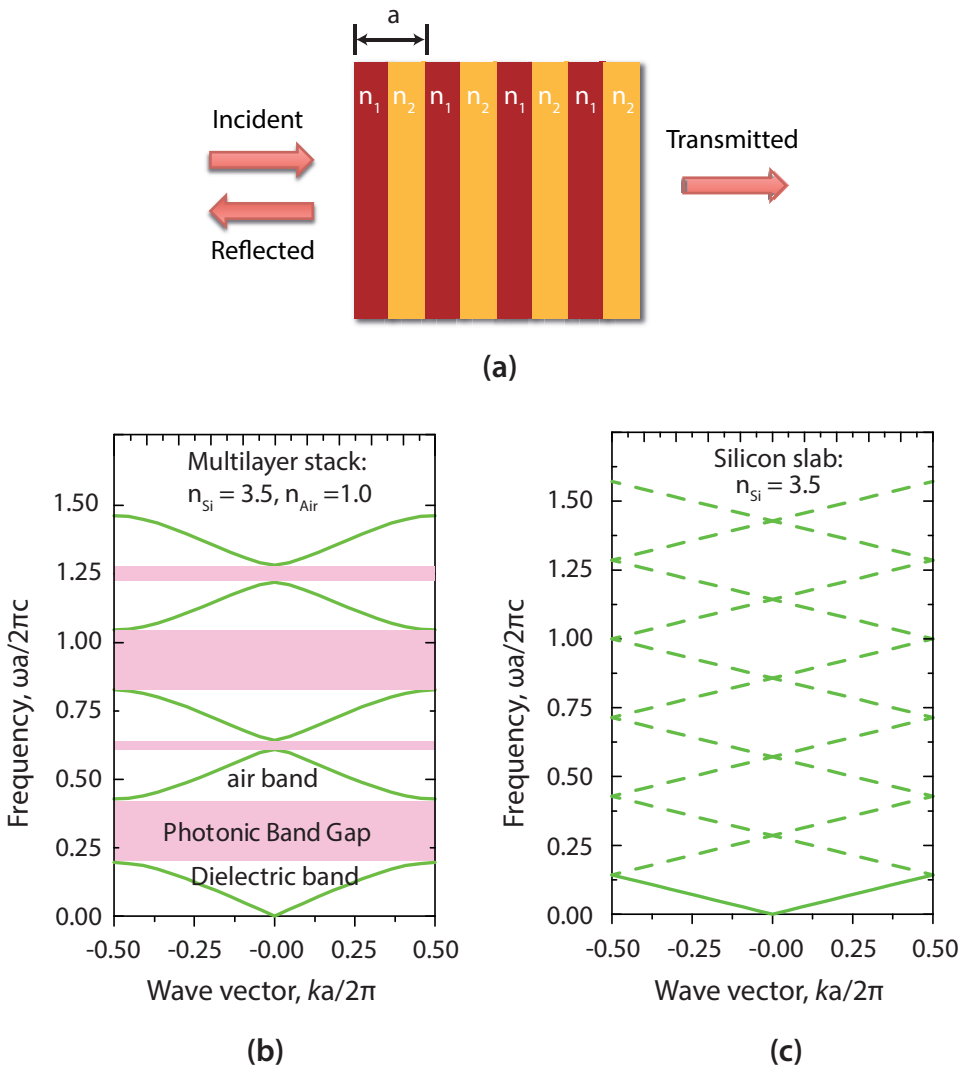

Figure 2.2: One dimensional photonic crystals (PhCs) with dispersion behaviour: (a) a multilayer stack with periodic index variation in one dimension (distributed Bragg reflector), the dispersion relation for (b) a silicon-air multilayer, quarter-wavelength stack/DBR and (c) a uniform silicon slab, where the dashed lines show the folding effect of applying the Bloch theorem with an artificial periodicity a.

of a silicon-air stack of quarter-wavelength layers is shown. In the dispersion plot, the frequency and wave vector are plotted in dimensionless units $\omega a/2\pi c$ and $ka/2\pi$, respectively. This is done in order to take the scaling property of the PhC structures into account. In the previous subsection, we have already discussed the principle behind the opening of bandgaps from the dispersion relation perspective. For a periodic structure, two modes with Bloch wavenumbers $k_z = k'_z = k_z + m \cdot 2\pi/a$ are equivalent since they correspond to the same phase factor. Thus, a complete solution of the basic equation for all modes can be extracted from a wave vector value interval of $k = 2\pi/a$ in the direction of the primitive lattice vector. So, to show the dispersion relation we plot the

solutions within the non-redundant range of $-\pi/a < k_z < \pi/a$ which is known as the Brillouin zone. In the case of 1D PhC/DBR, the bandgap appears at the edge of the Brillouin zone ($k = \pi/a$), as in Figure 2.1b. The dispersion relation plotted here is for a normal incidence to the layer boundary. However, the bandgap position will vary with the angle of incidence as the optical path length varies if the slab is rotated [126, 138]. In Figure 2.1c the dispersion diagram for an infinitely long silicon slab (homogeneous dielectric medium) is shown to compare with the case of the multilayer stack. For any homogeneous dielectric medium, the dispersion is linear ($\omega(k) = ck/n$) i.e., allowed modes lie along the light line. Now, if an artificial periodicity with a period a is induced in the homogeneous medium ($n_1 + n_2 = n_{\mathrm{Si}}$), k would repeat itself outside the Brillouin zone and the light line folds back into the zone when it reaches an edge (as shown by the dashed lines in Figure 2.1c). This can be considered as a way of relabeling of the mode solutions in which $k + 2\pi/a$ is replaced by k. Furthermore, the $k = -\pi/a$ mode lies at an equivalent wavevector to the $k = \pi/a$ mode, and at the same frequency. So there is a degeneracy at the zone boundary, $k = \pi/a$ and there exists no bandgap for this homogeneous dielectric medium. Comparing the dispersion relations in Figure 2.1b & c, we observe that the PhC structure behaves similarly to a homogeneous medium for lower frequencies independently on the configuration of materials. This is because the period of the structure is much smaller than the wavelength of the propagating light, so that the wave perceives it as a homogeneous-like medium. However, as the frequency increases, the dispersion relation stops behaving linearly and tends to flatten. The flattening mostly takes place at the edges of the Brillouin zone and leads to the opening of photonic bandgap (PBG).

When a 1D PhC is realised in practice, the dimensions of the structure cannot be infinite. Both the direction and length of the index variation and the other two dimensions are of finite extent unlike in the case of the ideal proposal. Thus, a practical 1D PhC is fabricated with finite width and thickness. Periodicity can be achieved in many different ways. One of the most common geometry is a periodic dielectric waveguide with circular air holes. This type of structures exhibit photonic bandgaps in their periodic direction. In addition, they can confine light in the other two directions by the principle of index guiding/total internal reflection. Photonic band structure for such a suspended 1D PhC waveguide has been shown in Figure 2.3, with a schematic of the

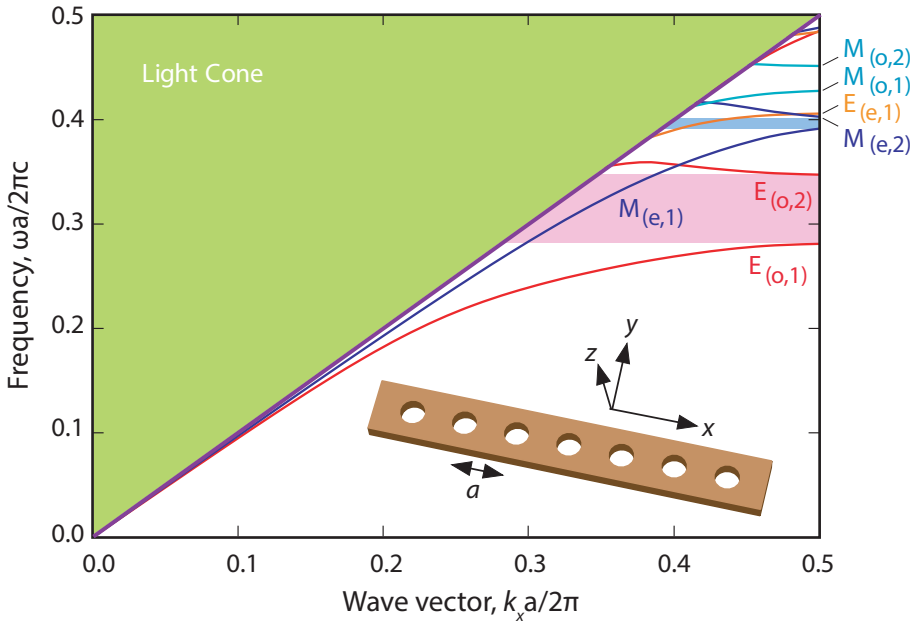

Figure 2.3: Photonic band structure for a 1D PhC with finite thickness and width: The Band diagram for the PhC waveguide structure has been plotted for the range of wave vectors within the irreducible Brillouin zone. For the PhC structure, the wave vector k is conserved along the direction of periodic variation, there exists a light cone $\omega \geq ck$ of the extended states in air and the discrete guided modes below the light line. The image is reproduced from [126]

PhC geometry in the inset. In the PhC waveguide, air holes are designed to appear with periodic spacing 'a' along the x-axis. Due to the periodic index variation, the wave vector k is conserved (Bloch's theorem) along the direction x in the 1D PhC waveguide and there exists a light cone ($\omega \geq ck$) beneath which the discrete guided modes are allowed. For a 1D PhC waveguide, the Brillouin zone is finite and the range $\pi/a < k < 2\pi/a$ is equivalent to the range $-\pi/a < k < 0$. Again, the range $-\pi/a < k < 0$ is the reverse of the $0 < k < \pi/a$ irreducible Brillouin zone. A light cone can be assigned within each of these zones. The tip of the original light cone, which occurred at $k = 0$ for the unpatterned waveguide, is now repeated periodically at $k = 2\pi/a, 4\pi/a, \ldots$. Similarly, the lowest band of guided modes, starting at zero frequency from $k = 0$, must flatten at $k = \pi/a$ and then bend downwards to return to zero frequency at $k = 2\pi/a$. This causes a bandgap to open up between the first two guided modes. However, the opened bandgap is considered incomplete because only the guided modes are excluded from the gap, whereas radiating modes (the modes within the light cone) exist for any ω.

In the band diagram (Figure 2.3), only the range of wave vectors within the irreducible Brillouin zone is shown. The purple line is the light line ($\omega = ck_{\|}$). Above this

line, there exists allowed modes for every possible frequency. The green shaded region above the light line ($\omega > ck_{\|}$) is known as the light cone which represents the continuum of states extending into both the substrate dielectric and the air/media around it. There are several guided bands which are complex in nature due to two mirror symmetry planes ($z = 0$ and $y = 0$) supported by the PhC waveguide structure. All these modes can be classified as even or odd with respect to both z and y reflections. The z-even and odd modes are similar to Transverse Electric (electric fields are in the plane of periodic variation) and Transverse Magnetic (electric fields are in the plane of periodic variation) modes, respectively. Thus, in the band structure z-even modes are labeled with "E" and z-odd with "M". Subscripts "e" and "o" are used to indicate the even and odd modes under y reflection, and a numerical subscript for the band number. For example, in the band diagram (Figure 2.3), the label $\mathrm{E}_{(\mathrm{o},2)}$ indicates the z-even, y-odd mode from the second band. The band structure also reveals that the PhC waveguide opens bandgaps for each symmetry type individually and the largest gap is observed between $\mathrm{E}_{(\mathrm{o},1)}$ and $\mathrm{E}_{(\mathrm{o},2)}$. Finally, one of the most interesting and useful property of this type of 1D PhCs is that they can act as high quality cavities when defects states are engineered in the bandgap. The idea of the 1D PhC cavity will be introduced later in this chapter.

2.2.5 Two dimensional photonic crystals

A two dimensional photonic crystal is implemented by periodically modulating the refractive index of the dielectric media in two directions while the third dimension/direction remains homogeneous. The principles of light propagation in 2D PhCs is very similar to those encountered in the case of 1D PhCs as the same physics governs the Bloch states and band-structure formation. However, the additional dimension in the 2D PhC increase the complexity of the system when we consider the two dimensional lattice or polarization of the EM modes. There are several different geometries through which a two dimensional periodic variation can be realised. The square and the triangular lattices are two of the most common examples of such geometries, as shown in Figure 2.4. The lattices can be defined by two arbitrarily chosen lattice vectors $\mathbf{a}_1$ and $\mathbf{a}_2$. These direct lattice vectors then determine the reciprocal lattice vectors $\mathbf{b}_1$, $\mathbf{b}_2$, $\mathbf{b}_i \cdot \mathbf{a}_i = 2\pi\delta_{ij}$, which specifies the reciprocal lattice.

A 2D PhC can provide bandgaps in the xy plane where periodic index variations

are implemented and thus, it can prevent light from propagating in any direction within the xy plane. In the ideal case, the system is considered infinitely long in the homogeneous z-direction. Oscillatory modes can exist in this direction as there is no restrictions imposed for k_z. The system holds discrete translational symmetry in the xy plane, $\varepsilon(\mathbf{r}) = \varepsilon(\mathbf{r}+\mathbf{R})$ where $\mathbf{R}$ is a linear combination of the primitive lattice vectors $\vec{a}_1$ and $\vec{a}_2$. Using the Bloch's theorem and considering the the values of $k_{\|}$ $(= \sqrt{k_x^2 + k_y^2})$ within the Brillouin zone, the sustainable EM modes can be expresses as

$$\mathbf{H}_{(n,k_z,\mathbf{k}_{\|})}(\mathbf{r}) = e^{j\mathbf{k}_{\|}\cdot\rho} e^{jk_z z} \mathbf{u}_{(n,k_z,\mathbf{k}_{\|})}(\rho), \tag{2.8}$$

where n gives the band numbers for labelling the modes, ρ is the projection of $\mathbf{r}$ in the xy plane and $\mathbf{u}(\rho)$ is a periodic function, $\mathbf{u}(\rho) = \mathbf{u}(\rho + \mathbf{R})$, for all lattice vectors $\mathbf{R}$. The modes of the 2D PhC structure appears very similar to the case of the 1D PhCs except from the fact that $k_{\|}$ is restricted in the Brillouin zone and k_z is unrestricted. The role of these two vectors are opposite in the case of a 1D PhC. In 2D PhC structures,

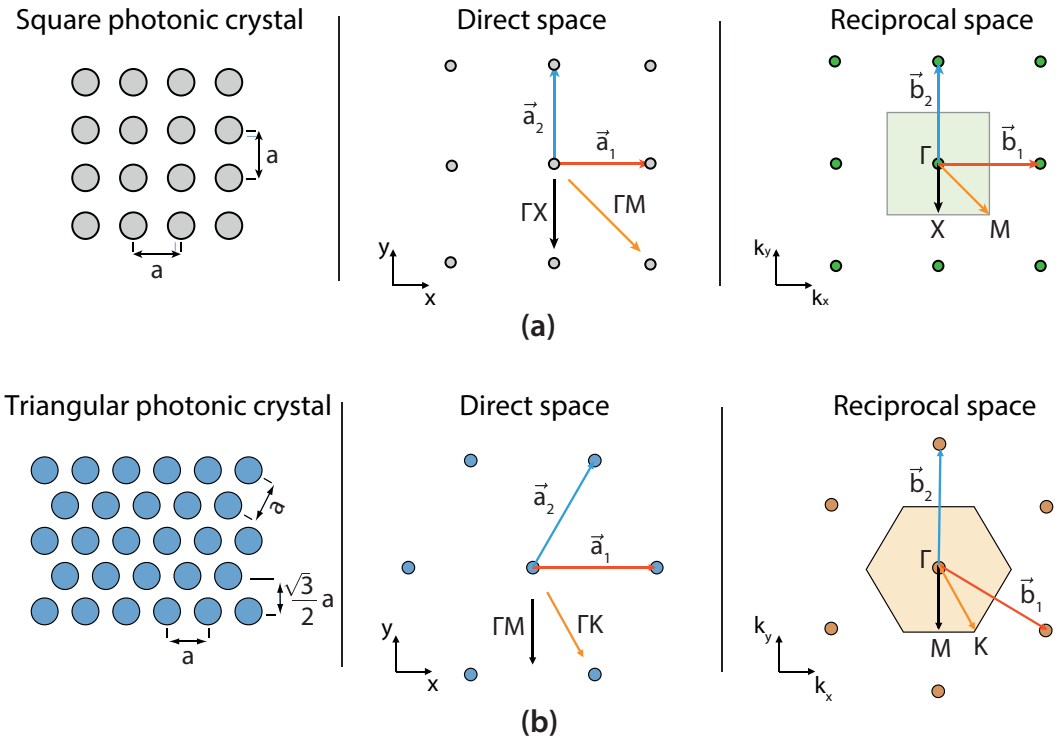

Figure 2.4: Two dimensional lattice geometry for photonic crystals (PhCs): Two-dimensional photonic crystal with circular holes with a lattice constant **a**, direct basis vectors ($\vec{a}_1$, $\vec{a}_2$) and the reciprocal lattice ($\vec{b}_1$, $\vec{b}_2$) - (a) square lattice and (b) triangular/hexagonal lattice.

modes propagating parallel to the xy plane ($k_z = 0$) do not vary when reflected through the xy plane. This mirror symmetry condition gives rise to the allowed modes with two different polarisations in the case of 2D PhCs. These polarisations are orthogonal and known as Transverse-electric (TE) and Transverse-magnetic (TM). TE polarisation possesses nonzero E_x, E_y and H_z components whereas TM polarisation have nonzero H_x, H_y and E_z. Thus, in 2D PhC structures, TE modes retain $\mathbf{H}$ normal to the plane ($\mathbf{H} = H(\rho)\hat{\mathbf{z}}$) and $\mathbf{E}$ in plane ($\mathbf{E}(\rho) \cdot \hat{\mathbf{z}} = 0$); while opposite is true for TM modes: $\mathbf{E} = E(\rho)\hat{\mathbf{z}}$ and $\mathbf{H}(\rho) \cdot \hat{\mathbf{z}} = 0$. TE and TM modes can lead to quite different band structures where their bandgaps do not overlap. Careful bandgap engineering i.e., device design is required to obtain a complete/overlapping bandgap for both polarisations.

In Figure 2.5, the photonic bandstructure for a 2D PhC with a triangular lattice of air-holes is illsutrated. Figure 2.5a shows the band structure for an ideal 2D PhC where the system has an infinite extension in the third dimension. It has been observed that a lattice of isolated high-index dielectric material opens a TM bandgap where as connected lattices of high index material support a TE bandgap [126]. To show the band structures of 2D PhCs, the frequency is plotted against the in-plane wave vector $\mathbf{k}_{\parallel}$. Starting from left (e.g., Figure 2.5a), the in-plane wave vector follows the triangular edge of the irreducible Brillouin zone (from Γ to M to K) along the horizontal axis. A carefully designed triangular lattice of air holes in high-index dielectric media can act as a compromise between two kinds, supporting both TE and TM bandgaps. Thus, a 2D PhC with triangular lattice of air holes is capable of providing a complete bandgap, as illustrated in Figure 2.5a. Since the third dimension is considered as a homogeneous dielectric with an infinite extent, there is no restriction for out-of plane wave propagation and the bandstructure for the out-of-plane direction shows no bandgap. A detailed analysis of all the aspects for photonic band structures are beyond the scope of this work and we will limit our discussion for in-plane propagation only.

Finally, when realised in practice, 2D photonic crystals have a finite thickness in the third dimension. This finite thickness enables 2D PhC slabs to exhibit qualitatively new behaviour. With the incorporation of defect states, photonic cavities/waveguides can be implemented with 2D PhC slabs. The formation of photonic crystal cavities is discussed in detail in the next section as photonic cavities are the main focus of this work. In Figure 2.5b, the band structure for a 2D PhC slab of finite thickness is

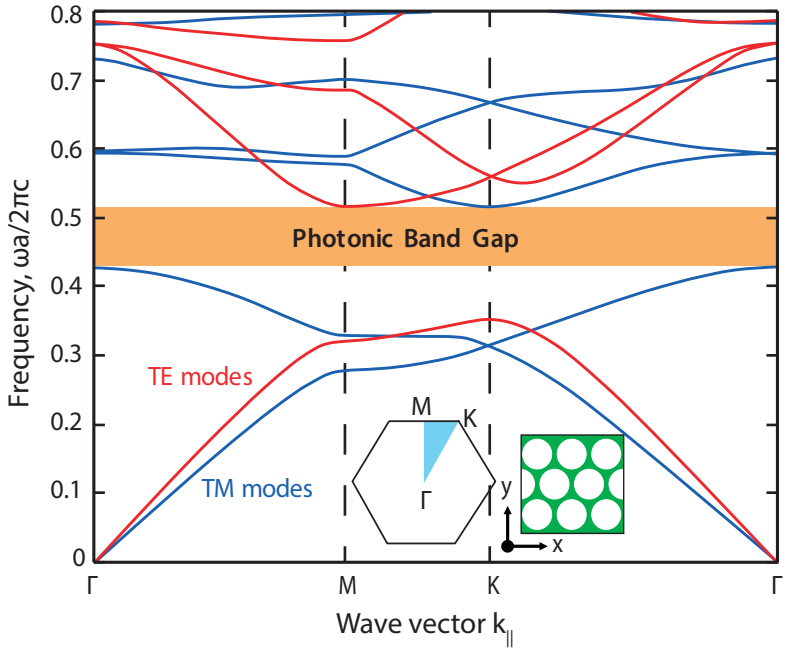

(a)

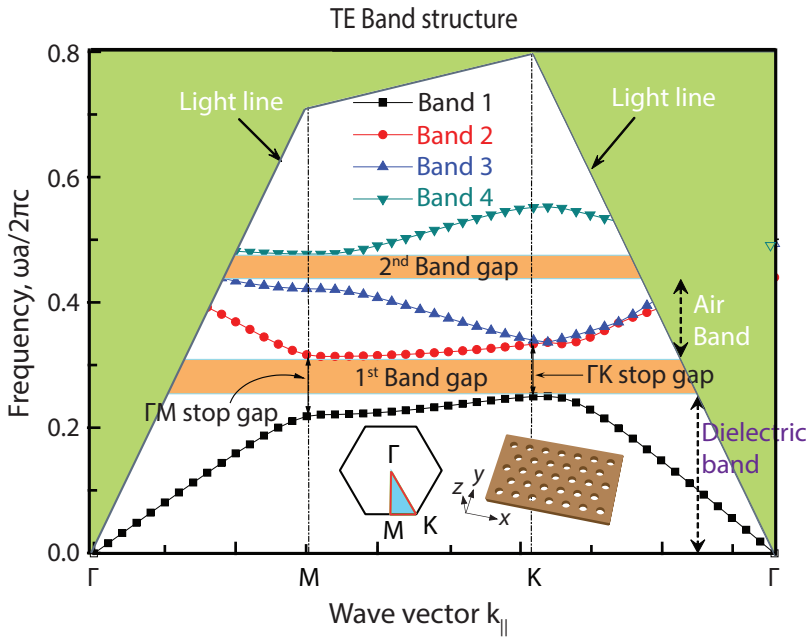

(b)

Figure 2.5: Photonic band structure for two dimensional photonic crystals: Band structures for a 2D PhC with triangular lattice of air columns in a dielectric substrate - (a) A complete bandgap for an ideal 2D PhC where the substrate is assumed to have infinite thickness in z-direction. TM and TE bands are plotted with blue and red lines, respectively. The high-symmetry points at the corners of the irreducible Brillouin zone are shown in the inset. (b) Band structure for a 2D PhC slab with a finite thickness in the third dimension (along z-axis). Four TE bands have been plotted with different colors in the band structure below the light-line. The open bandgaps are for TE modes only. Images are adapted from [126, 139]

illustrated. For a suspended membrane/slab 2D PhC (Inset, Figure 2.5b), there exist discrete translational symmetries in the two directions of periodic index modulation. With such symmetry conditions, the in-plane wave vector $\mathbf{k}_{\parallel} = (k_x, k_y)$ is maintained but the out-of-plane wave vector k_z is not conserved. The projected band structure for a suspended slab 2D PhC is obtained by plotting ω versus $\mathbf{k}_{\parallel}$ in the irreducible Brillouin zone of the 2D lattice. Similar to the case of practical 1D PhC, the band diagram of a slab 2D PhC depicts the extended modes propagating in air (the light cone with $\omega \geq c|\mathbf{k}_{\parallel}|$) and the discrete guided bands below the light cone. The guided bands are discrete and pulled down below the light cone due to the high refractive index of the substrate membrane and the modes can be categorised into TE-like (even) and TM-like (odd) modes. In Figure 2.5b, only the TE bands are shown as the triangular/hexagonal lattice in the suspended slab PhC favours the bandgap for TE modes.

2.3 Photonic crystal cavities

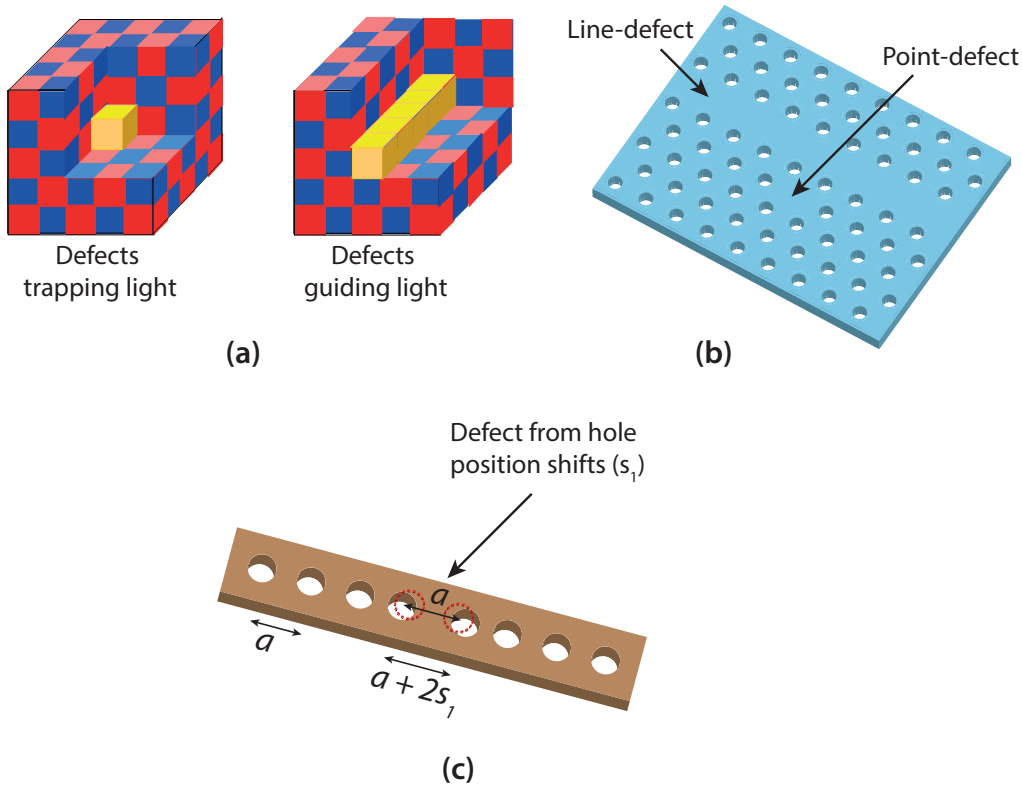

Figure 2.6: Photonic crystal (PhC) cavities: schematics of defects in periodic dielectric structures with a (a) 3D, (b) 2D and (c) 1D index variation, images are adapted from [126]

Incorporating defects into photonic crystals can give rise to very interesting phe-

nomena. Depending on the type of intentional defects, single or multiple allowed modes are created in in the bandgap. These allowed and confined modes can be used for trapping or guiding light very efficiently. Schematics of defects in periodic dielectric structures i.e. photonic crystals have been shown in Figure 2.6. In principle, defects in 3D periodic structures (Figure 2.6a) would provide the most efficient light trapping or guiding effect. However, fabricating 3D periodic structures/PhCs efficiently and incorporating deliberate defects into them is challenging [135, 140–145]. Thus, we focus on 2D and 1D PhCs and the incorporation of defects in them (Figure 2.6b & c) to achieve high-Q photonic cavities.

2.3.1 Photonic crystal cavities: introduction of defects

Defects are created in the PhC structure by breaking the periodicity of the perfect lattice. Similar to periodic variations in PhCs, defects can also be incorporated in many different ways. For example, for a multilayer 1D periodic structure, a defect state will be created if we change the width of a layer from its periodic value. Introducing the defect breaks the periodicity and translational symmetry which in turn allows localised modes inside the bandgap. Localised modes exist in the bandgap and exponentially decay when they enter the crystal. This is achieved due to the frequency-selective mirroring of the periodic structures around the defects, localising light of certain frequencies. In section (2.2.4), we discussed a practical 1D PhC structure implemented with a periodic array of circular air holes. There are many ways to introduce a cavity in this practical 1D PhC, for example, by changing the radius of a single hole, the spacing between a pair of holes or using a combination of both. Here, we start our discussion with a 1D PhC cavity implemented by increasing the spacing between a pair of air holes. The holes under consideration are shifted away from each other and a defect is formed due to the extra dielectric material between the hole pair (as shown in the inset of Figure 2.7a). The band diagram of such a cavity is shown in Figure 2.7a. The presence of extra dielectric material in the structure forces a mode down into the bandgap from the upper allowed [$E_{(o,2)}$] band and gives rise to a TE-like defect state, as in in Figure 2.7a. From the band diagram, it can be observed that the bandgap for the practical 1D PhC cavity is incomplete due to the presence of the light cone modes for all frequencies. Thus, the defect states of a practical 1D PhC cavity are leaky resonances

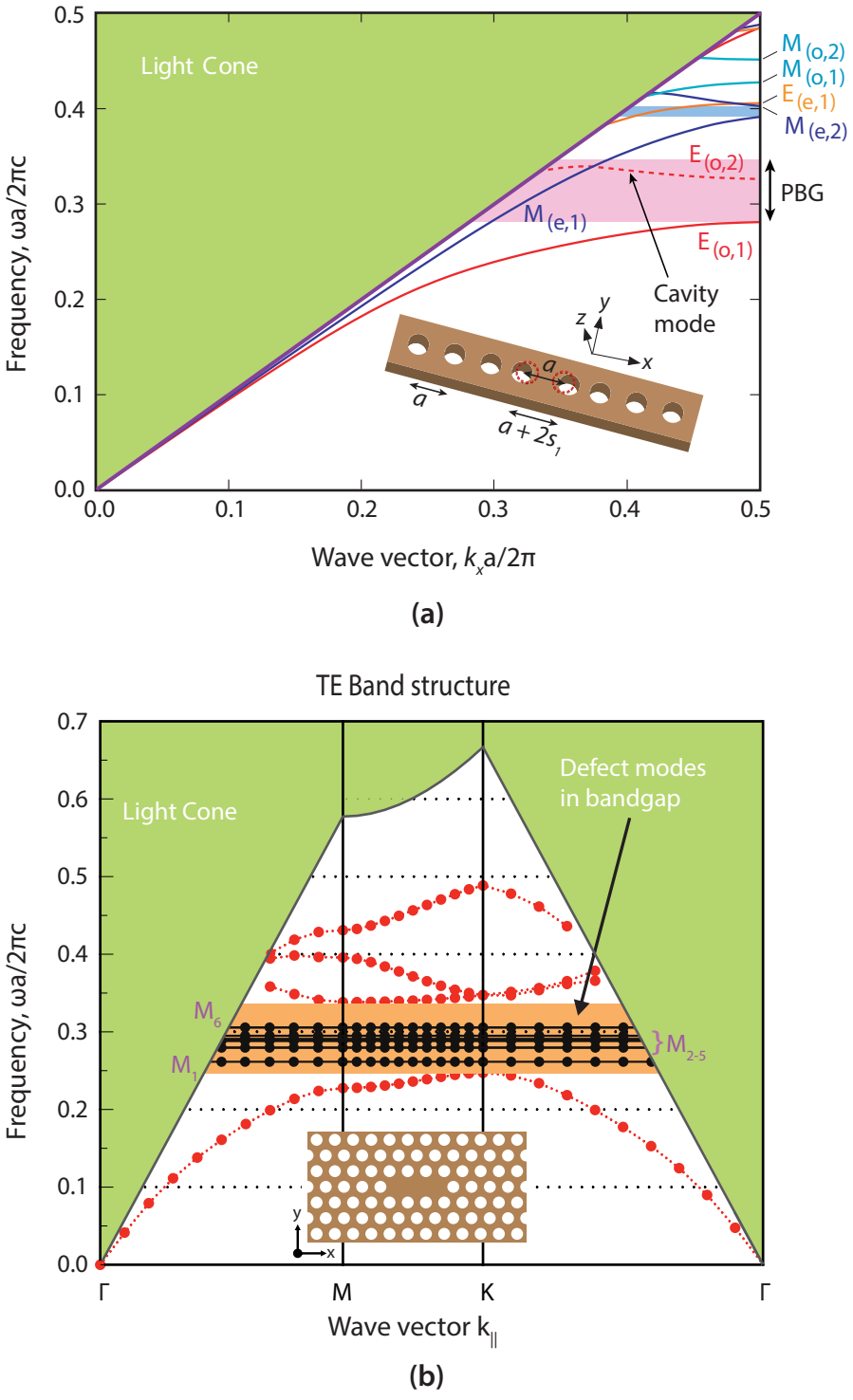

Figure 2.7: Photonic band structures and defect states for PhC cavities: Band diagram with defect states for (a) 1D PhC cavity where a defect is introduced by shifting a pair of holes to the outward direction (schematics of the structure is in the inset), (b) 2D PhC cavity where a defect is introduced by removing three holes from the 2D PhC lattice (schematics in the inset), images are adapted from [126, 146]

and the cavity suffers from intrinsic radiation losses to some extent. However, this resonant structure still can be used to spatially redistribute the emission and enhance

external quantum efficiency of the emitter located inside the cavity.

Similar to 1D PhC cavities, localised modes can be attained inside the bandgap for 2D PhC structures by introducing point-like defects in the PhC lattice. An example of localised modes for the ideal 2D PhC with a point defect is shown in Figure 2.6c. The localised modes for a practical 2D PhC slab with a defect are similar to the ideal case. However, the finite dimensions of the practical 2D PhC slab induce the light cone modes and an incomplete bandgap, as shown in Figure 2.7b. Thus, the localised modes in the 2D PhC slab are also leaky resonances, allowing some vertical radiation to escape the PhC cavity. In principle, point-like defects can be introduced in a 2D PhC lattice by perturbing a single or few lattice sites. This can be achieved by removing some of the dielectric material from the periodic structure or by adding some extra dielectric material where it does not belong. For a 2D PhC with a triangular lattice of air-holes, a resonant cavity can be obtained by manipulating the size, position and/or the presence of air holes in the crystal. One of the most efficient and versatile defect geometry in the 2D PhC slab is the L3-type cavity which is implemented by removing three holes in a row from a triangular/hexagonal lattice of air holes [147–149]. The band diagram and cavity modes of an L3 cavity is presented in Figure 2.7b along with the schematics of the slab structure in the inset. In principle, an L3 type 2D PhC cavity is capable of accommodating six dispersion free i.e., localised modes inside the photonic bandgap (PBG) [146, 150, 151]. The lowest frequency mode is the fundamental one which is closest to the dielectric band and well separated from the higher order modes. This fundamental mode, labeled as M_1 in the band diagram (Figure 2.7b), also provides the highest cavity quality factor among all modes. Thus, the fundamental mode of the L3-type defect is most suitable for realising a high quality photonic cavities. Moreover, L3-type PhC cavities are robust to fabrication imperfections and can be further improved to increase its quality and light extraction efficiency [148, 149]. For these reasons, the L3 PhC cavity is very popular in the photonic crystal research community and chosen in this work as a candidate for a resonant structure to investigate emission enhancement in silicon.

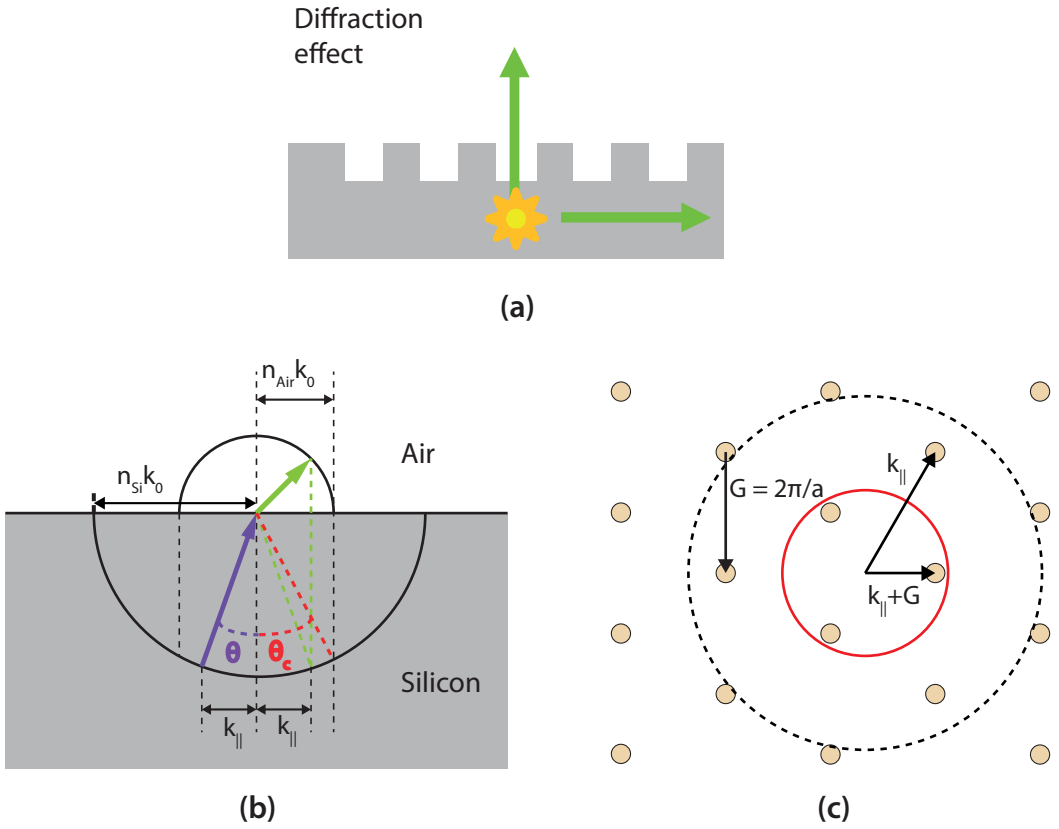

Figure 2.8: Light extraction from photonic crystal structures: (a) schematics of vertical emission enhancement using diffraction, (b) **k**-vector diagram of a silicon/air interface. The conservation of the in-plane wave vector $\mathbf{k}_{||}$ allows light to escape silicon only when the incident angle is less than the critical angle i.e., $\Theta < \Theta_C$ and (c) Bloch mode diffraction mechanism in a PhC slab. The presence of a periodic grating brings the in-plane wave vector $(k_{||} + n\mathbf{G})$ back within the air circle (radius $= n_{air}k_0$) represented by the red circle in the figure. This gives rise to leaky modes which radiate into the air.

2.3.2 Photonic crystal cavities: extraction of emission

Photonic nanostructures such as photonic crystals, gratings etc. can enhance the light extraction from high-index materials. As discussed before (Chapter 1, Section 1.3.2), it is difficult to extract light from unpatterned high-index material due to total internal reflection (TIR). Photonic nanostructures help to bypass the difficulties of light extraction by using the diffraction [94]. PhC structures can act as diffraction gratings and open pathways for photons to leave the structure through diffraction effects, schematic and mechanism of this effect is shown in Figure 2.8.

The restriction on light extraction from a high index material can be understood from the length conservation of the in-plane **k**-vector, $\mathbf{k}_{||}$, for the light travelling across different media. In the case of a silicon/air interface, light emission inside the silicon

can only escape to the air, if the length of $\mathbf{k}_{\|}$ for the light is smaller than $k_0 n_{Si} \sin\Theta_C = n_{air} k_0$. Here, $k_0 = 2\pi\lambda_0$ is the length of the vacuum wave vector, Θ_C is the critical angle for TIR. The light propagation from silicon to air is allowed only when the incident angle is smaller than the critical angle, as shown in Figure 2.8b. For all other cases, the light experiences TIR and gets trapped inside the high-index media. The incorporation of a PhC structure can help to scatter light outside the high-index substrate material. The light diffraction to air is allowed only when an in-plane wave vector lies within the so-called air circle which has a radius of $n_{air} k_0$. For an unpatterned structure, the light coupling to the air is restricted as the in-plane wave vector resides outside the air-hole, as shown in Figure 2.8c. When the periodic structure is incorporated, the in-plane wave vector can couple to other harmonics along the reciprocal lattice points and satisfy the condition $\|k_{\|} + n\mathbf{G}\| < k_0$, where $\mathbf{G}$ is the reciprocal lattice vector [152, 153]. Thus, the in-plane wave vector $(k_{\|} + n\mathbf{G})$ is brought back within the air circle (radius $= n_{air} k_0$), which gives rise to leaky modes (Figure 2.8c). Quantitative analysis and techniques for further improvements of extraction efficiencies for the specific cases are discussed in detail in a later chapter (Chapter 4, Section 4.5.2) that covers the design and simulation of PhC cavities considered in this work.

2.3.3 Photonic crystal cavities: quality factor

In a PhC cavity, the periodic variation in the refractive index around the defect acts as a highly reflective Bragg mirror and helps to trap light of certain wavelength. The total internal reflection (TIR) is exploited additionally for keeping light inside a 1D/2D PhC cavity in the direction , which shows no periodic variation in the electromagnetic media. However, practical PhC cavities with finite thickness and/or width experience an incomplete bandgap and suffer from radiative losses. The loss in any practical cavity is quantified by a dimensionless number, known as the quality-factor (Q). The quality-factor Q for a cavity can be interpreted in many ways. For example, $1/Q$ resembles the decay rate of the resonant modes inside a lossy cavity, which can be estimated from the relation [126, 154, 155]

$$\frac{1}{Q} = \frac{P}{\omega_0 \mathscr{E}}, \tag{2.9}$$

where ω_0 is the resonant frequency, $\mathscr{E}$ is the electromagnetic energy localized in the

cavity and $P = -\frac{d\mathscr{E}}{dt}$ represents the dissipated power. Thus, the quality factor provides an estimate for the cavity lifetime as it gives the number of optical periods until the light energy in the cavity decayed by $e^{-2\pi}$.

A PhC cavity can suffer from several loss mechanisms, causing the resonance to decay. Different loss mechanisms can be attributed with their own Q-values. For a practical PhC cavity, imperfect confinements lead to losses both in the in-plane ($\parallel$) and out-of-plane ($\perp$) directions. These are intrinsic losses as they are inherent to the PhC cavities and corresponding quality factors can be expressed as $Q_{\parallel}$ and $Q_{\perp}$. The losses arising from issues such as structural/fabrication imperfections, material absorption etc. are considered as the extrinsic ones and the Q-values representing them can be labeled respectively as Q_S, Q_M etc. Thus, the total Q-value (Q_{Tot}) is estimated by taking all the losses into account and can be expressed as

$$\frac{1}{Q_{Tot}} = \frac{1}{Q_{\parallel}} + \frac{1}{Q_{\perp}} + \frac{1}{Q_S} + \frac{1}{Q_M}. \tag{2.10}$$

Equation 2.10 shows that the total value of Q is dominated by the strongest loss mechanism. So, to get a high quality factor, both the intrinsic and extrinsic losses have to be minimised. Obtaining high Q-values for PhC cavities with an incomplete bandgap is challenging because there is no optimum approach in the PhC cavity design to minimise the intrinsic losses. Though very high Q-values have been demonstrated by several research groups [149, 156, 157], the optimisation techniques depend on the design and type of the PhC cavities. In most of the cases, high-Q cavities are achieved by optimising some structural parameters in the design, which suppress the dominant radiative component. Techniques for improving Q-values will be discussed in detail in the chapter (Chapter 4, Section 4.5.1) addressing the design and simulation of high-Q cavities.

2.4 Bragg gratings

The Bragg's law describes the diffraction of waves from periodic structures for wavelengths comparable with the periodic spacing [158–160]. For certain wavelength, the reflected lights from successive planes of the periodic structure can interfere constructively and make intense peaks. The famous Bragg's law [158] relates the period of

the structure to the wavelength of the diffracted wave and provides the conditions for the constructive interferences. Hence, the gratings satisfying the Bragg condition are called the Bragg gratings.

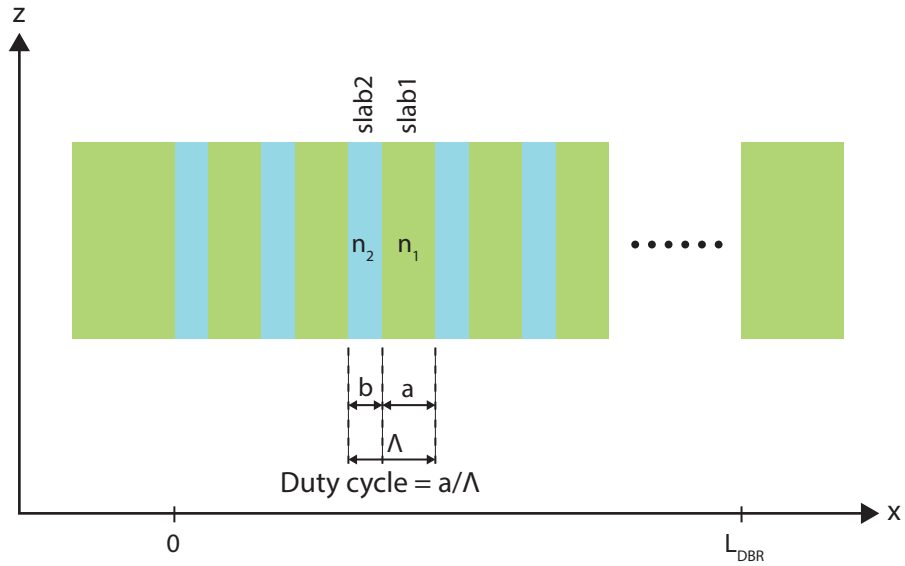

Figure 2.9: Bragg waveguide gratings: schematic of a Bragg waveguide grating formed with a periodic stack of two slab waveguides, named slab 1 and slab 2. The grating period is Λ. The thickness and refractive index of slab 1, 2 are a, b and n_1, n_2 respectively

In the simplest form, a Bragg waveguide grating can be formed with a periodic stack of two slab waveguides where the two slabs have different refractive indices, as shown in Figure 2.9. For a certain Bragg order N, wavelength λ_{Bragg} and a grating period Λ, the condition for the constructive interference is [161]

$$2n_{\text{eff}}\Lambda = N\lambda_{\text{Bragg}}, \tag{2.11}$$

where n_{eff} is the effective refractive index of the waveguide under consideration. The effective refractive index n_{eff} can be calculated by averaging the dielectric function $\varepsilon(x,z) \equiv n^2(x,z)$ along the direction of periodic variation of refractive index[161]. Thus,

$$n^2_{\text{eff}}(z) = Dn^2_{\text{a}}(z) + (1-D)n^2_{\text{b}}(z), \tag{2.12}$$

where D is the duty cycle of the periodic variation; n_{a} and n_{b} are the refractive index of slab 'a' and slab 'b', respectively.

2.4.1 Circular gratings

As discussed in Section 2.2, the necessary information to describe the behaviour of a photonic system can be obtained by solving the Helmholtz/Basic equation. To extract the modal field for a circular Bragg resonator (CBR), we have to consider cylindrical coordinates due to the geometry of the device. Neglecting the polarization effects due to the waveguide structure, we can start from the scalar Helmholtz equation for the z component of the electric field in cylindrical coordinates [162–165]

$$\left[\frac{1}{r}\frac{\partial}{\partial r}\left(r\frac{\partial}{\partial r}\right)+\frac{1}{r^2}\frac{\partial^2}{\partial\varphi^2}+k_0^2n^2(r,z)+\frac{\partial^2}{\partial z^2}\right]E_{\mathrm{z}}(r,\varphi,z)=0, \tag{2.13}$$

where r, φ, z represents the radial, azimuthal, vertical coordinates, respectively and $k_0=\omega/c=2\pi/\lambda_0$ is the wavenumber in vacuum.

In a passive uniform medium with the dielectric constant $n^2(r,z)=\varepsilon_{\mathrm{r}}(z)$, the modal field for an azimuthally propagating eigenmode, E_{z}, can be expressed as

$$E_{\mathrm{z}}(r,\varphi,z)=E_{\mathrm{z}}^{(m)}(r,z)\exp(im\varphi)=\left[AH_m^{(1)}(\beta r)+BH_m^{(2)}(\beta r)\right]Z(z)\exp(im\varphi), \tag{2.14}$$

where A and B are amplitudes of the radial field in the cavity; $H_m^{(1)}(\beta r)$ and $H_m^{(2)}(\beta r)$ are the Hankel functions of the first and second kind. The Hankel functions in cylindrical coordinates are equivalent to the complex exponents in the Cartesian system, hence, representing the radially incoming ($H_m^{(1)}(\beta r)\Rightarrow\exp(+i\beta r)$) and outgoing (($H_m^{(2)}(\beta r)\Rightarrow\exp(-i\beta r)$)) waves. Furthermore, m is the angular mode number, $\beta(=k_0n_{\mathrm{eff}})$ is the propagation constant and Z(z) is the fundamental mode profile in the slab waveguide under consideration. The in-plane propagation constant β and the fundamental mode Z(z) for the slab waveguide satisfies the following relation

$$\left(k_0^2\varepsilon_r(z)+\frac{\partial^2}{\partial z^2}\right)Z(z)=\beta^2Z(z). \tag{2.15}$$

We can define, $x=\beta r$ for normalising the radial coordinate and add an extra field term $\Delta E(x,z)$ in the modal field to include the vertical radiation. The modal field then becomes [165]

$$E_{\mathrm{z}}^{(m)}(x,z)=\left[A(x)H_m^{(1)}(x)+B(x)H_m^{(2)}(x)\right]Z(z)+\Delta E(x,z). \tag{2.16}$$

We adopt this approximate solution approach by incorporating the field term $\Delta E(x,z)$ for the vertical radiation, because the exact solutions for the in-plane radial wave propagation and the radiation normal to the grating are rather complicated to derive. It can be assumed that this normal field term $\Delta E(x,z)$ has an exponential relationship ($\exp(\pm ik_0 z)$) with z values in free space, which gives us

$$\left[\frac{1}{r}\frac{\partial}{\partial r}\left(r\frac{\partial}{\partial r}\right) - \frac{m^2}{r^2}\right]\Delta E = 0. \tag{2.17}$$

The scalar Helmholtz equation in cylindrical coordinates (equation (2.13)) can be solved using equations (2.16) and (2.17) which, in turn, provides the vertical radiation field. To solve the equation (2.13), several approximations have been introduced [162, 163, 165–167] such as the cavity radius is large enough so that the derivatives of the Hankel functions can be approximated very close to their exact values; the second order derivatives of $A(x)$ and $B(x)$ are negligible; the incoming, outgoing waves and the source driving them have close phase dependence etc. Under these approximations, we use the modal solution (2.16) in the scalar Helmholtz equation and the result can be arranged in separate groups with similar Hankel functions. From the groups of terms with similar Hankel functions, we can get the following sets of coupled equations:

$$2i\frac{\mathrm{d}A}{\mathrm{d}x}H_m^{(1)}Z + i\frac{k_0^2\varepsilon_\mathrm{i}}{\beta^2}AH_m^{(1)}Z = \frac{k_0^2\Delta\varepsilon_0}{\beta^2}\left(a_{-2}BH_m^{(1)}e^{2i\delta\cdot x}Z + a_{-1}\frac{\Delta E}{\left|H_m^{(1)}\right|}H_m^{(1)}e^{i\delta\cdot x}\right), \tag{2.18}$$

$$i\frac{k_0^2\varepsilon_\mathrm{i}}{\beta^2}BH_m^{(2)}Z - 2i\frac{\mathrm{d}B}{\mathrm{d}x}H_m^{(2)}Z = \frac{k_0^2\Delta\varepsilon_0}{\beta^2}\left(a_2AH_m^{(2)}e^{-2i\delta\cdot x}Z + a_1\frac{\Delta E}{\left|H_m^{(1)}\right|}H_m^{(2)}e^{-i\delta\cdot x}\right), \tag{2.19}$$

$$\left(k_0^2\varepsilon_r + \frac{\partial^2}{\partial z^2}\right)\Delta E = k_0^2\Delta\varepsilon_0\left(a_1A\left|H_m^{(1)}\right|e^{-i\delta x}Z + a_{-1}B\left|H_m^{(1)}\right|e^{i\delta x}Z\right), \tag{2.20}$$

where $\Delta\varepsilon(r,z)$ is a small deviation from the exact perturbation profile and $a_l(z)$ is the lth-order expansion coefficient of $\Delta\varepsilon(r,z)$ at a given z. $\delta = \left(\beta_{design} - \beta\right)/\beta$ is the nor-

malised frequency detuning factor that takes variations in the resonant frequency from the designed values into account. Very small values (Ideally zero) for δ are required for obtaining good (maximum) radial confinement of the modal field [162, 163, 165–167]. From equation (2.20) we can express ΔE as following

$$\Delta E = \left(s_1 A e^{-i\delta \cdot x} + s_{-1} B e^{i\delta \cdot x} \right) \left| H_m^{(1)} \right|, \tag{2.21}$$

where

$$s_l = k_0^2 \Delta\varepsilon_0 \int_{-\infty}^{\infty} a_l(z') Z(z') G(z,z') \mathrm{d}z', \tag{2.22}$$

and $G(z,z')$ is the Green's function which agrees with the following relation

$$\left(k_0^2 \varepsilon_r(z) + \frac{\partial^2}{\partial z^2} \right) G(z,z') = \delta(z-z'). \tag{2.23}$$

2.4.2 Circular gratings: far-field emission

Circular Bragg gratings (CBGs) can provide an in-plane light confinement and form circular resonators. They have been proposed and used for realising distributed feedback (DFB) and distributed Bragg reflector (DBR) lasers for almost last three decades [166, 168–172]. CBGs satisfying the first-order Bragg condition ($\lambda_{\text{Bragg}} = 2n_{\text{eff}}\Lambda$ - from equation (2.11)) can achieve very good in-plane light confinement [173, 174], but they provide a poor vertical emission i.e. outcoupling efficiency. The outcoupling of emission can be improved significantly by incorporating secod-order Bragg gratings ($\lambda_{\text{Bragg}} = n_{\text{eff}}\Lambda$). The use of second-order gratings has been first proposed and started for surface-emitting circular Bragg lasers [162, 163, 165–167] as second-order CBGs can focus vertical radiation in addition to providing the in-plane feedback for lasing. In section (2.4.1), we have derived an expression (equation (2.21)) relating vertical and in-plane fields of CBGs for the radiation pattern at the emission surface. We can express the field at the emission surface for a CBG design with $m = 0$ as the following

$$\Delta E = \left(s_1 A e^{-i\delta \cdot x} + s_{-1} B e^{i\delta \cdot x} \right) \left| H_0^1 \right|, \tag{2.24}$$

where s_1 and s_{-1} for the near-field can be estimated numerically from the equation (2.22) for the CBG cavity under consideration. The far-field radiation pattern for a

CBG cavity can be deduced from the case of light diffraction from a circular aperture, using the parallel ray approximation [166, 175]

$$\begin{aligned} U(\mathbf{R}) &\propto \iint_{aperture} \Delta E(r,\varphi)\frac{\exp\left(ik\left|\mathbf{R}-\mathbf{r}'\right|\right)}{4\pi\left|\mathbf{R}-\mathbf{r}'\right|}\mathrm{d}\mathbf{r}' \\ &\approx \frac{e^{ikR}}{4\pi R}\iint_{aperture}\Delta E(r,\varphi)\exp\left(-ik(\mathbf{r}'\cdot\hat{\mathbf{R}})\right)\mathrm{d}\mathbf{r}' \\ &= \frac{e^{ikR}}{4\pi R}\int_{\varphi=0}^{2\pi}\int_{r=0}^{r_b}\Delta E(r)\exp\left[-ikr\sin\theta\cos\left(\varphi-\phi\right)\right]r\mathrm{d}r\mathrm{d}\varphi \\ &= \frac{e^{ikR}}{2R}\int_0^{r_b}\Delta E(r)J_0(kr\sin\theta)r\mathrm{d}r, \end{aligned} \tag{2.25}$$

where $\mathbf{r}' = r\cos\varphi\hat{\mathbf{x}} + r\sin\varphi\hat{\mathbf{y}}$ is the radial distance for the source point and the radial vector for the far field is $\mathbf{R} = R\sin\theta\cos\phi\hat{\mathbf{x}} + R\sin\theta\sin\phi\hat{\mathbf{y}} + R\cos\theta\hat{\mathbf{z}}$. From the field pattern, the intensity of the far-field radiation pattern can be expressed as

$$I(\mathbf{R}) = U^*(\mathbf{R})U(\mathbf{R}) = |U(\mathbf{R})|^2. \tag{2.26}$$

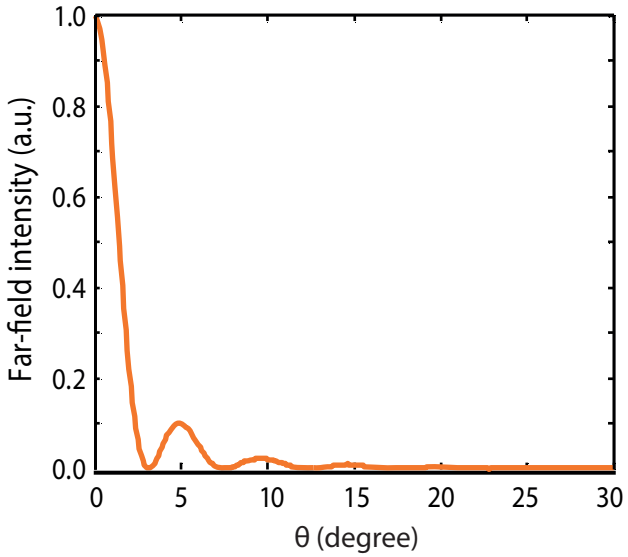

Figure 2.10: Far-field emission pattern of a circular Bragg resonator: The far-field intensity pattern of the fundamental mode of a CBR, image is reproduced from [165].

If the far-field intensity pattern is plotted for the fundamental mode, as shown in Figure 2.10, it shows the focussed emission pattern of the CBG cavity. When the light is diffracted from a circular aperture, it forms different lobes in the far-field pattern, cor-

responding to different diffraction orders. From Figure 2.10, we find that the strongest lobe corresponds to the zeroth-order diffraction and this property gives the CBG cavity its focussed vertical radiation i.e., better outcoupling efficiency.

2.4.3 Circular gratings: light confinement

As discussed in section 2.3.3, the quality factor (Q-factor) is a dimensionless property used to characterise any resonant system. It relates the energy dissipation with the energy stored in a resonant system. Thus, for any optical cavitiy, the quality factor describes how efficiently light/photons will be confined in the cavity structure. The most fundamental way to determine the Q-factor (as in equation (2.9)) is to calculate it from the ratio of the energy stored in the cavity and the energy lost from the cavity in one period [126, 154, 155]

$$Q = \omega_r \frac{\text{energy stored in the mode}}{\text{average power dissipated}} = \frac{\omega_r \mathscr{E}}{P}, \tag{2.27}$$

where, ω_r is the resonant angular frequency, $\mathscr{E}$ is the total energy stored in the resonator for certain mode and P the energy lost per unit time.

Similar to the PhC cavities, the contributing components to the total quality factor of the CBG can be categorised into the intrinsic and extrinsic Q-values. The extrinsic Q-value depends on structural/fabrication imperfections, which is difficult to control. Thus, we mostly focus on the intrinsic Q-values as this can be improved by careful design. It has already been mentioned (Section 2.4.2) that CBGs with first order grating show negligible out-of-plane scattering. Therefore, the Q-factors for first-order CBGs depends mostly on the in-plane component. Thus, the calculation of the Q-factor in this particular case becomes a two-dimensional problem. Jebali *et al.* have developed a 2D analytical model to calculate the Q-factor for the first-order CBGs, considering the in-plane peripheral power leakage as the only source of energy dissipation [173, 174]. First-order grating cavities can provide the desired photon confinement, but we also need the vertical emission for efficient extraction of photons from the cavity. The second order grating cavity can fulfil this outcoupling requirement in addition to the confinement effect. However, when the vertical radiation component is considered for the second-order grating, it becomes a three dimensional problem and developing an analytical model, i.e., rigorous analysis is challenging. Xiankai Sun *et al.*, in their work

on surface emitting lasers, define an unnormalised quality factor to estimate the loss due the vertical emission of disk Bragg resonantor structures [165–167]. This unnormalised Q-factor is proportional to the exact Q of the cavity and can be estimated when the fundamental mode profile $Z(z)$, the in-plane & vertical radiation fields E & ΔE for the slab waveguide are known. Thus, the unnormalised Q-factor, Q', is determined as

$$\begin{aligned} Q' &= \frac{\int |\mathbf{E}|^2 \mathrm{d}V \,(\propto \text{the energy stored in cavity volume})}{\int |\mathbf{E}|^2 \mathrm{d}S \,(\propto \text{the outflow power through CBG surface})} \\ &= \frac{\int_0^D \mathrm{d}z \int_0^{2\pi} \mathrm{d}\varphi \int_0^{r_b} |E(r,z)|^2 r \mathrm{d}r}{\iint\limits_{grating} |E(r=0,z)|^2 r \mathrm{d}r\mathrm{d}\varphi + \int_0^D \mathrm{d}z \int_0^{2\pi} |E(r=r_b,z)|^2 \mathrm{d}\varphi} \\ &= \frac{\int_0^D Z^2(z)\mathrm{d}z \cdot \int_0^{x_b} |E(x)|^2 x \mathrm{d}x}{\int\limits_{grating} |\Delta E(x,z=0)|^2 x \mathrm{d}x + \int_0^D Z^2(z)\mathrm{d}z \cdot |E(x=x_b)|^2 \beta x_b} \end{aligned} \tag{2.28}$$

where β is the in-plane propagation constant and D is the thickness of the slab under consideration.

In case of a high vertical emission, the second order grating cavities or circular Bragg resonators experience very limited confinement in the out-of-plane ($\perp$) directions which, in turn, restricts the maximum attainable quality factor. Therefore, it is not possible to obtain high Q-value and extraction efficiency simultaneously for CBR structures. Thus, in case of practical implementations, the CBR designs are optimised to make an acceptable trade-off between these properties according to the specific requirement [176–178]. In our work, we estimate Q-values, extraction efficiencies etc. through numerical simulation and optimise the CBR design based on the simulation results. The detail of the simulation and optimisation process will be discussed in the chapter covering the design and simulation of photonic cavities (Chapter 4, Section 4.3).

2.4.4 Circular Bragg resonator

A concentric circular grating structure surrounding a defect in the centre can act as a planar semiconductor microcavity [176–179]. A disk or pillar like structure at the centre serves as the cavity and concentric trenches as radial reflectors. The diffraction from the circular Bragg mirror aids the momentum transfer from the in-plane guided

modes to the resonant extracted modes [180]. The second order grating properties of such a circular Bragg resonator (CBR) can be utilised for the efficient out-of-plane extraction and collection of light from high refractive index media [176–178, 181] which is otherwise very difficult due to total internal reflection.

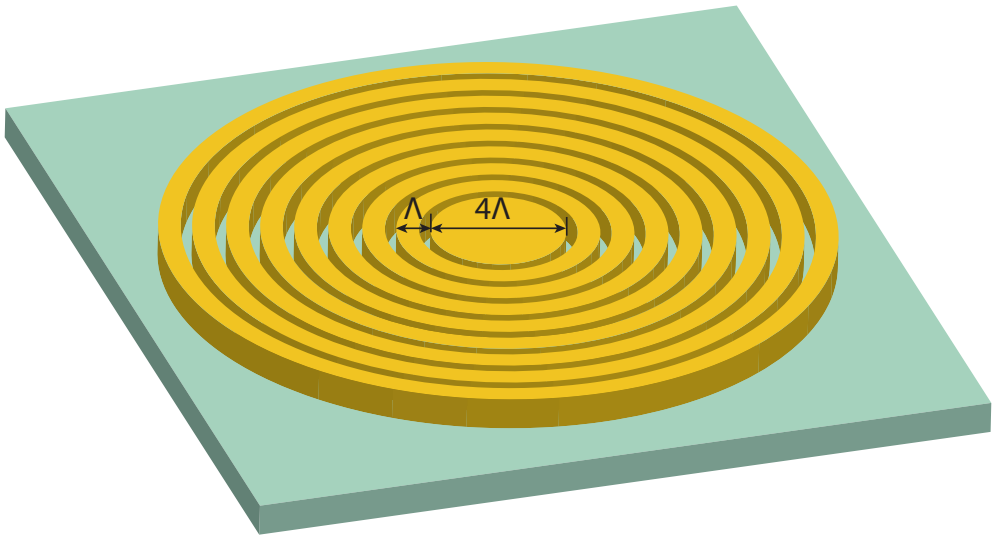

Figure 2.11: Circular Bragg Resonator: schematic of a circular Bragg resonator with a grating period Λ and defect diameter 4Λ.

To design the gratings in the CBR structures, one need to solve the Helmholtz equation in appropriate geometry. Now, the solution of the Helmholtz equation in cylindrical coordinates involves the Hankel/Bessel functions, as briefly described in Section 2.4.1. Therefore, the concentric trenches/radial reflectors constituting the CBG should be positioned according to the roots of Bessel functions, leading to an aperiodic grating design [162, 163, 166, 167]. However, realising concentric trenches at ideal positions extracted from from mathematical Bessel function is challenging. Even though the trenches are placed at the ideal positions for the Bessel mode grating, the corrugations/irregularities in the practical structure introduces further complex phase perturbations and prevents to achieve the optimal performance of the design. This issue can be tackled by elaborate optimisations on parameters of each radial reflector which is extremely time consuming and computationally demanding for a truly three-dimensional geometry [182]. Furthermore, it has been found in the literature that the Bessel mode aperiodic gratings and resonators provide a performance (Q-factor, extraction efficiency) of similar order or only a marginal improvement over a simple periodic CBG structure [165–167, 176–178, 182, 183]. Both aperiodic and periodic CBG

structures offer/provide Q-values of few hundreds [166, 167, 176, 177] and collection efficiency $\gtrsim 80\%$ [167, 176] with realistic parameters. Thus, in this work, we choose the periodic CBG design for implementation as it is simpler to optimise for the requirement and relatively robust against fabrication imperfections. Finally, for CBR designs with regular/periodic gratings, the circular grating section and the cavity/central disc section are optimised separately [176–178, 180]. In case of CBR devices aimed for reasonable Q-values and good collection efficiency, the grating section is first chosen to fulfil second order Bragg condition $\Lambda = \lambda_{\text{res}}/n_{\text{eff}}$, which allows reflective feedback to the cavity and near-vertical upwards scattering. Then, the radius of the central disk is optimised to maximise the vertical extraction of light via numerical (finite difference time domain) simulations. It has been found that optimum light collection/extraction efficiency and Q-value are obtained when the disc radius is about twice the grating period ($R \approx 2\Lambda$) [176–178]. Figure 2.11 shows the schematic of a circular Bragg resonator with a grating period, Λ and a defect disc radius, 2Λ.

2.5 Summary

We have discussed the concept of photonic band gap and the formation of photonic cavities by incorporating intentional defects in periodic dielectric media. After a generic introduction of the subject, our discussion mainly has focussed on specific cases of 1D PhC cavity, L3 type 2D PhC cavity and circular Bragg resonator structures. These cavity structures have been deliberately selected due to their flexibility in design and efficient practical implementations. The light confinement (Q-factor) and far-field emission properties of these cavities are also discussed in detail. These provide the necessary insights into further design optimisations for optimally enhancing emission and extraction of no-phonon D^0X transitions in/from silicon.

Chapter 3

Photoluminescence measurements of phosphorus D^0Xs in silicon

3.1 Photoluminescence spectroscopy

Photoluminescence (PL) is the emission of light observed from a material when it is excited with photons of higher energy i.e., shorter wavelength ($\lambda_{ex} \leq \lambda_{em}$). The spectral analysis of PL emission can reveal distinctive material properties of the specimen under investigation. For solid-state samples, the emission originates from the band-gap structure of the crystalline lattice and from the level structure of impurities present in the lattice. The host matrix serves as an antenna for the impurity emitters and also modifies the impurity energy levels. The resulting spectra are significantly altered with respect to the impurity optical spectra observed in vacuum [184]. The presence of such impurity emitters or luminescence centres can produce emissions which are much stronger than the intrinsic emission of the host material, even at low concentrations ($<$ 1 ppm). The high sensitivity to impurities and defects has made photoluminescence spectroscopy a widely used tool for studying the optical properties of semiconducting materials, their microscopic electronic processes and for the determination of impurities, crystalline defects etc.[184]

3.2 PL spectroscopy of impurities in silicon

For last six decades, photoluminescence (PL) spectroscopy has been employed as an efficient tool for optically characterizing defects and impurities in silicon [185]. Varieties of impurities such as shallow-level [60, 186], deep-level [187, 188], isoelectronic

[189–191], metal [192–194], transition metal [195], inert gas ion [196], even interstitial impurities [197] have been successfully studied, using PL spectroscopy.

The PL intensity related to a particular impurity in silicon depends on various factors such as the relative and absolute concentrations of different impurities present, excitation power density, operating temperature, surface properties, presence of strain, non-radiative channels etc. So, both careful measurement and analysis are required to extract the relevant information from a PL spectra. For this reason, the use of PL spectroscopy began as a qualitative technique for evaluating the relative contents of impurities and defects. The first successful low temperature (at liquid helium temp.), quantitative analysis of shallow impurities in silicon was demonstrated in the late-1970s by Tajima *et al.* [60, 198, 199]. In their work, Tajima *et al.* [60, 198, 199] used the PL intensity ratio between the intrinsic and extrinsic spectral components to determine the impurity concentrations in bulk silicon samples; and managed to detect boron impurities down to a concentration of 1×10^{11} cm^{-3} and phosphorus to 5×10^{11} cm^{-3}. This method, for the first time, allowed a highly sensitive and nondestructive detection of the concentration of a small amount of impurities in a relatively small volume (1 mm excitation spot) of the specimen [60]. Nakayama *et al.* explored the dependence of the PL intensity ratio of bound excitons (BEs) to free excitons (FEs) on the excitation power and impurity concentration. They devised a rate equation that can be used to explain the PL intensity ratio of BEs to FEs at low excitation powers (≤ 0.15 Wcm^{-2}) and also to estimate the impurity concentration and compensation ratio efficiently [200].

Furthermore, in the early 1980s, Tajima *et al.* demonstrated that PL spectroscopy is capable of characterising both intrinsic and extrinsic impurities in epitaxial (layer thickness $\sim$ 3 μm) silicon [201]. Conventional techniques such as resistivity/capacitance-voltage measurements, secondary ion mass spectroscopy (SIMS) and activation analysis are not efficient for studying impurities in thin films. For example, a C-V measurement is incapable of detecting the species of impurities and SIMS is a destructive method which works only for higher concentrations ($> 10^{16}$ cm^{-3}) of impurities. On the other hand, PL spectroscopy can provide a sensitive and nondestructive way to detect impurities in very small physical dimensions and analyse the quantitative relationship between the emission spectra and the impurity concentrations [201]. This capability of probing thin films of silicon also enables the

characterization of silicon-on-insulator (SOI) type structures with PL spectroscopy. The quality of SOI structures is extremely important in modern microelectronic industries for realising state-of-the-art, reliable electronic devices and integrated circuits. PL spectroscopy has allowed us to nondestructively probe not only standard SOI wafers (with several microns thick silicon i.e., device layer) [202] but also ultrathin SOI wafers (with top device layers less than 100 nm) [203]; and analyze their quality, the sources & effects of defects & impurities [204] etc. Recombination channels and emission lifetimes of different impurity emitters in SOI structures have also been investigated with PL spectroscopy [191, 205, 206].

In this thesis, PL spectroscopy is employed to probe phosphorus impurities and their excitonic properties in silicon and SOI chips. Our main interest is the no-phonon transition from phosphorus donor bound excitons (D^0Xs) formed at low temperature. We investigate the optical detection limit in terms of the minimum number of donors with a standard PL set-up, which will be discussed in the next section.

3.3 Photoluminescence measurement set-up

A simple photoluminescence set-up requires components for focussing the excitation light to a small spot on the sample, the efficient collection of emitted light and for the spectral analysis of the collected light. Additional components such as motorised stages and a cryostat are necessary for precise sample positioning and low temperature measurements.

In this work, we use a confocal setup for our experiments. In a confocal measurement set-up, the same microscope objective is used for focussing the excitation light onto the sample as well as for collecting the emitted light. With such a set-up, an excitation spot size smaller than 1 μm can be obtained, depending on the excitation wavelength and the numerical aperture of the microscope objective. Furthermore, a spatial filtering of the collected light can also be achieved by using a pinhole with this confocal system.

Due to a low dissociation energy ($\sim 5-6$ meV) of the D^0X in silicon [57, 90], any D^0X related measurement has to be carried out below 40 K. We have used a standard confocal microscope system with a helium flow cryostat (MicrostatHe2 Rectangular Tail - continuous flow, optical window cryostat from Oxford Instrument) for photolu-

minescence measurements of the ^{31}P D^{0}X transitions. The schematic of the PL measurement set-up used in our experiments is illustrated in Figure 3.1, including the model numbers of all major components, acquired from Thorlabs.

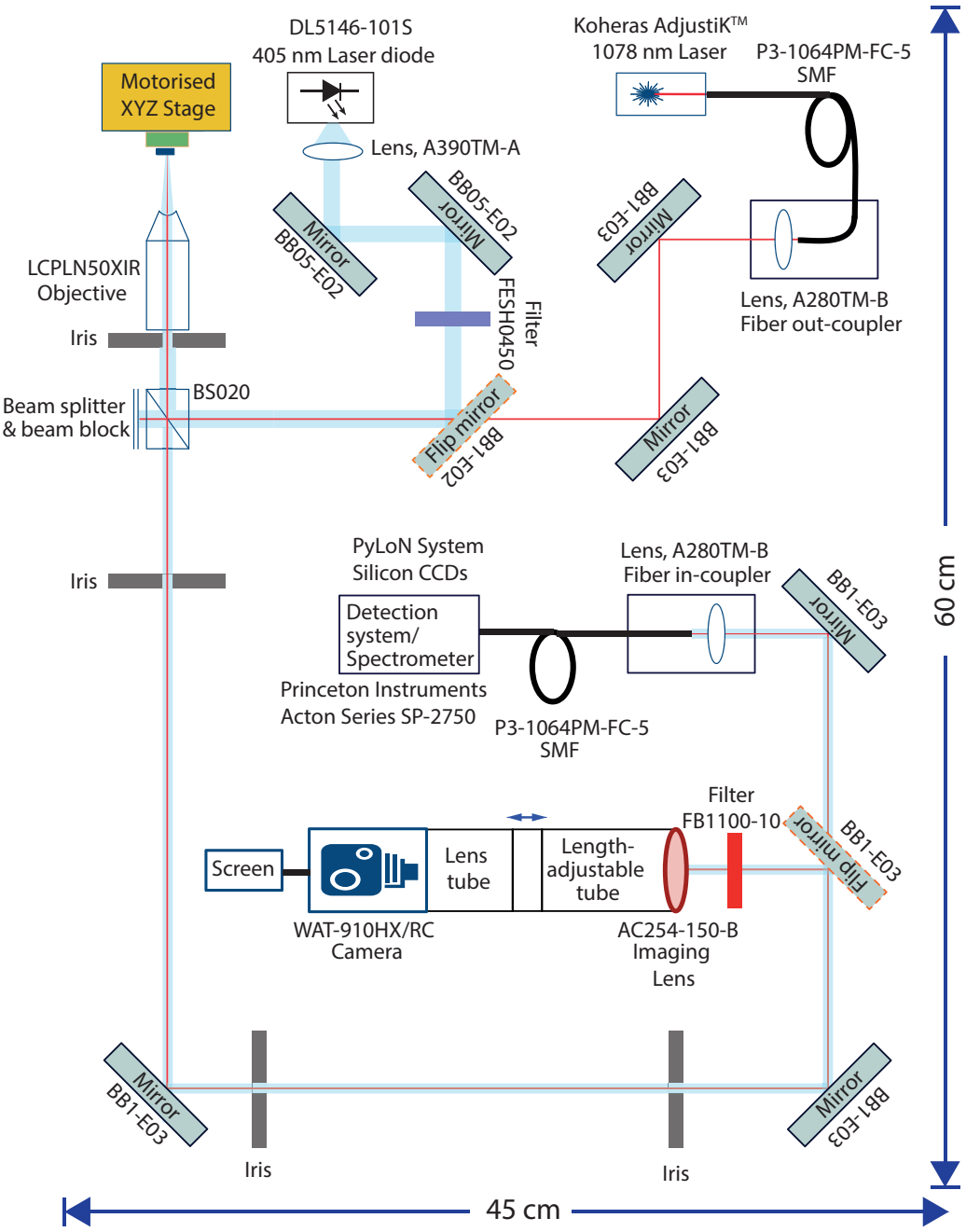

Figure 3.1: PL measurement set-up for ^{31}P D^{0}X characterisation

In principle, any light source with a photon energy higher than the emission energy can be used for excitation. A laser diode (DL5146-101S) with a centre lasing wavelength of 405 nm has been used primarily as the above bandgap excitation source. We have also used longer excitation lights with wavelength of about 632 nm and 780 nm

from fiber-coupled continuous-wave (CW) lasers to excite deeper into the sample. Another fiber-coupled CW laser (NKT Koheras AdjustiK system), lasing at about 1078 nm is used for sample focussing purposes. Switching between the laser diode (LD) and the fiber-coupled lasers is done by using a flip-mount mirror, as shown in Figure 3.1. The collimated 405 nm light beam is guided first by broadband dielectric mirrors (BB05-E02) with a coating suitable for 400 nm - 700 nm light and then through a high quality shortpass filter (FESH0450) with a cut-off wavelength at 450 nm. The shortpass filter removes any unwanted long wavelength components from the LD spectrum.

We use a 30:70 (R:T) non-polarising beamsplitter (BS020) before the microscope objective to inject the excitation light into the optical path and to the sample. The microscope objective (Olympus LCPLN50XIR) used in the set-up is specially built for near infrared applications which has a numerical aperture (NA) of 0.65 and a working distance (w.d.) of ~ 4 mm. The objective lens can focus the excitation light beam of 405 nm and 780 nm in a spot less than or around 1 μm on the sample. The PL emission from the sample is collected with the same objective. The collected photons is then sent through the beam-splitter and guided along the collection path. Before the collection arm, a second flip-mount mirror is used which sends light to a low-light, high-sensitivity and monochrome camera (WAT-910HX/RC) for sample surface inspection and focussing purposes. All the guiding mirrors (BB1-E03) after the beam-splitter have a dielectric coating suitable for 750 nm to 1100 nm light, covering efficiently the PL emission wavelength from the ^{31}P D^0X transitions. In the collection arm, the light from the PL emission is coupled into a single mode fiber and then sent to the spectrometer (Acton Series SP-2750, Princeton Instruments). Before entering the spectrometer, the collected light is passed through a premium grade longpass filter (FELH0900) which filters out the excitation light reflected from the sample. The Acton SP-2750 spectrometer has a focal length of 0.75 m and facilitates a triple indexable gratings with a triple grating turret. In our system, gratings incorporated are 1500 g/mm, 1200 g/mm and 300 g/mm with blaze wavelengths of 500 nm, 750 nm and 1000 nm respectively. Although a grating with larger groove density provides better resolution, it covers a smaller wavelength range. In addition, the diffraction efficiency of the grating depends on the blazing angle. As our PL emission is very weak and the signal detection is critical, we have used the 300 g/mm grating in our experiments, which is optimised

for 1 um of wavelength (the blaze wavelength). For the 300 g/mm grating, we get a resolution of approximately 100 pm around the ^{31}P D^{0}X transition wavelengths. The dispersed light from the grating is detected by a Si-based CCD array (PyLoN System Silicon CCD Camera) and recorded/analysed in the computing unit.

3.4 PL measurement of ^{31}P D^{0}X transitions in bulk silicon

As briefly illustrated in Section 3.2, PL spectroscopy of impurities in silicon is a mature field of research. The main focus of this work is the PL emission from phosphorus donors in silicon and to research any effective technique to enhance it. To investigate the characteristic emission properties of phosphorus donors in silicon, PL and PLE techniques had been used efficiently and regularly for a long time [60, 88, 89, 186, 205, 207, 208]. Here, the PL measurement technique is primarily employed to observe the the ^{31}P D^{0}X transitions. In addition, it is also used to investigate the detection limit for ^{31}P D^{0}X transitions, effects of excitation energy, the donor reneutralisation time with commercially available excitation and detection systems. The information obtained is used as a reference to design photonic structures to enhance the ^{31}P D^{0}X emission in silicon.

The confocal system used for the PL measurement can perform spatial filtering by using a suitable pinhole or by sending the light through a single mode fiber. A

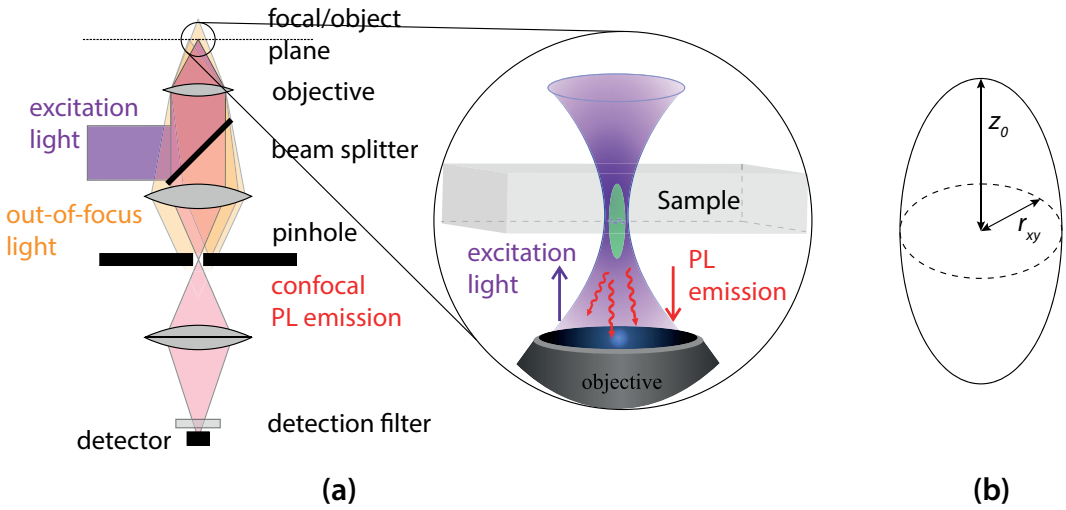

Figure 3.2: Principle of confocal measurement system with schematics of the (a) detection system and observation area, (b) collection volume.

schematic of such a confocal system is provided in Figure 3.2a. The microscope system collects photons from a certain volume of the focal plane and guides the collected photons to the detection unit. Hence, the intensity of collected light is proportional to the number of ^{31}P donors residing inside the collection volume seen by the confocal system. The confocal volume approximately has the shape of an ellipsoid, which depends on the spot-size ($2r_{xy}$) of the incident beam and the depth (z_0) of the confocal focus, as shown in Figure 3.2b. Thus, this volume can be expressed as an ellipsoid with two equal axes r_{xy} and a length z_0. The diffraction limited values for the spot-size and the collection depth depends on parameters such as the excitation wavelength (λ_{exc}), the numerical aperture of the objective (NA) and the refractive index of the medium (n). The spot-size and the collection depth can be estimated from the relations $2r_{xy} = 1.22n\lambda_{exc}/NA$ and $2z_0 = 2n\lambda_{em}/NA^2$, respectively [209]. However, in this work, the excitation spot has been made deliberately 3 to 4 times larger than the collection spot at the emission wavelength. This allows to obtain an overlap of the collection and the excitation spots, which ensures the maximum photon collection. One important issue is that the light penetration in silicon is wavelength dependent. For example, the penetration depth is almost 10 µm for an excitation wavelength of 780 nm, whereas the value is around 200 nm – 250 nm for a 405 nm excitation [210–212]. Thus, the effective collection depth can also be shorter than the diffraction limited values when the photon penetration/excitation depth is smaller and the free exciton diffusion is not significant.

In this section, samples from two different types of commercially available silicon wafers, grown by Czochralski (Cz) and Float Zone (Fz) methods, are studied by PL. The main difference made by the growth techniques is the amount of unwanted impurities such as carbon and oxygen remaining in the grown silicon ingots, which in the long run affect the emission properties. For Cz-Si, the amount of contamination is usually more than an order higher compared to the case of Fz-Si [213–215]. The samples used in the PL characterisation of D^0Xs are 525 µm thick, $\sim 5 \times 5$ mm chips from Fz and Cz silicon and have a phosphorus concentration of $\sim 10^{15}$ cm^{-3}.

We have tested several above-band excitation wavelengths, ranging from blue, 405 nm up to near-infrared (NIR), 1047 nm. In addition, to excite the emitters, the time required for reneutralising ionised donors is strongly influenced by the excitation

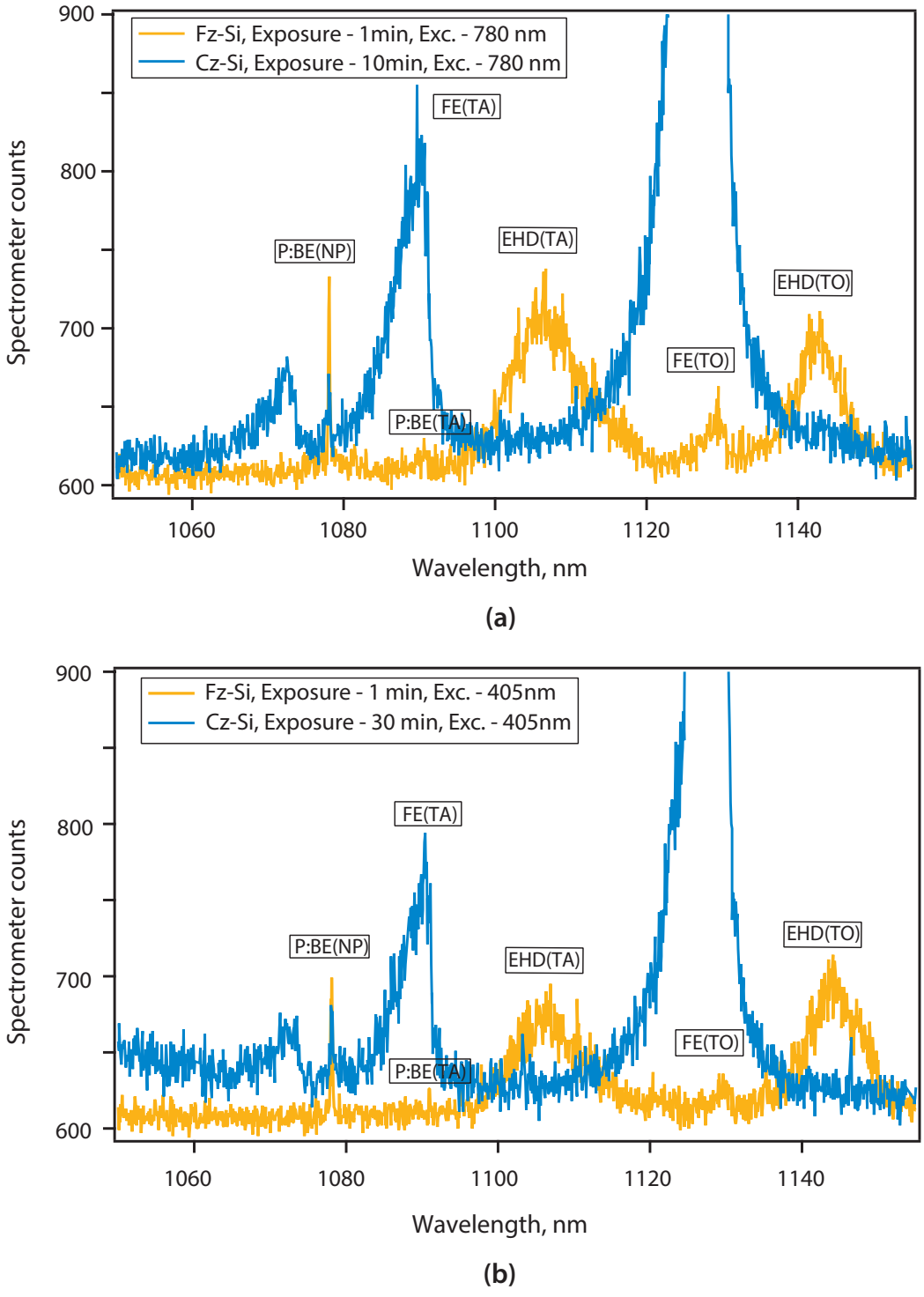

Figure 3.3: PL measurement of ^{31}P D^0X transitions in commercially available silicon wafers (Cz and Fz types): PL signal with (a) an excitation of 780 nm, (b) an excitation of 405 nm.

energy and power. For resonant or slightly above bandgap excitation (1047 nm) and excitation laser power densities in the range of a few mW/mm^2, the reneutralisation time for ionised P donors is in the order of milliseconds [90], which along with the

poor quantum efficiency in silicon offers a very low photon emission rate. Thus, we picked 780 nm and 405 nm excitation sources for the PL measurements. Figure 3.3a and 3.3b show PL measurements with excitations from the 780 nm fiber laser and the 405 nm Laser Diode, respectively. The PL signals from Fz and Cz are considerably different in terms of emission properties. In the case of the Fz-Si, we clearly see the ^{31}P D^0X emission (at 1078.1 nm) with an exposure of one minute, accompanied by the phonon assisted bound-exciton (BE), free-exciton (FE) and electron-hole droplet (EHD) transitions at longer wavelengths, as in Figure 3.3. On the other hand, the PL spectra of the Cz-Si is complicated due to presence of various unwanted impurities and structural defects [216–218]. Our set-up is designed to detect signals around the ^{31}P D^0X emission line and extract the photon counts efficiently, not for high-resolution spectroscopic analysis. Thus, investigating the PL spectra from the Cz-Si thoroughly is beyond the capability of our system. We observe that the PL signals from ^{31}P D^0X transitions are weaker by more than an order of magnitude for the Cz-Si. For 780 nm excitation, an exposure time of 10 minutes was required to obtain an observable ^{31}P D^0X signal (Figure 3.3a) and still the intensity is half that of the Fz-Si signal. With the 405 nm excitation, the D^0X emission is even weaker, an exposure time of 30 minutes has been required before observing a clear signal (Figure 3.3b). The estimated photon count rate in the Cz-Si sample from the PL data has been found to be $\sim 60\times$ weaker than in the case of the Fz-Si sample. This happens most probably due to the more shallow excitation profile ($\sim$ 250 nm) of the 405 nm LD, which addresses fewer donors and the presence of unwanted impurities and defects near the surface affects the formation of D^0Xs more seriously than deeper into the host silicon. The no-phonon (NP) line of ^{31}P D^0X transition is broader in the Cz-Si, as expected due to the impurity related strain. Furthermore, we see broad and comparatively strong phonon-assisted emissions from free-excitons (FEs) in the case of the Cz-Si but there is no observable trace of EHD signals which are prominent for the Fz-Si. Due to these facts, in this study, the Fz-type silicon has been chosen as the reference for the ^{31}P D^0X emission properties.

In Figure 3.4a, the PL signals using excitations from the 780 nm fiber laser and the 405 nm Laser Diode are compared. The diffraction limited collection depth of the confocal system is around 2.5 µm for the $\sim$ 1078 nm D^0X emission. The minimum stable excitation power of the 405 nm LD is almost double of the maximum power available

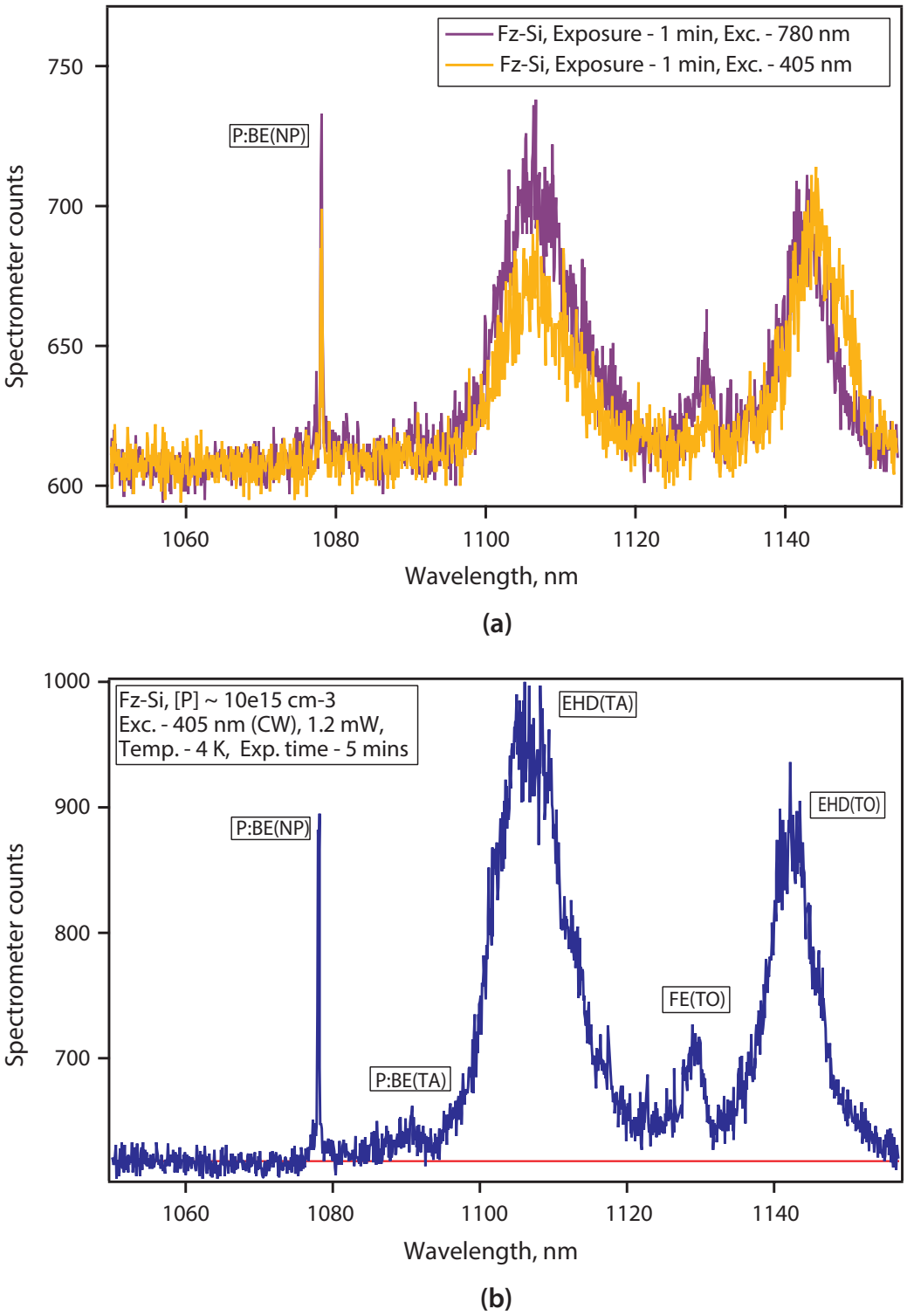

Figure 3.4: PL measurement of ^{31}P D^0X transitions in Fz-type silicon: PL signal from Fz-Si (a) comparison between 780 nm and 405 nm excitations and (b) detailed PL spectrum of reference Fz-Si sample.

from the 780 nm fiber laser. A higher energy and higher power excitation provides more free carriers/excitons and faster donor reneutralisation [91], respectively. Thus, a

stronger D^0X emission is expected for the 405 nm excitation when the free exciton (FE) diffusion is dominant. However, when measured using the same exposure time (e. g. 1 minute), we observe that the photon counts for the 405 nm excitation is half of that for the 780 nm excitation, as shown in Figure 3.4a. To understand this, we consider the free exciton (FE) diffusion in silicon carefully. The free exciton (FE) life-time (τ_{FE}) is very short in doped silicon. For a donor concentration of $N_D \sim 10^{15}$ cm^{-3}, τ_{FE} is around a nanosecond [184, 219]. The FE diffusivity in silicon is also considerably influenced by the presence of of impurities. In moderately doped silicon ($N_I \approx 10^{16}$ cm^{-3}), the measured value of the FE diffusivity (D_{FE}) is ~ 11 cm$^2/s$ at 12 K [220]. These project an FE diffusion length ($\sqrt{D_{FE}\tau_{FE}}$) of ~ 1 µm or less. Similar to the impurity dopants, the structural and surface defects also trap the FEs. Moreover, in case of high densities, the condensed FEs form electron-hole droplets (EHDs) at low temperatures (≤ 25°C) [221]. EHDs have a diffusion length of only few tens of nanometers [206] which further reduces the chance of the FE diffusion into the silicon substrate. All these facts suggest that FEs diffuse into only a thin layer (few hundred nanometers) of the sample and form D^0Xs within that layer. This slow FE diffusion in doped silicon plausibly explains the reduced photon counts (Figure 3.4a) for an excitation that prompts a faster free carrier/exciton generation and donor reneutralisation. With a negligible FE diffusion, we can further assume that the effective excitation and collection depth for the 405 nm light is close to its penetration depth. Therefore, the 405 nm LD is chosen as a reference excitation source as our aim is to excite the impurities residing only in the thin silicon layer at the sample surface.

In PL measurements, only a fraction of the emitted photons are detected. To estimate the number of detected photons, we have to take into account several issues such as the number of effective emitters in the collection volume, the outcoupling efficiency for emitted photons, path losses in the optics, efficiency of the detectors etc. Thus, the photon count or detection rate obtained from a certain detection system can be expressed by the following relation:

$$\text{Photon Count} = \frac{Q.E. \times O.E. \times \text{path loss factor} \times D.E. \times \text{no. of emitters}}{2 \times \text{ion neutralisation time}} \quad (3.1)$$

where, $Q.E.$ = quantum efficiency

$O.E.$ = outcoupling efficiency

$D.E.$ = detector efficiency

The luminescence quantum efficiency of the ^{31}P D^0X recombination in silicon is $\sim 10^{-4}$ [59]. The outcoupling efficiency for any unpatterned silicon sample is only about 1.5% for an objective with $NA = 0.65$ (See Figure 1.7). The efficiency of silicon based detectors at the near bandgap wavelength range is also poor, around 1%. The optical set-up incorporates some loss as well, due to the non-ideal behaviour of filters, gratings, single-mode fiber (SMF) coupling etc. The path losses in the optics are almost 90%. To estimate the photon count rate, we carry out a measurement with an exposure time of 5 minutes to get a signal well above the noise floor and use the outcome as a reference. Figure 3.4b shows the result of the reference PL measurement on the bulk Fz-Si sample. With a spotsize of ~ 2.2 µm and an effective collection depth around 250 nm, we can estimate that there are $\sim 1 \times 10^3$ effective emitters inside the collection volume. We observe the ^{31}P D^0X transition line centred at ~ 1078.1 nm (Figure 3.4b). However, at the top, the NP line seems to split into two peaks at ~ 1078 nm and ~ 1078.2 nm, presumably due to strains from sample mounting. The actual linewidths are not resolvable due to the limitation in the spectrometer resolution. From the PL data, we can deduce that the photon count rate is ~ 3.25 cps. With these numbers, we can estimate the P donor reneutralisation time using Equation (3.1). Thus, for a 405 nm excitation we obtain a reneutralisation time in the order of 230 ns, which serves as a reference. The data suggest that photon detection from a single donor would be possible if the total photon emission efficiency is enhanced by three orders of magnitude. In principle, high-Q photonic cavities are capable of boosting the total photon emission efficiency to such a level. However, high-Q photonic cavities can only be fabricated in free-standing, thin silicon membranes. Furthermore, to achieve the cavity enhancement effect, emitters have to be positioned deterministically in the field maxima of the cavity. Thus, special substrates (e.g. Silicon-on-Insulator (SOI) wafers), impurity doping techniques (e.g. ion implantation) are required to fulfil the fabrication and donor positioning criteria. In the following sections, we discuss about our investigations on the ion implantation

for donor positioning in Si and SOI wafers, activation of implanted donors, repair of implantation related damages and the PL measurements of these samples.

3.5 Donor implantation and implant related damages

3.5.1 Ion implantation process

The deliberate introduction of impurity dopants in semiconductor samples is a very important process step for realising electronic devices. The conventional way of introducing impurities is to use predeposition diffusion where dopants diffuse into the semiconductor from a source deposited on the surface of the wafer. The diffusion doping process/profile depends on several factors such as surface concentration, solid solubility of the predeposited source material, diffusivity of the dopants. So, it is difficult to control the diffusion doping profile and carry out a depth and area selective doping. The ion implantation (I/I) technique was developed to overcome these shortcomings. In this technique, ionised impurity atoms are accelerated using an electrostatic field and guided to strike the surface of the target wafer. Charged particles can enter beyond the surface area when they have sufficient penetration energy. After the penetration, the ions decelerate rapidly by collisional, stochastic processes and eventually come to a rest at some depth within the sample lattice. The penetration depth and impurity concentration can be effectively controlled by regulating the acceleration energy and the ion-dose, respectively. A lateral confinement of implanted dopants can also be obtained to some extend through a masked implantation. The sideways spreading of implant atoms under a mask is roughly one third of the vertical range for a particular energy [222]. A range of energies from few keV to several MeV are regularly used for ion implantations which allow average implant ion depths, ranging from few nanometers to tens of microns. Ion doses can be varied from 10^{11} ions/cm^2 to 10^{18} ions/cm^2.

3.5.2 Phosphorus implantation process in silicon

The ion implantation process for ^{31}P donors in silicon is well developed. The ion projected range (R_P) is statistically distributed and the deviation in the range is described by the straggle (ΔR). If the projected range R_P and the straggle ΔR are known for a certain material, the impurity concentration can be determined as a function of depth, from the following relation [223]

$$N(x) = \frac{\phi}{\sqrt{2\pi}\Delta R_P} e^{-(x-R_P)^2/2\Delta R_P^2}, \tag{3.2}$$

where, ϕ is the implant dose.

There is one more important issue that has to be considered when an implantation is carried out into single-crystal materials such as silicon in our case. For a single crystal host material, some of the ions can travel long distances with almost no energy loss when the ion velocity is parallel to a major crystal orientation. This phenomenon, known as channeling, takes place due to the inefficient nuclear stopping and low electron density in the channel. Channeling can be characterised by a critical angle Ψ. To avoid channeling, ions should be injected at an angle larger than this critical angle Ψ with respect to the major crystal axis of the substrate [223]. The critical angle can be calculated from the following relation

$$\Psi = 9.73^\circ \sqrt{\frac{Z_i Z_t}{E_0 d}}, \tag{3.3}$$

where E_0 is the incident energy in kV and d is the atomic spacing along the ion direction in $\mathring{A}$; Z_i and Z_t are the proton number of the ions and the target, respectively.

The desired implant ion profile (dopant depth, concentration) in the substrate from an ion implantation process depends on parameters such as the substrate material and orientation, ion species and energy, ion dose etc. So, to carry out an efficient implantation, it is important to estimate suitable values for the process parameters. A simulation of the ion implantation process is carried out for this purpose. There are several I/I process simulator software packages which use either semi-analytical or Monte Carlo (MC) techniques to calculate the interactions of energetic ions with the target material. The Monte Carlo simulation technique is more efficient than the semi-analytical ones because it can rigorously consider elastic scatterings, surface and interface phenomena, energy and angular distributions, physical damage, channeling effects, compound and/or multilayered target materials etc. Hence, in this work, we use a MC based software package - SRIM (The Stopping and Range of Ions in Matter) to simulate the ^{31}P implantation process in a silicon substrate. SRIM is a collection of programs for computing the stopping and range of ions (for 10 eV - 2 GeV) into the target material using a quantum-mechanical treatment of collisions between the ions and the target atoms

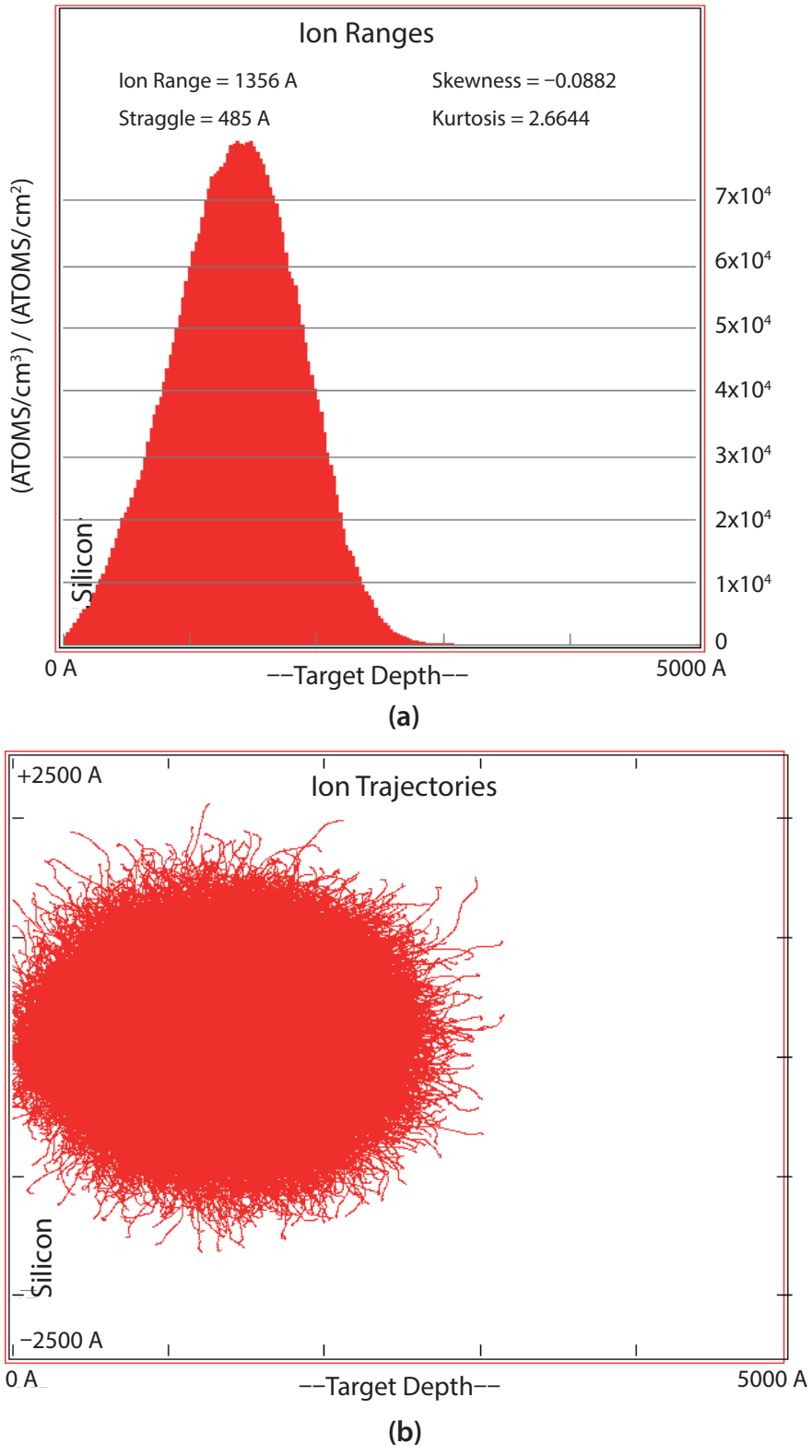

Figure 3.5: Simulation of ion distribution and trajectories of ^{31}P in silicon: Simulated ion (a) range and (b) trajectories into silicon for a ^{31}P implantation at an implant energy of 100 keV and with a tilt of 7° to the [100] normal of the crystalline silicon substrate. Simulation of the ion implantation process has been carried out with the SRIM software package [224].

[224, 225]. Within the SRIM package, we start with a program called 'Stopping and Range Tables' and calculate the projection range (penetration depth) and straggle values of ^{31}P ions in silicon for a given range of implant energies. From the calculated table, we select our suitable projection range and corresponding energy value. This energy value is then fed into a program called TRIM (Transport of Ions in Matter) to simulate the ion trajectories, ion distribution, recoil cascade & damages etc. inside the target with full animation. Figure 3.5 shows the simulated ion distribution and trajectories into silicon for a ^{31}P implantation at an implant energy of 100 keV and with a tilt of 7° to the [100] normal of the crystalline silicon substrate. In the ion distribution profile (Figure 3.5a), a distribution of implants is expressed with a normalised unit of $\left(\text{Atoms/cm}^3\right) / \left(\text{Atoms/cm}^2\right)$ and plotted against the implant penetration depth. The interesting fact with this distribution values is that we can multiply any implant dose with these and readily get the ion concentration vs. depth information for the particular dose under consideration. Finally, the suitable ion energy, dose and tilt angle values from the SRIM simulations are used as the process parameters in the real implant operation to obtain the desired ^{31}P concentration and depth profile in silicon and SOI samples.

3.5.3 Donor implantation related damages in silicon

Ion implantation is a good candidate method for incorporating single or few donors in order to realise single donor quantum bit or memory units in silicon [226–228]. However, ion implantation always comes with structural damage of the host material and most of the impurities incorporated do not occupy a substitutional lattice position in the silicon matrix immediately post-implant. The penetrating ion displaces many host atoms from the silicon lattice before coming to a rest. For example, an estimate shows that a 100 keV arsenic ion dislocates around 2000 silicon atoms in its path before stopping [222]. The type and amount of damage depend on the implant parameters such as types of implant ions (heavier ions cause more damages), acceleration energy, ion dose and current (high current gives rise to collision avalanche). Dopants start to precipitate if their concentration crosses the solid solubility limit. Thus, higher doses of phosphorus or arsenic (larger than 10^{14} cm^{-2}) can cause amorphisation of crystalline silicon [222]. When the implant dose is low (less than 10^{14} cm^{-2}), point defects such

as vacancies and interstitials occur. Sometimes cluster of point defects are also created in the host lattice even with a low ion dose. Higher doses extend damages and defects such as dislocation loops start to form in the crystalline silicon. Dislocation loops usually form very close to the amorphous/crystalline interface, hence, they are known as end-of-range (EOR) defects.

Thermal treatment is required to repair the ion implant related damages or defects. However, the thermal anneal can treat the damages only up to some level. If the implant damage is too high, the thermal treatment can only repair the structural damages by re-crystallisation of the amorphous region, but cannot restore the primary or point defects completely. Instead, more complicated defect structures such as dislocation loops and rods are often formed during the thermal treatment. These defect structures, aggregated from the primary defects, are known as the residual or secondary defects [229–232].

Finally, in all types of commercially available crystalline silicon samples, unavoidable structural defects and unwanted impurities such as oxygen, carbon, nitrogen etc. are always present to some extent. These defects and/or impurities are incorporated during the growth process and their concentration depends on the growth technique of the single-crystal silicon. Typical concentrations of oxygen and carbon in Czochralski type silicon (Cz-Si) are in the order of 10^{18} cm^{-3} and 10^{15} cm^{-3}, respectively [213–215]. In the Float-Zone (Fz) process, zone-melting is used for the crystal growth and the molten silicon does not contact any substances other than the ambient gas. Thus, higher quality silicon is produced than in the case of Czochralski process. In Fz-Si, the presence of unwanted impurities is considerably lower; the typical concentration of oxygen and carbon are around 10^{15} cm^{-3}. It is very difficult to get rid of these impurities completely and their presence in silicon is sometimes beneficial against thermal stress, mechanical deformation etc. So, in commercially available silicon, these impurities are allowed to remain in a controlled way [215, 233]. However, the presence of unwanted defects and impurities affect the ion implantation and damage repair step. For example, it has been found that the elimination of end-of-range (EOR) disorders caused by phosphorus implantation is less demanding when the host silicon wafer has smaller concentrations of the inherent oxygen impurities [234]. Antos *et al.* [234], have implanted phosphorus into Cz-Si with a dose of 5×10^{15} cm^{-2} at 40 keV. The Cz-Si has an intrinsic oxygen concentration of 7.3×10^{17} cm^{-3}. After phosphorus im-

plantation, a two step thermal treatment for damage repair and donor activation was carried out. A defect analysis was performed with the plan-view transmission electron microscopy (TEM) after the repair step. TEM micrographs revealed that the concentration of atoms bound by the extrinsic end-of-range dislocation loops (trapped interstitials) was around 14.3×10^{13} cm^{-2} for the Cz-Si sample. To compare the effect of thermal treatment in the presence of the oxygen impurities, the phosphorus implantation and thermal treatment process was carried out on a Fz-Si sample under the same process conditions. The Fz-Si sample contains two order of magnitude less oxygen impurities ($[O] < 5 \times 10^{15}$ cm^{-3}) in it compared to the Cz-Si substrate. The post thermal treatment defect analysis shows a remarkable decrease of the concentration of atoms bound by the EOR dislocation loops for the FZ-Si sample compared to the Cz one. The concentration of atoms bound by the EOR dislocation loops for the Fz-Si sample is found to around 4.3×10^{13} cm^{-2} [234]. Thus, it is clear that the presence of oxygen impurities plays an important role in defect kinetics and treatments of ion implanted silicon samples. Similarly, the presence of other impurities and point defects also affects the damage repair which are not always straightforward to quantify. Thus, it is implicit that the ion implantation related damages are complex in nature and difficult to repair.

3.6 Activation of implanted phosphorus donors in Fz-Si

The goal of the implant activation step is to set the dopants in substitutional positions in the host lattice, where they are electrically active. The first requirement is to repair the structural damage and restore the initial crystalline order. After recrystallisation, the dopants have to diffuse to the vacant positions and occupy the lattice sites. High temperature annealing ($\sim 1000 - 1200\,^{\circ}$C) is expected for an effective activation of the implanted donors [235]. However, the diffusion of donors in silicon at elevated temperatures increase significantly. The phosphorus diffusivity in silicon is 8.17×10^{-17} cm^2/s at 767 °C and becomes 1.45×10^{-12} cm^2/s at 1227 °C which is more than 4 orders magnitude higher [236–238]. This very high diffusion rate at elevated temperatures can hold back the fundamental goal of the deterministic donor positioning. So, a short duration anneal at elevated temperature is preferable for donor activation. On the other hand, a low temperature ($\sim 550\,^{\circ}$C) anneal is favourable for crystal regrowth and struc-

tural damage repair [239]. Hence, treating the crystal regrowth and the donor activation process separately can be advantageous. For efficient damage annihilation and donor activation, often multistep thermal treatments are required where the temperature and the duration of each step are critical [239]. In literature, a range of anneal temperatures and step lengths can be found. However, in practice, the optimum treatment temperature & step length depend on the degree, type of defects and are limited by the available process tools.

In this work, the multistep thermal treatment has mainly been attempted on the implanted samples and a number of recipes have been devised for this by researching the available literature on the post-implant thermal treatment. Step temperatures and lengths have been varied in the recipes to investigate a range of temperatures and process times. For the damage repair or recrystallisation step, we have used two step temperatures - $\sim$ 600°C and $\sim$ 850°C with a step length of 40 minutes. In the case of the activation step, a broader range of temperatures, 600°C to 1150°C, has been investigated. In the literature, short step lengths less than or around a minute are suggested to be more effective for donor activation considering the diffusion at elevated temperature [239–241]. In this work, activation step lengths spanning from tens of seconds to an

Damage repair step		Activation step			
Temperature	Time	Temperature	Time		
550 – 600°C (Furnace)	40 min	650°C (RTA)	30 s	60 s	90 s
		850°C (RTA)	30 s	60 s	90 s
		850°C (Furnace)	40 min		
		1000°C (Furnace)	1 hr		
		1050°C (RTA)	15 s	30 s	60 s
		1150°C (RTA)	15 s	30 s	60 s
850°C (Furnace)	40 min	1050°C (RTA)	30 s		
		1150°C (RTA)	30 s		

Table 3.1: Thermal treatment recipes for post implant anneal

hour have been investigated. Short length activation steps are implemented using the RTA tool. Conventional thermal treatment recipes [242, 243] with hour long activation steps also have been investigated. A thermal furnace with resistive heating was used to implement longer activation steps. A brief summary of the thermal processes investigated is provided in Table 3.1. PL characterisation of the treated samples are described in the following sections.

3.7 PL measurement of Fz-Si samples after post-implant activation

To investigate the ^{31}P D^0X formation and their transitions, bulk Fz-type silicon wafers were implanted with phosphorus at different doses and depths. Ion implantation parameters such as ion energy, dosage etc. were chosen carefully so that a peak implant concentration of 5×10^{15} cm^{-3} is obtained at depths of 60 nm and 120 nm. The peak concentration was chosen deliberately to match the diffusion doped ^{31}P concentration of Fz-Si investigated in Section 3.4. The depth profiles are selected considering the photonic structure pursued in this work and the penetration range of the 405 nm excitation source. The recipes provided in Table 3.1 are used for post-implant activation. The efficiency of implant activation is usually checked by Secondary Ion Mass Spectroscopy (SIMS). However, the implant concentration in our case is below the sensitivity of SIMS. Therefore, we have directly attempted the PL measurement step, skipping the SIMS analysis. The PL characterisation was carried out as discussed in Section 3.4. The summary of measurements is presented here with representative spectra shown.

Figure 3.6a shows the PL spectra from the Fz-Si samples which are furnace annealed at 850°C for 40 minutes along with the reference signal from the diffusion doped Fz-Si sample. Prior to the activation step, a 40 minutes long damage repair step was carried out at $\sim$ 600°C. According to the implantation parameters, the samples have peak implant concentration (5×10^{15} cm^{-3}) at $\sim$ 60 nm and $\sim$ 120 nm. After furnace annealing (FA), impurities diffuse in the sample. Inside the thin film and the collection depth of interest ($\sim$ 250 nm), the amount of ^{31}P dopants are assumed to be very close to the number of dopants in the reference Fz-Si. So, ideally, the PL signals from the implanted samples after the activation should have similar intensities compared to that

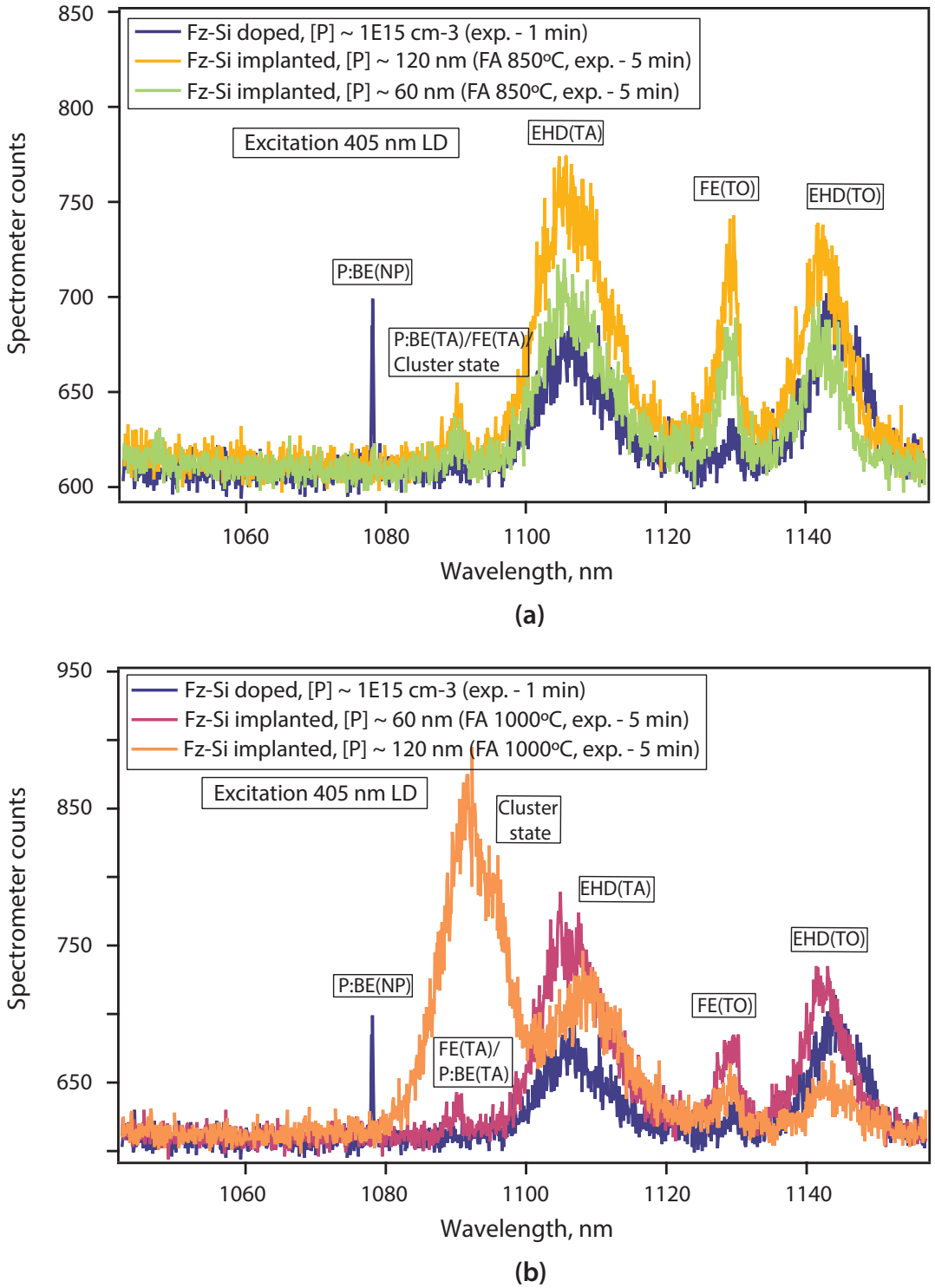

Figure 3.6: PL of implanted bulk Fz-Si after thermal treatment: PL signal from Fz-Si, with ^{31}P implanted at different depths and after donor activation in the furnace at (a) 850°C and (b) 1000°C.

from the reference signal. However, the PL signals are significantly reduced in the activated samples. In Figure 3.6a, compared to the reference sample, a five times longer exposure is used to obtain clearly observable PL signals from implanted samples. The

EHD and FE signals from both the transverse acoustic (TA) and transverse optical (TO) phonon assisted emissions are observed clearly but no trace of NP:BE signals from the activated ^{31}P dopants is found in the PL spectra. Interestingly, the emissions from the free excitons (FEs) appear stronger in this case - the intensity of the FE(TO) line is comparable to that of the EHD(TO) line. Furthermore, a broad distinguishable line is observed at $\sim$ 1090 nm. But it is difficult to attribute this broad emission to a certain transition, because emissions from the FE(TA), ^{31}P D^0X(TA) and ^{31}P donor cluster states emit at about 1090 nm wavelength. The PL spectra from the implanted samples also reveals that the emission is larger from the sample in which dopants are implanted deeper into the substrate. This is probably due to the surface properties of the sample. Surface roughness, termination, trapped charges, surface oxide etc. have a complex effect on the availability of free carriers, dopant segregation and exciton formation. Thus, the change of surface properties due to ^{31}P implantation seems to be responsible for the weaker emission from the sample with shallow implants.. Figure 3.6b shows the PL spectra from the samples with the furnace annealed activation at 1000°C for an hour. Though a more effective implant activation is expected, the diffusion of ^{31}P dopants at 1000°C is almost two orders magnitude faster compared to that at 850°C. To investigate the result of these effects, we again have measured the implanted samples with five times longer exposure time than in the case of the diffusion doped, reference Fz-Si sample. The PL spectrum from the sample with the shallow implants (peak concentration at $\sim$ 60 nm) in Figure 3.6b, apart from the reduced FE(TO) emission, does not show any significant change compared to the spectra from the sample activated at 850°C. We also do not see any ^{31}P D^0X(NP) signal from the samples activated at 1000°C. However, the spectrum from the sample with deeper implants (peak concentration at $\sim$ 120 nm) shows a very interesting feature around 1090 nm. We observe a broad and intense emission peak at 1090 nm which is most probably arising from the ^{31}P cluster states. Sumikura *et al.* observed and investigated similar cluster state emissions of ^{31}P donors from implanted SOI samples [205]. They have found that, in cases of high ion doses, ^{31}P donors have a tendency to cluster together during the post-implant activation rather than staying as isolated donors. The formation of these cluster states is detrimental to the D^0X formation. Thus, the cluster states along with the presence of non-cured structural, surface defects completely suppress the ^{31}P D^0X emission.

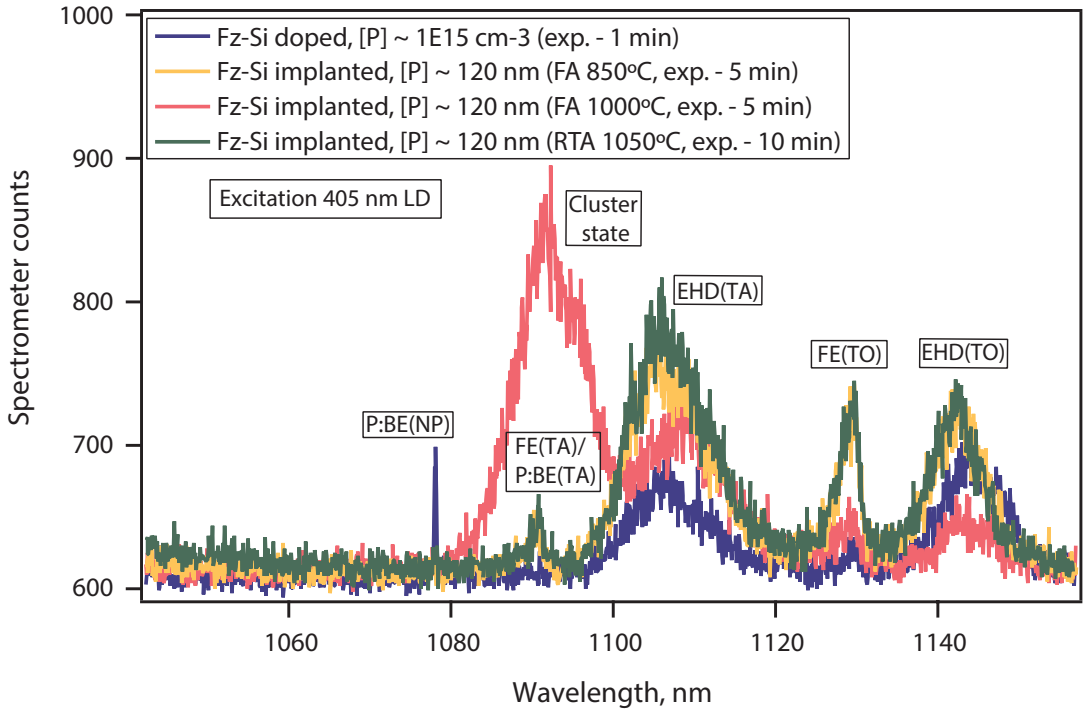

Figure 3.7: Comparison between Furnace and Rapid Thermal Anneal: PL measurement of ^{31}P implanted samples, activated using Furnace Anneal (FA) and Rapid Thermal Anneal (RTA). Furnace Anneals have been carried out at 850°C and 1000°C for 40 minutes and an hour respectively. The activation with RTA has been performed at 1050°C for 30 s.

In Figure 3.7, a comparison of thermal activation processes (FA and RTA) is presented using PL measurement spectra from activated samples. The samples used for the comparison have peak implant concentrations at $\sim$ 120 nm and been through a damage repair step at $\sim$ 600°C for forty minutes. The PL spectrum from the diffusion doped Fz-Si sample has also been included in the figure as a reference (Figure 3.7). Furnace anneals were carried out at 850°C for 40 minutes and at 1000°C for an hour. The activation with RTA were performed at 1050°C for 30 s. The difference between the spectra from the samples activated using FA and RTA around 1000/1050°C is noticeable. The RTA activated sample does not show the strong cluster-state emission under PL excitation as in the case of the high temperature FA. On the contrary, the spectra is very similar to that from the sample activated in the furnace at 850°C. This suggests that the diffusion of implanted impurities is less in the case of RTA treatment which in turn has altered the cluster-state formation. However, from Figure 3.7, we find that the RTA activated sample needs a longer exposure time for PL measurement, twice as long compared to the case of FA activation at 850°C, to reach a similar intensity

for FE/EHD emissions. This probably happens because the short duration RTA treatment cannot efficiently cure the secondary defects/dislocations from the initial lower temperature damage repair step. An hour long FA is effective for treating secondary defects[244] in addition to the dopant activation. Thus, the remaining defects in the RTA activated sample act as traps for free carriers, impurities, free excitons etc. and reduce D^0X, FE, EHD related emissions. This also explains the absence of D^0X emission in the PL spectra of the RTA activated Fz-Si sample. From this PL study we see that one has to find out the optimum window for step length and temperature in order to get efficient damage repair and activation while keeping the implant diffusion to a minimum. Furthermore, the available literature reveal that the electrical activation of the implanted ^{31}P donors strongly depends on the ion dose. An activation ratio of $\sim 42\%$ has been reported for an ion dose of $\sim 10^{13}$ ions/cm^{-2}, however the ratio reduces to less than 1% for an ion dose of $\sim 10^{11}$ ions/cm^{-2} [205, 245, 246]. Therefore, it can be concluded that compared to diffusion doped silicon samples, we need more donors in the collection volume in case of implanted silicon for PL detection of ^{31}P D^0X signals.

3.8 PL measurement of implanted, thin Cz-SOI sample

To enhance the ^{31}P D^0X(NP) emission, the donors have to be positioned at a certain location and depth in the samples to place them at the field maxima of photonic cavities. As discussed in Section 3.5, ion implantation is one of the most suitable technique for a deterministic positioning of impurities in the sample substrate. The PL study on ^{31}P implanted Fz-Si samples in the previous section has revealed that the activation of the implanted donors in silicon is low; and the actual implant concentration required, to observe ^{31}P D^0X emission, should be larger than for the case of the diffusion doped donor concentration. However, increasing the donor concentration arbitrarily is not helpful for observing ^{31}P D^0X emissions in silicon because of the induced strain and damage by higher implant doses, chance of cluster formation or reaching the degeneracy level. Therefore, an optimum implant concentration needs to be determined, which is sufficient for providing a detectable emission from ^{31}P D^0X transitions, but low enough to avoid the ^{31}P cluster formation and the introduction of any significant strain/damage. In this section, we investigate samples from a thin SOI wafer for optimal activation parameters, implant concentration etc.

3.8.1 Thin SOI wafers

To realise photonic cavity devices resonant around the ^{31}P D^0X transitions, we need silicon-on-insulator(SOI) wafers with a device layer thickness of $\sim$ 200 nm and a $2-3$ µm buried oxide (BOX) layer (photonic cavity designs are discussed in Chapter 4). SOI wafers with such thin device layers are commercially manufactured using Smart-Cut technology [247, 248]. In this technique, a silicon substrate is oxidised and implanted with hydrogen below the oxide layer. The oxidised substrate is then fusion bonded with another silicon substrate known as the handle layer. The hydrogen implantation creates a weakened damage layer at the end of the ion's range inside the silicon lattice. The implanted wafer goes further through a heat treatment which splits the wafer into two parts across the damage plane. This splitting process, known as Smart-Cut, allows a thin layer of silicon to be transferred to the handle layer to form the SOI structure. Finally, in order to treat defects and surface damages, the thin SOI wafer is annealed and polished using Chemical Mechanical Polishing (CMP) and touch polishing techniques.

3.8.2 PL measurement of thin Cz-SOI samples

The samples used here for ^{31}P implantation and PL measurements are from a thin SOI wafer, consisting of a 220 nm Cz-typre silicon device layer; a 2 µm BOX layer and a 725 µm Cz-Si handle layer. The device and handle layers are boron doped, p-type silicon with a resistivity of $\sim$ 10 kΩ-cm. An undoped device layer would be preferred for our experiments, but thin SOI wafers are rare and expensive. Therefore, we have initially used a thin, Cz-SOI wafer for the ion implantation and optical experiments. Implantation parameters such as ion dose, energy are varied to obtain implant concentration peaks at different depths. The implant concentration is varied from 1×10^{15} cm^{-3} to 3×10^{17} cm^{-3} and the implant depth has been tailored from $\sim$ 75 to $\sim$ 130 nm. After the ion implantation step, the samples were activated using the recipes provided in Table 3.1, followed by an investigation with PL measurements. In case of the Cz-SOI sample, the donor activation is inefficient compared to the case of the bulk Fz-Si sample due to several issues such as the presence of boron impurities, segregation and trapping of phosphorus dopants into the oxide interface/layer, structural defects in the device layer etc. In Figure 3.8, notable findings from the PL measurements of the thin,

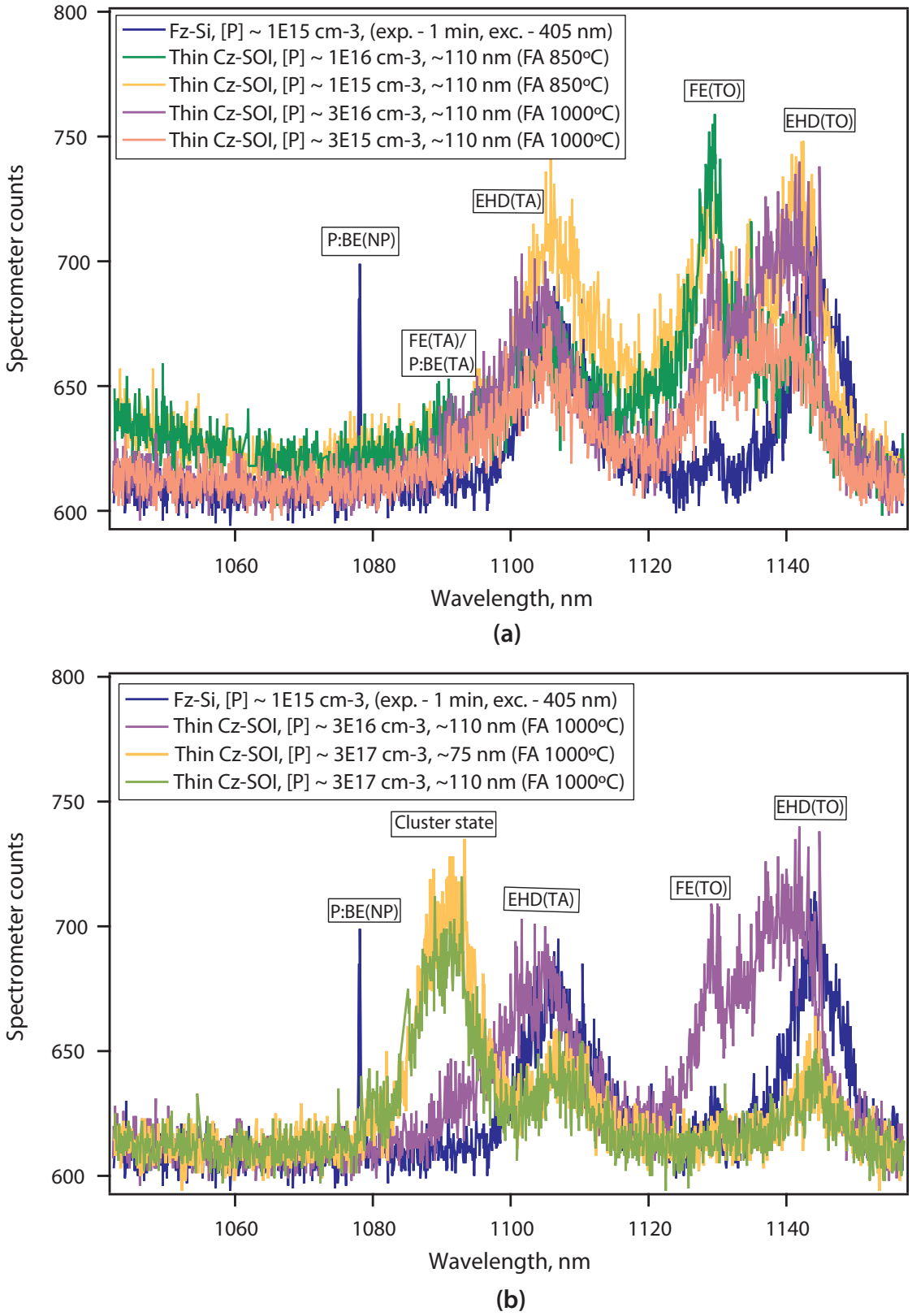

Figure 3.8: PL measurement of implanted, thin Cz-SOI after thermal treatment: PL signal from thin Cz-SOI with ^{31}P implanted (a) at same depth and activated at different temperatures, (b) at different depths and activated at 1000°C.

Cz-SOI samples are presented. Figure 3.8a shows PL spectra of samples with different peak concentrations at the same implant depth of $\sim$ 110 nm. The implanted samples have been through activation steps with a furnace anneal at 850°C and 1000°C. No ^{31}P D^0X(NP) or cluster state emission have been observed even for a implant concentration of 3×10^{16} cm^{-3} which is larger by an order of magnitude than the doping concentration (1×10^{15} cm^{-3}) of the reference Fz-Si sample. Whereas, in the bulk Fz-Si samples, a post-implant activation step at 1000°C gives rise to a very clear and broad cluster state emission for an implant concentration of 5×10^{15} cm^{-3} (as shown in Figure 3.6b). In Figure 3.8b, we further investigate the effect of implant depth and concentration variation on the PL emission in thin, Cz-SOI samples. The PL spectra reveal that the implant depth variation has a negligible effect on the emission properties. On the other hand, when the peak concentration is increased to a value of 3×10^{17} cm^{-3}, we still do not observe any BE(NP) emissions but a strong and broad cluster state emission appears in the PL spectrum irrespective of the implant depths. Finally, when the cluster state appears in the spectrum, the FE and EHD emissions become weak because most of the electron-hole pairs are captured by the cluster state.

3.9 PL measurement of ^{31}P D^0X transitions in doped SOI samples

Our investigation on the ion implanted bulk silicon samples has revealed that the optimum activation of implanted dopants is challenging. In the case of SOI wafers/chips additional defects accumulate in the device layer of SOI wafers during their fabrication and thinning processes. The presence of a buried oxide (BOX) layer also complicates the situation, for example, ^{31}P donors near the silicon-oxide interface have a tendency to segregate into the oxide layer. Furthermore, charges can be trapped at the oxide interface and defects in the oxide layer can give rise to non-uniform strain etc. All these issues affect the dopant activation, free carrier generation and PL emission from ^{31}P implanted SOI chips. Therefore, we studied different SOI samples to find optimal conditions for D^0X emissions and their detection. We begin with the PL spectroscopy of ^{31}P doped, thick SOI samples although our main goal is to obtain ^{31}P D^0X emission from ion implanted, thin SOI wafers with which we can fabricate photonic structures

to enhance the emission.

3.9.1 PL measurement of thick 2 µm SOI

We start our investigation with SOI samples manufactured using the wafer bonding technique. Wafer bonding is the simplest way to make silicon-on-insulator structures. The buried oxide layer is formed with the direct bonding of two silicon wafers where either one or both of the silicon substrates are pre-oxidised [222]. The device layer is thinned afterwards to get the desired thickness. The advantage of this technique is that the top device layer properties such as material quality, crystal orientation, doping concentration, thickness etc. do not depend on the handle wafer properties and can be optimised independently. The only downside is the requirement of a careful thinning with an etch stop layer and a real time thickness monitoring in order to achieve a device layer thickness of less than 5 µm. For this reason, the minimum device layer thickness found for commercially available, bonded SOI wafers is around ~ 2 µm. The 2 µm thick device layer is not suitable for fabricating photonic structures such as photonic crystal cavities, circular Bragg gratings etc. To fabricate the photonic structures, we require SOI wafers with a device layer thickness of around $150-250$ nm and a BOX layer of around $2-3$ µm. However, such thin SOI wafers with suitable material quality, doping type and concentration are either commercially not available or extremely expensive and rare. As a first step to investigate the ^{31}P D^0X emission in a SOI wafer, we start with the 2 µm thick device layer, bonded SOI wafer. The BOX layer and the handle layer of the SOI wafers are ~ 3 µm and $\sim 500-600$ µm thick, respectively.

Figure 3.9 shows the the PL spectra from a 2 µm thick device layer of bonded SOI samples. We investigate two different SOI samples. The first sample is from a Cz-Type SOI wafer i.e., both the device and handle layer are of Cz process grown silicon. The device and handle wafers are doped with ^{31}P with a concentration of $\sim 1\times10^{15}$ cm^{-3}. To investigate the ^{31}P D^0X emission, the sample is excited with 405 nm and 780 nm sources and then compared with the reference Fz-Si bulk sample results. The emission spectra are shown in Figure 3.9a. We see a ^{31}P D^0X emission line from Cz-SOI sample but much weaker compared to the signal from the reference Fz-Si sample (which also has been observed with the bulk Cz-Si samples in Figure 3.3, Section 3.4). The 780 nm excitation can penetrate deep (~ 10 µm) into the silicon, so, it excites donors both in

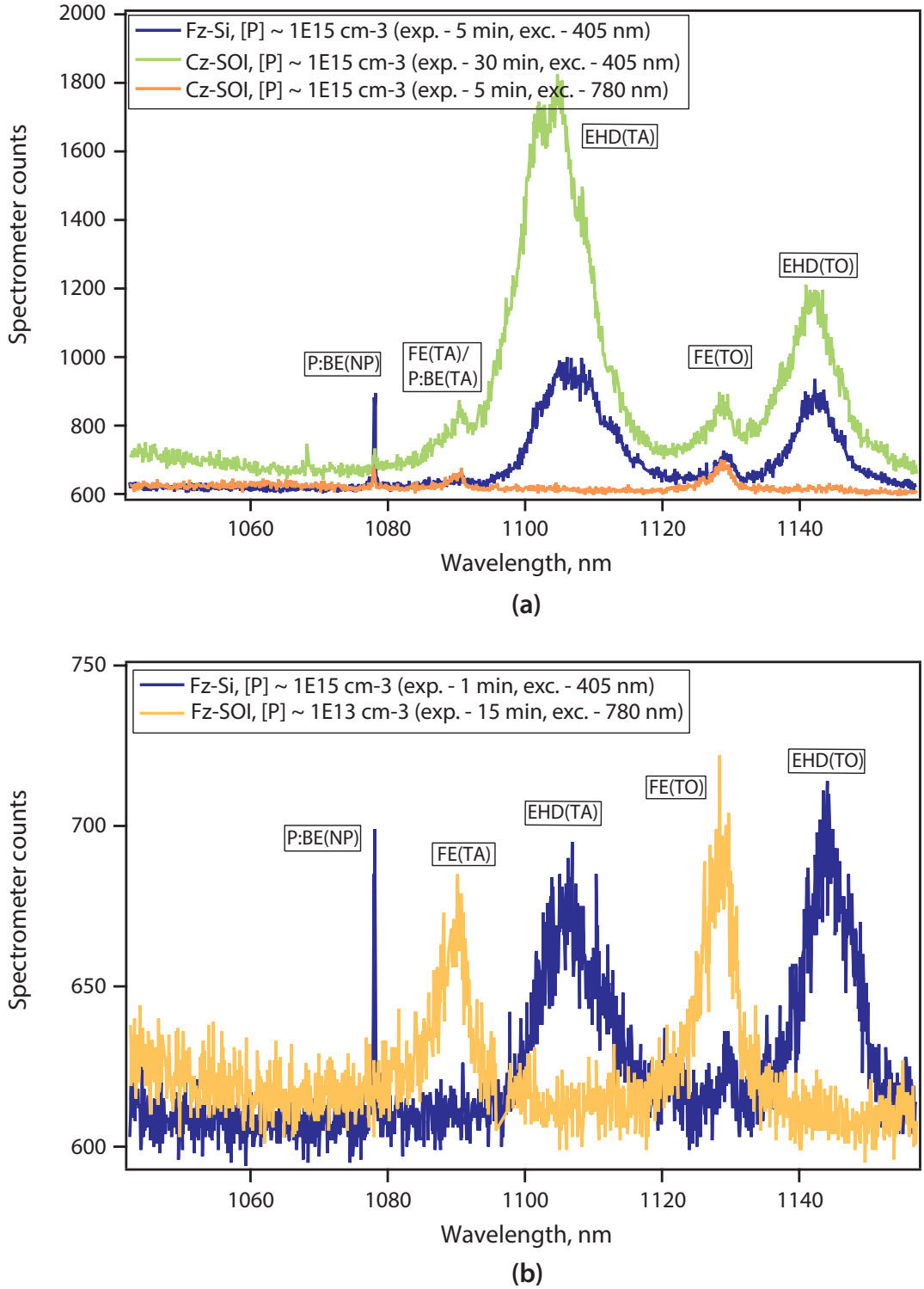

Figure 3.9: PL measurement of diffusion doped SOI sample: PL spectra from 2 µm thick device layer of (a) Cz-SOI sample and (b) Fz-SOI sample.

the device layer and within a few microns into the handle layer. The confocal collection volume is $\sim$ 2.5 µm but the scattered emission from the handle layer also reaches the device layer to some extent and is also collected by the objective system. We see weak

but distinguishable ^{31}P D^0X and FE emission lines with a 5 minutes exposure time and no trace of EHD lines in the spectra. The 405 nm excitation is used next in order to excite a thin fraction of the device layer and avoid any scattered emission from the handle layer. We manage to see a very weak ^{31}P D^0X emission after 30 minutes of exposure. Comparing the photon counts, it is found that the BE(NP) signal from the Cz-SOI sample is $50-60\times$ weaker than the signal from the reference Fz-Si sample. This is quite consistent with the case of the bulk Cz-Si samples observed in Section 3.4. Interestingly, in addition to ^{31}P D^0X and FE lines, we clearly observe EHD lines in the spectrum from the 405 nm excitation. The EHD emissions indicate that enough free carriers and electron-hole pairs are generated with the excitation and managed to form droplets even in the presence of unwanted impurities and defects in the host. This provides an evidence of better excitation efficiency at 405 nm.

In the next step, we investigate a ^{31}P doped Fz-SOI sample. The wafer dimensions are the same as the Cz-SOI one but the silicon layers are grown with the float-zone (Fz) technique. The silicon quality of both the device and the handle layer are better due to less impurities (as described briefly in Section 3.5). The high quality device layer is good for our D^0X related optical experiment, however, commercially available Fz-SOI wafers have either intrinsic or high-resistivity (low-doping concentrations) silicon layers. The wafer we use in this experiment has high-resistivity ($\sim 1000\,\text{k}\Omega$-cm) device and handle layers. The device layer is ^{31}P doped, n-type silicon. The resistivity value indicates a doping concentration around 1×10^{13} cm^{-3} which is two orders magnitude lower than the donor concentration in the reference Fz-Si sample. In Figure 3.9b, the PL spectrum of the Fz-SOI sample is presented. The spectrum contains FE emission lines, however, no ^{31}P D^0X emission is observed in the spectrum even when excited with the 780 nm light and long exposure times (e.g. 15 minutes in Figure 3.9b). This can be anticipated as the number of donors in the collection volume is too small to provide detectable D^0X transitions for our measurement system.

3.9.2 Thinning and PL measurements of the thinned Cz-SOI

In Figure 3.9a, we have managed to observe the ^{31}P D^0X transitions in a ^{31}P doped SOI sample. Unfortunately, most of the ^{31}P doped, commercially available SOI wafers have a minimum device layer thickness of 2 µm which is too thick for fabricating pho-

tonic devices. So, we require a process to thin down the device layer which will not affect the optical properties of the thinned SOI sample. A silicon layer can be thinned by several ways such as dry etching, wet etching, oxidation etc. However, the critical issue in our case is a controlled etch of the target layer without damaging the surface. We have attempted dry etching and oxidation techniques for thinning. Wet etching has been avoided because of the poor control over the etch rate. In case of dry etching, the silicon layer is etched with a Reactive Ion Etching (RIE) tool using CHF_3 and SF_6 gas chemistry (silicon dry etch process has been discussed in detail in the Chapter 5 covering fabrication processes). The silicon etch rate using CHF_3 and SF_6 gas chemistry is around 70 nm/min for an RF power of $150-200$ W. The device layer of the Cz-SOI sample has been thinned down to 1 μm with 16 minutes etch. A cyclic etch process with 1 minute etching and 2 minutes cool down steps has been used in order to minimise surface damage. We also use oxidation techniques for thinning the device layer. In the oxidation thinning process, a thermal oxide layer is grown on the silicon surface at 1100°C in a furnace and then the oxide layer is removed using a Hydrofluoric (HF) acid etch. With this thinning technique, a very good surface quality can be maintained. However, the thermal oxide growth process is very slow. As the oxide layer grows, it starts to work as a protective layer and slows down further growth. The growth time increases rapidly after a few hundred nanometres of oxide is grown. For example, a calculation of the thermal oxide growth time projects that a 200 nm layer growth would need ~ 5 hrs whereas, a 1 μm oxide layer would require almost 5 days of process time. So, we use several iterations of oxide growth and removal steps to thin the device layer down to 1 μm.

The spectra of the thinned, Cz-SOI samples are presented in Figure 3.10. The dark blue spectrum is the PL signal from the reference Fz-Si sample, the orange and the green are from the thinned Cz-SOI samples using the RIE and thermal oxidation (TOx) techniques, respectively. In the case of the RIE thinned sample, we find none of the usual emission features observed in ^{31}P-doped silicon samples. This suppression of emission features happens due to the damage and contamination incorporated by the RIE process. Several types of damages can be inflicted to the sample, specially to the surface during the RIE process due to the ion bombardment, radiation effect, charge build up etc. There is also the potential for the accumulation of ultra-thin layers

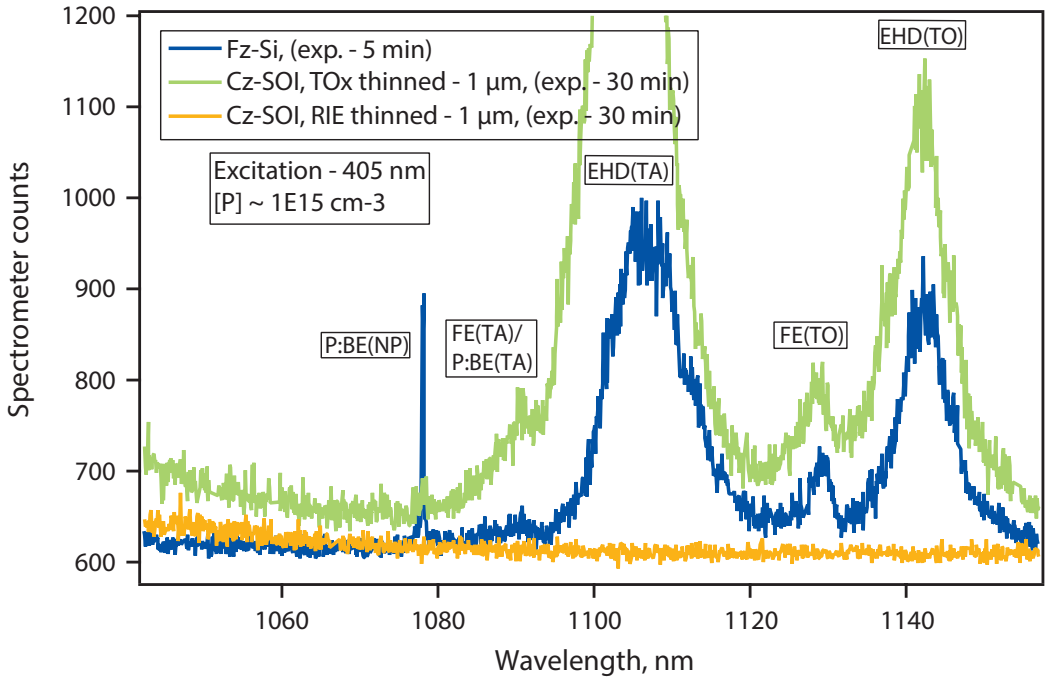

Figure 3.10: PL measurement of thinned Cz-SOI sample: PL spectra from 2 µm thick device layer of Cz-SOI sample.

of reaction products on the sample surface, bond damage and the permeation of impurities such as carbon, hydrogen, cathode and/or chamber materials into the sample [249]. Silicon etching with a CHF_3/SF_6 gas chemistry or hydrogen containing plasma can cause electrical deactivation, lattice damage and/or amorphisation near the etch surface. Furthermore, a formation of donor-like defect centres, deep into the sample has been reported in literature for the CHF_3/SF_6 based etching [250, 251]. The extent of the damage depends on the etch rate, power, voltage bias during the RIE process. All this damage affects the formation of free carriers and excitons which explain the strong suppression of any exciton related emissions in the RIE etched samples. The RIE related damage could, in principle, be repaired to some extent with thermal anneal and surface treatment. However, a careful study is required to devise an efficient damage repair process, without compromising further fabrication processes and the performance of fabricated devices. Therefore, RIE thinning is is viewed as poorly suited for our purpose. The thermal oxidation (TOx) thinning, on the other hand, is significantly less aggressive. It might incorporate some surface irregularity transferred from any defects at silicon-oxide interfaces but does not introduce any major damage or source of contamination. The PL spectrum from the TOx thinned Cz-SOI wafer (Figure 3.10) depicts

this. We can clearly see the exciton related emissions in the PL spectrum. Similar to the unetched sample in Figure 3.9a, it needs a 30 minutes exposure to obtain an observable ^{31}P D^0X transition. The ^{31}P D^0X emission line from the thinned Cz-SOI sample appears slightly broader and weaker than the case of the unetched sample which, can be attributed to the surface irregularity, strain and scattering effects. However, the PL measurements are carried out without any surface treatment after thinning which, again, verifies the fact that the damage incorporated by the TOx process is not severe and the optical properties of the sample have not degraded beyond recovery.

3.10 PL measurement of ^{31}P D^0X transitions in implanted, thick SOI samples

Our investigations on ^{31}P doped, thick SOI samples have revealed that the D^0X(NP) emission can be observed if there are sufficient substitutional donors in the collection volume and the formation of D^0Xs is not completely suppressed by the presence of unwanted impurities. In the case of ion implantation, we have found that the D^0X emission is completely suppressed in ^{31}P implanted, thin Cz-SOI samples (Section 3.8) due to the excessive amount of defects and unwanted impurities in the device layer. Thick, bonded SOI wafers, on the other hand, suffers less from defects/structural damages as their manufacturing process does not require any hydrogen implantation or wafer splitting step. So, in this section, we investigate the ^{31}P implanted, thick SOI samples using PL spectroscopy as a proof of concept study to observe the ^{31}P D^0X emission in ion implanted SOI wafers.

3.10.1 PL measurement of implanted Cz-SOI sample

Here, we study a 2 μm thick, Cz-type SOI sample that is implanted with a moderately high dose ($\sim 10^{12}$ ions/cm^{-2}) of ^{31}P ions motivated by observations by Sakimura *et al.* [205], that the fraction of electrically activated phosphorus increases with the implant dose. The implanted Cz-SOI sample we use here, is provided by one of our collaborators from London Centre for Nanotechnology, UCL [252]. The samples are metal-oxide-semiconductor field effect transistors (MOSFETs) fabricated for the electrical detection of Rydberg series and optical transitions from the hydrogen-like phosphorus impurity in the silicon FET devices [252]. The MOSFET device consists of source,

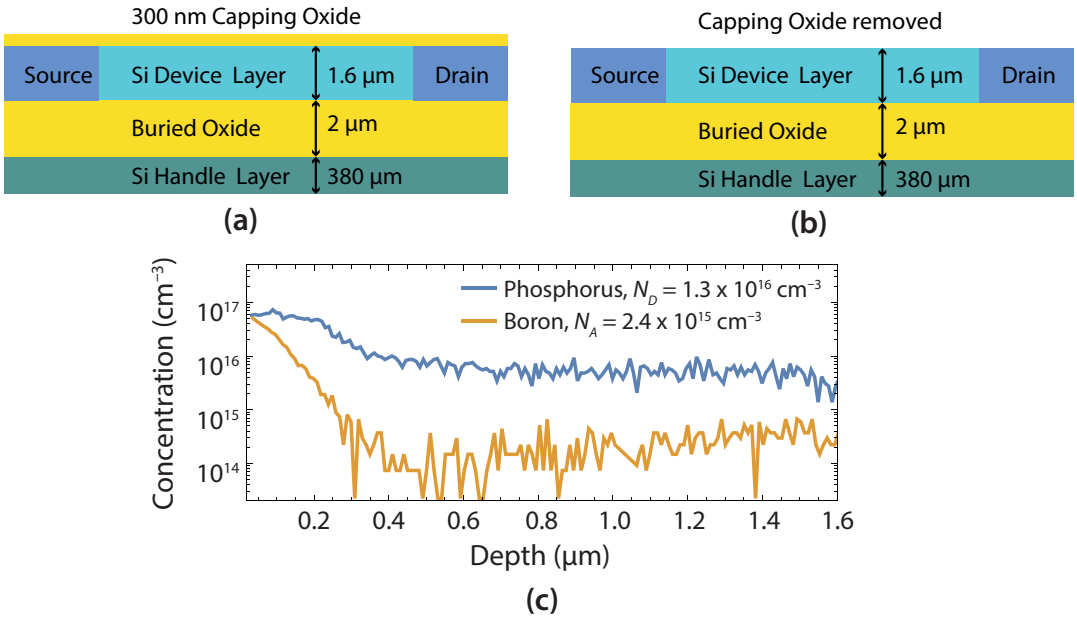

Figure 3.11: ^{31}P implanted, thick Cz-SOI sample: (a) The cross section of the MOS structure with ^{31}P implanted device layer, (b) after removal of capping oxide layer, (c) the dopant concentration within the device layer, from the secondary ion mass spectroscopy measurement. Images are reproduced from [252]

drain, voltage probe leads and the active region. The 450×450 µm active region has been implanted with ^{31}P ions at a dose of 1.5×10^{12} ions/cm^{-2} and an implant energy of 120 keV. Donor activation has been carried out using a furnace anneal at 1050°C for 1 hr. Figure 3.11a and b depict a cross-section of the MOS structure revealing the implanted device layer, the source, the drain and handle regions. A secondary ion mass spectroscopy (SIMS) measurement of the ^{31}P implant profile in the device layer is also presented in Figure 3.11c [252]. In this work, we are interested in the active device region of the MOS structure, because it resembles a ^{31}P implanted SOI structure, rather than a MOSFET device.

We have carried out PL measurements on the ^{31}P implanted active device region using 405 nm excitation and compared the result with the PL spectra from both Cz and Fz-type bulk silicon samples, as shown in Figure 3.12. The sample MOS structure has a 300 nm capping oxide (Cap-Ox) layer on top of the device layer; Figure 3.11a shows the device cross section with the capping oxide layer. When the active region of the MOS sample is excited without removing the Cap-Ox layer, a PL emission spectrum with severely broadened features appears. The emission peaks of the FE and EHD lines are broadened and overlap with each other. When the signal is integrated

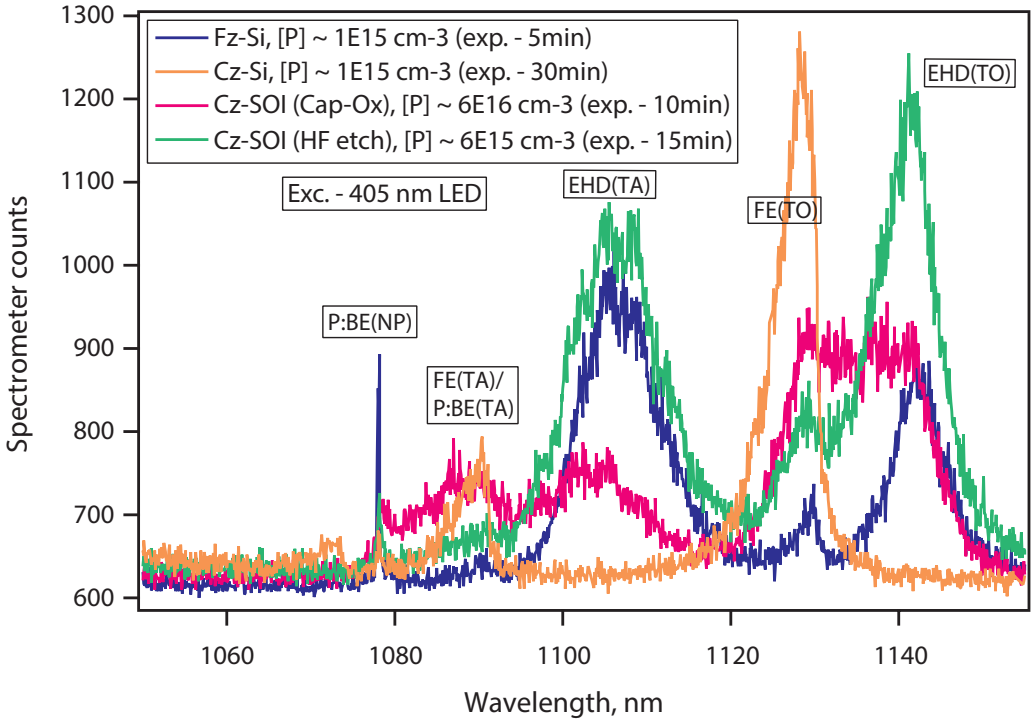

Figure 3.12: PL measurements of ^{31}P implanted, thick Cz-SOI sample: PL spectra from thick Cz-SOI samples, before and after the removal of the capping oxide, are compared with the spectra from bulk Fz-Si and Cz-Si samples

for 10 minutes or longer, the presence of a broad peak can be just identified around 1078 nm (red curve in Figure 3.12). But it is not clear how much the ion implantation damage contributes to this broadening and reduction in the PL signal, since the strain, interface-contamination and light scattering from the presence of the capping oxide layer can also strongly affect the PL emission properties. To verify this issue, we remove the Cap-Ox layer from the top of the device layer using a HF etch, the schematic of the etched cross-section is shown in Figure 3.11b. The result of the PL measurement on the active device region after the Cap-Ox removal is shown (green spectrum) in Figure 3.12, revealing that the Cap-Ox layer was mainly responsible for the broadening, as it disappears with the removal of the oxide layer. However, no significant increase in the D^0X emission intensity was observed. Figure 3.11c shows that diffused implants have got a roughly uniform concentration profile ($\sim 6 \times 10^{16}$ cm^{-3}), throughout the excitation depth ($\sim$ 250 nm) for the 405 nm light, after thermal activation. Estimating from the PL data, we find that the photon count rate for the device region without Cap-Ox of the implanted Cz-SOI sample is $\sim 10\times$ larger and $\sim 8\times$ smaller than the case of the bulk Cz-Si and the case of the bulk Fz-Si sample, respectively. However, with a near

surface donor concentration of $\sim 6 \times 10^{16}$ cm^{-3} in the active device region, the number of donors inside the effective collection volume in the implanted Cz-SOI sample will be almost two orders of magnitude higher than the case of diffusion doped silicon samples. This suggests that, with same number of donors in the effective collection volume, the emission of the implanted Cz-SOI sample would be weaker by one order of magnitude than for the bulk Cz-Si sample and three order magnitude than for the bulk Fz-Si sample. This indicates a strong effect of the implantation related damages on the ^{31}P D^0X emission.

3.10.2 PL measurement of implanted Fz-SOI sample

From the investigation on the ^{31}P implanted, Cz-SOI wafer, it was observed that one or two orders more donors are required to be in the collection volume in order to obtain a detectable ^{31}P D^0X emission. Optimum window for implantation and donor activation parameters were found, which allowed us to observe a ^{31}P D^0X emission from an ion implanted SOI sample (Figure 3.12). As a next step and to investigate the ^{31}P D^0X emission in the implanted Fz-SOI sample, we attempt a 2 μm thick, Fz-type SOI wafer for the ^{31}P donor implantation and activation. For ion implantation, we start with implant parameter values very close to the ones used for the Cz-SOI/MOSFET sample (see Section 3.10.1). The useful dose window is not wide, because high doses can result in the formation of the cluster states and if the dose is too low then there are insufficient effective emitters inside the collection volume. The Fz-SOI wafer used here is a SOI prime wafer from ultrasil corporation which has a 2 μm thick device layer, a 2 μm BOX layer and a 510 μm handle layer. Both the device layer and the handle layer are made of high resistivity ($>$ 1000 Ω-cm) Fz silicon. Two 2.5×2.5 cm chips from the Fz-SOI wafer are used for the ion implantation. The ^{31}P ion implantation is carried out at an ion implantation energy of 100 keV with a different dose for each chip - 7×10^{12} ions/cm^2 and 2×10^{13} ions/cm^2. The implanted chips were thermally treated with a 1 hr activation step at 1050°C. It is the same recipe which has been used for activating the implanted, thick Cz-SOI samples. Figure 3.13 shows the implant profile in the thick, Fz-SOI chips before and after the thermal treatment for the donor activation. After activation, the chips are cleaved into suitable (e.g. 5×5 mm) sizes and PL measurements have been carried out on the samples.

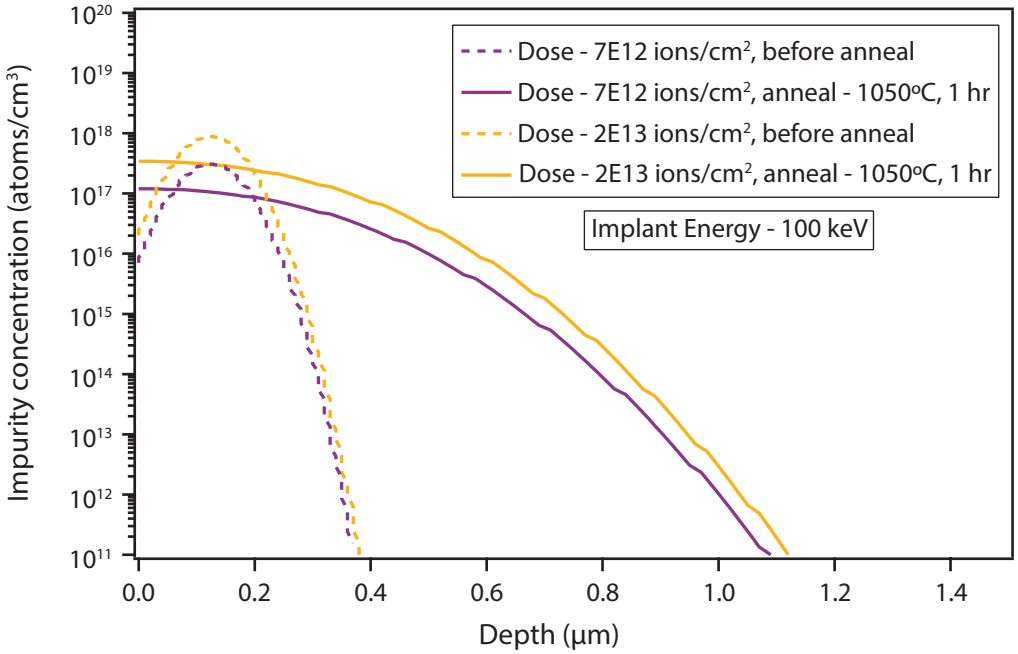

Figure 3.13: Simulation of implant profiles in thick, Fz-SOI samples after the ^{31}P ion implantation: Implant (^{31}P) profile in Fz-SOI samples for two different implant doses at an implant energy of 100 keV. The dotted and solid lines indicate the implant profile before and after the thermal anneal of 1 hr at 1050°C.

We start the PL measurement with the sample implanted for a higher donor concentration. According to the implantation parameters, the peak implant concentration would be at $\sim$ 130 nm below the surface. However, the implants diffuse inside the sample during the high temperature activation step and a near-uniform implant concentration ($\sim 3 \times 10^{15}$ cm^{-3}) is obtained throughout the excitation depth ($200 - 250$ nm), as shown in Figure 3.13. So, the number of implanted ^{31}P donors inside the collection volume is two orders of magnitude higher than in the case of the reference Fz-Si sample. For the PL spectroscopy, the sample is excited with the 405 nm source at its maximum available power (2 mW at the sample surface) because higher power is expected to provide faster donor reneutralisation and bound exciton formation [91]. In the PL spectrum, strong and broad emission peaks appear for the ^{31}P D^0X transitions and the cluster states, even with only a one minute exposure time (Figure 3.14). The line broadening occurs due to the strain in the silicon lattice caused by the high concentration of impurities and defects due to the high implant dose. The FE lines and P:BE(TA) lines overlap with broad cluster states and/or EHD emissions, making it difficult to discern them. The most significant feature observed with this sample is that the

strength of the ^{31}P D^0X emission reduces with repetitive measurement and completely disappears after a few of cycles. As shown in Figure 3.14, the green curve is the first PL spectrum after sample cooldown showing a strong D^0X(NP) emission line. For next cycle/measurement (the red spectrum) the intensity of the D^0X(NP) emission reduces significantly and during the third cycle, in the orange spectrum, the D^0X(NP) line completely disappears. The most plausible reason behind this seems the local heating effect in the SOI structure. The oxide layer in the SOI structure is both electrically and thermally insulating. So, an intense local heating at the top silicon layer would take place if the heat cannot be distributed or dissipated to the bulk. For example, at the maximum power of LED (40 mW), the power delivered to the sample surface after the path losses is around $\sim$ 2 mW. With this power ($\sim$ 2 mW), the power intensity for a spot size of $2-3$ µm will be ~ 30 kW/cm^{-2} which can create an intense surface heating. Without efficient dissipation, this can cause donor redistribution, complete ionisation and even lattice damage to the surface silicon layer. Moreover, the rise of temperature due to heating aids phonon assisted recombinations and the trapping of free carriers/excitons by the cluster states. All these hinder the formation of bound excitons and thus, contribute to the suppression of the D^0X(NP) emission.

After experiencing the broadening and suppression of the ^{31}P D^0X emission in the sample having a high implant concentration ($\sim 3\times10^{17}$ cm^{-3}) at high power excitation, we conduct PL measurements at lower excitation powers on both the high (dose - 2×10^{13} ions/cm^2) and moderately (dose - 7×10^{12} ions/cm^2) implanted Fz-SOI samples. We gradually reduce the excitation power for PL measurements in several steps. Finally, the laser diode is set just above the lasing threshold which delivers an excitation power of $\sim$ 200 µW at the sample surface. At an excitation power of $\sim$ 200 µW, the PL emission is stable for both of the samples. This power level is an order of magnitude less than the maximum power available from the laser diode and we observe no significant suppression of the PL emission even after several repetitive measurements. In Figure 3.15, the results of the PL measurements on implanted Fz-SOI samples at $\sim$ 200 µW are plotted and compared with the PL spectrum from the reference sample. When PL spectra from different implant concentrations are compared, as shown in Figure 3.15, another important feature is clearly revealed - the broadening of the D^0X(NP) emission line increases with the implant concentration or dose. As discussed

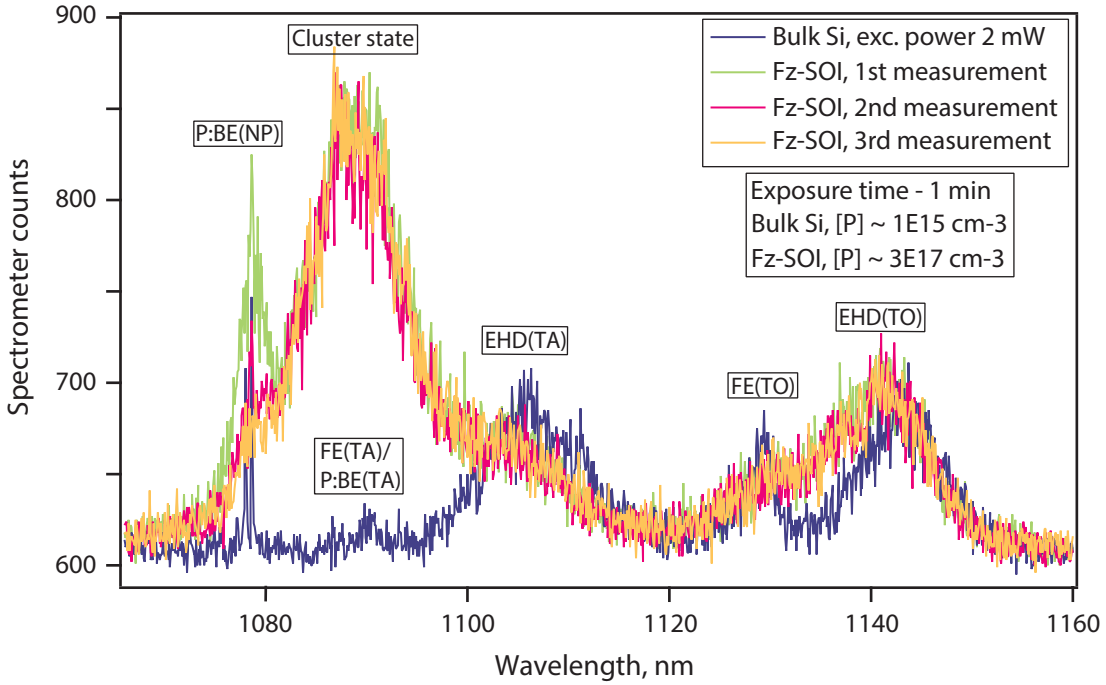

Figure 3.14: PL measurements of the ^{31}P implanted, thick Fz-SOI sample at high excitation power: The effect of high excitation power ($\sim$ 2 mW) on the PL emission from the ^{31}P implanted, thick Fz-SOI sample has been studied.

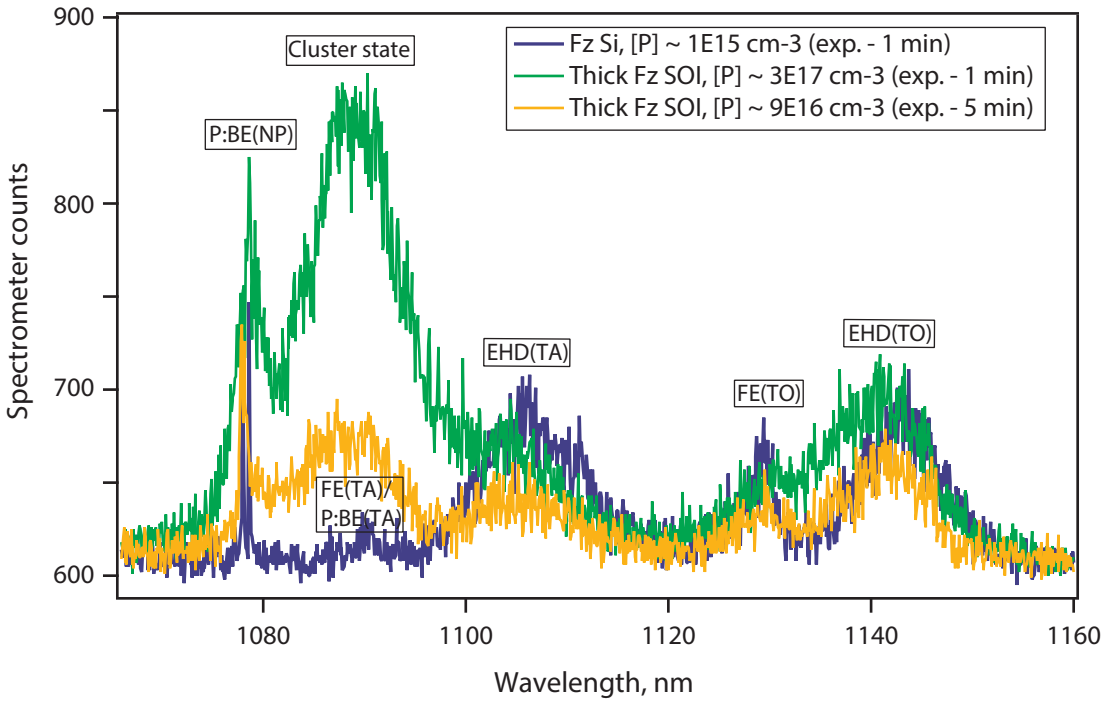

Figure 3.15: PL measurements of thick Fz-SOI sample with different ^{31}P implant concentration at low excitation power: The effect of the ^{31}P implant concentration on the PL emission at low excitation powers ($\sim$ 300 µW) has been studied and compared with the reference Fz-Si sample's case.

Doping technique	^{31}P concentration	^{31}P D^0X(NP) linewidth
Diffusion	$\sim 1 \times 10^{15}$ cm^{-3}	~ 0.1 nm [1]
Ion implantation	$\sim 9 \times 10^{16}$ cm^{-3}	~ 0.2 nm
Ion implantation	$\sim 3 \times 10^{17}$ cm^{-3}	~ 2 nm

Table 3.2: ^{31}P concentration vs. ^{31}P D^0X(NP) emission linewidth

before, the deformation and strain in the crystal structure increase with the impurity concentration in the host lattice. Moreover, the implantation damage is difficult to repair completely. Thus, the remaining defects also contribute to the random structural deformation and strain. All these strains result in an inhomogeneous broadening of the optical emission from the emitters inside the host material. Hence, any increase in impurity concentration, implant dose, energy etc. is reflected in the broadening of the emission line. The D^0X(NP) emission in silicon is so sensitive to any kind of strain that even the mounting of the sample can affect the emission lines. The ^{31}P D^0X(NP) emission linewidths observed in Fz-Si and SOI samples (see Figure 3.15) for different ^{31}P concentrations are presented in Table 3.2.

3.11 Summary of the PL measurements of the ^{31}P D^0X transitions in silicon

The main goal of the PL measurements of this chapter was to demonstrate the proof of concept for no-phonon (NP) emission from ^{31}P D^0X transitions in ion implanted silicon-on-insulator structures. We have started the PL measurements with diffusion doped bulk samples, then continued our investigation through ion implanted bulk silicon samples, diffusion doped SOI samples and finally to ^{31}P implanted SOI samples of both Cz and Fz grown silicon. We have focussed on the PL emission from ^{31}P D^0X transitions, the detection of the emission and the effect of material quality and implant damage on D^0X(NP) emission. In Figure 3.16, PL spectra of 2 μm thick SOI wafers are presented along with the PL spectrum of the reference Fz-Si sample. Estimating the total photon counts for the ^{31}P D^0X(NP) emission from each type of sample, the effect of ion implantation and material quality on emission can seen. It was found that the

[1] Limited by spectrometer resolution.

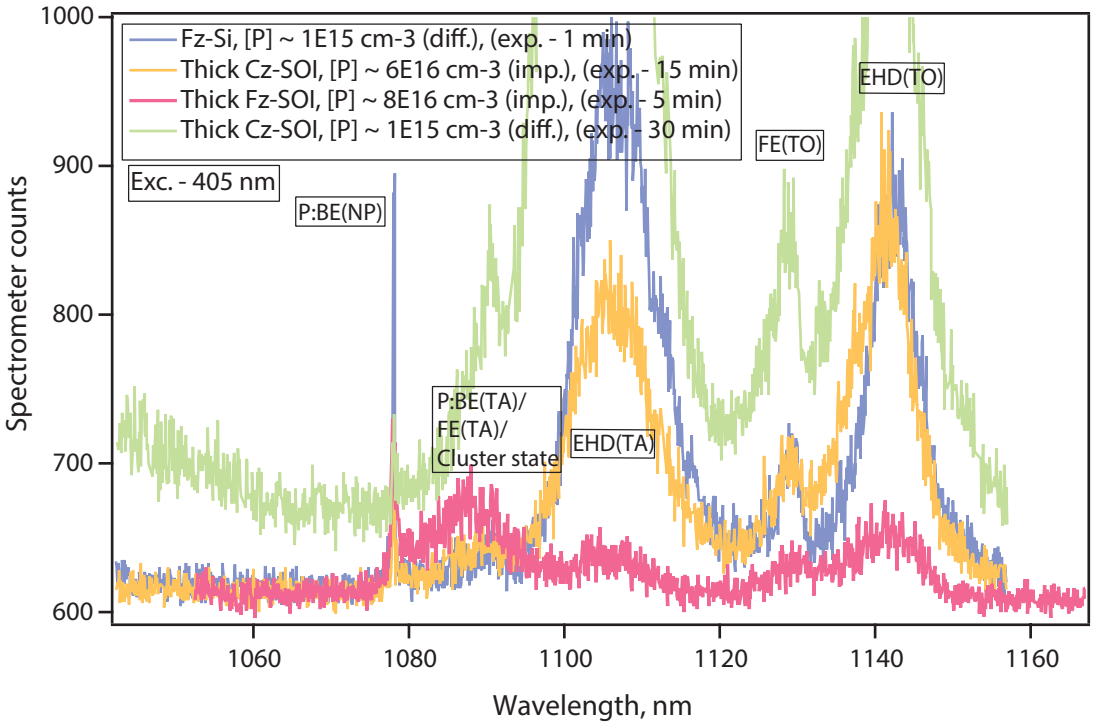

Figure 3.16: Comparison of ^{31}P D^0X(NP) emissions in bulk silicon and SOI samples: PL spectra of thick CZ- & Fz-SOI samples with diffusion and ion implantation doping are compared with the reference Fz-Si sample.

photon count rate of D^0X (NP) emission from diffusion doped Cz-type, bulk silicon and thick Cz-SOI samples match closely (Section 3.4 and 3.9) for the same value of donor concentration, but the photon count rate for doped Cz-Si/SOI samples is $\sim 50\times$ smaller than that of the reference bulk Fz-Si sample (which is 3.25 count per seconds (cps)). This reduction in emission/photon count rate for Cz-type silicon can be attributed to the material quality and growth related defects. In the case of ion implanted samples, we find that the photon count rate for D^0X(NP) emissions are almost two order magnitude smaller/slower than the case of diffusion doped samples which is true for both the thick Cz- and Fz-type, ^{31}P implanted SOI wafers. The severity of damage or defects incorporated by the ion implantation process is observed by this reduction in D^0X(NP) signals. Finally, the PL study in this chapter reveals that, in principle, there is no barrier for observing ^{31}P D^0X transitions in ion implanted SOI samples, however, the starting material quality and efficient repair of ion implantation damages are crucial for obtaining a detectable signal.

3.12 Chapter Summary

The goal of the chapter was to investigate the feasibility of the cavity mediated radiative emission enhancement from ^{31}P donors in silicon through PL measurements. For this purpose, we focussed on three specific issues ? (i) identify the minimum number of ^{31}P donors required in commercially available silicon for detecting ^{31}P D^0X emission with a practical measurement setup which gives us the idea about the magnitude of emission enhancement we would need to probe a single ^{31}P donor, (ii) incorporate ^{31}P donors in a deterministic/controlled way into a silicon substrate suitable for cavity realisation (e.g. thin SOI substrate) and activate the implanted ^{31}P donors into effective emitters, and (iii) investigate ^{31}P D^0X emission from implanted samples and evaluate the radiative emission/linewidth for cavity mediated enhancement.

To find out minimum number of ^{31}P donors for detectable emission signals, we first carried out PL measurements on commercially available silicon substrates (Cz and Fz-type silicon samples). We detected ^{31}P D^0X emissions with minimum measurement times from substrates which had diffusion doped ^{31}P concentration of 10^{15} cm^{-3} i.e., 10^3 μm^{-3}. With same donor concentrations, Fz-Si samples provided stronger intensity and narrower linewidth (0.1 nm with spectrometer resolution limited measurements) ^{31}P D^0X emission compared to Cz-Si samples. Isotopically purified silicon (^{28}Si) is even better for ^{31}P D^0X emission experiments due to small inhomogeneous broadening, ultra-narrow emission linewidth (Section 1.2.2), however, suitable substrates with ^{28}Si for photonic cavity realisation are not commercially available yet. So, we took ^{31}P D^0X emission properties from bulk Fz-Si as the reference in our PL measurements. Photonic crystal cavities, circular Bragg resonators etc. devices have mode volume about unit cubic wavelength ($V_{\text{mode}} = (\lambda/n)^3$). We adjusted the excitation source (405 nm), focal spot in such a way that collection depth ($\sim$ 200 nm) and volume ($\sim 1 - 1.5$ μm^3) imitate the collection conditions of photonic cavities in the bulk silicon samples. Thus, the result of PL measurements on bulk silicon (Fz-type) samples revealed that we need at least $\sim$ 1000 donors in the collection volume to get a detectable ^{31}P D^0X emission signal within a realistic measurement time. This information about minimum number ($\sim$ 1000) of ^{31}P donors for detectable emission also projects that an enhancement of around three orders of magnitude in the total emission efficiency (η_{total}) would be required to optically probe single ^{31}P donor in silicon.

In principle, the ^{31}P D^0X emission linewidth ($\lesssim 0.1nm$) from bulk Fz-Si is suitable for coupling with any photonic cavity with a Q-value around $10,000$ because the linewidth of the emitter would still be narrower than the linewidth of the cavity mode and strong Purcell enhancement can be achieved. However, realising high-Q photonic cavities on bulk substrate is not practical with existing fabrication techniques. Moreover, deterministic positioning of emitters at the cavity field maxima is also very important for ensuring effective emission/Purcell enhancement. Thus, for practical emission enhancement, we require an efficient technique for donor incorporation at desired location and SOI substrates from which freestanding silicon membranes with photonic cavities can be released. We investigated ion implantation process for controlled donor incorporation and positioning. It was found that the implantation process itself is straightforward implement. The challenges came in when we attempted to activate the implanted donors. Thermal curing of implant related damages is complicated in commercial grade silicon and SOI wafers, specially in the presence of unwanted impurities, manufacturing defects in the sample substrates (discussed in Section 3.5). We attempted various implant doses and thermal treatment recipes to find out an optimum dose window and a recipe which will provide sufficient amount of activated ^{31}P donors in the samples. In case of thermal curing, a reasonable result was found when the implanted samples were thermally treated with a 1 hour activation step at 1050°C. Poor activation efficiencies for low implant doses and ^{31}P donor cluster formation for high implant doses ($> 10^{13}$ ions/cm^2) [205] make it difficult to find an effective range of doses which allows sufficient activated donors for detecting D^0X(NP) emissions with our measurement setup. After many trials with different doses, a narrow window of implant doses ($\sim 5\times10^{12}$ - 2×10^{13} ions/cm^2) was identified which can provide detectable D^0X(NP) emissions after activation. We carried out ion implantation on both Cz and Fz-type silicon samples, promising results (in terms of D^0X(NP) emission intensity and linewidth) have been observed with Fz-type silicon samples as was the case with diffusion doping. The optimum D^0X(NP) signal was obtained from a Fz-SOI sample implanted with an implant energy of 100 keV and dose of $\sim 7\times10^{12}$ ions/cm^2. Such an implant profile provides a ^{31}P donor concentration of $\sim 9\times10^{16}$ cm^{-3} throughout the excitation depth (for 405 nm light) after thermal treatment, which in turn allows detection of D^0X(NP) signal strength and linewidth (0.2 nm) comparable to the case

of diffusion doped Fz-Si. However, in the implanted case, the actual amount of donors present in the collection volume almost two order of magnitude higher than the case of diffusion doped samples. This projects that the efficiency of ^{31}P implant activation is still poor ($\lesssim 1\%$) in commercially available Fz-SOI samples. Another critical issue with SOI substrates is that we need thin (~ 200 nm) Fz-Si device layer with reasonably thick ($\sim 2-3$ μm) sacrificial oxide layer for effective photonic cavity fabrication and ^{31}P D^0X(NP) emission experiments. However, such a combination of SOI substrate dimensions and material quality is rare and expensive. So, to demonstrate the proof of principle for ^{31}P D^0X(NP) emission in implanted Fz-SOI samples, a commercially available SOI substrate with a ~ 2 μm thick Fz-Si device layer was used in this work. We have attempted thinning the ~ 2 μm thick Fz-Si device layer of available SOI substrates but it turns out thinning below ~ 1 μm is not efficient for bonded SOI wafers.

Finally, the ^{31}P D^0X(NP) emission from the implanted (dose $\sim 7\times10^{12}$ ions/cm^2) Fz-SOI sample showed an ensemble linewidth of 0.2 nm, which is broader by at least a factor of two compared to the emission linewidth $\lessapprox 0.1nm$ in diffusion doped (^{31}P conc. $\sim 10^{15}$ cm^{-3}) Fz-Si samples. Now, even with the linewidth broadening, the ensemble emission from implanted sample can be coupled to photonic cavities with Q ~ 5000. For similar situations, practical Purcell enhancements of ~ 42 [70] and ~ 70 [253] have been observed in yttrium orthosilicate (YSO) and diamond platforms, respectively. Furthermore, photonic crystal cavities can also enhance light extraction from high index substrates by more than an order of magnitude compared to unpatterned samples [176, 254, 255]. Thus, with carefully designed cavities, three orders of magnitude enhancement in total efficiency (η_{total}) of D^0X(NP) emission from ^{31}P implanted Fz-SOI samples should be attainable with realistic parameters.

Chapter 4

Photonic cavities: design and simulation

4.1 Photonic cavities and their numerical simulation

To obtain the desired light-matter coupling effect, a cavity system has to be designed carefully for the suitable cavity mode. Properties of the cavity mode such as the field distribution, polarisation, optimum mode volume and quality factor (Q-factor) are important since they control the rate of the radiative recombination of an emitter embedded in the cavity (as discussed in Chapter 1 Section 1.3.3). The design of the cavity structure and a detailed analysis of its modes require solving the electromagnetic (EM) wave equations in complex systems which in turn demands powerful computational resources. Though EM waves (embodied in Maxwell's equations) are continuous in nature, they must be discretised in time and space in order to be solved with a computer. This discretisation can be achieved by using the Yee-cell technique on a discrete three-dimensional mesh [256]. There are several numerical solver methods in computational electromagnetics for solving Maxwell's equations and predicting the evolution of an EM field in a dielectric medium. These solver methods, in general, can be categorised into frequency-domain or a time domain approaches [257–259]. The Finite-Difference-Time-Domain (FDTD) method is particularly advantageous for the simulation of complex and largely inhomogeneous structures due to its straightforward and explicit approach. The FDTD method scales linearly with problem size, whereas most of the other numerical solvers scale exponentially. FDTD is also efficient for simulating nonlinear behaviours, broadband and/or transient problems etc., and it has

become one of the most popular numerical methods for simulating and modelling in a broad range of EM applications. We have used the FDTD method to design photonic cavities and analyse their behaviour. In the following section, we briefly provide the principles, important issues of the FDTD simulation technique.

4.1.1 Numerical simulation: The FDTD method

The Finite-Difference-Time-Domain (FDTD) method is a technique that solves electromagnetics problems in the time domain. The Maxwell's equations are first discretised spatially and temporally using central finite differences and then they are numerically solved to predict the evolution of EM field in the media under consideration.

The formulation of the FDTD method starts from Maxwell's curl equations in the time domain, which, in the case of a linear, isotropic and nondispersive medium and for a source free region, can be written as

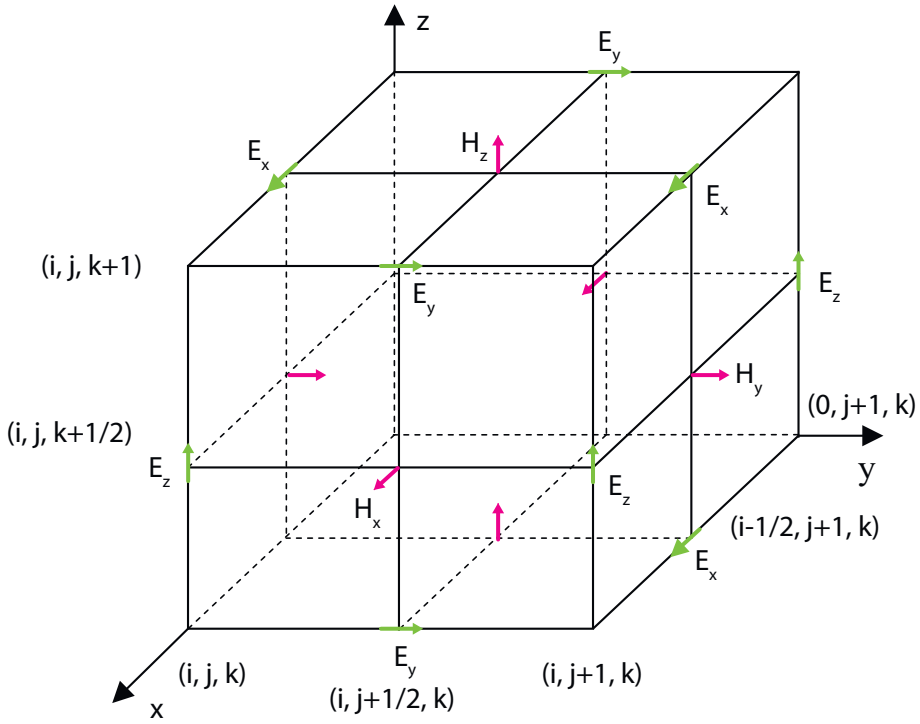

Figure 4.1: Field discretisation on a staggered grid with finite difference approximation: The Maxwell's curl equations are discretised on a staggered grid or the Yee cell geometry using the central finite-difference approximation [256]

$$\begin{aligned}\frac{\partial \mathbf{H}}{\partial t} &= -\frac{1}{\mu}\nabla \times \mathbf{E},\\ \frac{\partial \mathbf{E}}{\partial t} &= \frac{1}{\varepsilon}\nabla \times \mathbf{H},\end{aligned} \tag{4.1}$$

where $\mathbf{H}$, $\mathbf{E}$, μ and ε are respectively the usual symbols of the magnetic field, electric field, magnetic permeability and electric permittivity. These equations can be solved directly by approximating the temporal and spatial derivatives with central differences on a discretised grid (Figure 4.1). The electric and magnetic fields have to be staggered in space and time to obtain valid finite difference equations, implemented with the Yee algorithm [256]. For central difference approximations, we obtain one order of accuracy improvement over forward or backward differences due to a cancellation of truncation error terms. Hence, with central difference approximation, we deal with second order accurate first order derivatives for solving Maxwell's equations. For a simple depiction of the discretisation process, we consider a function $f^n(i,j,k)$ that can designate any component of electric and magnetic fields at a discrete point in the space and time

$$f^n(i,j,k) = f(i\Delta x, j\Delta y, k\Delta z, n\Delta t), \tag{4.2}$$

where the variables i, j, k are integers used for spatial indexing and Δx, Δy, Δz are the lattice space increments in the x, y, z directions, respectively. The variable n is also an integer, which is used for time indexing; and Δt corresponds to the increment in time. The spatial and temporal derivative of the function $f^n(i,j,k)$ can be approximated with the Taylor's series central difference expansion and expressed as

$$\begin{aligned}\frac{\partial f^n(i,j,k)}{\partial x} &= \frac{f^n(i+1/2,j,k) - f^n(i-1/2,j,k)}{\Delta x},\\ \frac{\partial f^n(i,j,k)}{\partial t} &= \frac{f^{n+1/2}(i,j,k) - f^{n-1/2}(i,j,k)}{\Delta t}.\end{aligned} \tag{4.3}$$

Now, all the partial derivatives in Maxwell's equations (4.1) can be discretised using equations (4.3) and solved numerically. The electric and magnetic fields are staggered

in space and evaluated at alternate half time steps to form valid finite difference equations. Now, if we start from calculating the curl of electric field **E** then we can estimate the change the magnetic field **H** at the center of the curl. Thus, we can update the magnetic field for the next time step and calculate the corresponding change in the electric field from the curl of magnetic field. This cycle, known as the leap-frog technique, can be repeated for required amount of time to estimate the future time values of the electric and magnetic fields. The generic update equations from Maxwell's curl equation (4.1) can be written as

$$\begin{aligned} \mathbf{H}\big|^{t+\Delta t/2} &= \mathbf{H}\big|^{t-\Delta t/2} - \frac{\Delta t}{\mu}\left(\nabla \times \mathbf{E}\big|^{t}\right), \\ \mathbf{E}\big|^{t+\Delta t} &= \mathbf{E}\big|^{t} + \frac{\Delta t}{\varepsilon}\left(\nabla \times \mathbf{H}\big|^{t+\Delta/2}\right). \end{aligned} \tag{4.4}$$

4.1.2 Numerical simulation: accuracy and stability of the FDTD method

As any practical EM problem is continuous in nature, the discretisation of the Maxwell's equations for the numerical calculation introduces errors into the spatial and temporal derivatives. Thus, it is important to choose the spatial step sizes (Δx, Δy, Δz), i.e., the cell size and the time step (Δt) carefully in order to ensure the numerical stability and sufficiently accurate results. If the spatial cell and time step are large, the field values might oscillate, making the marching algorithm unstable and causing the calculation to explode. On the other hand, if the spatial and temporal steps are too small then the requirement for computing resources can become unrealistic. The cell size therefore has to be (a) small enough to efficiently resolve the smallest feature in the model where the fields will be simulated, (b) has to be smaller than the shortest wavelength ($\lambda_{\min}$) of the EM wave in the media under consideration and finally (c) large enough to carry out the computation with available resources. For most of the problems, using a spatial step size around $\lambda_{\min}/10$ ($\Delta x = \Delta y = \Delta z = \Delta \approx 0.1\lambda_{\min}$) works reasonably well or at least as a good start. After initial trial, the cell size can be adjusted to improve the results depending on the available computing resources. Once the spatial step sizes are known, the bound for the time step can be obtained from the Courant condition [260]. According to this condition, a field component should not

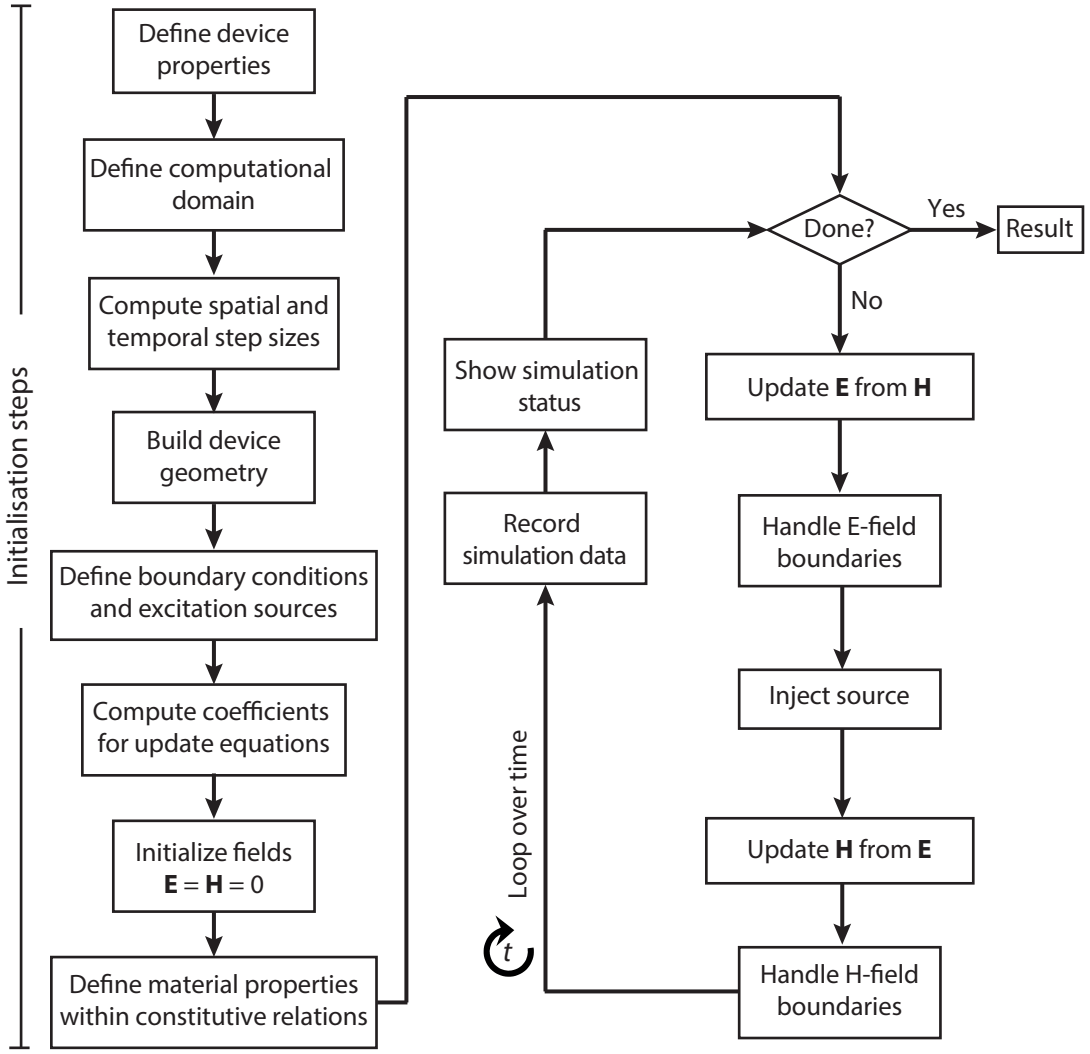

Figure 4.2: The FDTD algorithm, adapted from [257]

propagate more than one cell size in a single time step in order to maintain the stability of the time-stepping algorithm. The Courant stability bound condition for the time step size can be expressed as following

$$\Delta t \leq \Delta t_{\max} = \frac{1}{c\sqrt{\frac{1}{(\Delta x)^2}+\frac{1}{(\Delta y)^2}+\frac{1}{(\Delta z)^2}}} = \frac{\Delta}{c\sqrt{3}}\bigg|_{\substack{\text{cubic}-\text{cell}\\ \text{space lattice}}}, \tag{4.5}$$

where c is the velocity of the EM wave inside the dielectric medium under consideration. This time step condition must be satisfied for all cells within the entire computational domain in the FDTD to obtain an accurate result.

4.1.3 Numerical simulation: the FDTD algorithm

For a complete simulation of an EM problem, several other issues such as the computational domain, excitation sources, boundary conditions, material properties, accuracy and stability etc. have to be taken into consideration and incorporated into the simulation steps in an appropriate sequence. First of all, a computational domain has to be defined for the problem or the photonic device under consideration. This is the physical region where the computation and simulation will be performed. Next, the spatial cell and the time step sizes should be chosen to ensure stability and desired accuracy of simulation. The size of the spatial cell had to be estimated in such a way that even the smallest feature in the device geometry can be resolved efficiently. Boundary conditions are important for avoiding unwanted scatterings from the boundaries of the finite domain. An absorbing boundary condition such as a perfectly matched layer (PML) are commonly used for simulating PhC devices. In the case of PML boundaries, electric and magnetic conductivities are adjusted in such away that the wave impedance remains constant and a complete absorption takes place at the boundary. The type of the excitation source should also be defined properly. The coefficients for the update equations are constant for a particular problem or system. So, it is more efficient to calculate them in advance before entering the main time stepping loop. The initialisation of field components and the incorporation of material properties are also carried out before starting the time loop. Once all these initiation steps are completed, the time stepping loop starts. The time evolution of the electric & magnetic field components are computed in this time stepping loop, which in turn provides the desired result. A block diagram of the FDTD algorithm with most essential steps is presented in Figure 4.2.

4.2 Cavity for enhancing radiative emission: design parameters

Ideally in the weak coupling regime, the cavity mediated enhancement of emission is proportional to the ratio of cavity quality factor to field mode volume. The total oscillator strength, spontaneous emission rate of an emitter and quality factor of the cavity determine the transition threshold between weak and strong coupling regime for a certain cavity, as described in section 1.3.3. To restrict atom-photon interaction to

the weak coupling regime, the coupling constant or coherent interaction rate, g must be less than damping rates, i.e. $g/(\Gamma, \kappa) \ll 1$. The coupling constant, g can be determined from the follwing relation [261, 262],

$$g = \left(\frac{1}{4\pi\varepsilon_r\varepsilon_0} \frac{\pi e^2 f_{\text{osc}}}{m V_{\text{mode}}}\right)^{1/2}, \tag{4.6}$$

where, $f_{\text{osc}} =$ oscillator strength

$V_{\text{mode}} =$ cavity mode volume

$\varepsilon_r =$ relative permmittivity

$m =$ the free electron mass

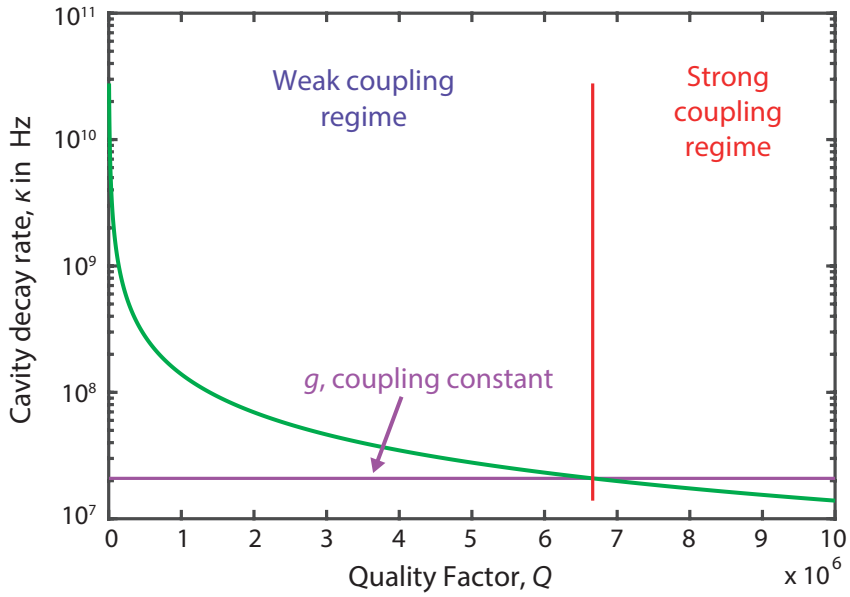

Figure 4.3: Cavity-coupling for ^{31}P $D^0X \rightarrow D^0$ transitions in silicon: Cavity decay rate vs. cavity quality factor plot reveals the coupling strength between the emitter and the cavity. The emitter-cavity system enters in the strong coupling regime when the coherent interaction rate becomes larger than the cavity decay rate

The total oscillator strength of the phosphorus bound exciton transition in silicon is 7.1×10^{-6} and radiative lifetime is ~ 2 ms [71, 72]. The mode volume of all the cavities considered in this work is around a cubic wavelength i.e., $V_{\text{mode}} \sim (\lambda/n)^3$). From these we get the value for the coupling constant, $g \approx 20.8$ MHz. Now the cavity decay rate is determined by cavity quality factor as $\kappa = \omega_c/2Q$ (Q = cavity quality factor). Comparing the cavity decay rate with the coherent interaction rate we can define a

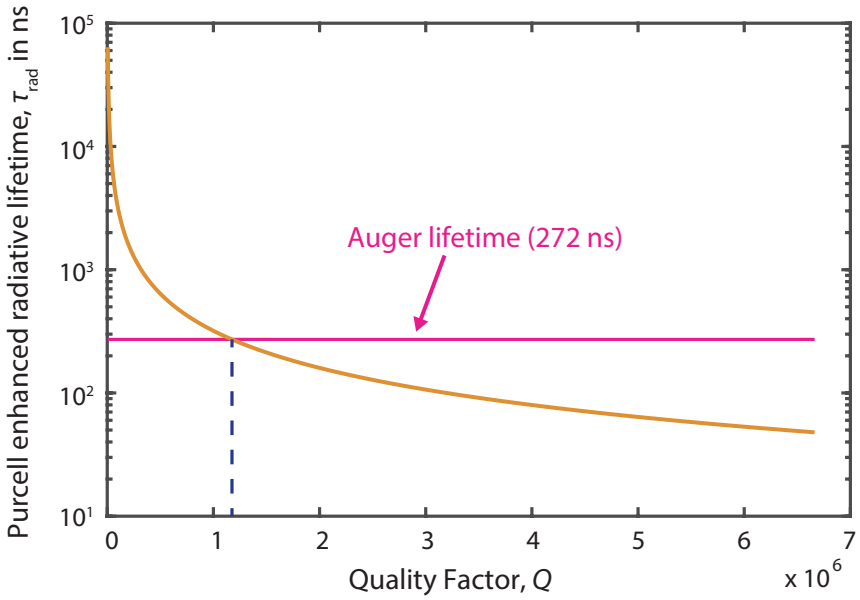

Figure 4.4: Purcell enhanced radiative lifetime in an ideal cavity: The Purcell enhanced radiative lifetime (τ_{rad}) for ^{31}P D^{0}X $\rightarrow$ D^0 transitions is plotted as a function of the cavity quality factor (Q) for a constant mode volume ($V_{mode} \sim (\lambda/n)^3$).

threshold between the strong coupling ($g \gg \max(\kappa,\Gamma)$) and the weak coupling ($g \ll \max(\kappa,\Gamma)$) regimes. For the ^{31}P D^{0}X emitter-cavity system, the coherent interaction rate becomes larger than the cavity decay rate when $Q \gtrsim 10^7$. Thus, the system enters the strong coupling regime only when $Q \gtrsim 10^7$, as illustrated in Figure 4.3. In the weak coupling regime ($Q < 10^7$), enhancement of radiative emission can be achieved when the emission linewidth is narrower than the linewidth of the cavity mode [263]. Now, in highly enriched ^{28}Si, ensemble linewidths as narrow as ~ 0.15 picometres ($\sim$ 150neV) were measured from ^{31}P D^{0}X $\rightarrow$ D^0 transitions and the lifetime limited linewidth for a single donor is ~ 2.4 femtometre (2.4 neV) [59, 73, 88]. For a Q-value of $\sim 5 \times 10^6$, the linewidth of the cavity mode around the ^{31}P D^{0}X $\rightarrow$ D^0 transition is ~ 0.2 picometres, which is still broader than the ensemble linewidth of the ^{31}P D^{0}X emission in highly enriched ^{28}Si. Thus, in principle, we can exploit a cavity in silicon that has Q-factor up to $\sim 10^6$ for enhancing the ^{31}P D^{0}X emission.

In a resonant condition, the cavity mediated spontaneous emission enhancement factor (Purcell factor) becomes $F_p = \frac{3}{4\pi^2} \cdot \frac{Q}{V_{mode}/(\lambda/n)^3}$ (equation (1.4)). The mode volume of the cavities (CBRs, 1D PhC cavity, L3 PhC cavity etc.) under consideration is $\sim (\lambda/n)^3$ and remains almost constant relative to Q-factors [156, 176, 264]. Therefore, the emission enhancement mostly depends on the Q-value (i.e. $F_p \propto Q$). In Figure 4.4,

we have plotted the Purcell enhanced radiative lifetime (τ_{rad}) for ^{31}P $D^0X \rightarrow D^0$ transitions as a function of the cavity quality factor (Q). At $Q \sim 10^6$, the Purcell enhanced radiative lifetime ($\sim$ 300 ns) becomes comparable with non-radiative/Auger lifetime ($\sim$ 272 ns) (see Figure 4.4). Thus, in an ideal cavity with $Q \sim 10^6$ and $V_{mode} \sim (\lambda/n)^3$, under perfect spectral and spatial matching between an emitter and the cavity mode, the radiative decay can compete with the Auger process. However, to detect emission from single ^{31}P donor level in silicon, we do not need the radiative emission to compete with the Auger process and a cavity with Q as high as $\sim 10^6$. From the PL measurements in Chapter 3, we have found that a total emission (collected photoluminescence) enhancement by around three orders of magnitude is required for optically detecting a single ^{31}P donor in silicon. Thus, a Purcell enhancement (F_P) of $\sim$ 1000 would be sufficient for detecting single ^{31}P donor, which in principle can be obtained from a cavity with $Q \sim 10^4$ and $V_{mode} \sim (\lambda/n)^3$. Now, the total emission (collected photoluminescence) enhancement depends not only on the emission rate of photons into the cavity mode, but also on the outcoupling (extraction and collection) efficiency of light from the cavity. Carefully designed photonic cavities can also improve light outcoupling significantly [176, 254, 255], which is otherwise difficult for emitters inside high refractive index substrates. The improvement in the outcoupling efficiency further relaxes the requirement of a high Purcell enhancement. For example, if a cavity design can improve the outcoupling efficiency by an order of magnitude, then we would require a Purcell enhancement of $\sim$ 100 to achieve the aimed three order magnitude enhancement in the total emission/collected photoluminescence.

In the above, we have discussed design parameters for ^{31}P D^0X emission enhancement considering an ideal cavity-emitter coupling. Experimentally, the Purcell enhancement can be determined by measuring the change in the lifetime of an emitter or ensemble coupled to the cavity. Lifetime measurements are carried out using time-resolved photoluminescence (PL) technique. In this technique, the emitter is excited using a pulsed laser and the PL decay curve (temporal profile of the PL emission) is recorded. This temporal profile of the PL emission is then fitted by a single exponential function to extract the decay lifetime (τ). When the resonant lifetime ($\tau_{resonant}$) and off-resonant lifetime ($\tau_{off-resonant}$) of the emitter inside the cavity are known, we can extract the Purcell enhancement using the relation $F_P = \left(\frac{1}{\tau_{resonant}} - \frac{1}{\tau_{off-resonant}}\right)\tau_R + 1$,

where, τ_R is the radiative lifetime of the emitter in bulk substrate [253, 265]. Now, in practical cavity-emitter systems, specially in the optical domain, the observed emission enhancement is much less than the expected values from ideally coupled systems. For example, in photonic crystal cavity systems, experimental Purcell enhancements (F_P) of ~ 42, ~ 43 and ~ 70 have been observed in rare-earth-ion-doped crystal (Nd^{3+} ion in yttrium orthosilicate (YSO)) [70], InGaAs quantum dot [266] and diamond NV centre [253] platforms, respectively. These experimental F_Ps attained in PhC cavity-emitter systems are only a fraction of their ideal values [70, 253, 266]. The discrepancy between ideal and measured F_P values is mostly attributed to the spatial displacement of emitters from field maxima and/or the misalignment between the emitter dipole moment and the local cavity polarisation [70, 191, 253, 266, 267]. Insufficient detector time resolution and slow carrier relaxation can also mask the actual Purcell enhancement in the cavity-emitter system [266]. Another important fact with all the previous examples of measured F_P is that emitters were coupled to only moderate Q ($\lesssim 5000$) cavities. In a system with a sufficiently narrow linewidth emitter/ensemble and high Q cavities, high Purcell enhancement should be achieved even with non-ideal coupling conditions. For example, an $F_P \sim 144$ has been observed from a cavity-emitter system where copper radiative centres in silicon coupled with a Si PhC cavity with a Q-value of 1.6×10^4 [191]. Very recently, Dibos *et al.* have coupled Er^{3+} ions in YSO crystal to high Q (7.3×10^4) silicon PhC cavities and demonstrated a Purcell enhancement of ~ 658 [267], which is so far the highest F_P value observed in the optical domain. Interestingly, Er^{3+} ions in YSO crystal have quite similar emission properties compared to ^{31}P D^0X emitters in silicon. The oscillator strength (f_{osc}), radiative lifetime (τ_{rad}) and ensemble linewidth ($\Delta\lambda_{ens}$) of Er^{3+} emitters in YSO are $\sim 1.095 \times 10^{-7}$, ~ 11 ms and ~ 4 pm, respectively [268]. In Fz-Si, those values are $f_{osc} \sim 7.1 \times 10^{-6}$, $\tau_{rad} \sim 2$ ms and $\Delta\lambda_{ens} \sim 5$ pm [71, 72, 269]. Therefore, silicon photonic cavities which can provide $Q \gtrsim 10^4$ and $\gtrsim 20\times$ improvement in outcoupling efficiency around ^{31}P D^0X emission wavelengths should afford the desired three orders of magnitude enhancement in the total emission, even in the case of non-ideal cavity-emitter coupling.

4.3 Circular Bragg resonators (CBRs)

In Chapter 2, we took a first look at the principles and properties of circular Bragg resonators (CBRs). CBR devices can provide a moderate light confinement and very good extraction efficiency in the high refractive index materials. The light confinement and extraction, resonant wavelengths, mode volume, far-field emission, quality factor etc. depend on the geometric properties of the CBR device. So, the parameters such as the size of the cavity, grating period, membrane thickness, trench depth and width have to be taken into account and carefully optimised within realistic values and available resources. We use FDTD simulations to design an optimum CBR structure for enhancing emission and/or extraction of photons from ^{31}P $D^0X \rightarrow D^0$ transitions. The optical properties of photonic cavities can be predicted accurately with the FDTD method, however, the simulation process requires significant computing resources and time. Therefore, we first review the literature and find a suitable CBR design for our work [176–178], then optimise the structure/geometry according to our specific requirements, material system and available sample substrates.

4.3.1 CBR in suspended silicon membrane

Circular Bragg resonators (CBRs) implemented in a suspended membrane provide the most suitable design for the efficient extraction of photons. Using suspended CBR

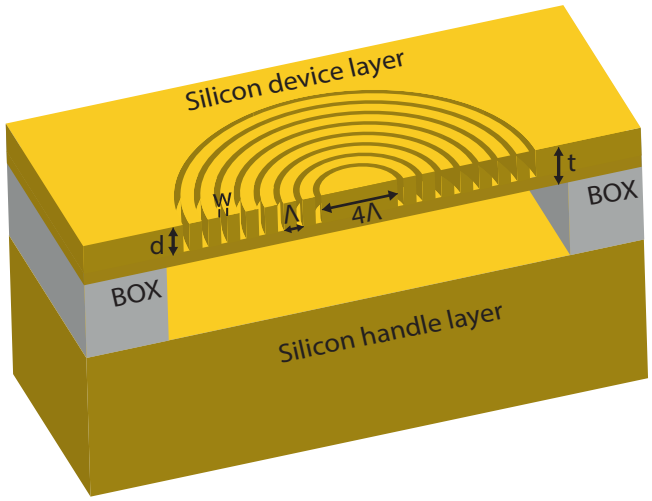

Figure 4.5: Schematic of a suspended circular Bragg resonator (CBR) structure: The CBR design has been incorporated in the thin top layer of a silicon on insulator (SOI) wafer. Afterwards, the supporting insulator i.e., the buried oxide (BOX) layer have been removed to obtain a suspended membrane. The schematic shows the cross-section of such a suspended CBR structure

structures, K. Srinivasan *et al.* demonstrated very efficient ($\sim 50\%$ with a NA of 0.4) extraction of single photons from epitaxially grown InGaAs quantum dots. Along with a near Gaussian far-field, the suspended CBR has been predicted to provide Purcell enhancement of $\sim 10-12$ [176–178]. We have adopted the design from K. Srinivasan *et al.* and then further optimised it for ^{31}P D^0X emissions in silicon. The design consists of a disc resonator surrounded by a circular grating. The radial period or lattice constant of the circular grating is Λ and the radius of the central disc is 2Λ. The circular trenches comprising the circular grating are partially etched in a thin membrane of host material. The trench depth d and width w are the critical parameters for adjusting the extraction/outcoupling efficiency and quality factors of the resonant modes. After patterning the design to the top silicon membrane, the supporting BOX layer below the thin silicon membrane is released to create a suspended CBR structure. A schematic of the cross-section of such an suspended CBR device is shown in Figure 4.5. The bullseye-like geometry provides a second-order Bragg grating structure [176, 181] which in turn favours the vertical outcoupling of photons emitted inside the central disc.

We aim to realise the CBR structure in the top silicon layer of a commercially available silicon-on-insulator (SOI) wafer. The thickness of the top silicon layer (t_{SOI}) and the supporting/sacrificial oxide layer (t_{ox}) are 220 nm and 2 µm respectively. The oxide layer can be later removed to obtain free-standing/suspended silicon membrane. Thus, we simulate the properties of CBR structures in a thin silicon slab (thickness = 220 nm) using the FDTD method. A series of simulations have been carried out to optimise the CBR design parameters for maximising the vertical outcoupling of emitted photons from ^{31}P $D^0X \rightarrow D^0$ transitions in silicon. The silicon slab supports both transverse electric (TE) and transverse magnetic (TM) polarised modes in it. We adjust the grating period Λ to satisfy the second-order Bragg condition for TE modes. The TE modes in the CBR are excited using a horizontally oriented electric dipole at the centre of the circular disc. The electric dipole resembles an ideally positioned broadband emitter inside the CBR. An ideal CBR consists of a large number of circular trenches to form the grating, however, a very large grating is not realistic for both simulation and implementation. We run simulations varying the number of trenches in the CBR design and find that a minimum of eleven partially etched trenches provide a reasonably efficient grating effect. Therefore, a number of eleven concentric circular trenches has

been chosen initially to implement the grating in the CBR design.

Any emitter located inside the silicon membrane radiates dominantly into the slab guided mode. The refractive index contrast attributed by the trenches gives rise to strong reflections and vertical scattering at silicon-air interfaces. These reflections and/or scatterings at silicon-air interfaces, in turn, provide the cavity mode and emission outcoupling. Next, we adjust the width and depth of the trenches to optimise the vertical extraction and cavity quality factors. The depth of the trench is particularly important as the amount spatial overlap between a trench and an incident slab-bound wave controls both the radiation outcoupling and mode reflections [177]. So, we set the width of the trench as one third of the grating period ($w = \Lambda/3$) and vary the trench depth within a range of $t_{\mathrm{SOI}}/2 < d < t_{\mathrm{SOI}}$. The requirements for efficient outcoupling and improved quality factor are self-contradictory. For example, deeper trenches provide better Q values but with a reduced upward radiation. Our simulations with varying depths reveal that a good trade off can be achieved around a trench depth of $d = 0.7t_{\mathrm{SOI}}$. This outcome agrees with the results in the work of K. Srinivasan *et al.* [176–178]. Furthermore, the wavelengths of resonant modes of the CBR structures depend on the radius of the disc resonator and grating geometry. We have defined the disc radius as 2Λ and found suitable values for width and depth for circular tenches. So, the grating period is the remains knob we need to tune to obtain resonances at desired wavelengths. Thus, we adjust the fundamental resonance of CBR devices around D^0X transition wavelengths by varying the grating period.

Figure 4.6a shows the simulation window for a CBR device in the Lumerical FDTD package [270] — the commercial FDTD simulation software we have used in this work. The yellow boundaries in the simulation window denotes the Perfectly Matched Layer (PML) boundary conditions. PML boundaries absorb incident radiation and suppress any unwanted scatterings from the boundaries of the finite simulation region. We try to minimise the simulation region as much as possible to reduce the computing time and resources. For lateral dimensions, we allow an area to cover all the circular tranches. A reasonable distance between the cavity and the PML boundaries has also been allowed in the vertical dimension to prevent the boundaries from absorbing the non-propagating, local evanescent fields existing within the cavity. In the case of meshing, we make the mesh size such a way so that there is an integer

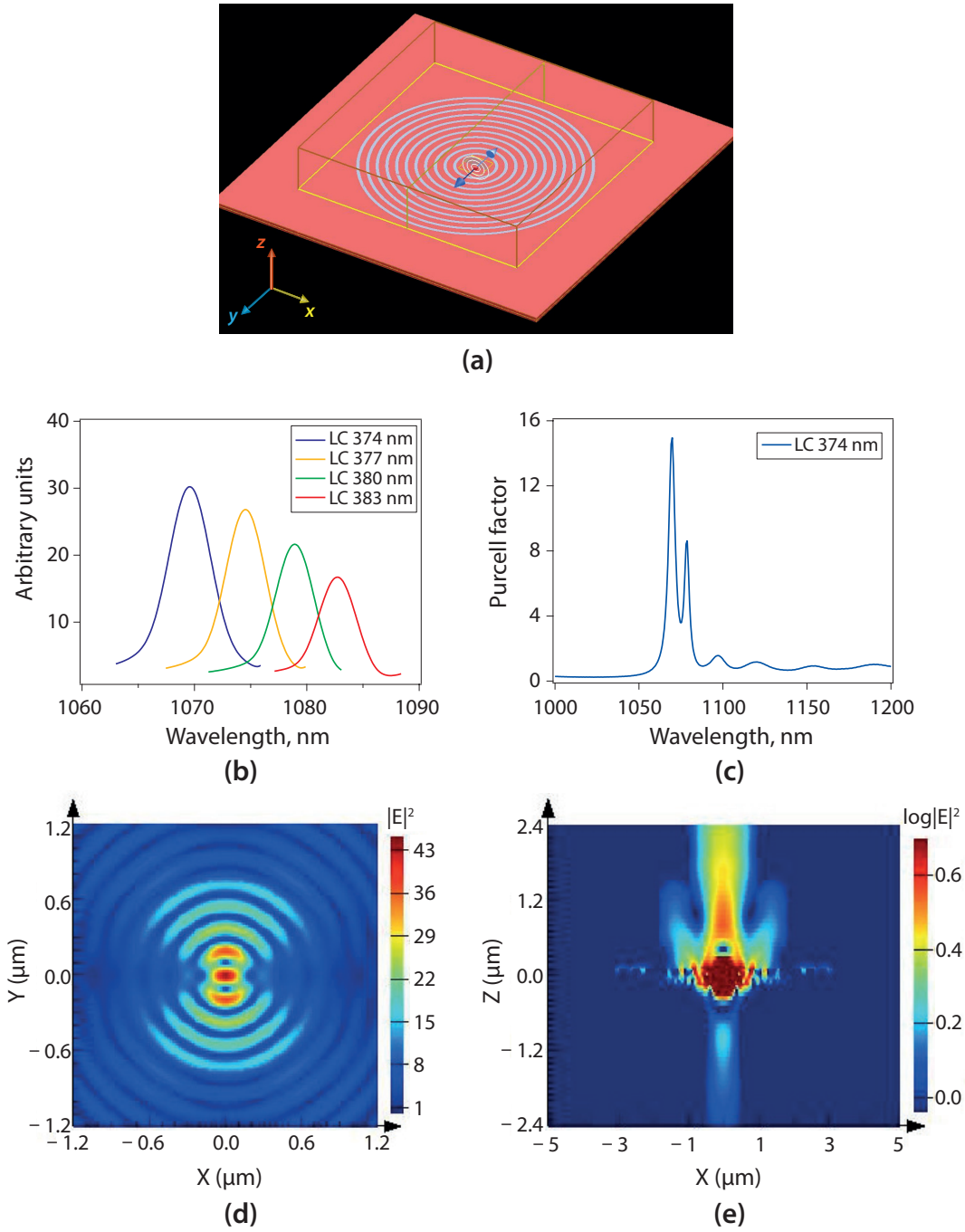

Figure 4.6: FDTD simulation of optical properties of suspended CBRs: Figure shows (a) the simulation window, (b) fundamental resonances with respective lattice constants/grating periods around the ^{31}P $D^0X \rightarrow D^0$ transition and (c) simulated Purcell enhancement of an example CBR with LC = 374 nm. Electric field intensity of the fundamental resonance in the (d) xy & (e) xz (log scale) planes has also been extracted from the FDTD simulation which reveals the field distribution and strength of the cavity mode

number of mesh cells per grating period. This is because a mesh size periodic with the structure provides the most efficient simulation result in the case of any periodic struc-

ture for the given mesh size. Setting a small mesh size increases the accuracy of the result, however, it also increases the computation time. Due to our limited computing resources, we have started with a coarse mesh and then gradually optimised to a finer mesh in order to ensure both accuracy and realistic computation time. The optimum value of the mesh size has been found as $\Lambda/20$ in the lateral dimension and the default non-uniform meshing scheme has been been chosen to set the appropriate mesh in the z-dimension. Finally, we set several monitors to record the optical properties, field evolution etc. The frequency domain monitors calculate the mode profiles from the time evolution by taking the discrete Fourier Transform of the time domain data. We vary lattice constants/grating periods to find desired resonance around ^{31}P D^{0}X emission. Fundamental resonances with respective grating periods around ^{31}P D^{0}X $\rightarrow$ D^0 transition are plotted in Figure 4.6b. Figure 4.6c shows the ideal Purcell enhancement that can be obtained for our CBR structures. The Purcell factor/enhancement in the simulation is calculated from the ratio of the power emitted by a dipole source in the cavity environment to the power emitted by the dipole in a homogeneous silicon substrate. The simulated Q value for the CBR structure and the extracted mode volume are around $220-250$ and $1.29(\lambda_{\text{res}}/n)^3$, respectively. The Purcell factor estimated from Q/V_{mode} is around $13-15$ which agrees very well with the value obtained from the other (power ratio) method in the simulation. The electric field intensity of the fundamental resonance in the xy & xz (log scale) planes have also been extracted from the FDTD simulation and shown in Figure 4.6d & e, respectively. These figures display the field distribution and strength of the cavity mode where the field distribution in the xz-plane reveals the directional emission properties of the CBR devices.

The extraction/outcoupling efficiency of any photonic device depends on the far-field radiation pattern induced by the structure under consideration. In the FDTD simulation, the far-field pattern is projected from the near-field data. This far-field projection is carried out by a decomposition of the near field data, using a set of plane waves propagating at different angles as the basis for the decomposition. Thus, EM fields can be calculated efficiently for any intermediate and/or far-field regions with this technique. We set the field monitor at a plane just above (below) the top (bottom) membrane surface. These monitors record the near-field data during simulation, which is post-processed afterwards to project the far-field pattern. Figure 4.7a & b shows far-field

intensity distribution of the CBR device in the upward ($z+$) and downward ($z-$) directions, respectively. From the projected patterns, it can be observed that the far-field intensity in the upward direction is stronger by an order of magnitude than that in the downward direction. A grating where the trenches are completely etched through the substrate membrane outcouples same amount of light in both upward and downward directions, so, even in the ideal case, only half of the extracted light can be collected for such a design. On the other hand, the asymmetric or partially etched trench design for the gratings allows to increase the upward extraction ratio, which significantly improves the total outcoupling efficiency. Figure 4.7c shows outcoupling efficiencies as a function of the numerical aperture (NA) in the case of both upward and total emitted

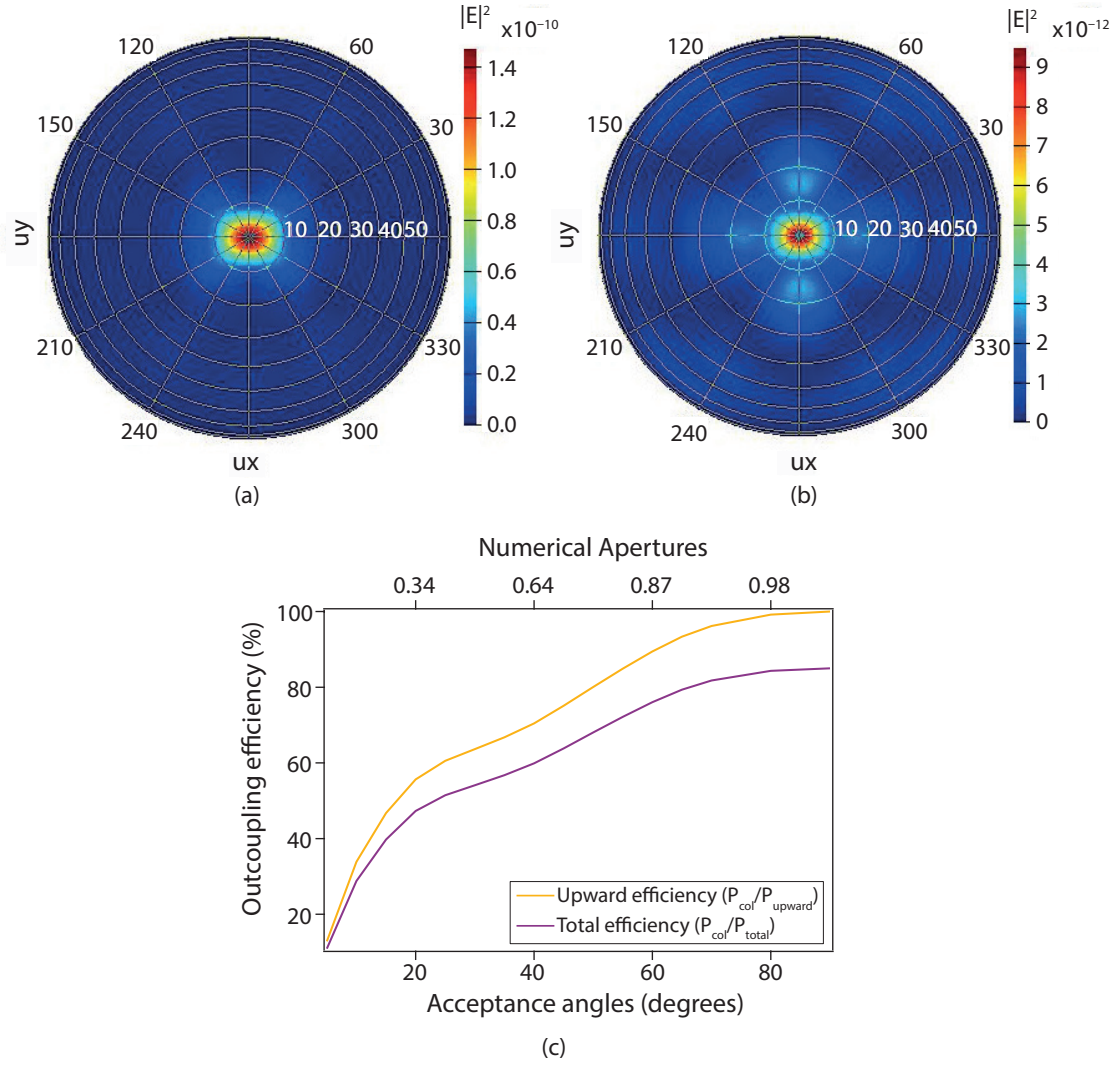

Figure 4.7: Far-field properties and collection efficiency of suspended CBR: Far-field pattern/intensity in the (a) upward ($z+$) and (b) downward ($z-$) directions. (c) Collection efficiencies compared to the upward and total radiation.

power. The upward (total) outcoupling efficiency (the orange (purple) curve in Figure 4.7c) provides the fraction of the upward (total) emission collected by the objective with certain NA. A comparison between the upward and total outcoupling efficiencies shows that most of the emitted power is outcoupled in the upward direction for the optimised CBR structure. With a moderate NA of 0.65, the achievable total collection is $\sim 60\%$ and this value can increase up to $\sim 80\%$ for high NA (≈ 1) objectives. Thus, the due to the combined effect of the improved extraction and Purcell enhancement , the CBR devices are ideally capable of increasing the total collection from the D^0X emissions by two orders of magnitude. This can allow us to probe signals from few tens of ^{31}P donors.

4.3.2 CBR in silicon membrane on oxide layer

Realising the CBR structure on a suspended silicon membrane demands two steps of lithographic patterning. This is due to the partially etched trench design. As the trenches are not completely through the membrane, they cannot be used as the opening for the wet etch removal of the sacrificial/supporting layer to create the suspended structure. So, we need to add deliberate openings in the design with a separate lithographic patterning and etching steps to facilitate the removal of sacrificial layer. Thus, the efficient realisation of the suspended CBR structure is quite demanding and time consuming. To avoid the multi-step fabrication process at the very first attempt and reduce the chance of failure, we start with a step by step realisation and process optimisation. With this strategy, we attempt the non-suspended CBR structures which can be realised in single patterning step. In this section, the optical properties of the non-suspended CBR structure on a SOI substrate is evaluated through the FDTD simulations. Figure 4.8a shows the simulation window for a non-suspended silicon CBR structure in which the thin (220 nm) silicon membrane is settled on/supported by a thick (2 μm) silicon oxide layer. Apart from the addition of a supporting oxide layer, the simulation configuration and methodology are exactly the same as in the case of the suspended CBR simulation. In Figure 4.8b, an example of the simulated resonance near $^{31}P\ D^0X \rightarrow D^0$ transition for a non-suspended CBR ($LC = 374$) is shown and compared with the suspended CBR case. The comparison reveals that a red shift of ~ 6 nm in occurs in the case of non-suspended CBR resonances. This shift in resonance is caused

by the change in the effective refractive index of the overall CBR structure due to the presence of the supporting oxide layer. Figures 4.8c & d show the simulated Purcell en-

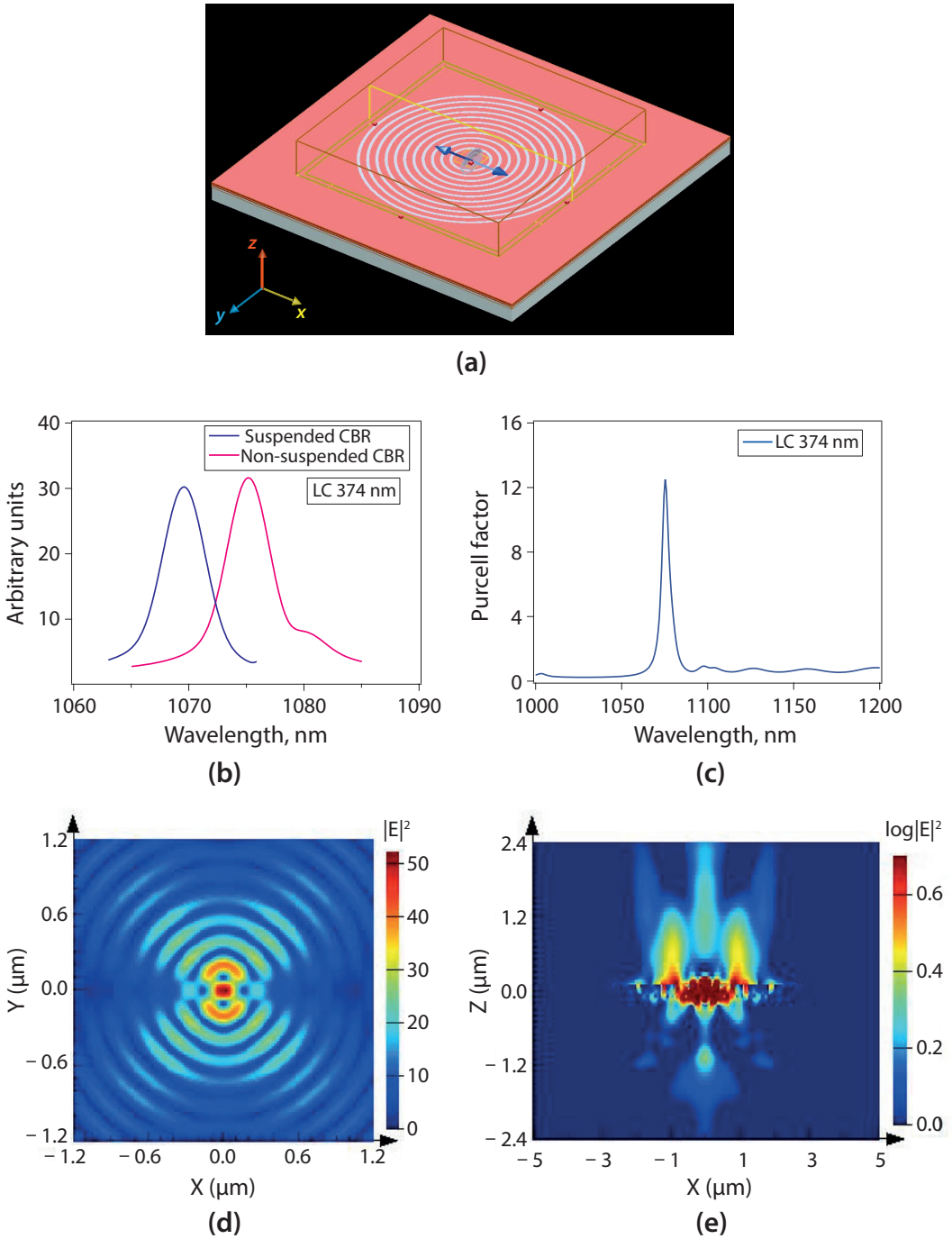

Figure 4.8: FDTD simulation of optical properties of a non-suspended CBR: (a) The simulation window shows the silicon membrane with CBR structure settled on/supported by the oxide layer. An example of simulated (b) fundamental resonance for non-suspended CBR (compared with the resonance for a suspended CBR) and (c) Purcell enhancement from a non-suspended CBR of the ^{31}P $D^0X \rightarrow D^0$ transition with a grating period of 374 nm. Electric field intensity of the fundamental resonance in the (d) xy & (e) xz (log scale) planes has also been extracted from the FDTD simulation which reveals the field distribution and strength of the cavity mode.

hancement and electric field distribution of the fundamental resonance in the xy plane, respectively. These properties of the non-suspended CBR appear similar to the case of the suspended CBR. However, a noticeable difference is seen in the vertical plane field distribution of non-suspended CBR, as shown in Figure 4.8e. The vertical field distribution reveals that much of the directional emission property of the CBR design has been diminished in the case of non-suspended structure. Again, the presence of the supporting oxide layer is responsible for this. The refractive index of the silicon oxide ($n_{ox} \approx 1.45$) is higher than that of the air ($n_{air} = 1$). So, the confinement of light by index guiding is different at the silicon-silicon oxide interface compared to the silicon-air interface which changes the overall vertical field distribution of the non-suspended

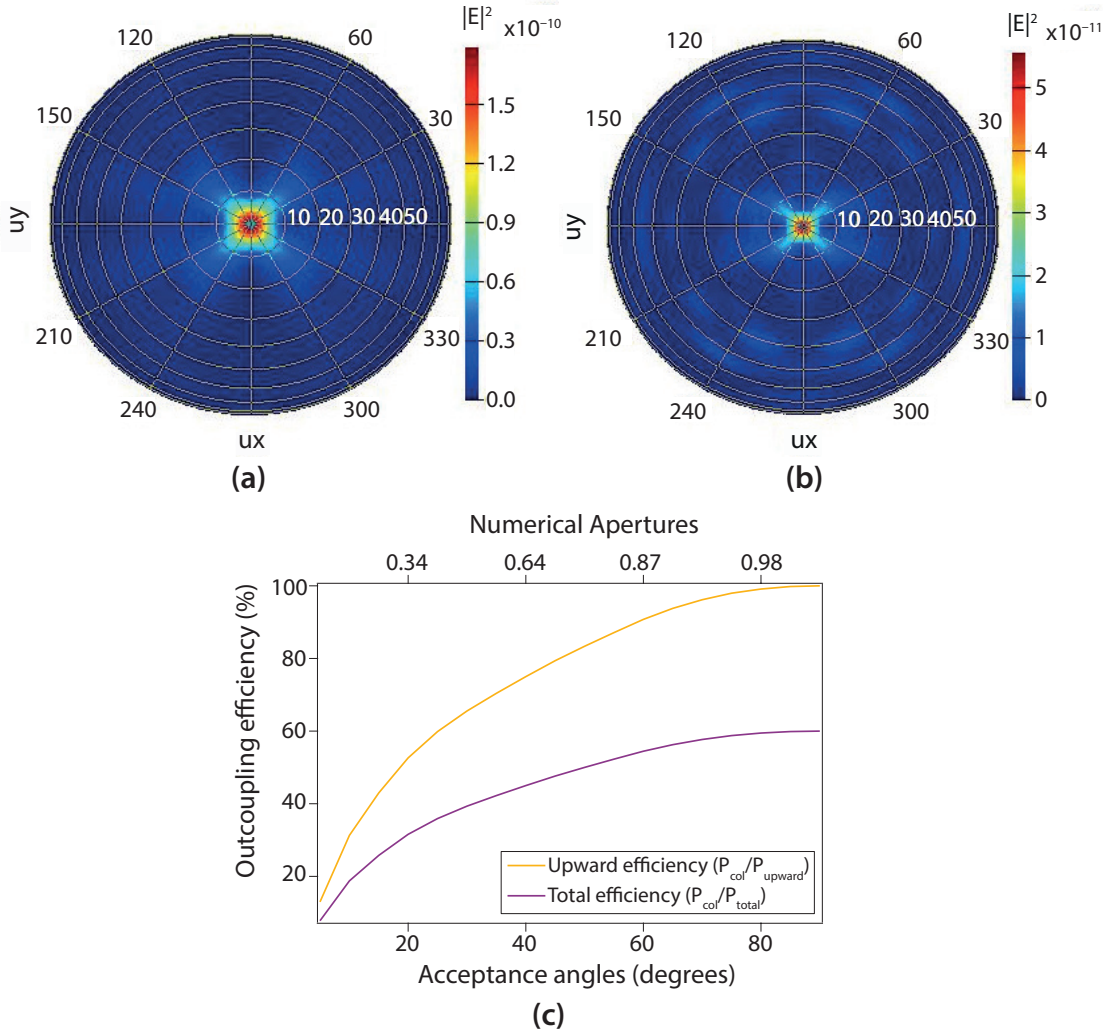

Figure 4.9: Far-field properties and collection efficiency of a non-suspended CBR: Far-field pattern/intensity in the (a) upward ($z+$) and (b) downward ($z-$) directions. (c) Outcoupling efficiencies compared to the upward and total radiation.

CBR structure. This also indicates an alteration in the outcoupling efficiency of the non-suspended CBR.

Figures 4.9a & b show the far-field intensity distribution of the non-suspended CBR device in the upward (z+) and downward (z-) directions, respectively. From the projected patterns, it can be observed that the far-field intensities for the upward (z+) and downward (z-) directions have become almost comparable due to the presence of the supporting oxide layer. The maximum upward far-field intensity is larger than the downward case by only a factor of two. So, the CBR device has lost most of its preference for the upward extraction compared to the suspended structure. However, the outcoupling efficiency of the non-suspended CBR structure is still superior to the photon extraction from the bulk silicon. Figure 4.9c shows outcoupling efficiencies of the non-suspended CBR as a function of the numerical aperture (NA) in the case of both upward and total emitted power. The upward outcoupling efficiency (the orange curve in Figure 4.9c) for the non-suspended CBR is quite similar to the case of suspended CBR. But the total outcoupling efficiency (the purple curve in Figure 4.9c) is significantly reduced and reflects the fact that the upward & downward emissions have become comparable. With a moderate NA of 0.65, the achievable total collection is $\sim 40\%$ for the non-suspended CBR structure which is still an order of magnitude higher than for the bulk silicon.

4.4 1D photonic crystal cavity

1D PhC cavities can provide smallest cavity geometry in dielectric media [156, 271] and support high Q/V_{mode} values for both TE and TM polarisation, even in low index materials [272]. These 1D structures also allow easy access to cavity near-fields which is useful for various applications such as sensing, optical trapping and optomechanics. Hence, 1D PhC cavities are a promising candidate for practical light-matter interaction applications. The basic concept of 1D PhC cavity can be implemented with a waveguide segment surrounded by two lattices of air-holes where each lattice act as a Bragg mirror. Thus, Bragg scattering provides the light confinement in the direction of periodic index variation and total internal reflection (TIR) is used to confine light in other two directions. However, only a low Q-value (of few hundreds) can be achieved with such a basic 1D PhC cavity design [273]. This inefficient light confinement arises from

light scattering at the interface between the Bragg mirror and the central cavity region. According to the design, photonic crystal mirrors reflect and trap the waveguide mode light in the cavity. But the cavity mode penetrates some distance into the mirror regions. If the fields of the cavity mode terminates abruptly at the mirror boundary as in the case of a simple 1D PhC cavity design, strong scattering loss occurs in the system and leads to low Q cavities. Now, this situation can be tackled and high Q-values for 1D cavities can be achieved by tapering the propagating mode of the cavity region into the exponentially decaying mode of the Bragg mirror. Such mode matching can be obtained by incorporating a multi-hole taper towards the cavity [156, 271, 274], as shown in Figure 4.10a. A near adiabatic conversion between the propagating cavity and the decaying Bragg modes can be obtained by increasing the number of holes in the ta-

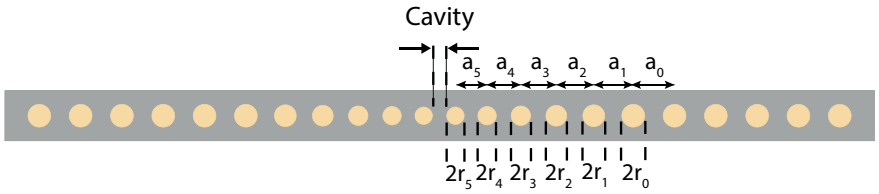

a_0 (nm)	a_1 (nm)	a_2 (nm)	a_3 (nm)	a_4 (nm)	a_5 (nm)	t (nm)	w (nm)	r (nm)	cavity (nm)
262	250	237	225	213	201	220	320	0.28a	91

(a)

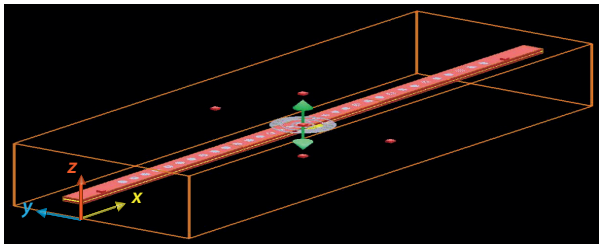

(b)

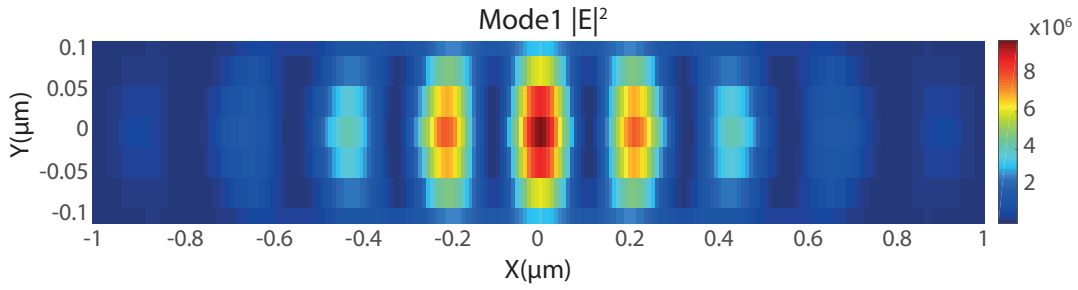

(c)

Figure 4.10: 1D Photonic crystal (PhC) cavity, (a) 1D silicon PhC cavity and design parameters, (b) simulation window, (c) E-field distribution for fundamental mode

per. With multi-hole tapers, the waveguide mode index slowly reduces and matches the Bragg index which strongly suppress the scattering and provides exponential increase in the cavity Q. The cavity length is also a very important parameter for obtaining high Q-values as the scattering loss strongly depends on this length. Therefore, to obtain a high-Q 1D PhC cavity, three design elements have to be carefully optimised — the photonic crystal mirror, the taper and the cavity length [156, 271]. In our design, we choose a PhC mirror with lattice constant or hole spacing $a_0 = 262$ nm and radius $r_0 = 0.28a_0$ which can provide a photonic bandgap around the wavelength of our interest ($\sim$ 1078 nm). To suppress the scattering loss from the incident lowest-order waveguide mode, we incorporate a five-hole taper section, in which the PhC mirror hole spacing $a_0 = 262$ nm is linearly tapered over a five hole section to $a_5 = 201$ nm. Once the taper section designed, the optimum Q-value has been estimated by adjusting the cavity length. A constant r/a ratio is maintained in the design, so, the hole radius in the tapered region is changed proportionally, Figure 4.10a shows a 1D cavity with the design parameters.

Table 4.1: Summary table for 1D PhC cavity

	Q-factor	Mode volume
Theoretical [156]	$\sim 10^7$	$\sim 0.39(\lambda/n)^3$
Experimental @ 1560 nm [156]	$\sim 7.7 \times 10^5$	$\sim 0.4(\lambda/n)^3$
Simulation @ 1078 nm	$\sim 6 \times 10^6$	$\sim 0.4(\lambda/n)^3$

An FDTD algorithm can simulate high-Q resonant structures with reasonable accuracy but it requires fine meshing and long simulation time to properly simulate the evolution of a cavity field because fields decay slowly in such structures. The FDTD method Maxwell solver (Lumerical FDTD Solutions [270]) used for this work, supports non-uniform meshing. Non-uniform meshing has been employed in the direction where the periodic variation in electromagnetic media and cavity exists. A mesh size of $\sim$ 6.5 nm was used for the tapered region and $\sim$ 26 nm for rest of the structure. With this simulation set-up and available computing resources, we could simulate designed cavities and extract Q values. Figure 4.10b & c show the simulation window in the FDTD solver and the electric field distribution of the fundamental cavity mode, respectively. Simulation results reasonably match with Q values for similar structures found

in literature [156, 271, 274], a brief comparative summary is provided in Table 4.1.

4.5 2D photonic crystal cavity

Theoretically, 1D PhC cavities can provide Q values as high as $\sim 10^7$ with small mode volume ($\sim 0.1 - 0.5(\lambda/n)^3$) [156, 275], but efficient realisation of these structures is difficult and their optical properties are sensitive to fabrication imperfections. Measured Qs for 1D PhC cavities are typically found to be around an order of magnitude lower than the designed value, as exemplified in Table 4.1. Furthermore, tailoring far-field radiation patterns for efficient collection without losing cavity quality factor is also difficult in 1D PhC cavities. These issues can be addressed using 2D/planar PhC cavities. In the case of 2D PhC cavities, PhC mirrors are incorporated in two directions for trapping light and confinement in the third dimension is obtained from total internal reflection. For 2D PhC cavities, similar to any PhC cavity, periodic variations and a cavity structure can be introduces in numerous ways. Among various planar cavity candidates, two types — heterostructure cavities [157] and L3 type cavities [149] — are capable of providing experimental Q values in the order millions. The highest Q ($\sim 9 \times 10^6$) has been measured in planar heterostructure silicon cavities near the telecom band ($\sim$ 1550 nm) [157]. However, they are more suitable for in-plane applications as the outcoupling efficiency is low and difficult to improve. Moreover, when heterostructure designs are scaled for the $\sim$ 1078 nm wavelength range, their implementation would require fabrication tools capable of realising nanometer scale variations in the design features. On the other hand, the L3 type of planar cavities, when carefully modified, can provide experimental Qs close to those of heterostructure cavities but demand less computational resources to design and are more robust to fabrication imperfections. The collection efficiency of L3 cavities can also be improved significantly using a simple tweak in the design. For these reasons, in this work, we focus on design and realisation of L3 planar PhC cavities.

4.5.1 L3 photonic crystal cavities: tuning for high-Q values

Planar PhCs are usually implemented by incorporating a hexagonal lattice of air holes in a high-refractive index substrate membrane. A row of three absent holes can form a cavity termed L3 type. The in-plane light trapping efficiency of these PhC cavities

is high but the total/effective cavity Q depends on the vertical light trapping efficiency determined by TIR conditions. For simple L3 type 2D PhC cavities, the total Q is typically limited to few thousands due to inefficient TIR conditions at the slab-air clad interface [264, 276]. The tangential component of the plane wave **k**-vector ($k_{||}$) at the slab-air clad interface defines how strongly light remains confined in the cavity ($0 \leq k_{||} \leq 2\pi/\lambda_0$ is the leaky region and a strong confinement is obtained where $k_{||} > 2\pi/\lambda_0$). Now, the cavity mode E-field profile can be represented as a modulated wave where the base is a fundamental sinusoidal wave of wavelength λ and the envelope function is defined by the cavity structure [264, 276]. For a simple L3 cavity, the envelope

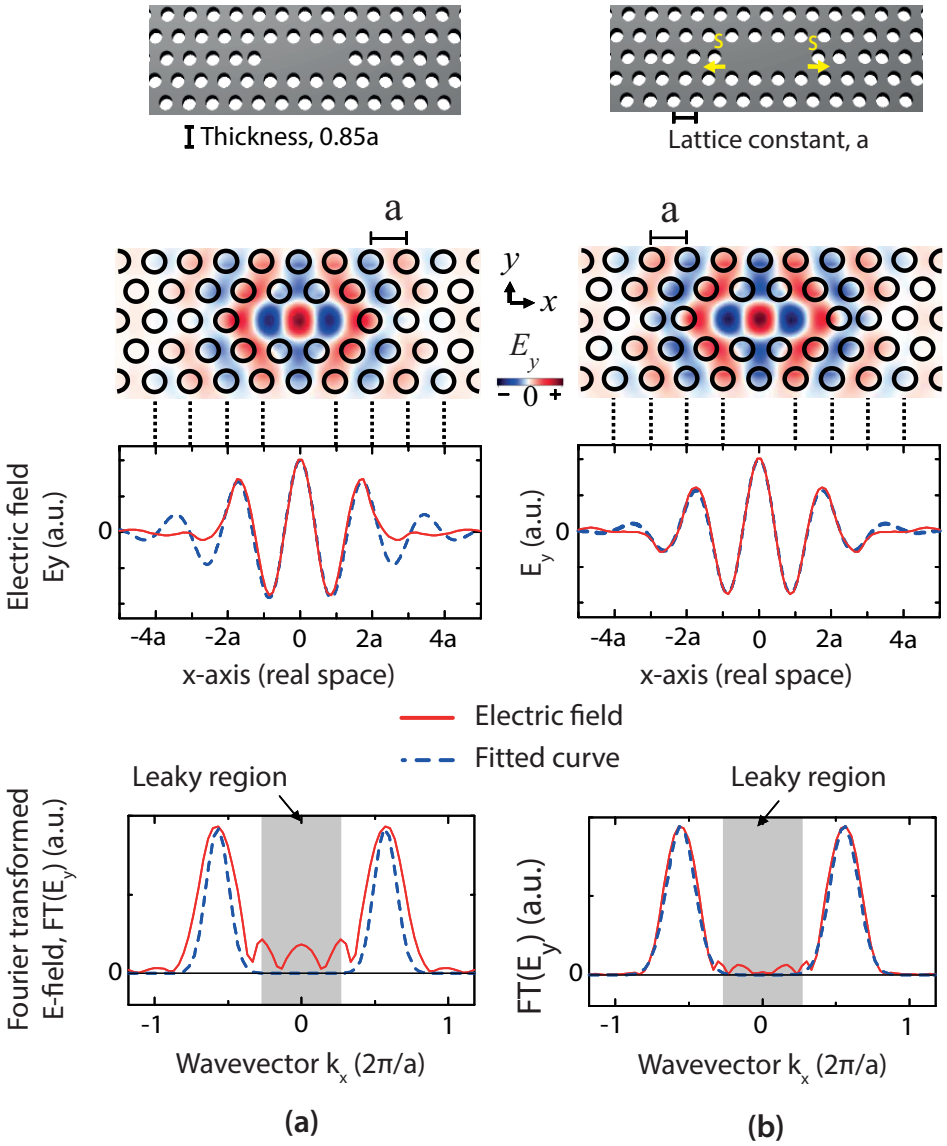

Figure 4.11: Tuning L3 cavities for higher Q (a) E-field distribution (E_y) for L3 planar cavity without air hole displacement near cavity edge, (b) E-field distribution (E_y) for L3 cavity with displaced air holes near cavity-edge, image reproduced from [264]

waveform varies abruptly at the cavity edge generating some wavevector components in Fourier space inside the leaky region, as shown in Figure 4.11a. Hence, the light escapes and degrades the cavity Q significantly. This situation can be improved by modifying the envelope function of the cavity mode E-field profile i.e., by reducing the abrupt envelope variation that causes the leak. It has been found that a smooth Gaussian envelope gives less leaky components and hence higher Q values [264, 276].

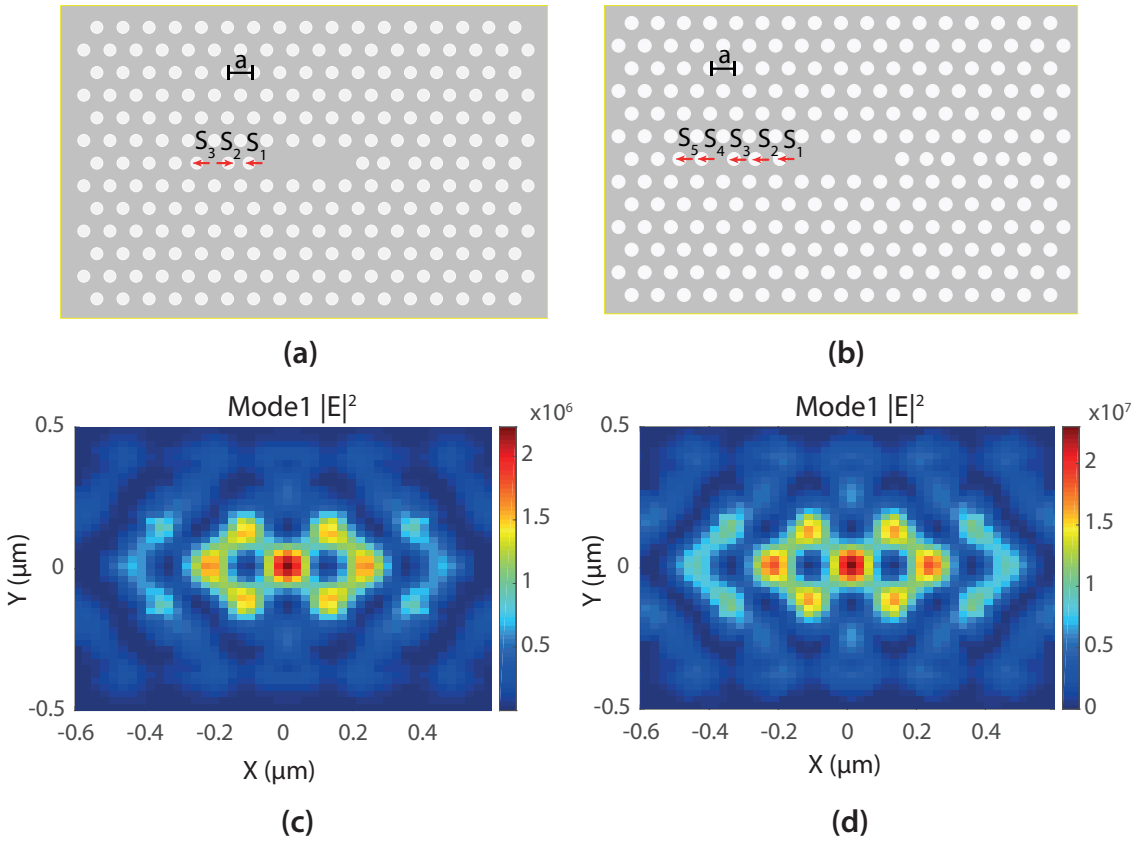

Figure 4.12: Fine-tuned and Super-L3 cavites and E-field distribution for first mode. (a) & (c) Fine tuned cavity with three near edge holes shifted and E-field distribution for first cavity mode, (b) & (d) Super-L3 cavity with 5 near edge holes shifted and E-field distribution for first cavity mode

Tweaking the periodicity of the air-holes near cavity edges can make the cavity mode E-field profile more similar to the Gaussian envelope function. The generation of leaky modes gets strongly suppressed when the E-field profile resembles the Gaussian envelope function closely (Figure 4.11b). By adjusting the positions of three holes near the cavity edges, the Q-factor can be optimised to $\sim 10^5$ [264]. More recently, an L3 cavity with Q-values exceeding $\sim 10^6$ for a cavity mode near telecom wavelength has been demonstrated. This super-L3 cavity was designed by rearranging the positions

of five air-holes near the cavity edges [149]. Figure 4.12 illustrates Fine-tuned L3 and Super-L3 cavities along with E-field distributions for their first resonant mode designed around $\sim$ 1078 nm, where the ^{31}P $D^0X \rightarrow D^0$ transition takes place. The design parameters for the Fine-tuned L3 cavities are: lattice constant, $a = 263$ nm; hole radius, $r = 0.3a$; membrane thickness, $t \approx 0.84a$; first hole shift, $s_1 = 0.17a$; second hole shift, $s_2 = -0.025a$ and third hole shift, $s_3 = 0.17a$. For Super-L3 cavities optimised design parameter are: $a = 250$ nm, $r \approx 0.25a$, $t = 0.88a$;, $s_1 = 0.337a$, $s_2 = 0.2706a$, $s_3 = 0.0874a$, $s_4 = 0.3223a$ and $s_5 = 0.1737a$. The simulated Q of the first cavity mode for Fine-tuned and Super-L3 structures are $\sim 3.1 \times 10^5$ and $\sim 4.76 \times 10^6$, respectively.

4.5.2 L3 photonic crystal cavities: outcoupling efficiency enhancement

In Section 4.5.1, we optimised an L3 design for high-Q values with resonant modes around our wavelength range of interest (1078 nm). However, when optimised for high Q values, outcoupling efficiencies from these cavities degrade considerably. Extracting light from a PhC cavity in a controlled way is inherently difficult because a cavity with small mode volume causes strong diffraction. Though the light extraction efficiency is better for PhC membranes than bulk materials, the light from a cavity is emitted mostly at grazing angles and the far field is usually broad. For this reason, objectives with moderate numerical aperture ($\leq$ 0.65) can collect only a small portion of emitted light. So, to the full potential of high-Q cavities for enhancing radiative emission, the far-field radiation has to be tailored in a suitable way so that the emitted light can be collected efficiently by the objective.

Low collection efficiency of light emitted from L3 PhC cavities can be improved considerably by implementing the band-folding technique which enhances directive emission [148, 254, 255]. To achieve high Q cavities, we optimise the design in such a way that the field components inside the light cone/leaky region are suppressed (Figure 4.11(b)). If we look at the field distribution in reciprocal space, it can be seen that after optimisation we have a peak at the first Brillouin zone (BZ) but almost complete suppression at the center ($k_x = 0$), as illustrated in Figure 4.13(a). This peak at $k_x = 0$ is responsible for radiation in the vertical direction. When this center peak is suppressed, most of the escaping radiation comes from the tails of the peak at the first BZ. The tails

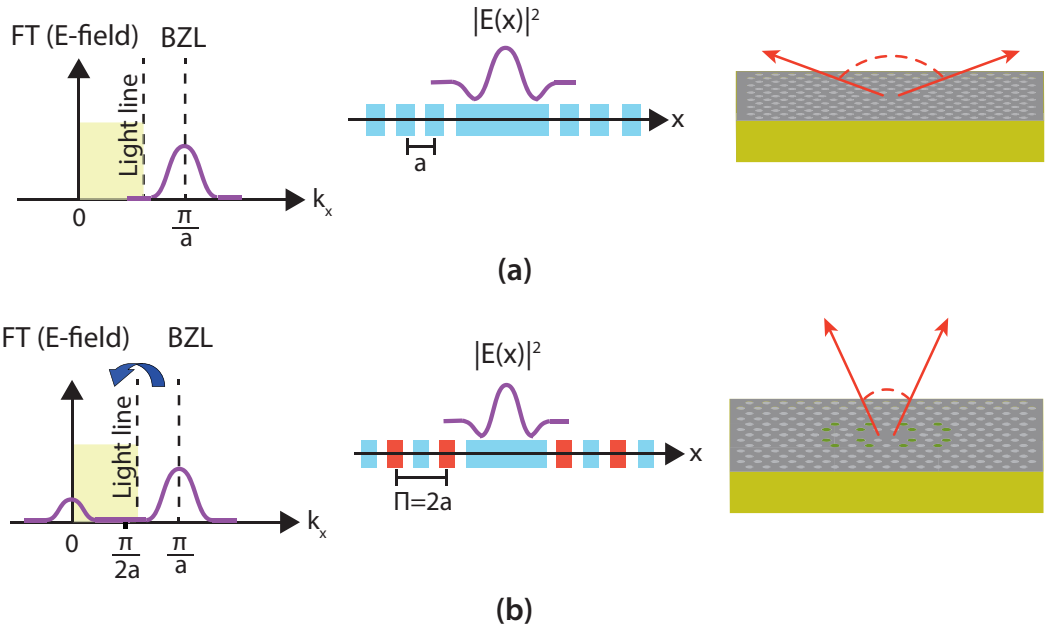

Figure 4.13: Tailoring far-field radiation pattern: The outcoupling from a high-Q cavity (a) before tailoring radiation pattern and (b) after tailoring radiation pattern with band-folding, images are reproduced from [255]

of the first BZ peak contributing to the radiation escape are very close to the light line, so, the emitted light escapes at grazing angles which in turn severely degrades the collection efficiency. In the band folding method, an additional subharmonic with a period of $\Pi = 2a$ is incorporated in the PhC lattice. The addition of this subharmonic of period $2a$ folds the main peak in the reciprocal space with respect to $k_x = \pi/2a$ and give rise to a replica peak at $k_x = 0$, Figure 4.13(b). This redistribution of near-field in reciprocal space and appearance of a replica peak at $k_x = 0$ allows light to escape vertically. Thus, incorporating a careful band-fold can significantly improve the collection of light from the cavity.

Figure 4.14 illustrates the effect of incorporating band-folding on a Fine-Tuned L3 cavity. A Fine-tuned L3 cavity can provide a Q as high as 3.2×10^5 but the collection efficiency is very low. After simulating the far-field radiation pattern (Figure 4.14(c)), it has been found that only $\sim 1\%$ of the emitted light can be collected by an objective with $NA = 0.5$. We have incorporated band-fold in the Fine-tuned L3 structure (schematic in Figure 4.14(b)) to improve collection efficiency, by modifying the size of certain air-holes (marked green in the schematic diagram). This hole size modifications superimposes a subharmonic lattice with twice the periodicity of the original

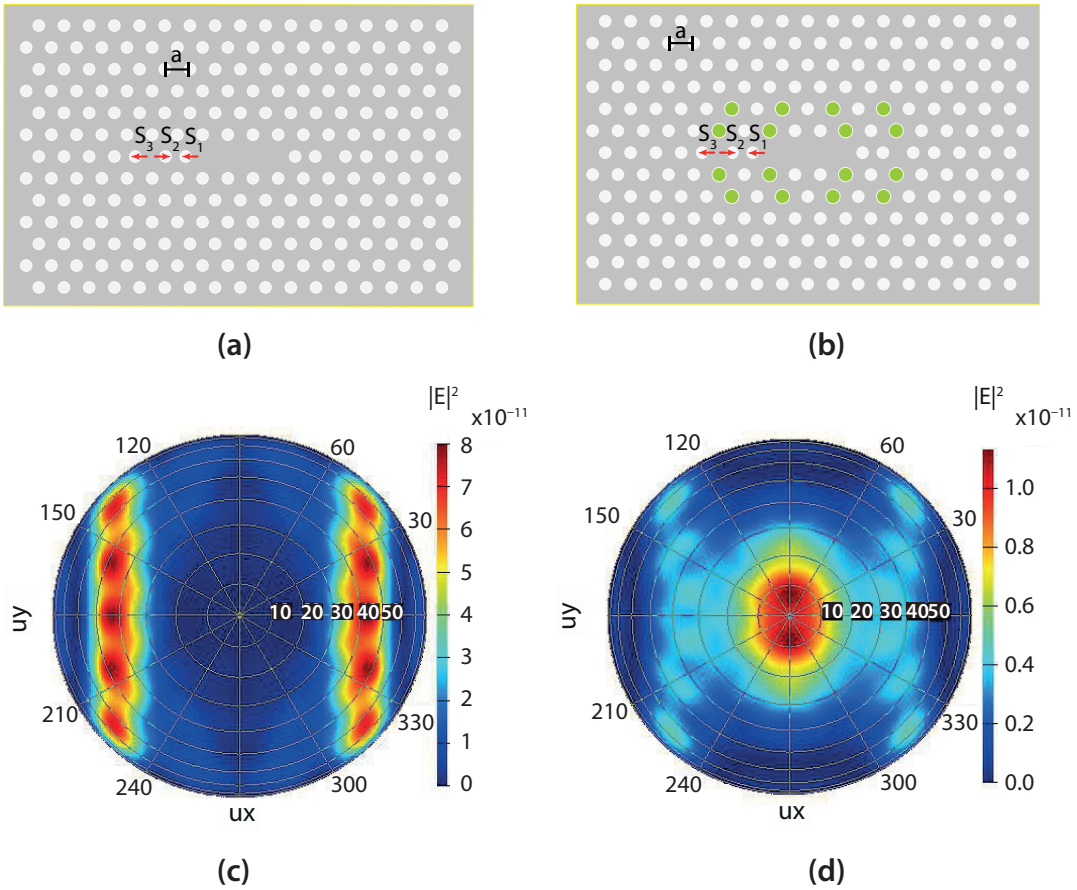

Figure 4.14: Implementation of band-folding technique on a Fine-tuned L3 cavity: (a) & (c) Schematic and far-field pattern of resonant mode before band-folding applied, (b) & (d) schematic and tailored far-field pattern of resonant mode with band-folding

PhC structure. Thus, the field peak outside the light cone is folded back to $k = 0$ which improves the vertical emission. We label this hole modification scheme, shown in in Figure 4.14(b), as the 'Design-1' for convenience in this thesis. The optimum value for the change in hole radii (i.e., the hole-size modulation) has been determined using a parameter sweep in simulation. When the radii of selected air-holes are increased by an amount $\Delta r = 0.01a$, $\sim 38\%$ of the emitted light is directed to the objective with $NA = 0.5$, as shown in Figure 4.14(d). A similar improvement was observed in the case of a Super L3 cavity when suitable band-folding was applied. However, the hole size modulations has to be implemented over a larger number of periods, as shown in Table 4.2. For an optimum $\Delta r = 0.005a$, we can the improve collection efficiency up to a value of 40% with an $NA = 0.5$, but such a small change is difficult to realise. Incorporating larger Δr improves the collection efficiency but degrades the Q-values. So, realising an optimum Super-L3 structure is challenging.

4.5.3 Summary: L3 PhC cavity

Table 4.2: Summary table for L3 PhC cavity, based on simulations using the Lumerical FDTD package

	Fine tuned L3 cavity	Super L3 cavity
Design without bandfold	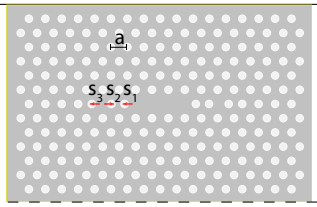	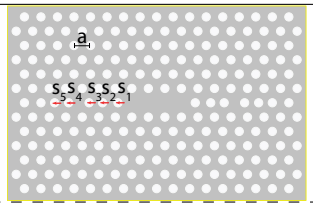
Q-factor	$\sim 3.2 \times 10^5$	$\sim 4.8 \times 10^6$
Far-field pattern	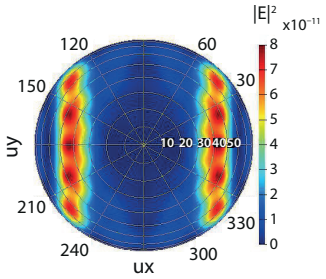	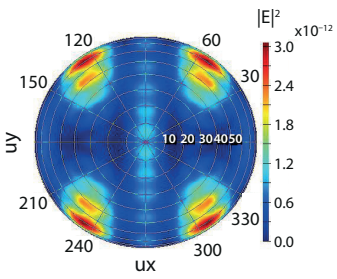
Outcoupling efficiency for NA = 0.5	$\sim 1\%$	$\sim 1\%$
Design with bandfold	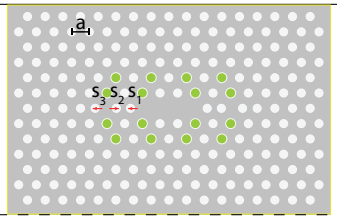	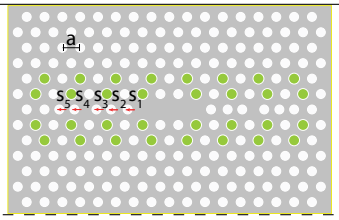
Q-factor	$\sim 1.5 \times 10^5$	$\sim 1.76 \times 10^6$
Far-field pattern	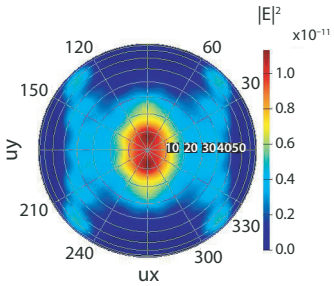	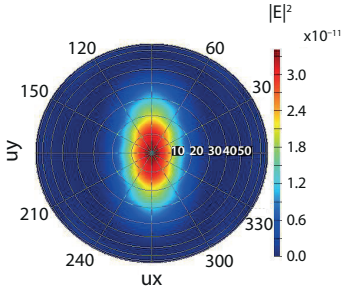
Outcoupling efficiency for NA = 0.5	$\sim 38\%$	$\sim 40\%$

In the preceding sections we have optimised various properties of the L3 PhC cavity to obtain a high quality factor and suitable far-field radiation pattern. Table 4.2 provides a brief summary of design optimisations we have carried out. After the near cavity-edge hole optimisation, Fine tuned and Super L3 cavities provide Q values of

$\sim 3.1 \times 10^5$ and $\sim 4.8 \times 10^6$ respectively but simulation for out-of-plane radiation reveals that both structures poorly outcouple light/photons to far-field. The calculated outcoupling efficiency is around 1% for both cases. To tailor the far-field radiation pattern, band-folding has been incorporated. Incorporation of the band-folding degrades the Q-values roughly by a factor of 3 for our designs. On the other hand, the outcoupling efficiency for both structures is improved by more than an order of magnitude which compensates the drop of Q-values (Table 4.2). A Super L3 cavity can ideally provide Q-values in the order of millions even after far-field optimisation. However, the optimum value for the variation in the radii of the air-holes is around 2 nm. The resolution limit of our lithographic system is also 2 nm which makes it difficult to fabricate an optimised Super L3 cavity. So, in this work, we focus on realising Fine tuned L3 cavities.

4.6 L3 PhC cavity: further optimisation of far-field radiation

In Section 4.5, we discussed the L3 type 2D PhC cavity and carried out design optimisations to achieve a high quality factor (in the order of 10^5) and moderate outcoupling of photons ($\sim 30-40\%$) for resonances at ^{31}P $D^0X \rightarrow D^0$ transitions. The reason for targeting high quality factors is that the ideal cavity enhanced radiative emissions from ^{31}P $D^0X \rightarrow D^0$ transitions can compete with the non-radiative recombinations for Q-values $\geq 10^6$ and $V_{\text{mode}} \sim (\lambda/n)^3$ (Figure 4.4), as discussed in Section 4.2. However, our reference PL measurement of the ^{31}P D^0X transition in bulk silicon (Section 3.4) suggests that photon detection from a single or few donors would be possible if the total photon emission efficiency is enhanced by three orders of magnitude. Such a total emission enhancement can be obtained even from a cavity with a Q-value of $10,000$ and an outcoupling efficiency of $\sim 30-40\%$. This provides room for a further optimisation of the far-field radiation and enhancement of the photon outcoupling from the L3 cavity. Moreover, a design for moderate Q-values ($20,000-50,000$) and larger hole-size modulations ($\Delta r \gtrsim 0.02a$) can relax the fabrication requirements and enable effective implementation of the designed structures.

In this section, we simulate and investigate two different modulation designs over

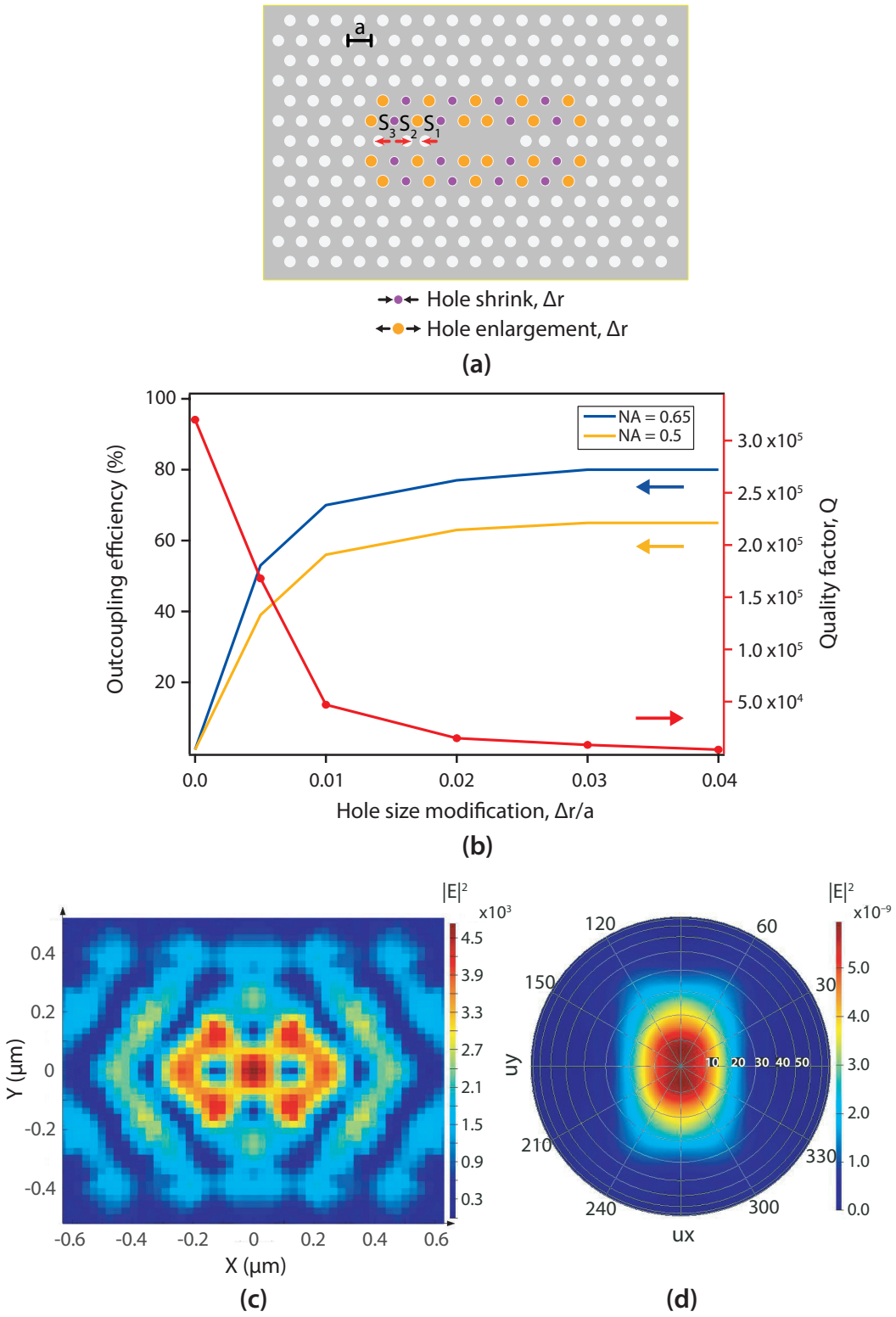

Figure 4.15: Outcoupling efficiencies for hole-size modulation with Design-2: (a) The schematic of the hole-size modulation design and (b) the outcoupling efficiency and Q-values of a Fine tuned L3 cavity for different amplitudes of hole-size modulation. (c) The E-field distribution at cavity plane and (d) the far-field radiation pattern for the resonance mode for a modulation amplitude, $\Delta r = 0.3a$

a larger range of modulation amplitudes in order to optimise the far-field radiation pattern of the L3 PhC cavity. As our target is to achieve a stronger band folding effect, we first attempt an denser hole-size modulation scheme capable of providing drastic change in the far-field radiation pattern. This is achieved by superimposing two subharmonic lattices on the original PhC structure where both of the subharmonics have a period of $\Pi = 2a$. So, in the final structure, more holes experience size modifications within a certain period compared to the case of any design implemented with superimposing single subharmonic lattice (e.g. Design-1, discussed in Section 4.5.2). We designate this hole-size modulation scheme Design-2 and the design schematic is presented in Figure 4.15a. In the schematic, the holes experiencing size modification are marked in orange and purple; the radii of orange (purple) holes are enlarged (shrunk) by an amount Δr, as shown in Figure 4.15a. We simulate the near and far-field properties for Design-2 within a range of modulation amplitudes $0 \leq \Delta r \leq 0.04a$. The outcoupling efficiencies for $NA = 0.5$ and $NA = 0.65$ are extracted from the simulated far-field patterns. In Figure 4.15b, the normalised outcoupling efficiency for the vertical upper space and the quality factor of the fundamental resonance are plotted as functions of the amplitude of the hole-size modulation. Figure 4.15b shows that the outcoupling efficiency improves quickly with the amplitude of the hole-size modulation up to $\Delta r \approx 0.01a$. The improvement in the outcoupling efficiencies becomes slow for modulation amplitudes $\Delta r > 0.01a$ and finally saturates when $\Delta r \gtrsim 0.03a$ at a value of $\sim 80\%$ and $\sim 65\%$ for $NA = 0.65$ and $NA = 0.5$, respectively. However, the improvement in far-field pattern i.e., outcoupling efficiency comes with a price of rapid decrease in the attainable Q-values. The red curve in Figure 4.15b shows the change in quality factors for increasing modulation amplitudes. The Q-value for the original fine tuned L3 PhC design is $\sim 3.2 \times 10^5$. It reduces by almost an order of magnitude when a modulation with an amplitude $\Delta r = 0.01a$ is implemented. The Q-value for $\Delta r = 0.04a$ is around 4×10^3 which is almost two orders in magnitude smaller than the no modulation case. Comparing the Q-values and outcoupling efficiencies for the range of modulation amplitudes ($0 \leq \Delta r \leq 0.04a$), we find that the optimum values (outcoupling efficiency $\approx 80\%$ and $Q = 8.5 \times 10^3$) at the hole-size modulation of $\Delta r = 0.03a$. The electric field distribution and far-field radiation pattern of fundamental resonance for Design-2 with the hole-size modulation of $\Delta r = 0.03a$ are shown in Figure 4.15c &

d, respectively.

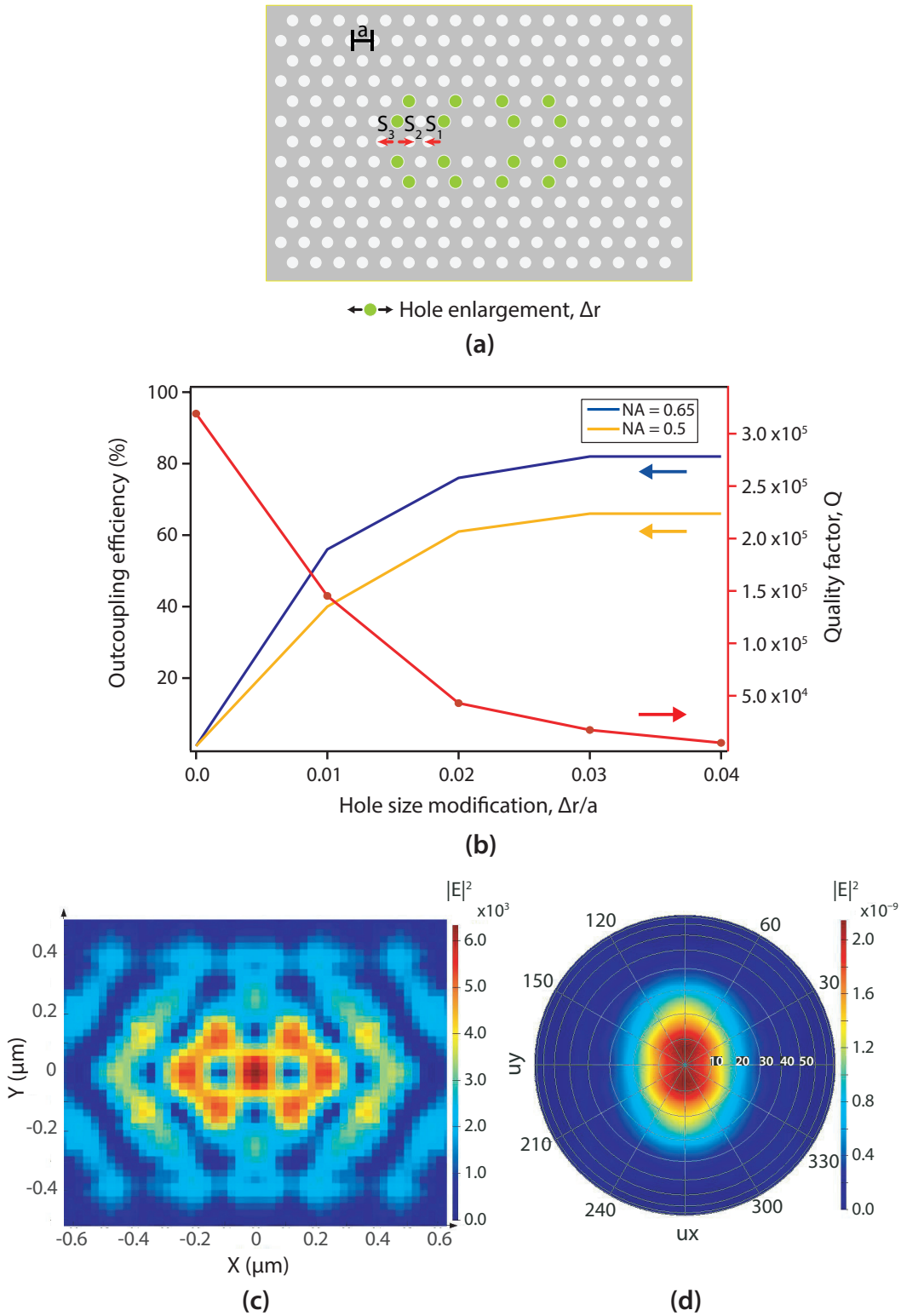

Figure 4.16: Outcoupling efficiencies for hole-size modulation with Design-1: (a) The schematic of the hole-size modulation design and (b) the outcoupling efficiency and Q-values of a Fine tuned L3 cavity for different amplitudes of hole-size modulation. (c) The E-field distribution at cavity plane and (d) the far-field radiation pattern for the resonance mode for a modulation amplitude, $\Delta r = 0.3a$

Although it provides high outcoupling efficiencies, Design-2 suffers from strong suppression of Q-values. On the other hand, the suppression of Q-values with increasing hole-size modulations is less severe for Design-1, as observed in Section 4.5.2. Therefore, we have also simulated the near and far-field properties for Design-1 (Figure 4.16a) over a range of modulation amplitudes $0 \leq \Delta r \leq 0.04a$, in order to investigate the outcoupling efficiencies and corresponding quality factors. The extracted outcoupling efficiencies and quality factors for Design-1 are plotted as functions of the amplitude of the hole-size modulation, as shown in Figure 4.16b. Similar to the case of Design-2, outcoupling efficiencies with Design-1 are also extracted for $NA = 0.5$ and $NA = 0.65$. These plots show that outcoupling efficiencies improve at a slower rate compared to Design-2 which indicate that band-folding takes place less drastically in case of Design-1. For example, Design-2 provides an outcoupling efficiency of 70% in the case of a modulation amplitude $\Delta r = 0.01a$ and $NA = 0.65$ (Figure 4.15b), whereas the value obtained with Design-1 for the same conditions is about 56% (Figure 4.16b). Beyond $\Delta r \approx 0.03a$, the outcoupling efficiencies for Design-1 also saturate around the same values ($\sim 80\%$ for $NA = 0.65$ and ~ 65 for $NA = 0.5$) obtained for Design-2. However, we find that the decrease in quality factor is less severe for Design-1, most probably due to a gradual band folding effect. Over the range of modulation amplitude considered here, the Q-value reduces by an order of magnitude for Design-1 compared to the no modulation case, whereas a reduction by almost two orders of magnitude has been found in the case of Design-2. Thus, for larger modulation amplitudes ($\Delta r > 0.02a$), Design-1 appears more promising as it can provide higher Q-values than in the case of Design-2 while maintaining the same level of photon outcoupling. The optimum outcoupling efficiency and Q-value for Design-1 are also found at the modulation amplitude $\Delta r = 0.03a$. But the extracted Q-value, 2.5×10^4, in this modulation scheme is larger by almost a factor of three than the case of Design-2. The electric field distribution and far-field radiation pattern of fundamental resonance for Design-1 with the hole-size modulation of $\Delta r = 0.03a$ are shown in Figure 4.16c & d, respectively.

According to the optimum outcoupling efficiencies and Q-values obtained, we find that both modulation schemes (Design-1 and Design-2) can provide enough emission and extraction enhancement to detect photons from a single ^{31}P D^0X emitter in silicon. In the case of an ideal implementation, Design-1 has the additional advantage of higher

attainable Q at the optimum modulation. However, in practice, the performances are also strongly affected by the structural and fabrication imperfections, i.e., the effective realisation of the modulation schemes. Therefore, in this work, we fabricate L3 PhC devices with both modulation schemes and experimentally characterise and compare their properties, which will be discussed in detail in Chapter 6.

4.7 Summary

In this chapter, the light confinement (Q-factor) and far-field emission properties of several photonic cavity structures such as circular Bragg resonators (CBRs), 1D PhC cavity and L3-type 2D PhC cavities have been evaluated using FDTD simulations. We focussed on the fundamental resonant modes around ^{31}P $D^0X \rightarrow D^0$ transitions for these cavities and carried out design optimisation accordingly. In case of CBRs, we have simulated the properties of both suspended and non-suspended structures. Non-suspended CBR has been selected for practical implementation because of relatively flexible fabrication requirements. Non-suspended CBR can provide Q-value $\sim 200-250$ and a light outcoupling efficiency at least an order of magnitude higher than the unpatterned, bulk silicon sample?s case. Thus, non-suspended CBRs are capable of enhancing total emission by two orders of magnitude compared to bulk silicon, which would allow detection of emission from few tens of ^{31}P donors in silicon.

1D and L3-type 2D PhC cavities can provide very high Q-values ($\sim 10^6$) with small mode volumes ($V_{\text{mode}} \lesssim (\lambda/n)^3$). We have simulated and optimised both 1D and L3 PhC cavities aiming for coupling with ^{31}P D^0X emissions. With careful designs, 1D PhC cavities can attain very high Q-values ($\sim 6\times 10^6$) for mode volume as low as $\sim 0.4(\lambda/n)^3$. However, effective realisation demands stringent fabrication requirements and efficient light outcoupling, i.e., tailoring far-field radiation is difficult with 1D PhC cavities. Similar facts are applicable for 2D Super L3 PhC cavities. Therefore, in this thesis, Fine-tuned L3 cavity (design with three side hole shifts) has been selected for practical implementation. We have further incorporated band folding technique in the Fine-tuned L3 cavity design for enhancing light outcoupling efficiency. Two band-folding schemes have been implemented and optimised in the design to obtain outcoupling efficiencies $\sim 70-80\%$ with realistic collection ($NA \geq 0.5$). With these optimised L3 cavity designs, Q-values around $10,000-20,000$ can be attained

with mode volume below $0.9(\lambda/n)^3$. Such Q/V_{mode} value would permit high Purcell enhancement (~ 100) even in the case of non-optimal/practical cavity-emitter coupling [70, 253, 268]. Thus, far-field optimised, Fine-tuned L3 cavities are ideally capable of providing the required three order of magnitude enhancement in the total emission, which would allow us to probe down to single/few ^{31}P donors in silicon.

Chapter 5

Fabrication of photonic structures

The optical properties of nanoscale photonic devices are sensitive to their structural integrity. Any unwanted irregularity or deformation in the realised structure can cause significant degradation of the ideal performance. Thus, the reliable fabrication is the key factor to ensure the desired optical properties of photonic devices. In this work, we investigate photonic structures such as silicon solid immersion lens (SiSIL), photonic crystal (PhC) cavities, circular Bragg resonators (CBRs) etc. for enhanced extraction and/or emission of no-phonon (NP) D^0X transitions in silicon. The characteristic dimensions of these photonic structures are either in the order of or smaller than the light wavelength (~ 1.078 μm) they are designed for. Therefore, the fabrication of such photonic devices with a high precision involves challenging and expensive process steps, where each step requires a careful optimisation and constant monitoring. In this chapter, we discuss fabrication processes which are used for realising the photonic devices under consideration. Several fabrication process recipes with/without step optimisations are attempted and explored to find out the most suitable candidate. The main goal of step optimisations is to achieve an efficient process implementation with available resources and minimise the fabrication cost as much as possible. The chapter starts with a brief introduction of the major process tools used, followed by an overview of different processes and optimisations attempted for efficient fabrication of our photonic devices.

5.1 Fabrication tools

In any device fabrication recipe, process steps can be broadly categorised into cleaning, deposition, patterning and etching. A complete fabrication recipe might involve many

different equipments, chemicals in several process steps depending on the intended device architecture and dimensions. Therefore, the selection of suitable process tools and chemicals is important to implement any fabrication recipe. In this work, we have mostly used solvent (acetone and isopropyl alcohol) cleaning. Various other tools are used for deposition of lithographic resists and etch masks. For the nanoscale patterning, we have implemented focussed ion beam (FIB) milling and electron beam lithography (EBL) techniques. In case of FIB milling, the pattern is directly transferred to the substrate. After the EBL patterning, dry etching steps are used for the pattern transfer to the substrate. The most important process tools used for device fabrication are briefly introduced in this section.

5.1.1 Focussed ion beam (FIB) system

In the focussed ion beam (FIB) milling system, ionised particles with a high velocity are used to sputter etch substrate materials from desired locations of the sample surface and fabricate complex structures in a single process step. Thus, the FIB milling can directly transfer a pattern, without requiring any lithographic mask/resist. Figure 5.1(a) shows a simplified schematic of an FIB system. The Gallium (Ga) FIB milling is already demonstrated as an effective tool for fabricating lens structures in bulk silicon [277, 278]. But, being heavy, Ga ions cause a significant damage to the target material through amorphisation and implantation (see Figure 5.1(b)). This damage adds strain and would degrade the optical property of an emitter inside silicon lattice. So, the Ga FIB milling is not useful for making lens structures in our case.

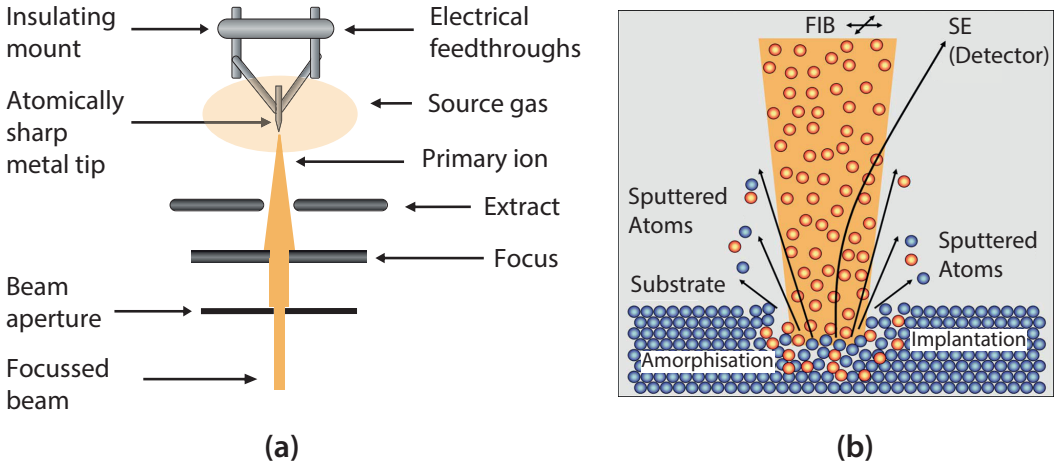

Figure 5.1: Focussed ion beam (FIB) milling system: (a) A schematic of an FIB system and (b) the effect of physical sputtering on a target, images reproduced from [279, 280]

In principle, the damage from an FIB milling can be considerably minimised by using lighter ions such as helium, neon etc. instead of conventional heavy Ga ions. In this work, we have used a Carl Zeiss ORION NanoFab, a novel FIB system that uses lighter ions (helium & neon) for milling. Gas field ion source (GFIS) guns are used for creating ion beams where gaseous helium or neon is ionised at an atomically sharp metal tip and then emitted as ions from a 'trimer'. The ions are focused through electrostatic optics in an ion column which is coupled with a high vacuum system containing samples. This Carl Zeiss ORION NanoFab helium and neon focused ion beam system can be used for making Sub -10 nm nanostructures and also for high resolution ($\sim$ 0.5 nm image resolution) imaging of nonconducting surfaces.

5.1.2 Electron beam lithography

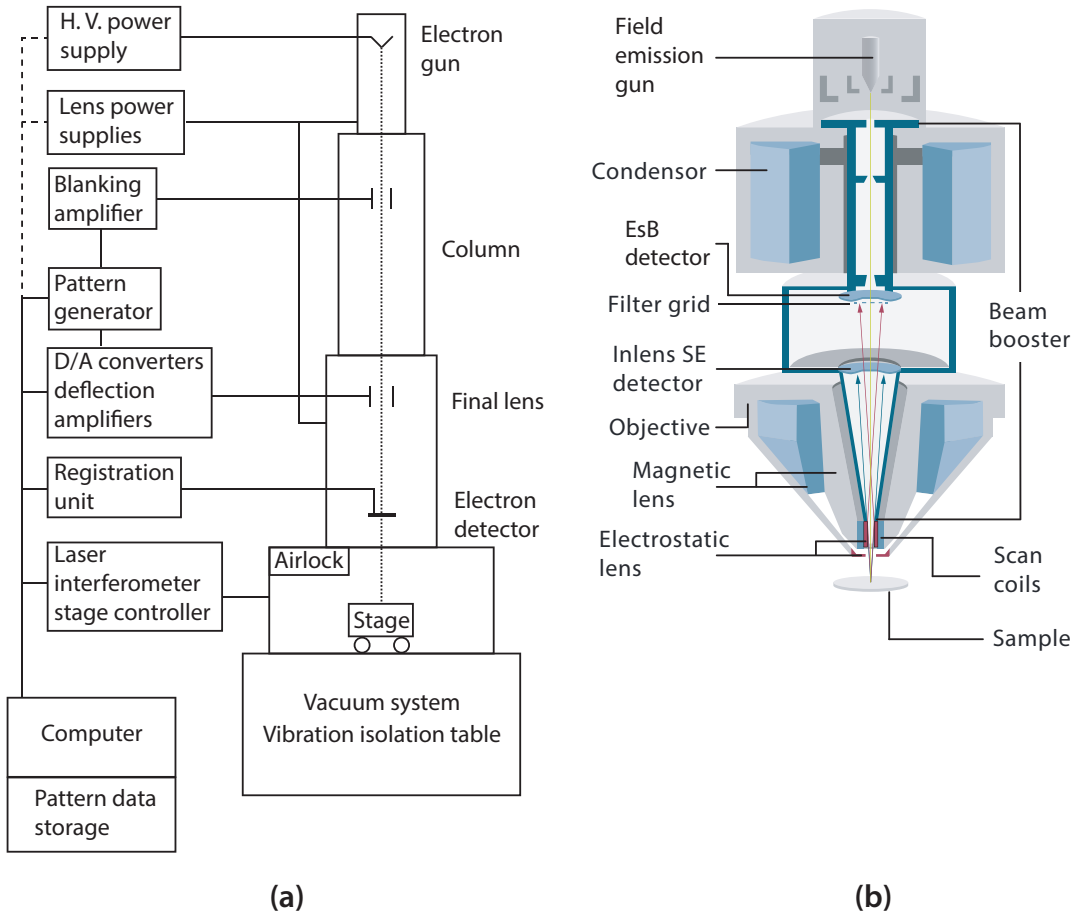

Figure 5.2: Electron beam lithography (EBL) system: (a) A block diagram showing the major components of a typical EBL system, adapted from [281]. (b) A schematic of the electron optics (with Gemini column technology from Zeiss) of the Raith 150 Two EBL system, image reproduced from [282]

In a lithographic process, the structural design is patterned into a medium or re-

sist for the purpose of subsequent transfer to the target substrate. Resists are generally polymers sensitive to either photon (in photolithography) or electron (in electron lithography) exposure. In the EBL technique, a highly collimated (< 5 nm) electron beam is used for writing patterns of almost any 2D shape into the suitable resist. The electron beam writing technique was initially evolved in early 1960s [281, 283] from the scanning electron microscopy (SEM) system. A pattern generator and beam blanker were added to the SEM system to carry out a controlled exposure of the target area under electron beam (e-beam) [284]. State of the art EBL systems are fully dedicated patterning systems which consist of high brightness electron sources, microscope columns for the e-beam focussing, alignment, exposure control etc. They also have high resolution mechanical stages which allow step-by-step exposure of large substrates [284]. Figure 5.2a shows a generic block diagram of a modern EBL system with its major functional components. Modern EBL systems allow patterning sub-10 nm features for nanoscale device realisation as well as for preparing the optical/nanoimprint lithography masks. However, being a serial exposure technique, the EBL patterning is slow for complex designs. So, large scale processes become quite expensive and time consuming. Another critical issue with the e-beam exposure is that energetic electrons get scattered when they hit the resist material. This scattering exposes larger areas in the resist than the beam spot size, which is known as the proximity effect. To achieve a reliable patterning, the proximity effect has to be minimised through a careful design or adjustment of the e-beam parameters. In our work, we mainly used a RAITH150 Two EBL system from RAITH Nanofabrication, available at the London Centre for Nanotechnology cleanroom. The RAITH150 Two EBL system uses an electron optics (Gemini technology from Carl Zeiss, see Figure 5.2b) which can provide a focussed e-beam with an acceleration voltage up to 30 kV.

5.1.3 Plasma enhanced chemical vapour deposition

Chemical vapour deposition (CVD) technique is a chemical process used in the semiconductor technology for growing high quality, thin films of solid materials on the target substrate. In a typical CVD process, vapour-phase precursors (source materials) are brought into a chamber containing the target substrate. Precursor gases diffuse to the substrate surface and chemical reactions take place at/near the hot surface, resulting in

the deposition of a thin film on the surface. Any other byproducts are pumped out of the chamber along with the unreacted gases. One issue with the conventional CVD system is that it requires high temperatures ($\gtrsim 700°C$) for stable chemical reactions and film depositions. However, a low deposition temperature ($\sim 200 - 300°C$) is desirable in many cases where the substrate or device properties are sensitive to high temperatures. This issue can be addressed by using the plasma enhanced chemical vapour deposition (PECVD) process. In PECVD systems, the decomposition and reactions of precursor gases are enhanced by using plasmas instead of the thermal energy [222, 283]. An electrical energy (radio frequency (RF) oscillating voltage or direct current (DC) discharge between two electrodes) is used for generating the plasma. The energy is then transferred into the precursor gas mixture through collisions with charged particles created in the plasma. Thus, PECVD provides deposition rates similar to the case of a thermal CVD at much lower process temperatures ($\sim 300°C$).

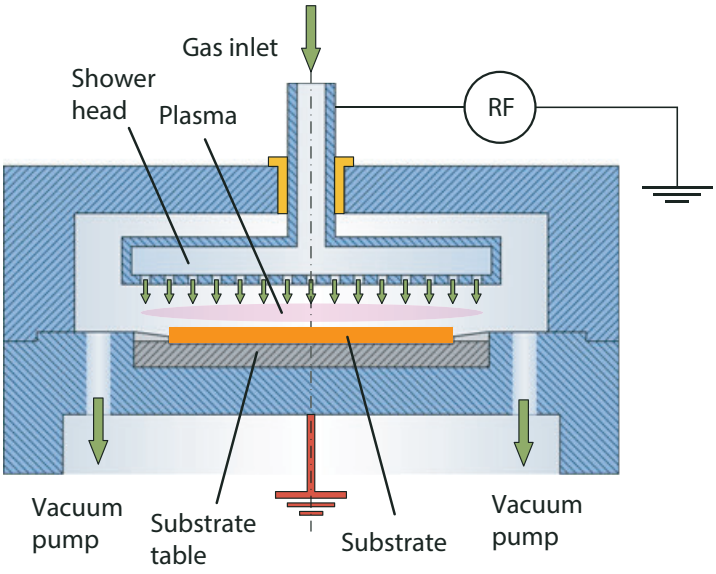

Figure 5.3: Plasma enhanced chemical vapour deposition (PECVD) system: Schematic diagram of a parallel plate PECVD system, image adapted from [283]

Figure 5.3 shows the schematic of a simple parallel plate PECVD system where the top electrode is connected to the RF power supply. The precursor gases are introduced through a shower head inlet integrated into the top electrode and pumped away around the bottom electrode. The bottom electrode is connected to the ground, which is also used for holding and heating substrates. In our work, we have used the PECVD tool (STS Multiplex PECVD System) at the LCN cleanroom for growing silicon diox-

ide film on SOI substrates. A high quality silicon dioxide films can be deposited at $\sim 300°C$ with the PECVD system while a conventional CVD requires temperatures in the range of $650 - 850°C$ to produce similar quality films. The oxide thin film is used as a dry etch mask for transferring patterns into silicon (discussed in Section 5.5). We prefer the low temperature PECVD process in order to avoid any redistribution (segregation) of implanted (doped) ^{31}P donors inside the thin silicon membrane of the SOI substrate.

5.1.4 Reactive ion etching

To realise any device, the patterns in the resist have to be transferred to the substrate. This is carried out by etching the substrate using the patterned resist as an etch mask. Etch processes in semiconductor fabrication are usually carried out either with various chemical reactions or with a physical removal (sputtering or ion milling) of substrate species. In case of photonic cavities such as PhC cavities, CBR devices etc., a highly anisotropic etch is essential to achieve desired optical properties [285]. Thus, a precise control over etch profiles (the etch selectivity, rate and anisotropy) are required for the implementation of effective devices. To obtain a precisely controlled etch, the reactive ion etching (RIE) process is very useful. In an RIE process, a combination of the chemical reaction and the physical etching are used for the removal of the target species from the substrate surface because neither of the etching approaches alone is sufficient to achieve the desired etch profiles.

In this work, we mainly used a parallel plate RIE system, Plasma Pro NGP80 from Oxford Instruments, to optimise and carry out the etch steps in our fabrication processes. A schematic of a parallel plate RIE system is shown in Figure 5.4. In this parallel plate configuration, the RIE system has a top electrode with an integrated 'shower-head' gas inlet and a parallel bottom electrode serving as the sample holder. The top electrode is electrically grounded and the bottom electrode, on which the sample is placed, is connected to an RF power source. The typical operating frequency of the RF source used in the RIE systems is 13.6 MHz. The bottom electrode is usually covered with a quartz or graphite plate in order to protect it from getting etched during the process steps [222, 283]. In ionic structures, an electron is several orders of magnitude lighter than an ion. Hence, electrons are able to follow the oscillations

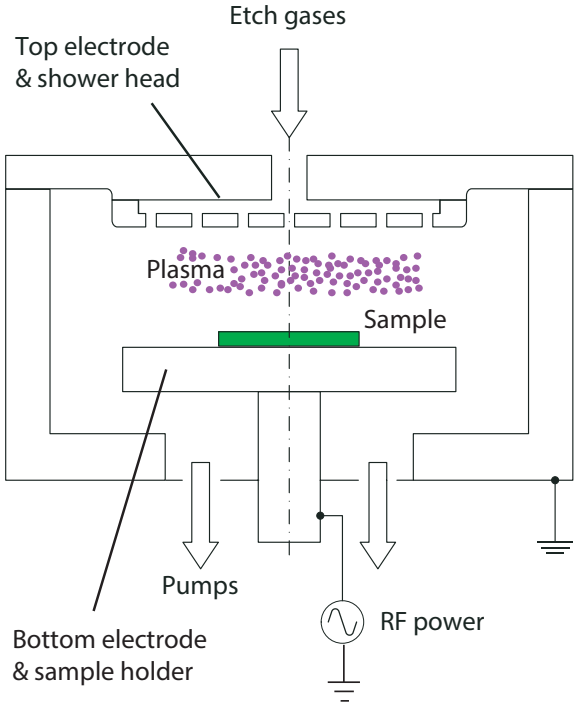

Figure 5.4: Reactive ion etcing (RIE) system: A schematic diagram of a parallel plate RIE system

of an applied RF field but ions cannot because of their much heavier mass. So, under the influence of the oscillating electric field, electrons get separated and oscillate between the electrodes. Inside the vacuum chamber, the oscillating electrons collide with the etching gas molecules and create a sustainable plasma [286]. Due to an RF induced DC bias, the positive ions from the plasma start to accelerate towards the negative bottom electrode which subjects the sample to a directional ion bombardment. As a result, the sample species experience not only a chemical attack (chemical etching) by radicals of the reactant gases, but also the vertical ion bombardment on the sample surface (the physical component of RIE causing the directional etch). Optimising an RIE process requires careful adjustment of several process parameters such as the RF power, chamber pressure, type and flow rates of etching gases etc. Details of an etch process optimisation for this work is provided in Section 5.5.

5.2 Fabrication of SiSILs with Ne FIB milling

We have carried out neon FIB milling with the Carl Zeiss ORION NanoFab system for fabricating SIL structures in the bulk silicon substrate. The helium ion beam is used for imaging as it is too light for milling our SIL structures within a reasonable time. The

depth of ion milling into a target surface depends on the beam dose and the exposure time. So, we can create steps of different depth by varying the dose. Grayscale bitmap masks are used for exposing sample to varied ion doses. If we use a grayscale mask with reasonably high resolution that can be used to fabricate curved structures, as illustrated in Figure 5.5(a). Ideally, we want to fabricate a full hemisphere with 180° opening angle. But dose tests have revealed that we cannot mill a complete hemisphere of radius of $2-2.5$ µm. This is because the metal tip in the ion source degrades to a non-usable state before the completion of milling. We have not fabricated smaller lenses (hemispheres of smaller radius) because they are unlikely to contain enough emitters to provide a detectable emission. So, curved structures with a base diameter of ~ 2.5 µm and height of roughly 300 nm are milled for SiSIL realisation, as shown in Figure 5.5(b). These SiSIL structures can be considered as slices from hemispheres with a radius of ~ 2.5 µm. The employed milling parameters are: beam current 3 pA, aperture

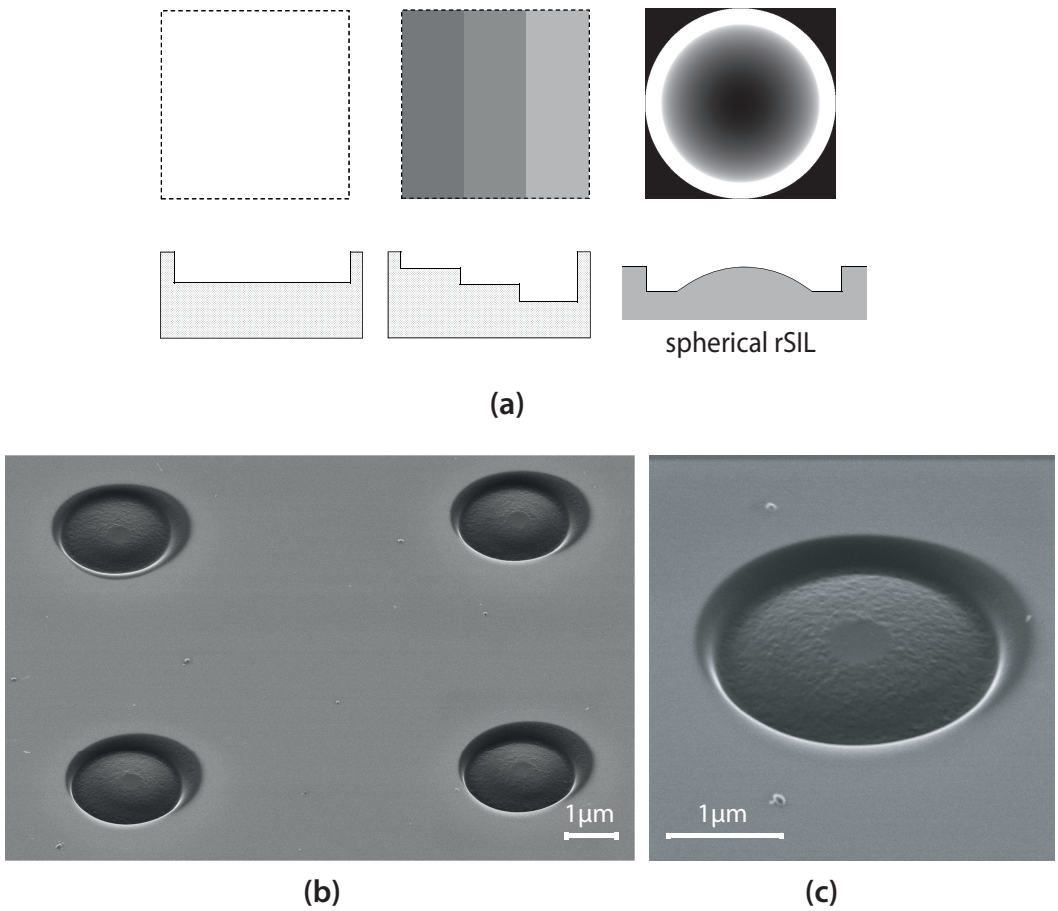

Figure 5.5: Ne FIB milling of SiSIL: (a) A grayscale bitmap mask for stair-step milling [277], (b) SiSILs fabricated with Ne FIB and (c) a high resolution image of fabricated SiSIL with He microscope

size 70 μm, acceleration voltage 13 kV, start dose 9 nC/μm^2 and end dose 3 nC/μm^2. The milling process was considerably affected by the degradation of the ionising tip and a stage drift. Thus, we have managed to fabricate only a few useful devices within the allocated instrument time. Finally, though the Ne FIB is less damaging than a Ga FIB milling, it is not completely damage-free. Careful examination under a high resolution He microscope shows that the fabricated lenses have a rough surface due to the milling. Moreover, the lens structures are slightly overmilled on the right side than the left, as can be seen in Figure 5.5(b), from which it also becomes evident that milled structures have suffered from a stage drift. To remove the surface roughness and amorphisation of silicon, a thermal treatment is carried out for 40 minutes at a temperature of 800°C. This results in the growth of a 10 nm oxide layer on the surface which is removed later by a HF etch. After the removal of the oxide layer, we have inspected the lens structures under the SEM and found that the lens surfaces are still rough. Further investigation is required to assess the curing of the substrate amorphisation with the heat treatment and adjust the recipe for the optimal damage control.

5.3 Fabrication of PhC cavities: Ne FIB milling

In principle, Ne FIB milling offers an effective way to fabricate photonic crystals. Being a direct pattern transferring tool, a Ne FIB system can make the array of holes in a single step (Figure 5.6(a)), with a higher spatial resolution than electron beam lithography. After drilling the holes, the patterned membrane can be released in another step by removing the buried oxide (BOX) with a HF etch. So, it would take two steps to get PhC devices completely fabricated on a suspended membrane. However, in practice, the process suffers from two technical issues: tip/trimer degradation and stage drift. The first issue is related to the Ne ionising mechanism of the FIB tool. In the Ne FIB, a positively biased, cryogenically cooled and atomically sharp metal tip is exposed to low quantity of neon gas under vacuum for generating ions. The atoms in the tip head are manipulated electrostatically in such a way that only three atoms remain at the end of the tip. These three atoms are referred to as the ‘trimer’. Under large positive bias, the trimer emits three streams of neon ions. One of these ion streams is then aligned and focused by the column optics and becomes the neon focused ion beam. One critical issue with this sharp metal tip is that the trimer arrangement of atoms survives for only

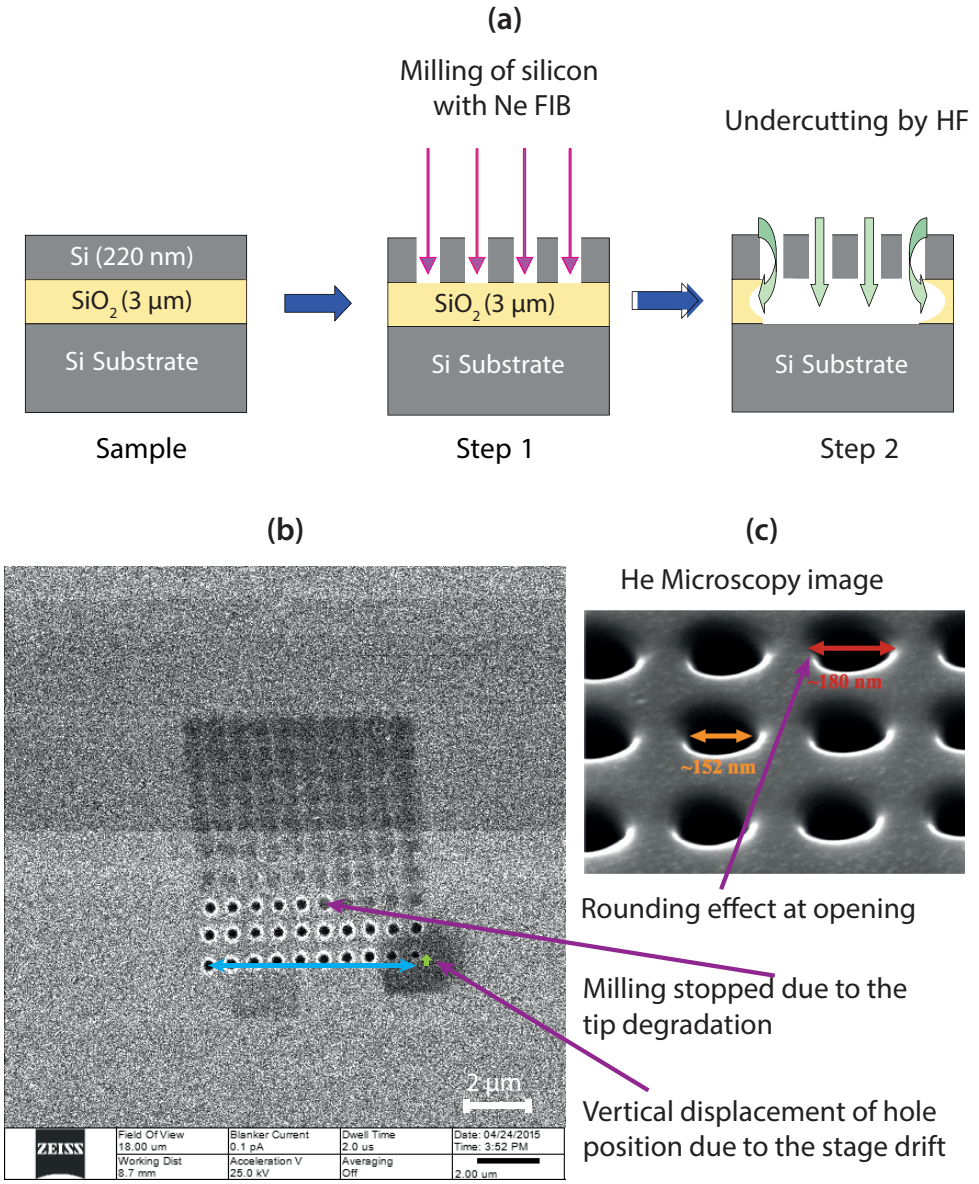

Figure 5.6: Ne FIB milling of planar PhC: (a) process steps for PhC cavity fabrication by Ne FIB milling, (b) effect of trimer tip degradation and stage drift on milling process, (c) rounding effect at hole opening (hole diameters were ~ 150 nm in the design)

a finite period of time, for example, the usual trimer lifetime found for our machine is around 8 hours for a milling current of 1 pA. With higher milling current the tip/trimer degrades even at a faster rate. When this three atoms arrangement of the ionising tip is lost, the machine cannot generate sufficient ions to provide required milling current. So, the trimer arrangement of the tip has to be reformed before starting the ion milling again. This issue becomes a critical one when we try to pattern designs that would take longer milling times than the trimer lifetime. Because if the tip degrades i.e., loses the three atoms arrangement during the milling process, the pattern transfer will be stopped

before completion due to insufficient generation of the ion beam. The second issue is related with stage drifts. This arises when the sample stage mechanism is not stable enough to drive the stage to intended positions with nanoscale accuracy. So, over time the position inaccuracy accumulates and causes an inaccurate pattern transfer.

Thus, the tip degradation and the stage drift limit the total milling time and accuracy of a pattern transfer. Their effects can be clearly observed in Figure 5.6(b), where a test design with a 10×10 array of holes is milled to investigate the limitations of the Ne FIB system. Before attempting to fabricate the 10×10 array of holes, we optimised a process recipe for milling a single hole. We found that with optimum parameters (beam current 1 pA, aperture size 40 µm, acceleration voltage 15 kV, spotsize 5 nm), it takes less than minute to mill a hole with a diameter of ~ 150 nm through the 220 nm 'device layer' of an SOI substrate. So, we estimated that milling a 10×10 hole array would take ~ 90 minutes. But in this test case, we did not start with a newly formed tip in order to investigate the tip degradation effect. In Figure 5.6(b), it is clearly seen that at the end of third row, milling was ceased due to the tip degradation. This indicates that we would be able to mill approximately a 25×25 array of air-holes within the maximum tip lifetime (8 hours). Each row/column of holes in the array acts as a Bragg reflector. A higher in-plane reflectivity would require larger number of reflecting layers. So, an array of $\sim 25 \times 25$ holes is not enough for implementing a high Q planar PhC cavity. Moreover, in the milled rows we can see that there is a slight upward drift in the hole positions (see Figure 5.6(b)), which was not intended in the design. According to the design, holes in a row should be in the same vertical level. We attribute this position displacement to the stage drift.

Finally, when observed under a He microscope, we found yet another issue with the milled holes. A rounding effect is evident at hole openings, as shown in Figure 5.6(c). Ideally the hole diameters would be 150 nm as in the design but in the He microscope image we see that at the opening the hole diameters have broadened to a value around 180 nm. This rounding effect can be minimised by using gas (e.g. XeF_2) assisted FIB milling. Use of a gas assisted FIB can provide higher vertical milling rates with less material redeposition. In summary, it seems that the Ne FIB system is not suitable for fabricating 2D PhC cavities requiring a large array of air holes. However, if the stage-drift is tackled and a suitable gas (e.g. XeF_2) source is incorporated in the

system, Ne FIB milling can be used to fabricate 1D PhC cavities.

5.4 Fabrication of PhC cavities: single layer resist process

High-Q PhC cavities demand nanometer-scale precision fabrication resources in order to accurately transfer the design to the desired substrate. The size, sidewall angle & roughness of air-holes are critical factors which strongly influence obtainable Q values. The surface of the cavity is also important; a rough surface allows light to leak hence reduces cavity quality factor. Since photolithography is not useful in the sub-micron range, electron beam lithography (EBL) based pattern transfers are necessary for PhC device fabrication.

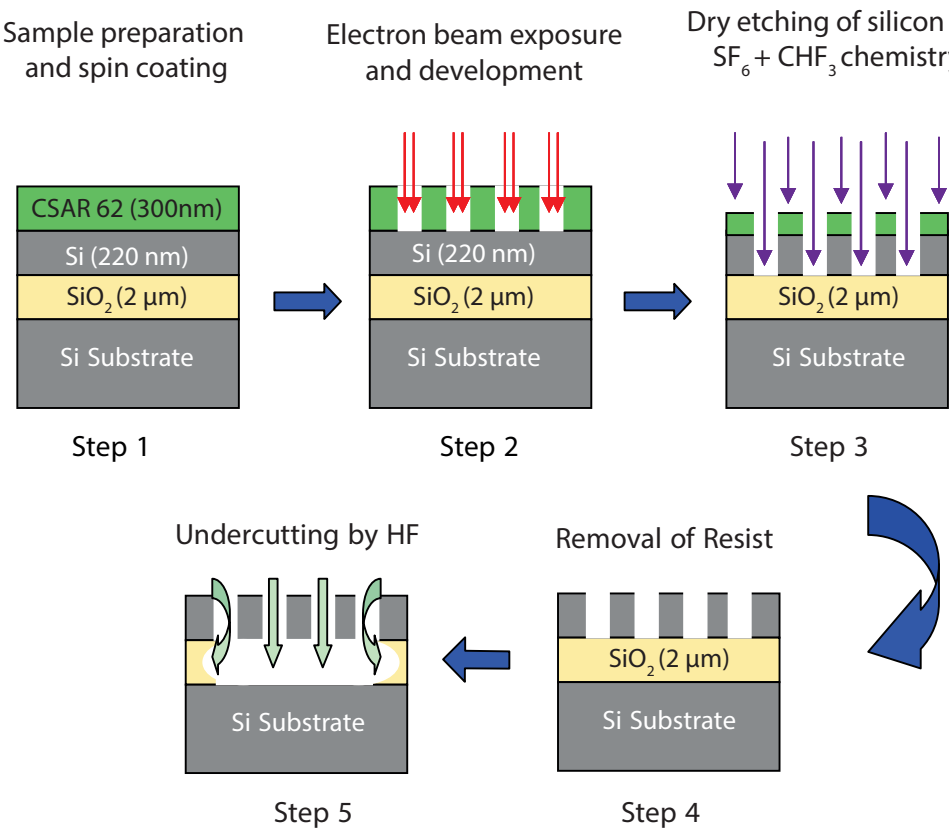

Figure 5.7: Process steps for fabricating PhC cavity with single layer resist

In the standard EBL process with single layer resist for fabricating PhC devices, a pattern is first written on the resist using electron-beam then transferred to the substrate through reactive ion etching (RIE), as shown schematically in Figure 5.7. We have carried out this standard fabrication of PhC devices with single layer resist at the

Table 5.1: Recipe of the optimized RIE process for CSAR-62/Si etching

Gas Composition	RF Power	DC Bias	Chamber Pressure	Si Etch rate
CHF_3 – 14.5 sccm SF_6 – 12.5 sccm	22 W	184 V	26 mTorr	110 nm/min

York JEOL Nanocentre in collaboration with Photonics group, Department of Physics, University of York. A silicon-on-insulator (SOI) wafer with 220 nm top silicon layer, 2 µm buried oxide (BOX) layer and 725 µm handle thickness is used for realising PhC cavities. The designs are transferred to the single layer of high resolution, plasma etch resistant e-beam resist (CSAR 62), which was spin coated on top silicon layer of SOI chips. The main components of CSAR 62 resist are poly(α-methylstyrene-co-methyl chloroacrylate), an acid generator and the anisole solvent. A Raith VOYAGER 50 kV Electron-beam lithography system is used for this pattern transfer with an optimum re-

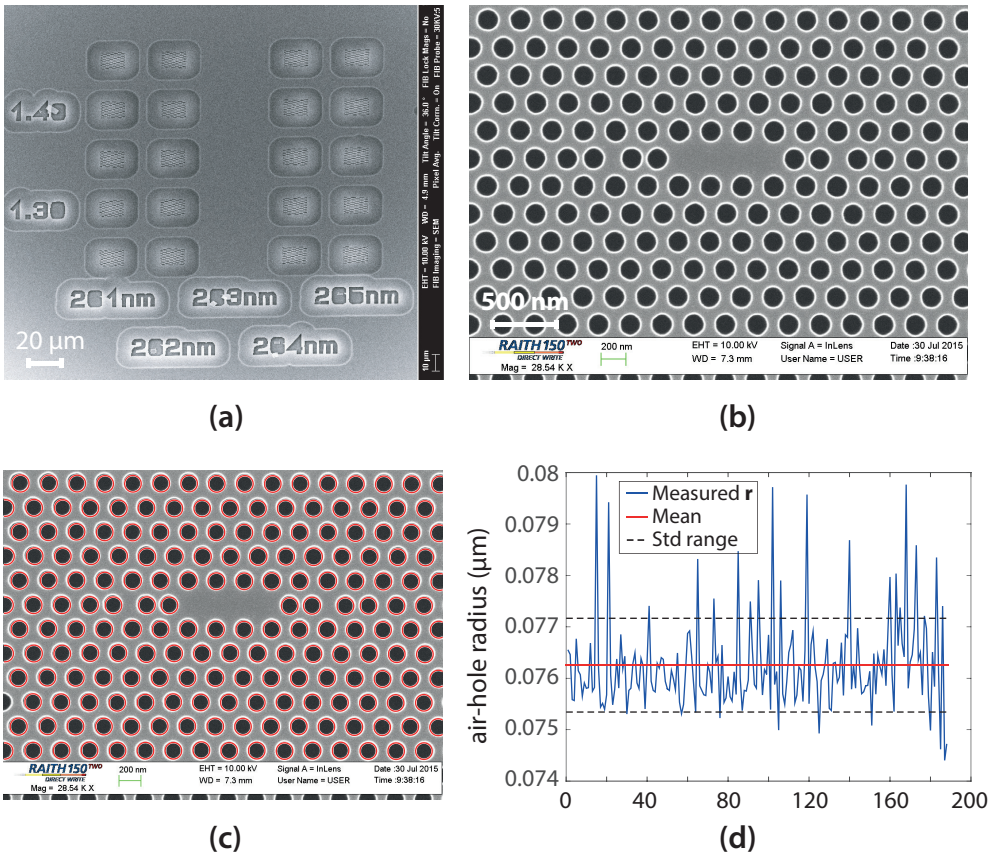

Figure 5.8: Fine-tuned L3 cavity fabricated with single layer resist process: (a) SEM image of cavities fabricated with varying parameters for lithographic tuning, (b) zoomed image of cavity from row-2 (dose factor - 1.3), column-2 position (lattice constant - 262 nm), (c) & (d) statistical estimation of air-hole radius

sist thickness of $\sim$ 300 nm. One major advantage of using 50 kV EBL system is that patterning does not suffer from any noticeable proximity effect which ensures efficient patterning. Patterns from resist are transferred to the top device layer of the SOI substrate using a reactive ion etching with fluorine based chemistry (mixture of CHF_3 and SF_6 gases). An in-house designed and built Reactive Ion Etching (RIE) system is used for silicon etching. Tthe etch recipe is provided in Table 5.1. After the RIE step, the chips were dipped in HF to remove the BOX layer below the patterned area and release the 220 nm thick suspended membrane containing PhC cavities.

In the EBL step, dose tests are carried out to find the right dose for a reliable pattern transfer. The air-hole size/radius slightly varies with e-beam dose around the optimum value. We have implemented and examined a range of doses to get close to the desired air-hole radii of $\sim$ 79 nm. The base dose used was 145 $\mu C/cm^2$ and dose factor varied from 1.25 to 1.45 with a step of 0.05. In addition to that, we have also fabricated cavity devices with varying lattice constant to facilitate lithographic tuning for the cavities, as illustrated in Figure 5.8 (a). With SEM imaging we have found that a dose factor of 1.3 provides us the air-hole size closest to the design. To get a more reliable estimate of the hole-size, a statistical average of hole radius is extracted by image processing, as shown in 5.8 (c) & (d).

5.5 Fabrication of PhC cavities: alternative process with multilayer resist

Conventional high resolution, positive-tone EBL resists such as PMMA (Polymethyl methacrylate) are mostly plastic polymers, which are not robust under plasma etches. There are plasma resistant positive resists such as ZEP520A, CSAR-62 but both the resists and their developers are expensive. They are also difficult to acquire for small-scale usage. Moreover, for efficient masking, thicker resist is required which in turn demands a higher energy EBL system (50 kV or higher) to avoid electron scattering in the resist. In this work, we attempt to optimise an alternative recipe with less expensive process steps using conventional EBL resist and a 30 kV EBL tool available at London Centre for Nanotechnology cleanroom. To develop a multilayer resist process, we first attempt a PMMA/HSQ bilayer where the HSQ layer is intended to be the hard mask.

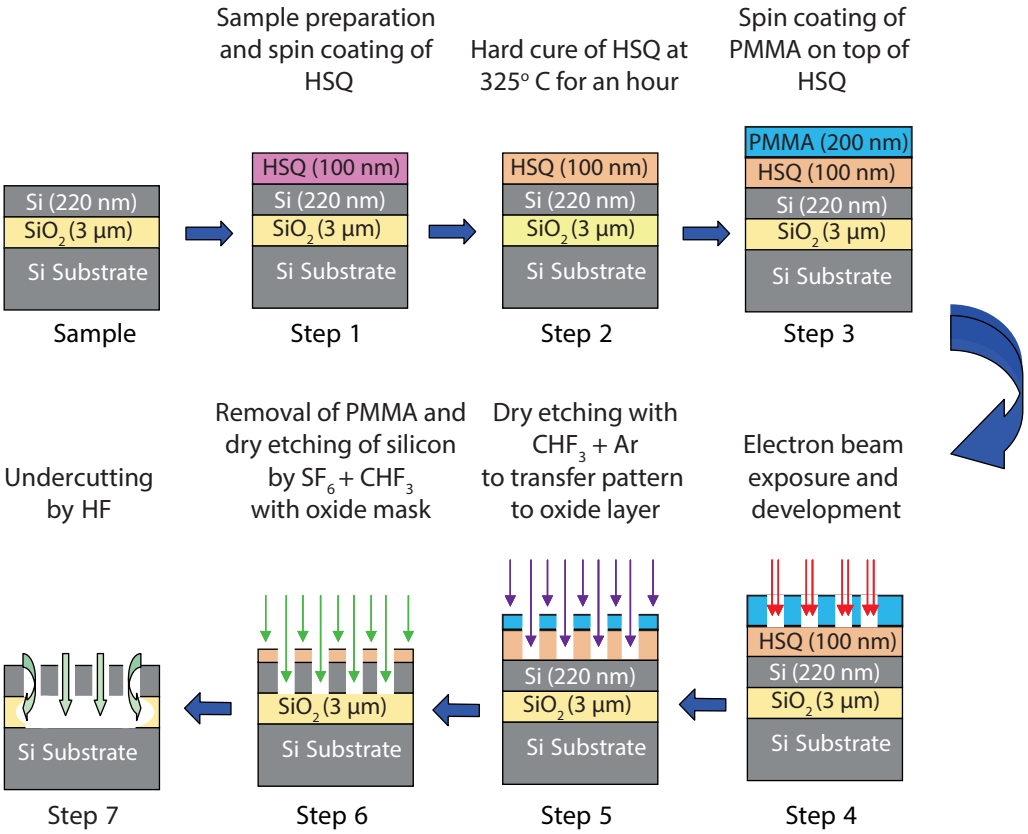

Figure 5.9: Process steps for fabricating PhC cavity with multilayer (PMMA/HSQ) resist

The HSQ layer, when thermally cured, converts to a form of etch resistant silicon oxide and can act as a hard mask [287]. In this bilayer resist process, a design is patterned on the high resolution PMMA using a 30 kV EBL and then the pattern is transferred to a HSQ (hydrogen silsesquioxane) layer through dry etch. Finally, the pattern from the HSQ hard mask is etched to silicon using an additional RIE step. The rest of the process steps are similar to the single layer process described in Section 5.7. The fabrication steps for this bilayer method are illustrated in Figure 5.9. To develop a working recipe for this novel process, each step was carefully adjusted. The process optimisation steps are discussed in the following sections.

5.5.1 Pattern transfer with E-beam lithography

Typical EBL systems use electron beams with energy of 10 to 100 kV for patterning. The wavelength of such electrons is so small (e.g. $\lambda \approx 8$ pm for 25 kV) that diffraction is negligible and does not limit the lithographic resolution. The resolution is mainly defined by the electron optics of the system and the scattering of the electrons in the resist material. The scattering of electrons in the resist or in the substrate broadens

the e-beam and may expose unintended areas. During the exposure process two types of electron scattering takes place — forward scattering and backward scattering. Forward scattering events (FSE) are inelastic where electrons are deflected by relatively small angles (blue arrows in Figure 5.10a). FSEs cause small beam broadening but are mainly responsible for the desired exposure. On the other hand, backscattering events (BSEs) take place when electrons elastically collide with heavier or substrate atoms. Backscattered electrons are deflected by large angles (orange arrow in Figure 5.10a) and cause unintentional exposure when return back through the resist. This phenomenon of pattern distortion due to electron scattering is known as the proximity effect [223, 283, 288]. In Figure 5.10a, scattering phenomena causing the proximity effect are shown schematically. In practical EBL systems, the proximity effect is the most critical issue that limits the efficient patterning of nanoscale features. The severity

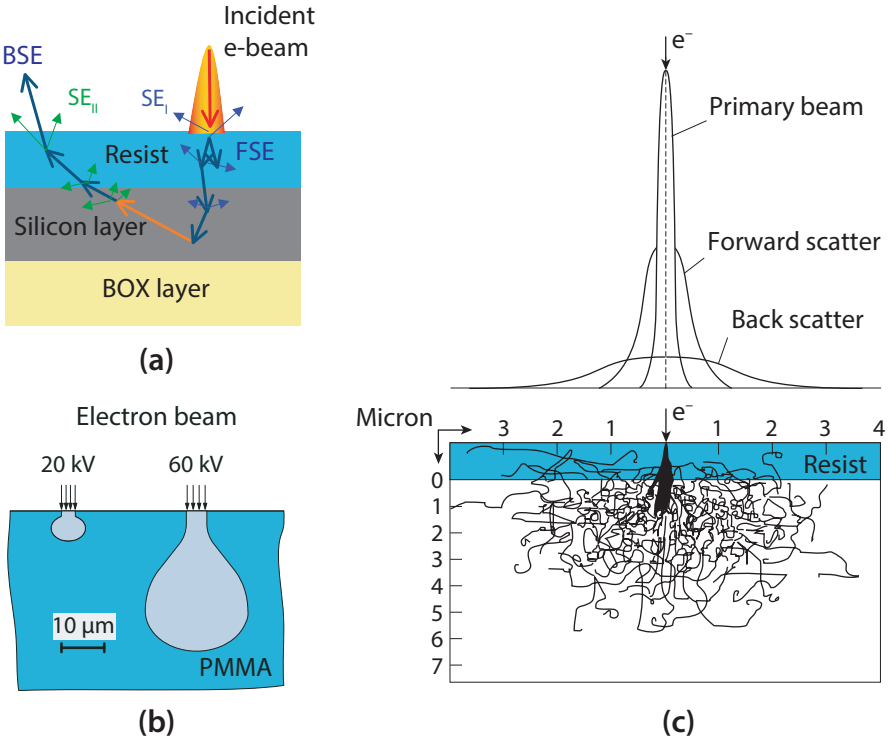

Figure 5.10: Proximity effect: (a) A schematic of electron scattering during e-beam exposure. The forward scattering event (FSE) and backscattering event (BSE) which cause exposure of resist and generation of secondary electrons are shown in the schematic. (b) The effect of acceleration voltage on the electron scattering or proximity error is shown in a schematic, image adapted from [283]. (c) Monte Carlo simulation of electron trajectories during an EBL exposure. The upper curve indicates the forward- and backscattered components of the beam, image reproduced from [223]

of the proximity effect depends on the type and thickness of the resist, the initial e-beam energy and the substrate material. Ideally, a thin layer of resist and low energy electrons would reduce the chance of electron scattering and provide high resolution patterning (Figure 5.10b). However, a thick layer of resist is necessary for pattern transfer through etching. For thick resists, high energy e-beam and/or proximity error correction (PEC) schemes are required. To implement PEC schemes, electron trajectories during e-beam exposure are usually simulated for certain exposure parameters and resist type (Figure 5.10c). Once the the scattering effects are estimated, an error correction is applied either by modulating the exposure dose or by adjusting the pattern shapes.

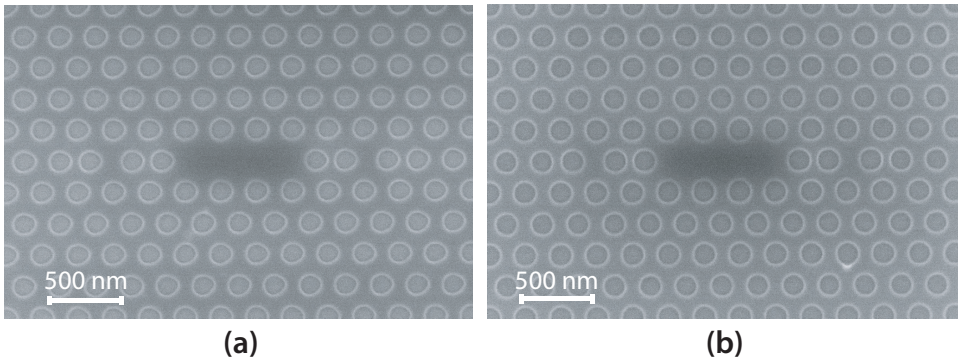

Figure 5.11: Proximity error correction (PEC) (a) pattern in PMMA without PEC, (b) pattern in PMMA after/with PEC

In our process, we use a 30 kV e-beam for patterning the PhC designs in PMMA. We have tried different apertures (10, 20 and 30 μm) and run dose tests for each of them. For the 30 kV e-beam, best results are obtained with 10 μm aperture and an area dose around 360 μC/cm^2. However, when we implemented PhC patterns without using any PEC scheme, noticeable distortions appear in the exposed patterns. Careful observation reveals that air-holes are not perfectly circular in PMMA, as shown in Figure 5.11(a). To address this issue, we have implemented a dose modulation based PEC scheme using the NanoPECS Proximity Effect Correction Software, available on our RAITH EBL system. Figure 5.11(b) shows that the pattern exposed in PMMA with PEC have improved considerably and no significant distortions are observed in the circular shapes.

5.5.2 Process with PMMA/HSQ bilayer resist

Due to its special material properties, the H-Si bonds in HSQ break and the ratio of Si-O increases when HSQ is treated with sufficient temperature (above 300°C) [287]. This makes the thermally cured HSQ similar to SiO_2. Thus, for transferring pattern to the HSQ layer, we started with an oxide etch recipe and optimised it for HSQ etch with PMMA etch mask. The optimised recipe for the HSQ etch is provided in Table 5.2. We have used Oxford Instrument's Plasma Technology NGP80 RIE system for all dry etch steps in our process.

Table 5.2: Optimized RIE recipe for pattern transfer from PMMA to hard mask (HSQ)

Gas Composition	RF Power	DC Bias	Chamber Pressure	HSQ Etch rate
$CHF_3 - 25$ sccm Ar -25 sccm	150 W	537 V	8 mTorr	$\sim$ 15 nm/min

The second etch step is the most critical one, as the pattern is finally transferred from the HSQ hard mask to silicon in this step. To implement efficient PhC devices, we need a highly anisotropic silicon etch because the air-hole sidewalls should ideally be vertical. If the sidewall profiles are not vertical then we would have conical holes instead of ideal cylindrical ones. Non-vertical/conical air holes reduce the PhC mirror reflectivity and cavity quality factor significantly. But a highly anisotropic silicon etch is quite challenging with a simple RIE system. Silicon etch needs SF_6 gas, which vigorously attacks most of mask materials. So, it provides poor surface quality and etches targets isotropically [289]. To tackle this issue, fluorinated/fluorocarbon plasmas are often introduced. There are also other approaches (e.g. inductively coupled plasma (ICP) etching, ion beam etching) and etch chemistries for anisotropic silicon etch [290], however, most of them are either expensive or use highly corrosive and toxic gases. In contrast, the fluorine gases are safer, less corrosive and can provide anisotropic etch profile with good surface quality [289, 291, 292]. Hence, we have used fluorine based chemistry (mixture of CHF_3 and SF_6 gases) for reactive ion etching of silicon. F and CF_2 in fluorocarbon plasmas behaves as an etching agent and the source of polymer deposition, respectively. The polymer deposition on the sidewalls makes the horizontal etch rate slower than the vertical one in the RIE process, which

give rise to the anisotropic etch profiles [292].

Table 5.3: Test recipes for silicon etch with HSQ mask

	Parameter values		
Parameters	Recipe - 1	Recipe - 2	Recipe - 3
RF power	27 W	27 W	150 W
DC bias	156 V	171 V	528 V
Pressure	15 mTorr	10 mTorr	10 mTorr
CHF_3 flow	37.5 sccm	58.33 sccm	50 sccm
SF_6 flow	25 sccm	25 sccm	15 sccm
Temperature	20°C	–	–
Comments	selectivity - good surface - rough anisotropy - moderate	selectivity - good surface - good anisotropy - poor	selectivity - poor surface - good anisotropy - good

We start with the recipe shown in Table 5.1, Section 5.4 and then adjust the etch parameters for the Oxford Instrument NGP80 RIE system. The amount of gas flow, chamber pressure, RF power are the most critical parameters which have to be adjusted carefully to obtain the desired etch profile. We have carried out test etches with varying these parameters to find out optimum parameter values. Table 5.3 and Figure 5.12 show the recipes and results of three test-examples. From the tests, it is observed that the HSQ mask selectivity is good for a lower RF power. We managed to etch through the top silicon layer of our SOI chips with low power recipes. But the anisotropy is found poor for the low RF power range (< 100 W) and the sidewalls are not vertical. Using CHF_3 gas in the range of 60% - 75% of the total flow seems to provide the best profile for a certain RF power and chamber pressure. Figure 5.12a & b show results of low power recipes 1 and 2, respectively. We have found that modifying the gas flows at low power does not enhance the anisotropy noticeably, however, surface quality can be improved. Better anisotropy is obtained by increasing the RF power, but at the cost of degraded selectivity of the HSQ mask. For the hard mask, we initially used ~ 100 nm thick, spin coated HSQ layer. When the RF power is increased to

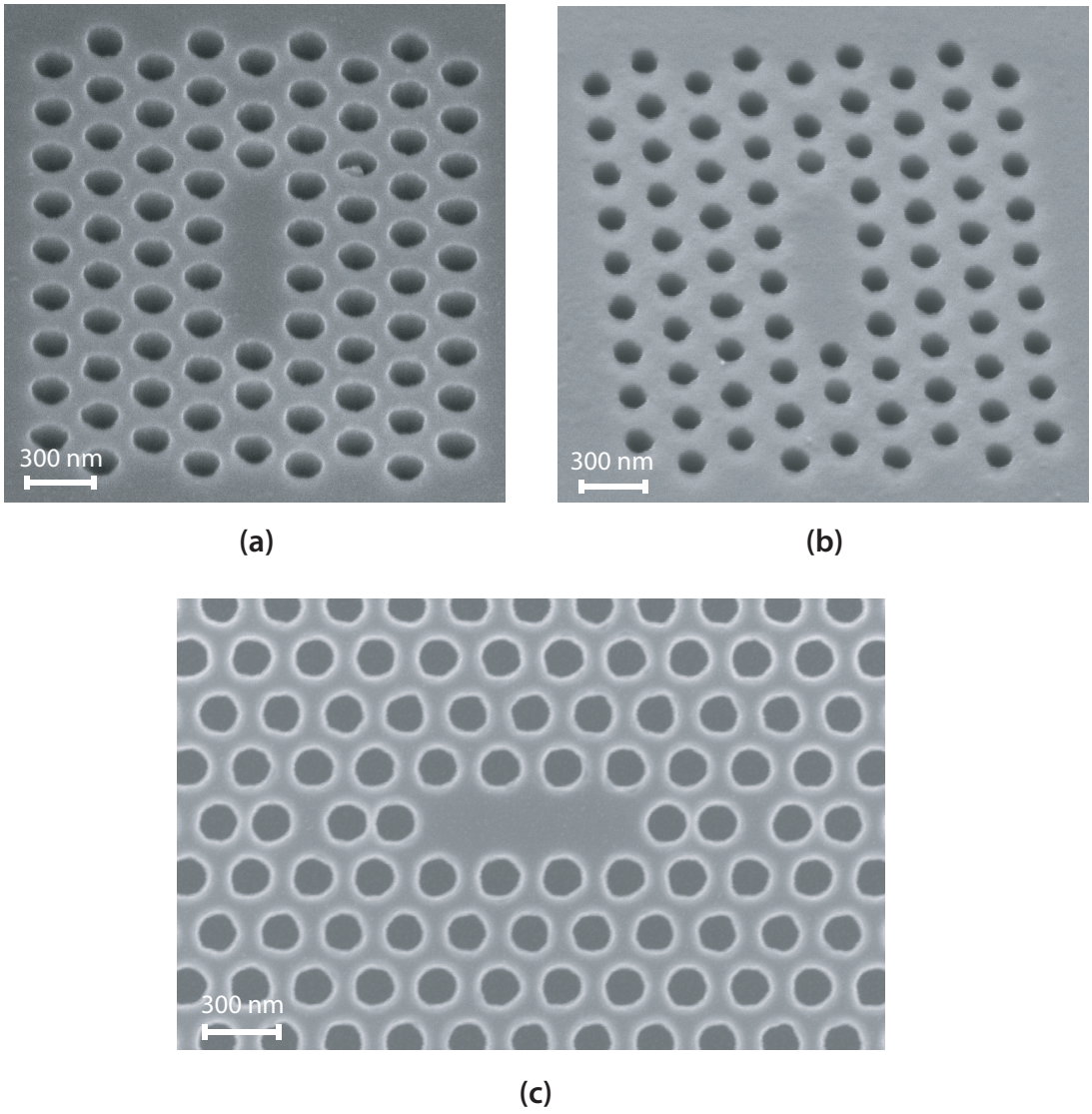

Figure 5.12: Silicon etch optimisation: SEM image of an etch profile (a) using recipe-1 (36° view), (b) using recipe-2 (36° view) and (c) using recipe-3 (top view)

150 W or above, the etch profile becomes anisotropic but the relative etch rate for the mask layer almost doubled compared to the low RF power cases. So, it turns out that $\sim$ 100 nm HSQ thickness is not enough to etch through the 220 nm top silicon layer of the SOI substrate. Result of an etch with an RF power of 150 W (recipe-3 in Table 5.3) is shown in Figure 5.12c. A top SEM view shows that the hole sizes become larger for the high RF power etch as the hard mask layer completely etched away. The ideal solution for this issue would be increasing the thickness of the HSQ layer. Commercially available resists from Dow Corning® comes as 2%, 4% and 6% solution of hydrogen silsesquioxane (HSQ) resin in a carrier solvent of methylisobutyl- ketone (MIBK) [293]. According to the data sheet, the 6% HSQ solution can provide up to a

spin-on film thickness of 180 nm [293]. But we have found that spin coating thicker (> 120 nm) HSQ films is difficult and the spin-on films becomes non-uniform. This implies that thicker HSQ films are not suitable for using as a hard mask and we need additional measures to implement the anisotropic etch.

5.5.3 Process with PMMA/Metal/HSQ multilayer resist

Metals such as aluminium, chromium etc. are robust (i.e. highly selective) against fluorinated plasma etches [294, 295]. For example, a 100 nm thick Al film as a mask is selective enough to etch several hundred microns deep into silicon [296]. But metal hard masks alone are not suitable for our process as the pattern transfer to metal films from PMMA is not possible with plasma etches. In this section, we explore the potential of a very thin ($\lesssim 10$ nm) metal layer along with the HSQ hard mask to tackle the reduced selectivity in case of high RF power etches. In addition, we have also used a thicker ($\gtrsim 30$ nm) metal mask to further investigate and optimise the silicon etch by fabricating nanopillars.

Two optimised recipes are provided in Table 5.4, and examples of fabricated nanopillars with each recipe are shown in Figure 5.13a & b, respectively. We managed to etch ~ 900 nm tall nanopillars with ~ 40 nm chromium mask. Pattern is transferred from PMMA to the metal mask layer by a lift-off process. Nanopillar structures clearly reveals the anisotropic etch profiles. The irregularity in nanopillar structures comes from the lack of uniformity in the chromium film and imperfection in the lift-off process. Figure 5.13b shows that straight pillars (diameter ~ 150 nm) and negligible undercuts are obtained using recipe-2 even with imperfect etch mask. Thus, we choose recipe-2 as the optimum one for anisotropic silicon etch in our fabrication process.

Once the optimum silicon etch process is selected, we start exploring the potential

Table 5.4: Optimisation of silicon etch recipes

	Gas flow	RF Power	DC Bias	Pressure	Si Etch rate
Recipe-1	$CHF_3 - 50$ sccm $SF_6 - 15$ sccm	150 W	528 V	10 mTorr	~ 50 nm/min
Recipe-2	$CHF_3 - 58$ sccm $SF_6 - 25$ sccm	150 W	542 V	10 mTorr	~ 55 nm/min

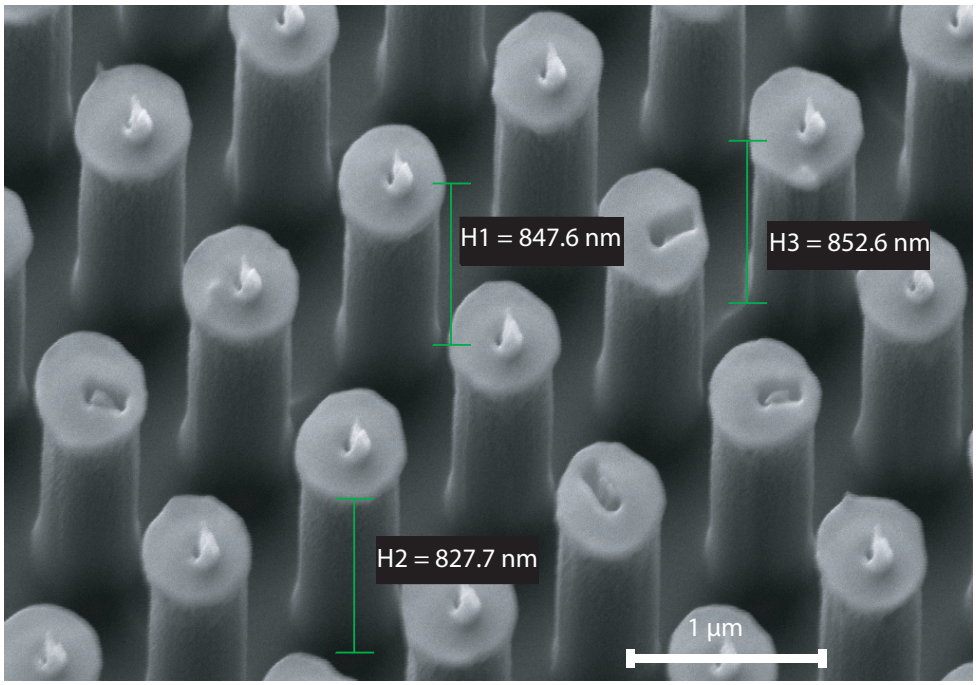

(a)

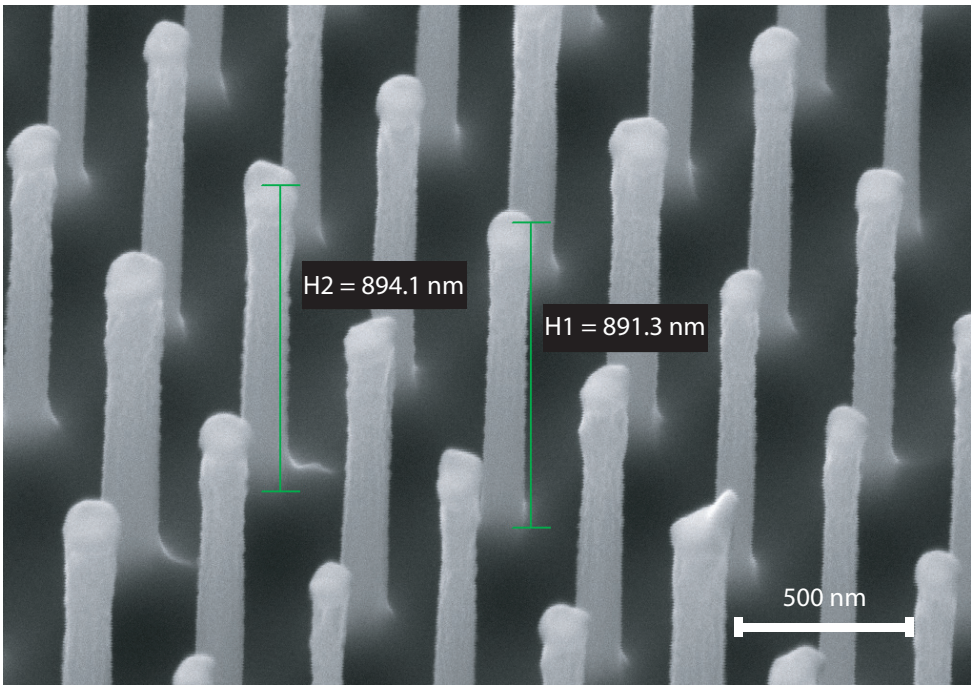

(b)

Figure 5.13: Fabrication of nanopillars to investigate the etch profile of the optimised recipe: Nanopillars of (a) diameter $\sim$ 400 nm and (b) $\sim$ 150 nm are fabricated using $\sim$ 40 nm chromium mask with recipe -1 and 2, respectively from Table 5.4

.

of a PMMA/Metal/HSQ multilayer resist. We choose aluminium for the intermediate metal layer as the uniform deposition and removal of chromium are found difficult. In

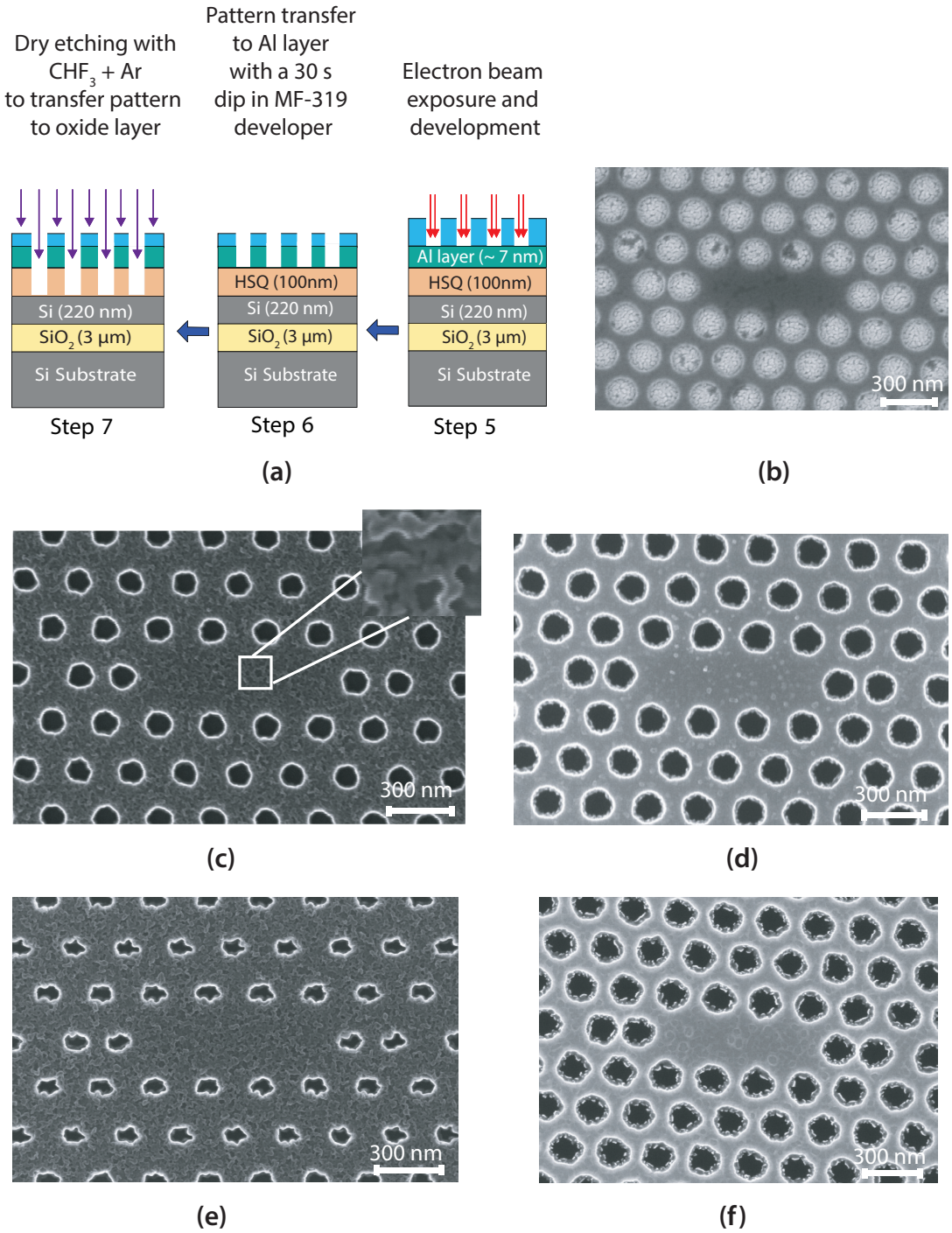

Figure 5.14: Fabrication of PhC cavity with multilayer (PMMA/Al/HSQ) resist: (a) Additional steps in PhC fabrication process when an intermediate Al layer ($\sim$ 7 nm) is added between PMMA and HSQ to improve etch selectivity. (b) An SEM image of patterns in PMMA. Grains of Al deposited on HSQ can be seen through the holes. (c) An SEM image of the transferred pattern in the Al/HSQ hard mask where Al thickness is $\sim$ 7 nm. Inset shows large Al grains formed during the deposition. (d) The image after the silicon etch and residue resist removal step. SEM images of a pattern (e) transferred to a $\sim$ 14 nm thick Al layer and (f) after silicon etch & final process step

this multilayer process, a thin ($\sim$ 7 nm) aluminium layer is sandwiched between PMMA and HSQ layers to improve the etch selectivity of the multilayer resist. Due to the addition of the Al layer, the fabrication recipe needs few extra process steps compared to the case of PMMA/HSQ resist process (see Figure 5.9). Additional steps required in PMMA/Al/HSQ multilayer resist technique are shown schematically in Figure 5.14a. We have used an Edwards A306 Box Evaporator tool available in the LCN cleanroom for thermal deposition of aluminium. The EBL resist (PMMA) is then spin coated on the Al layer. Figure 5.14b shows an SEM image after the EBL patterning and PMMA development; the trace of Al grains formed during the deposition can be clearly seen through the holes. The pattern is transferred to the Al layer with a $\sim$ 30 s dip of sample in MICROPOSIT MF-319 developer. MF-319 developer is an alkaline solution (2.45% Tetramethylammonium hydroxide in water) which strongly attacks metal (Al) without any significant reaction with polymer (PMMA). So, a quick dip in MF-319 selectively removes Al from the exposed area. Figure 5.14c & d show SEM images after the pattern transfers in HSQ and silicon, respectively. The SEM image of the pattern in Al/HSQ hard mask also reveals Al film quality (Figure 5.14c). We observe rough surface texture and hole edges in Al film due to the presence of Al nanograins (Inset, Figure 5.14c). The consequence of this nonuniform/grainy Al film becomes clearly visible when pattern is transferred to the substrate through silicon etch. We observe quite rough surface and hole edges in silicon (see Figure 5.14d), as any irregularity in the hard mask is intensified and transferred to the substrate during the etch step. We also investigate the effect of a thicker Al layer ($\sim$ 14 nm) in PMMA/Al/HSQ resist. SEM images of a pattern transferred in Al/HSQ hard mask and the silicon layer are shown in Figure 5.14e & f, respectively. These images clearly show that a thicker Al layer significantly worsen the quality of pattern transfer.

To investigate the post-process surface quality more carefully, we have taken SEM images of the tilted (36° view) sample. The sample is patterned with ($\sim$ 7 nm) Al layer. Images of the cavity region, a section of the PhC structure and an area without any pattern are shown in Figure 5.15a, b & c, respectively. The damage in the cavity surface can be seen in the SEM image (Figure 5.15a). The severity of the damage due to nonuniform Al layer becomes clear in the image of the non-patterned area (Figure 5.15b). This suggests that the deposition of Al film ($\sim$ 10 nm) using a thermal

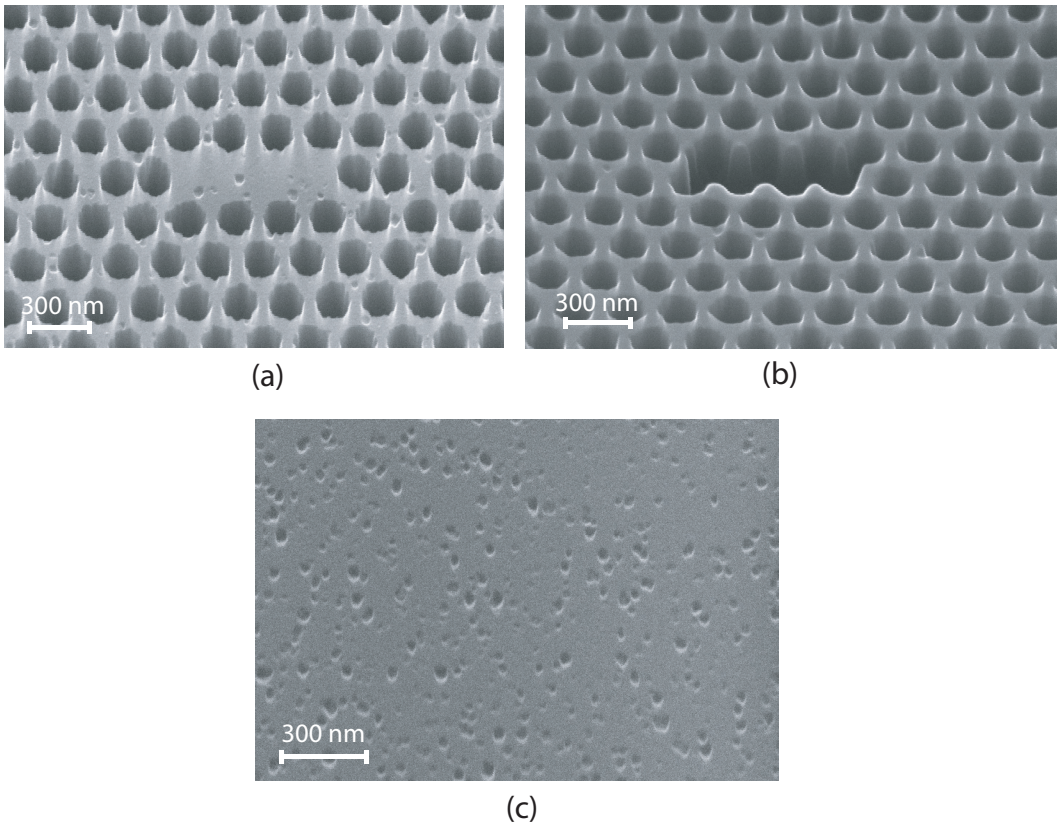

Figure 5.15: SEM images (36° view) of silicon surface after pattern transfer using the PMMA/Al/HSQ multilayer resist process: SEM images of (a) the cavity region, (b) PhC region where a section of the membrane is milled deliberately using FIB tool and (c) a region without any pattern

evaporator is not efficient enough for using in nanolithographic purposes. Although the incorporation of the thin Al layer provides enough selectivity to etch anisotropically through the silicon membrane, the poor surface quality and hole shapes obtained from the PMMA/Al/HSQ multilayer technique is not suitable for high-Q PhC cavity fabrication.

5.5.4 Process with PMMA/Oxide (PECVD) bilayer resist

As our attempt to improve the etch selectivity of the HSQ hard mask by adding a thin metal layer turned out inefficient for pattern transfer, we start looking for a suitable hard mask. Since we already have an optimised oxide etch recipe, PECVD grown silicon dioxide can be an effective alternative to the HSQ hard mask. Therefore, we start to grow and investigate silicon dioxide layers on our SOI substrate using the STS PECVD system. Growing a thin (< 400 nm) silicon dioxide with good quality/uniformity is difficult. However, after several trials, we have managed to adjust the process parameters and time to grow a ~ 300 nm PECVD oxide film with reasonable uniformity. It is found that the HSQ etch recipe (Table 5.2) with slightly increased chamber pressure works efficiently for etching the PECVD oxide, as shown in Table 5.5. One issue we encounter with this recipe is that the usual ~ 200 nm PMMA thickness is not enough for etching through ~ 300 nm PECVD oxide layer. To address this, we carefully increase the PMMA thickness. Test etches reveal that a PMMA thickness of ~ 230 nm

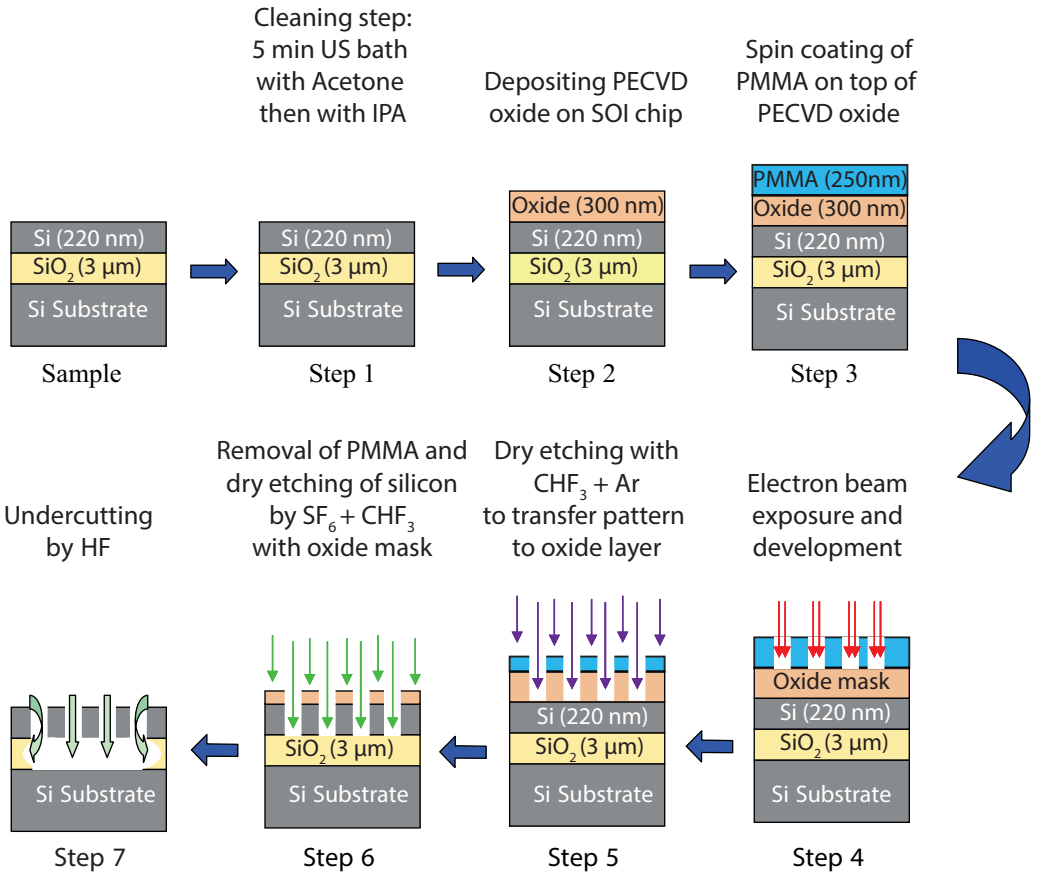

Figure 5.16: Process steps for fabricating PhC cavity with multilayer (PMMA/Oxide (PECVD)) resist

Table 5.5: Optimized RIE recipe for pattern transfer from PMMA to PECVD Oxide mask

Gas Composition	RF Power	DC Bias	Chamber Pressure	Oxide Etch rate
$CHF_3 - 25$ sccm Ar -25 sccm	150 W	537 V	30 mTorr	$\sim$ 15 nm/min

is at least required to etch efficiently through the oxide layer. The complete fabrication recipe with the PMMA/Oxide (PECVD) bilayer resist is shown schematically in Figure 5.16.

We have patterned and etched different test structures to evaluate the effectiveness of the PMMA/Oxide (PECVD) bilayer resist process. Figure 5.17 shows few test structures realised with this process. To check the etch profile and sidewalls we first pattern

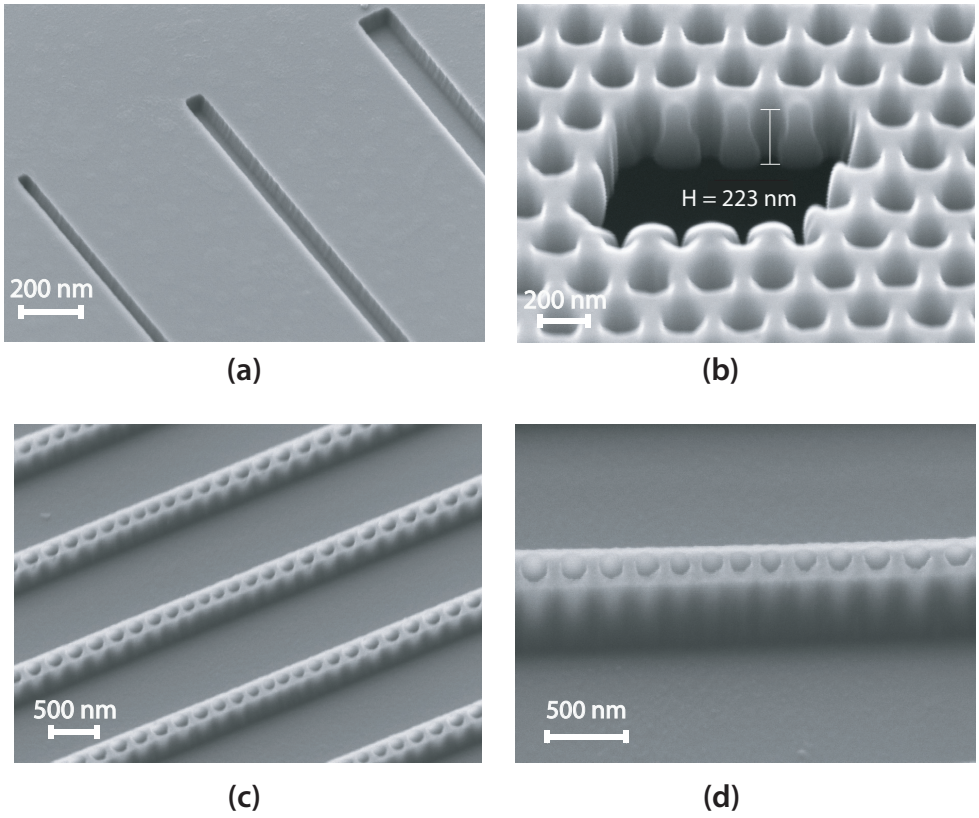

Figure 5.17: Etch profile of test structures realised with the PMMA/Oxide (PECVD) bilayer resist process: SEM images (tilted view) of (a) parallel trenches etched into silicon, (b) a PhC section on a suspended membrane which is cut with a Ga FIB tool. A non-optimum milling current and direction has caused damage/rounding effect around the milled section, however, the depth ($\sim$ 220 nm) information of the RIE etch is clearly revealed. (c) 1D PhC structures with steep (anisotropic etch profile) and smooth sidewalls, and (d) zoomed image of a 1D PhC.

some parallel trenches and then etch them into a silicon sample. Near vertical sidewalls for the trench structures can be observed from an SEM image with tilted view, as shown in Figure 5.17a. In Figure 5.17b, a 2D PhC section has been investigated with Ga FIB milling. The PhC section was initially etched into the 220 nm device layer of an SOI sample. Due to a non-optimum milling current and direction, structural damage/rounding effect took place around the milled section/edges. However, the depth ($\sim$ 220 nm) information of the RIE etch (through the device layer) is clearly revealed. To examine the etched sidewall profiles clearly, we realised 1D PhC structures with the PMMA/Oxide (PECVD) bilayer resist process. Figure 5.17c shows an SEM image (tilted view) of fabricated 1D PhC structures and Figure 5.17d shows the zoomed in view of a 1D PhC structure. SEM images of these 1D PhC structures reveal smooth and near vertical etch profile of the outer sidewalls.

From the test structures in Figure 5.17, we find that the optimised PMMA/Oxide (PECVD) bilayer resist process provides high etch anisotropy and a smooth sidewall for long rectangular shapes. However, the issue with edge roughness and irregularity in hole shapes has not improved to the desired level. We could see that the hole edges (shapes) are still rough (irregular) in both PECVD oxide mask and silicon membrane, as shown in Figure 5.18c and e, respectively. This was unexpected as the PMMA/Oxide (PECVD) bilayer resist technique does not involve any metal layer or obvious source of defects. Moreover, each layer is tested to provide sufficient etch selectivity and anisotropy. When investigated carefully, an interesting source for this inefficient pattern transfer is identified. We have created our PhC cavity layouts with CleWin 5 — a commercial physical layout editor available at the LCN cleanroom. It turns out that these layout files are not fully compatible with RAITH lithography software. Using them as EBL masks, the system can only carry out patterning in the raster scanning mode (see Figure 5.18a). However, the concentric scanning mode (see Figure 5.18b) can be more effective for patterning circular/cylindrical features [297]. We address this issue by creating RAITH system compatible layout designs using MATLAB. When the concentric scanning mode is implemented, irregularity in the hole shape reduces significantly in transferred pattern both in oxide (Figure 5.18d) and silicon membrane (Figure 5.18f). In the SEM image of the oxide layer, we still see some traces of damage, crack like spots on the surface as shown in Figure 5.18d. This probably happens due

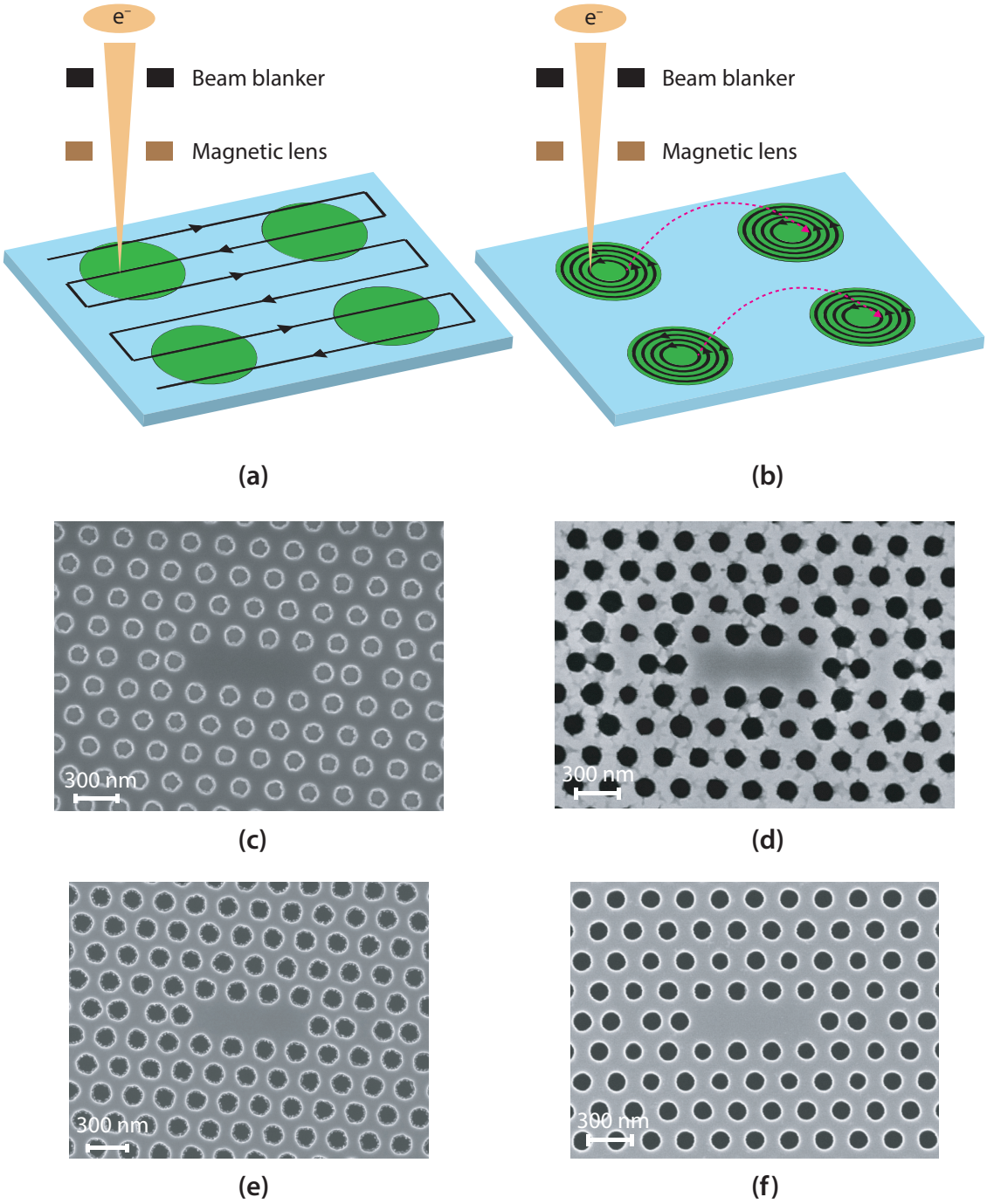

Figure 5.18: Effect of e-beam scanning mode on pattern transfer quality with EBL: Schematics of (a) raster and (b) concentric scanning mode available in RAITH150 Two EBL system. Transferred patterns in PECVD oxide with (c) raster and (d) concentric scan. Images of final devices in suspended silicon membrane - patterned with (e) raster and (f) concentric e-beam scanning mode

to long oxide etch time. Samples heat up when etch time is long and PMMA starts to flow at elevated ($\gtrsim$ 180°C) temperatures. Thus, pattern deformation and related damages become critical when the etch time is long. To circumvent this issue, we have

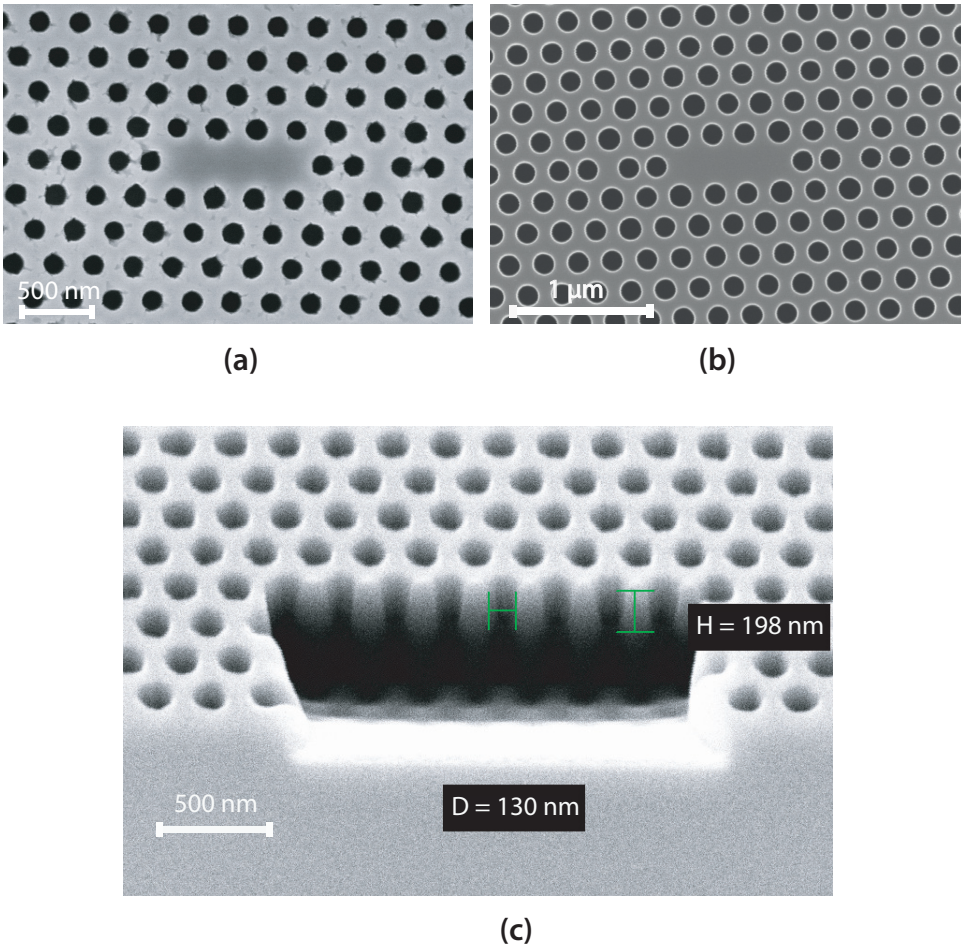

Figure 5.19: Pattern transfer with a cyclic etching of oxide hard mask: SEM images (top view) of patterns in (a) PECVD oxide and (b) silicon membrane. (c) An SEM image (tilted view) of a PhC section which is cut with the Ga FIB tool. The image clearly shows the anisotropic etch profile of holes in silicon

implemented a cyclic oxide etch process (cycles of 30 s etch and 2 minutes cooling) to transfer pattern to the PECVD oxide without any significant sample heating. With the cyclic etch technique, the surface damage issue in the hard mask (PECVD oxide) layer becomes negligible, as shown in Figure 5.19a. We do not see any noticeable surface damage and/or shape irregularity in the pattern transferred into the silicon membrane (see Figure 5.19b). Air holes with vertical sidewalls (i.e. anisotropic etch profile) are reinspected and reconfirmed by cutting a section in the PhC structure with the Ga FIB tool (see Figure 5.19c). Therefore, an optimised PMMA/oxide (PECVD) bilayer resist based recipe allows efficient pattern transfer and PhC cavity fabrication.

5.6 Fabrication of CBR devices with PMMA/Oxide (PECVD) bilayer resist

Similar to PhC cavities, CBR devices are ideally realised in suspended membranes. However, the circular trenches in standard CBR structures are only partially etched (discussed in Section 4.3.1). Due to this partial etch, it is not possible to make the undercut openings for releasing the suspended membrane within a single lithographic step. It needs an additional EBL patterning with alignment markers, followed by an

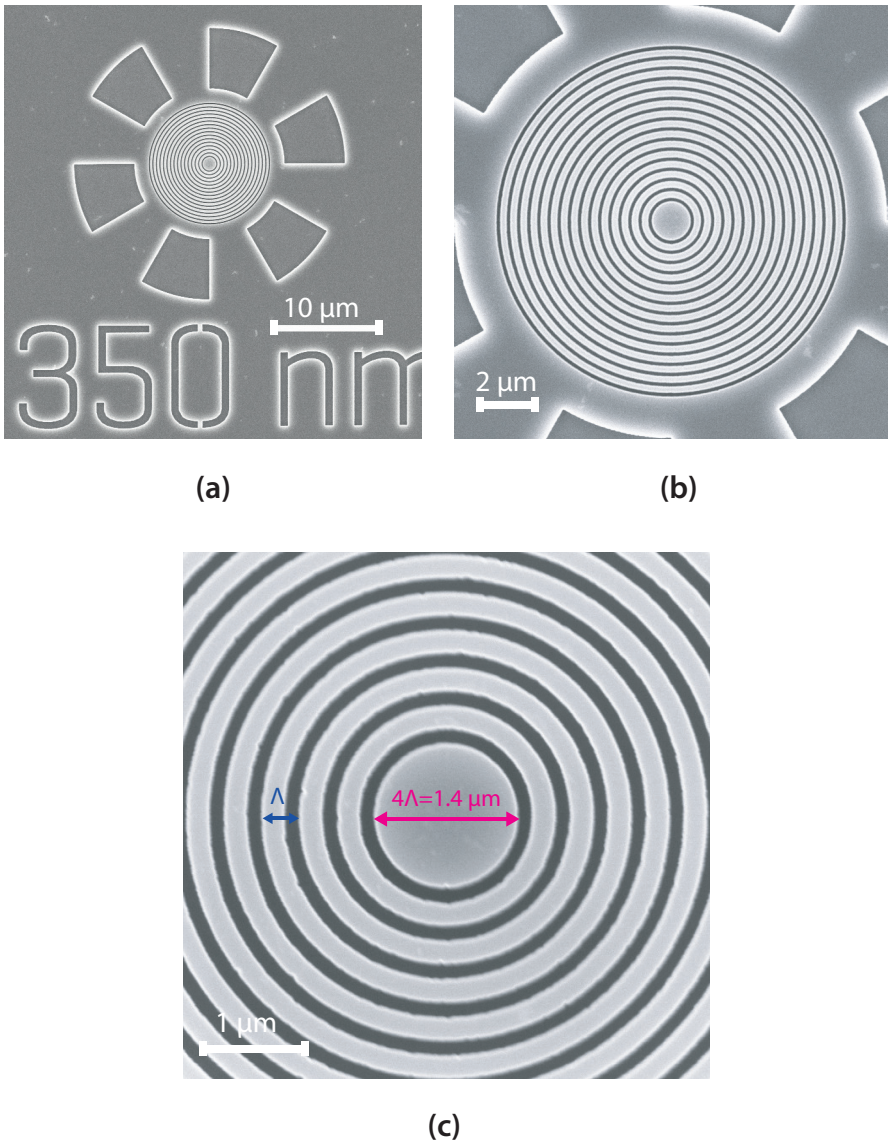

Figure 5.20: SEM images of Circular Bragg resonators (CBR): CBR devices are fabricated with PMMA/Oxide (PECVD) bilayer resist technique. SEM image (top view) shows (a) a complete device with identifying labels. A zoomed image of (b) the grating area and (c) disc resonator with grating period, $\Lambda = 350$ nm

RIE step to make the openings through the top device layer. This two step lithography becomes tedious with our bilayer resist process. Thus, in this work, we realise non-suspended structures (details in Section 4.3.2) as a first step to explore the potential of the CBR devices. With the optimised PMMA/Oxide(PECVD) bilayer resist technique, we efficiently fabricate non-suspended CBR structures with a single lithographic step. A trench depth of $d = 0.7t_{\mathrm{SOI}} \approx 160$ nm is achieved by adjusting etch time, and then confirmed by measuring the depth of large trenches etched deliberately around the device structure (see Figure 5.20a). Figure 5.20b and c show the zoomed SEM image of the gratings and device region, respectively.

5.7 Summary

In this chapter, we have discussed the fabrication processes of photonic devices under consideration. SiSIL devices were milled in a bulk silicon substrate using Ne-FIB tool. Photonic crystal cavities were realised with a fabrication recipe using a conventional EBL resist that can withstand plasma etch. We have also carefully optimised a unconventional, low-cost fabrication recipe using a bilayer (PMMA/Oxide (PECVD)) resist technique. The idea of bi/multilayer resist with oxide hard mask for PhC fabrication has been adopted from literature [287, 298–302]. However, in most cases, target substrates for realising PhC structures were III-V materials such as InP [287, 299–301], InGaAsP/InP [298], AlGaInP/GaInP [302] and GaAs [303] etc. Furthermore, the patterns were transferred to the targets substrates using specialised etch systems such as inductively coupled plasma reactive ion etching (ICP-RIE) [299, 302, 303], electron cyclotron resonance (ECR)-RIE [298], chemically assisted ion beam etching (CAIBE) [287, 300] etc. To the best of our knowledge, there has been no report of efficient fabrication of silicon PhC structures with lattice constants $\lesssim 300$ nm using a bilayer (PMMA/Oxide) resist and a conventional RIE system. With our bilayer resist (PMMA/Oxide (PECVD)) technique, we have efficiently fabricated Si PhC cavities and non-suspended CBR devices using a 30 kV EBL (RAITH150 Two) and a conventional RIE (Oxford Plasma Pro NGP80) systems. The optical measurement and/or characterisation of these devices are discussed in the following chapter.

Chapter 6

Optical measurement/characterisation of photonic devices

In this Chapter, we describe the optical experiments carried out on the different photonic nanostructures designed and fabricated to enhance photon emission/extraction and discuss the results of the measurements. We start with the photoluminescence (PL) measurement of SiSILs in order study their performance for the extraction of photons from ^{31}P $D^0X \rightarrow D^0$ transitions in silicon. The photonic cavities are then characterised with resonant-scattering measurements. The cross-polarisation setup used for the resonant-scattering measurement is described briefly before discussing the results of the cavity characterisations.

6.1 PL measurement of SiSILs

After milling the immersion lens structures with Ne-FIB, ~ 10 nm thermal oxide was grown and then etched with HF to treat amorphisation and surface damage, as described in Section 5.3. It was found that the SIL surfaces exhibit some roughness (few nanometres) in the SEM images even after the HF etch which is expected to cause additional strain on near-surface donors. This indicates that the repair step has not completely cured the surface damage. The sample used for SIL fabrication and PL measurement is a 500 µm thick, 6×10 mm chip of float-zone (FZ) silicon and has a phosphorus concentration of $\sim 10^{15}$ cm^{-3}.

PL measurements were carried out on the SIL structures fabricated on the silicon substrate. We carry out these experiments with the same PL measurement set-up (Figure 3.1) used for the case of bulk samples as discussed in Section 3.3. The re-

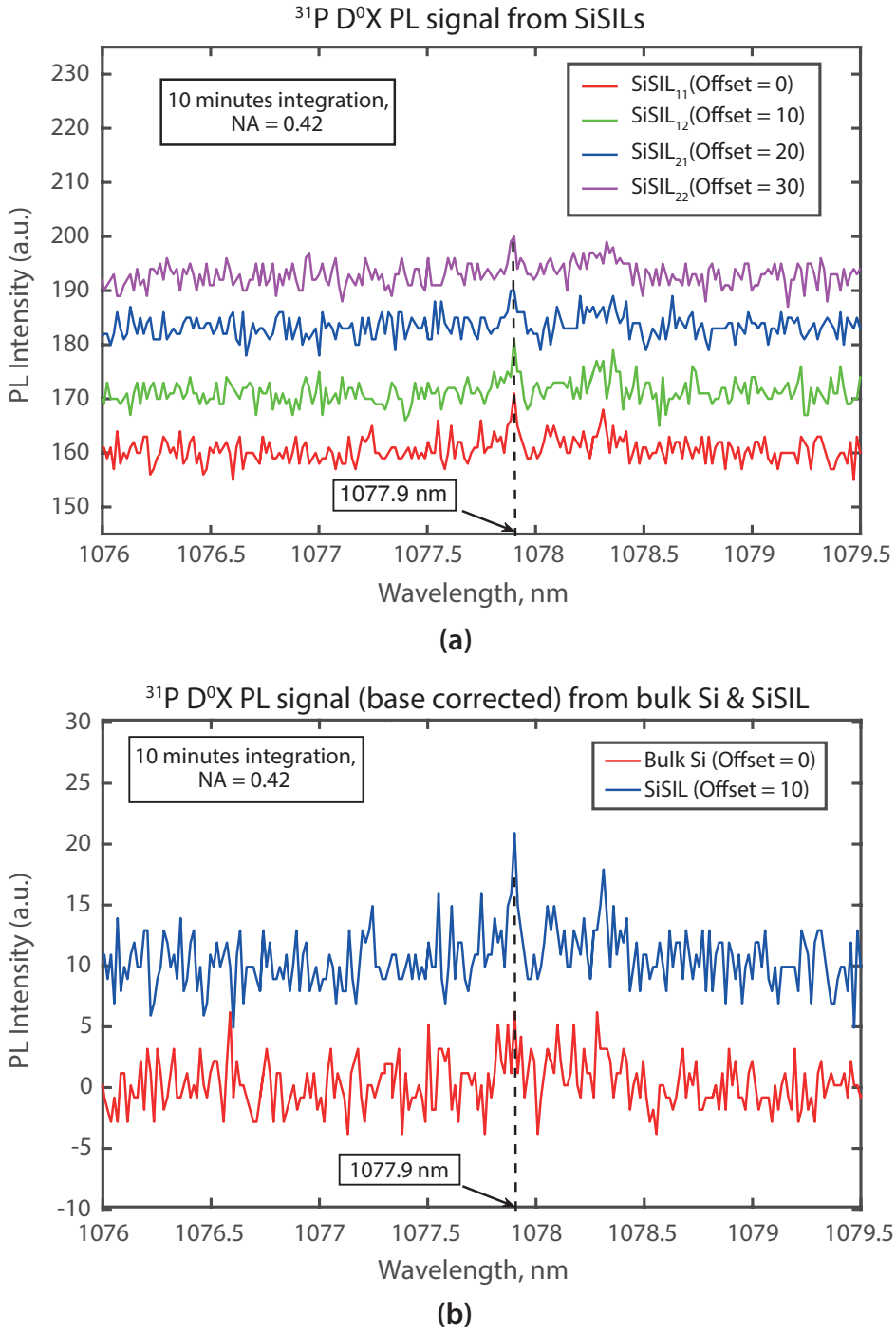

Figure 6.1: Detection of ^{31}P D^{0}X $\rightarrow$ D^0 transitions from SiSILs, (a) ^{31}P D^{0}X PL signal from SiSILs, (b) base-corrected ^{31}P D^{0}X PL signal from bulk Si and SiSIL. Each dataset from different measurements are shifted upwards by a certain value (Offset) in order to avoid overlapping plots

sults of the low temperature PL measurements on SiSILs are summarised in Figure 6.1. The PL measurement setup used is the same as that for bulk silicon, and the photon collection volume for SiSILs is also approximately same. So, in principle, the num-

ber of donors in the collection volume should be the same and the PL signal strength should be stronger than that from bulk Si due to better photon extraction with lenses. In contrast, measurements reveal much weaker PL signals from SiSILs. We get an observable signal from the ^{31}P $D^0X \rightarrow D^0$ transition only after 10 minutes integration, as shown in Figure 6.1(a). Strain split ^{31}P D^0X lines in the PL signals from SiSILs can be identified but the line at the longer wavelength ($\sim$ 1078.4 nm) is considerably broadened. This broadening is most probably the result of the additional strain from FIB milling related defects. To compare the effect of SILs on the detected signals, PL signals have also been collected from areas without lens structures. The PL data from areas far from the SILs contain a barely distinguishable trace of ^{31}P D^0X lines even with 10 minutes integration time. The reason for this loss of signal strength in non-milled areas is not clear yet. As the signal from no-SIL areas is weak, we apply base correction before comparing to the PL signals from SILs. Base corrected PL signals from SIL and no-SIL areas are plotted in Figure 6.1(b). Comparing the SIL and no-SIL PL signals clearly reveals that the photon counts have increased by a factor of 2 for the $\sim$ 1077.9 nm D^0X transition line by using the lenses. For our SIL structures, the collection efficiency is expected to be enhanced by around six times than the collection from bulk Si [304]. Thus, the observed increase in photon collection with lenses is less than the expected. One possible explanation can be a greater strain and/or damage in the SIL area which will suppress the ^{31}P D^0X emission stronger than in no-SIL areas. As a result, the collection of D^0X emission will be less than the expected even though the effective enhancement factor of SiSILs is large. Further investigation is required to confirm/quantify the reason for this loss of signal strength and the effect of annealing on the PL signals.

6.2 Cross-polarisation set-up for cavity characterisation

Photonic cavities such as photonic crystal cavities and circular Bragg resonators can be characterised using photoluminescence (PL) measurements of emitters inside the cavities and/or coupling of the cavity mediated photon emission to optical waveguides and near-field probes. However, PL is inefficient for cavity characterisation because of the

requirement of internal light sources in the cavity. The extraction of the quality factor (Q-factor) is also limited by the complicated cavity-emitter interaction and the resolution of the spectrometer used for PL measurements. Furthermore, the fabrication and coupling of waveguide structures, incorporation of the near-field probe and fiber taper are tedious and require special modifications of the measurement set-up. To overcome these issues, we use resonant-scattering (RS) for cavity characterisation. In RS, a probe beam is introduced to the cavity from free-space and the scattered light is collected with the same objective [305–308]. A pair of orthogonally oriented polarisers are used to distinguish scattering from minuscule optical structures from surface reflections and enables measurements of the intrinsic Q-factor and resonance wavelengths.

In an ideal cross-polarisation setup, the polarised light is focused on the sample with a high NA, polarisation preserving objective lens. The reflected light is is collected by a beam splitter and a cross-polarisation measurement is carried out using an analyser at the collection end. In Figure 6.2, a schematic depiction of the RS measurement using a cross-polarisation configuration is presented. In the cross-polarisation setup, the cavity axis maintains a 45° angle with both the polariser and the analyser, which

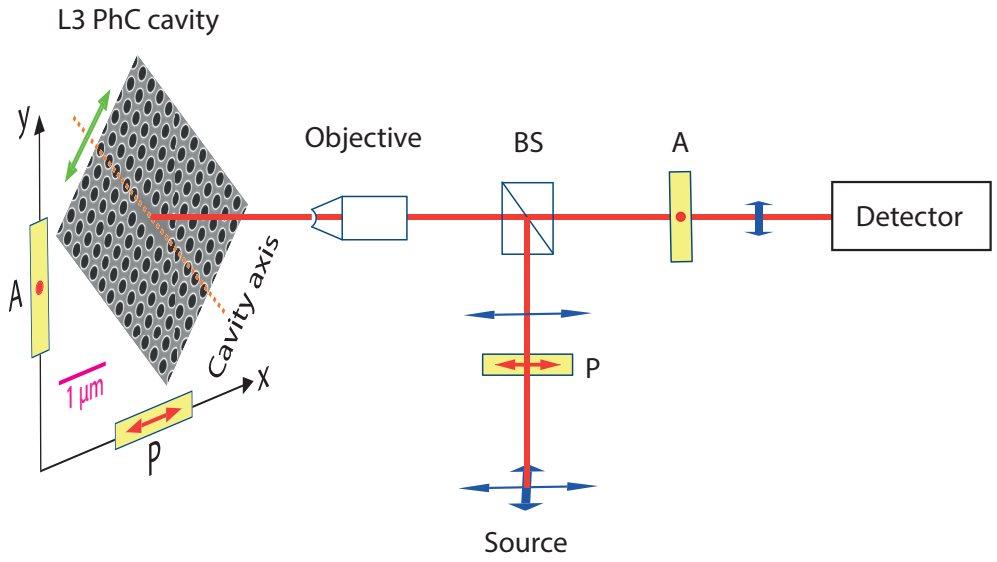

Figure 6.2: The resonant scattering technique with a cross-polarisation configuration: The sample orientation is adjusted so that the cavity axis maintains a 45° angle with both the polariser and the analyser to ensure maximum coupling. The orange dashed line through the cavity shows the L3 cavity axis and the green arrow indicates the polarisation of the fundamental cavity mode. Polariser (P) sends polarised light to the sample cavity and only the resonantly scattered light can obtain right polarisation to pass the analyser (A)

ensures maximum coupling. If we send non-resonant, x-polarised light on the sample, the reflected light from the cavity mainly preserves its initial x- polarisation and is filtered out by the y-polarised analyser at the collection end. When the incoming x-polarised light is on resonance, it interacts with the cavity mode and induces a net y-polarised component in the reflected light [305–308], which is picked by the analyser detected. Thus, the RS technique can reveal very weak optical responses from the cavity mode. We can find the resonant modes from the peak locations and Q-factors by fitting the cavity spectra to Lorentzian lineshapes.

We implement the experimental cross-polarisation setup for the cavity characterisation by incorporating a few modifications to our existing PL measurement setup (Figure 3.1). To realise the cross-polarisation configuration, we add three additional units: a broadband source, a pair of polarisers (LPVIS050-MP2) in orthogonal orientation and a spatial filtering unit. As our optical setup is modular, we can readily add/modify units and change back and forth from the PL to the cross-polarisation configurations by adding/removing few components and performing some optical realignment. The schematic of the cross-polarisation set-up is illustrated in Figure 6.3 where the major components are labeled with their model numbers from the manufacturers. The broadband source for the cavity characterisation should provide light with sufficient and uniform power for the whole wavelength range of interest. However, our wavelength range of interest, the near bandgap region of silicon, is quite unfavourable for both the detection and generation of light. So, it is very difficult to find an ideal light source in this wavelength regime. We pick a near infrared light emitting diode (M1050D1 LED on a Metal-Core Printed Circuit Board (MCPCB), Thorlabs) which can provide an output power of ~ 50 mW from 1050 nm to 1070 nm. According to the specification, the LED power decreases rapidly after 1070 nm and we get only $20-25\%$ of the peak power around 1080 nm. But considering the size, modularity and cost of the source, we find this M1050D1 LED is the most convenient broadband source available. In the source unit we also need a focussing/collimating lens with the broadband LED as the emission from the LED is highly diverging. The broadband emission has to be collimated in order to send it to the sample through the objective. The main function of cross-polarisation is implemented with two high extinction ratio, linear polarisers (LPVIS050-MP2) by adjusting them into an orthogonal orientation.

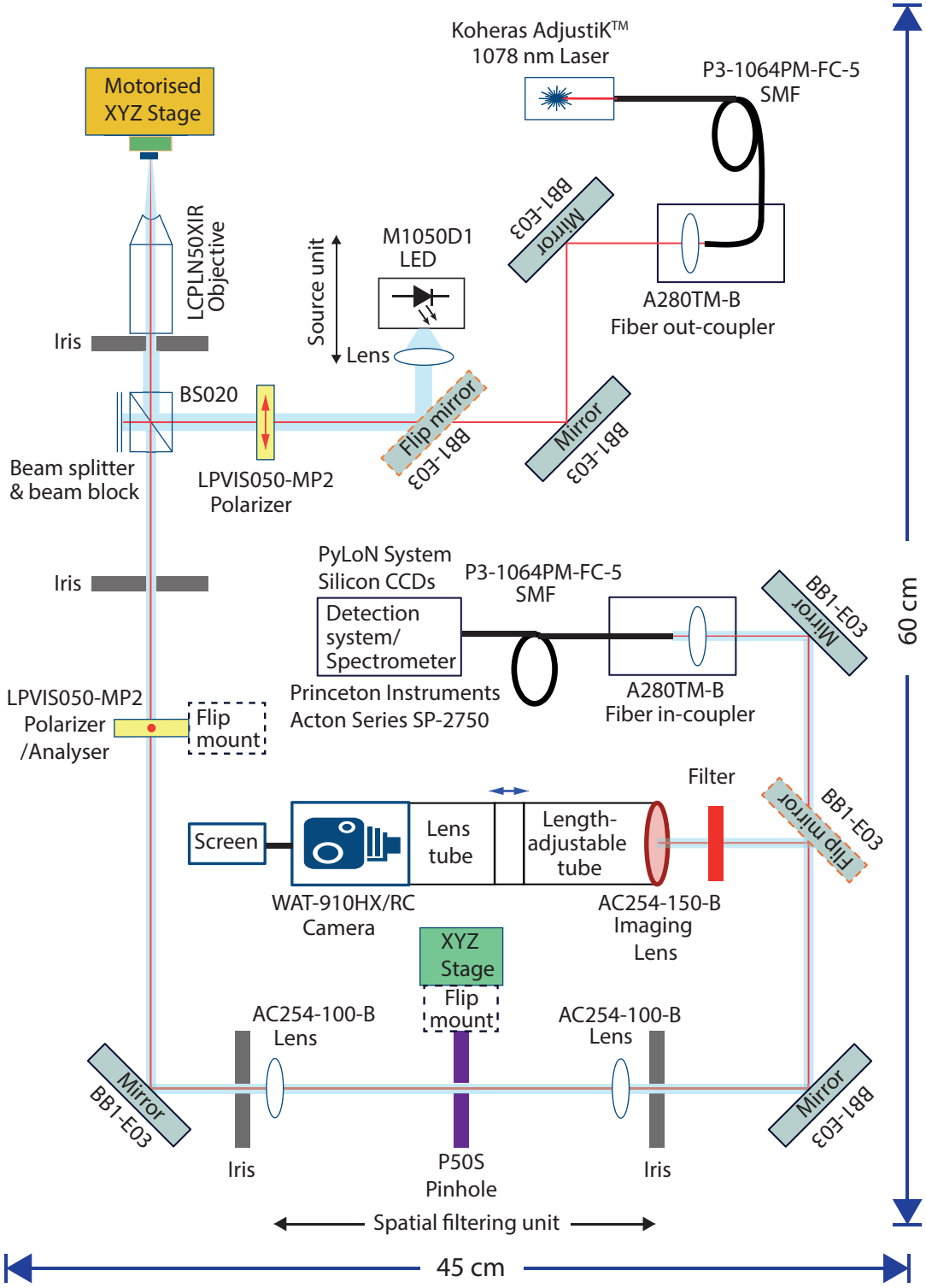

Figure 6.3: Schematic of cross-polarisation set-up for cavity characterisation

The first polariser is positioned before the beam-splitter in the excitation arm and the second one is in the collection arm after the beam-splitter, as shown in Figure 6.3. The second polariser is usually termed the 'analyser'. With careful adjustment of the polarisation axes, we regularly achieve a background suppression in the order of 10^5

to 10^6. The third unit incorporated in the cavity characterisation setup is the spatial filtering system implemented with a pair of achromatic doublet lenses (AC254-100-B) and a precision pinhole (P50S, with a diameter of 50 ± 3 µm), as shown in the schematic in Figure 6.3. Spatial filtering is a technique commonly used for reducing or eliminating the out-of-focus information and stray reflections from the optical beam under consideration and is useful for improved imaging resolution. The operation of the spatial filtering unit involves focussing of the light beam, then rejecting the unwanted part of the signal by placing a pinhole with an appropriate aperture on the

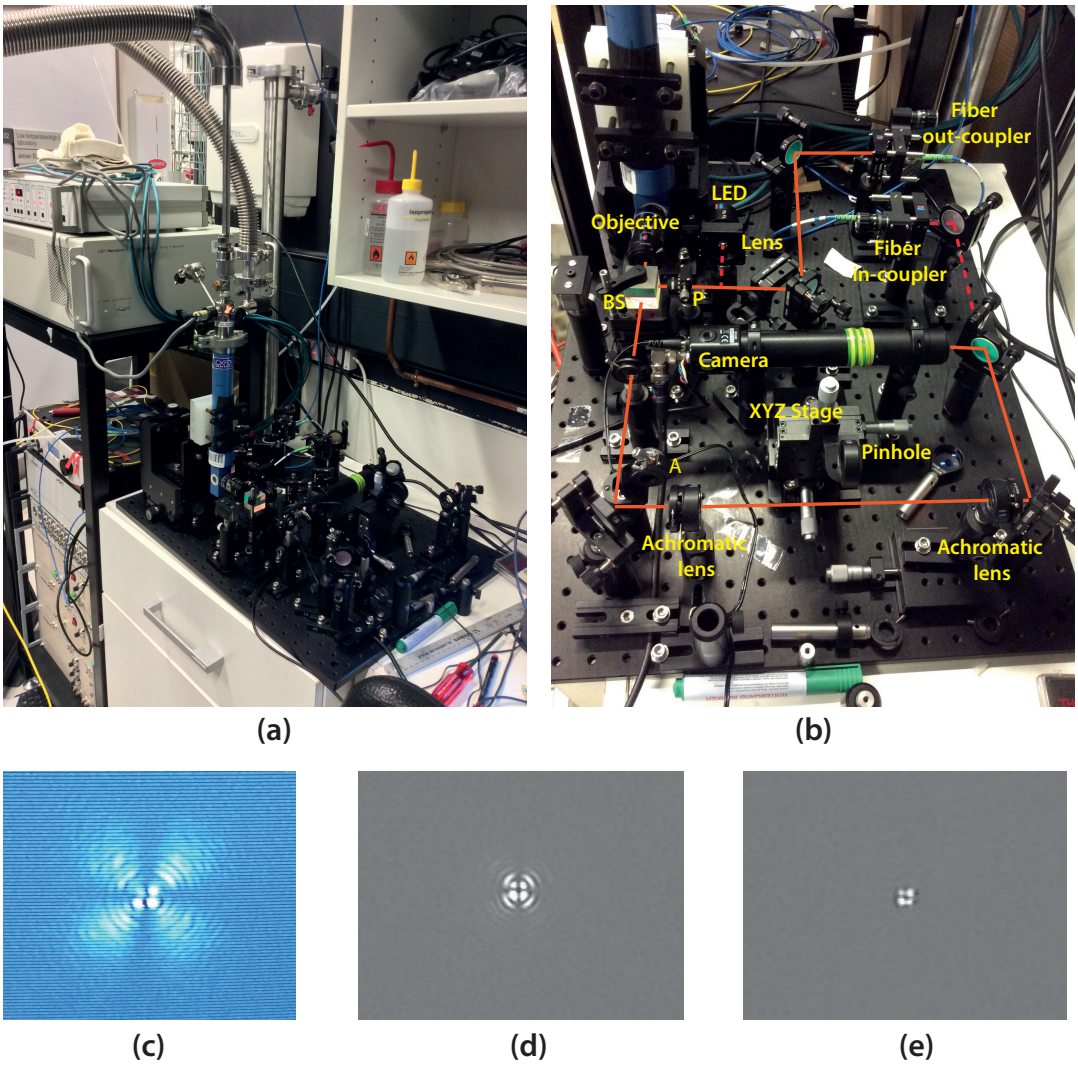

Figure 6.4: Experimental cross-polarisation set-up and imaging: cross-polarisation configuration with (a) the table top experimental setup with optical window, flow cryostat, (b) a zoomed view with labeled major components and beam paths. The mode image of the cross-polarised laser beam is captured. The lobe-pattern observed (c) on a screen, (d) with digital grabber and (e) after the implementation of spatial filtering.

central Gaussian spot at the focal point. The optimum pinhole aperture size is determined from the diffraction limited spot size of the focussed beam and usually estimated as $Pinhole\ Diameter = 1.5 * Beam\ spot\ size$. The beam spot size can be determined from the following relation — $Beam\ spot\ size = (1.27 * \lambda * f)/D$ where, λ, f and D are the wavelength of light, the focal length of the focussing lens and the input beam diameter, respectively. After the pinhole, another lens is used for defocussing and collimating the filtered beam. The experimental setup for cavity characterisation and examples of cross-polarisation imaging with and without spatial filtering are shown in Figure 6.4.

6.3 Optical characterisation of circular Bragg resonators (CBRs)

As discussed in Section 5.6, our first attempt to realise CBRs is based on an SOI wafer without removing the BOX layer (shown in Figure 6.5) with a single lithographic step. Our simulations show that quality factors of non-suspended CBR structures are similar to suspended ones and we still get some vertical emission enhancement in the upward direction towards our collection objective (Section 4.3.2). In this section, we carry out the resonant-scattering measurements on the fabricated CBR devices to characterise them and validate the simulation results.

We have fabricated arrays of CBR devices with a range of grating periods to obtain resonance with the ^{31}P $D^0X \rightarrow D^0$ transitions near silicon band-edge. This process is known as lithographic tuning. Redundant devices with same grating periods were fabricated to get around any random fabrication or structural imperfection. In each device array, the grating period is varied along the row and devices are replicated along the column of the array. Ideally, the grating period should be varied with a step size that is small enough to smoothly cover the wavelength range of interest. However, in practice, the minimum realisable step size depends on the resolution of the lithographic technique which is ~ 2 nm for our EBL system. We implement the grating period variation with several different step sizes such as 2 nm, 3 nm, 4 nm etc. in different batches of fabricated device arrays. The optical characterisation of these different batches reveals that the grating period variation with 2 nm step size has not been patterned reliably, evidenced by non-uniform shifts in the CBR resonance. Such irregular resonance shifts

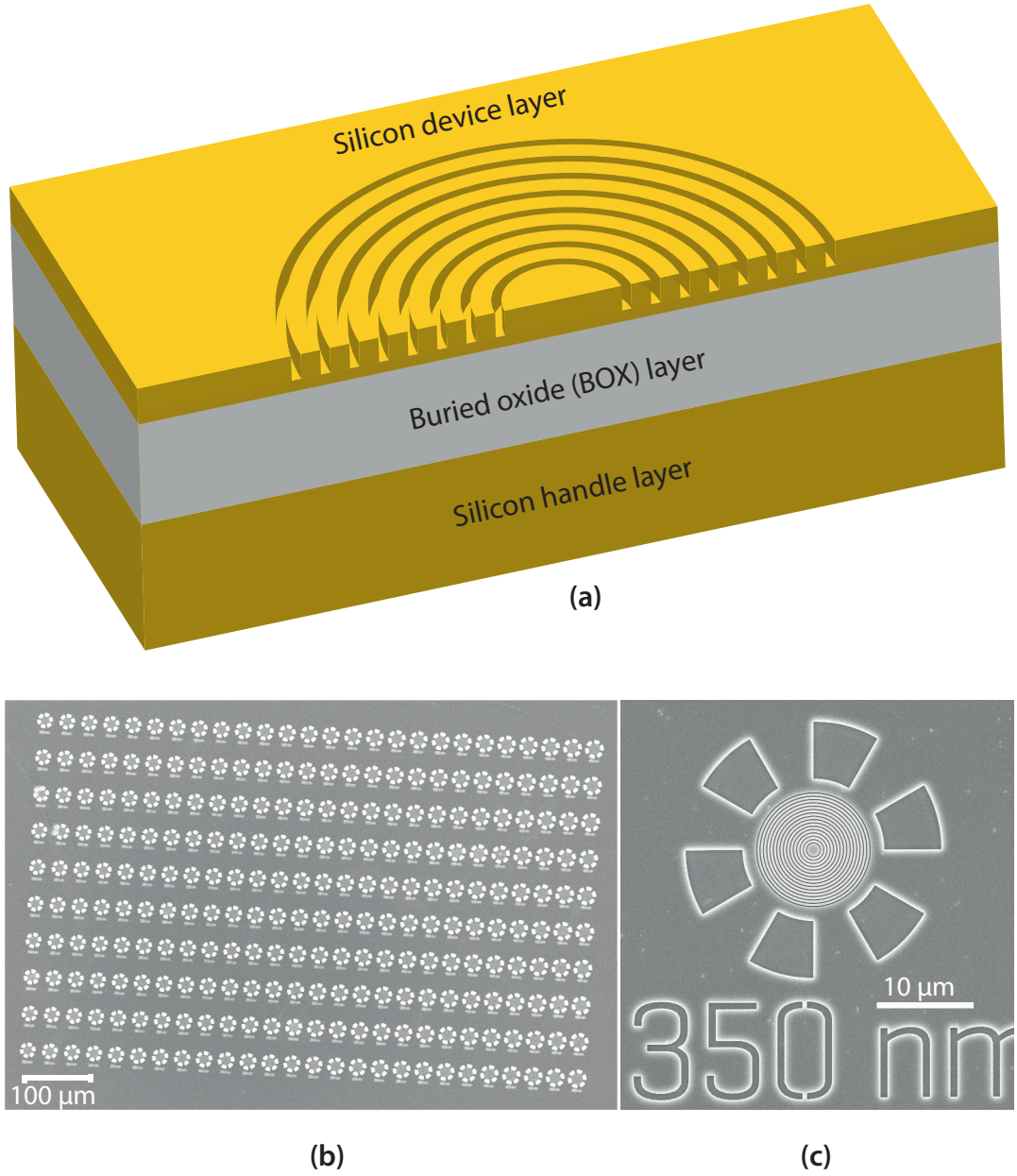

Figure 6.5: Circular Bragg resonators (CBRs): (a) The schematic of a CBR cross-section, (b) an SEM image of an array of fabricated CBRs with incremental grating periods and (c) a Zoomed in SEM image of a CBR with a grating period of 350 nm

were not observed for step sizes of 3 nm and above, so, we chose 3 nm as the optimum step size to implement lithographic tuning. To present the results of the CBR characterisation, we select an array of fabricated devices (shown in Figure 6.5(b)) where the device grating period is varied from 350 nm to 425 nm with a step size of 3 nm across each row and each column has 10 replicated devices. A zoomed scanning electron microscope (SEM) image of a device with a grating period of 350 nm is shown in Figure 6.5(c). We have etched the grating period values under corresponding devices

during fabrication process. Under the confocal microscope, these numbers are used as markers for locating target devices and sequentially measuring across a row of devices. In the measurement setup, the near infrared (NIR) excitation source (M1050D1 LED) is also used for locating and inspecting devices under the monochrome imaging camera (WAT-910HX/RC). Once a resonator device with the intended grating period and a reasonably clean surface is found within the imaging view, the cavity section is carefully positioned under the collection spot. The analyser and pinhole are then flipped back into the beam path to go back to the cross-polarisation configuration with the spatial filtering. The light scattered from the resonator is then guided to the spectrometer and detected by the Si-based CCD array (PyLoN System Silicon CCD Camera). The effective detection range our system depends on the combined effect of the excitation LED and the CCD array efficiencies. The output efficiency of the excitation LED becomes less than 10% below 950 nm and above 1100 nm. The silicon CCDs work very efficiently over the visible wavelengths to $\sim$ 900 nm light and start to become inefficient for longer wavelengths. The detector efficiency for wavelength 1000 nm is $\sim$ 14%, but falls to around 1% for 1078 nm and above.

Figure 6.6a shows the result of resonant-scattering carried out at room temperature on four CBR devices with grating periods, $\Lambda = 380$ nm, 383 nm, 386 nm and 389 nm. The fundamental resonant modes appears for these devices at 1065.9 nm, 1071.6 nm, 1077.7 nm and 1083.9 nm following the incremental order of the grating periods. From Figure 6.6a, it can be seen that a consistent 6 ± 0.26 nm red shift in resonance takes place for each 3 nm increase in the grating period. As the resonance shifts to longer wavelengths, the intensity of the signal starts to drop significantly, requiring a longer exposure time. For example, to get comparable signals for resonances at 1071.6 nm, 1077.7 nm and 1083.9 nm, use exposure times of 5 s, 10 s and 15 s respectively (as in Figure 6.6a). This requirement is a direct consequence of the limited excitation and detection efficiency of our measurement system at longer wavelengths. Finally, we observe overall linewidths for the fundamental resonant modes around 4 nm suggesting quality factors of few hundreds for these CBR devices. We extract the quality factor for each resonant modes using the Lorentzian fits, as shown in Figure 6.6b. The extracted quality factor values are 280 ± 9.5, 295 ± 15, 245 ± 15 and 225 ± 30 for resonances respectively at 1065.9 nm, 1071.6 nm, 1077.7 nm and 1083.9 nm. The

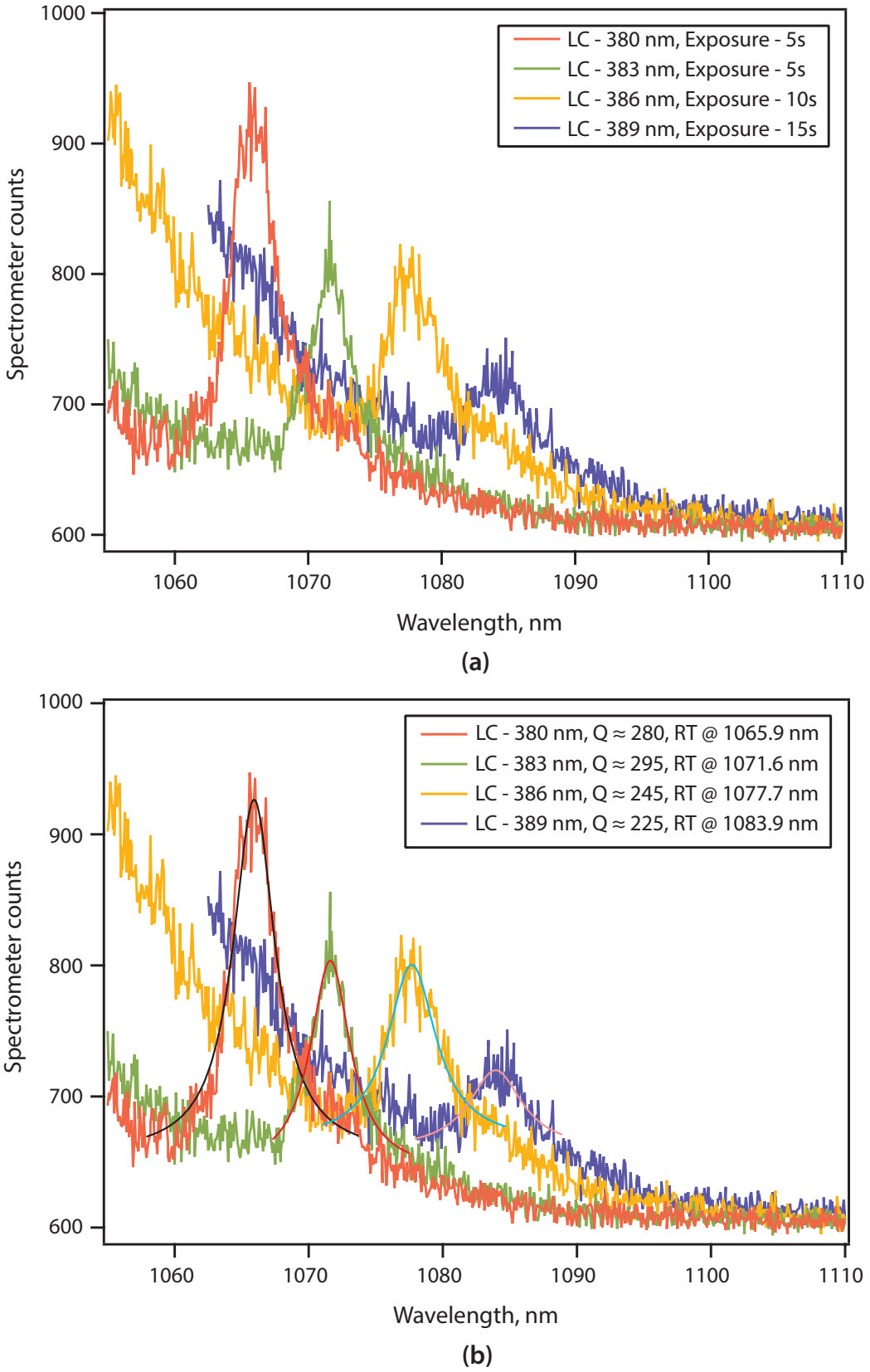

Figure 6.6: Room temperature characterisation of circular Bragg resonators (CBRs): (a) Grating period dependence of the fundamental CBR mode and (b) the Q-factor extraction with Lorentzian fits

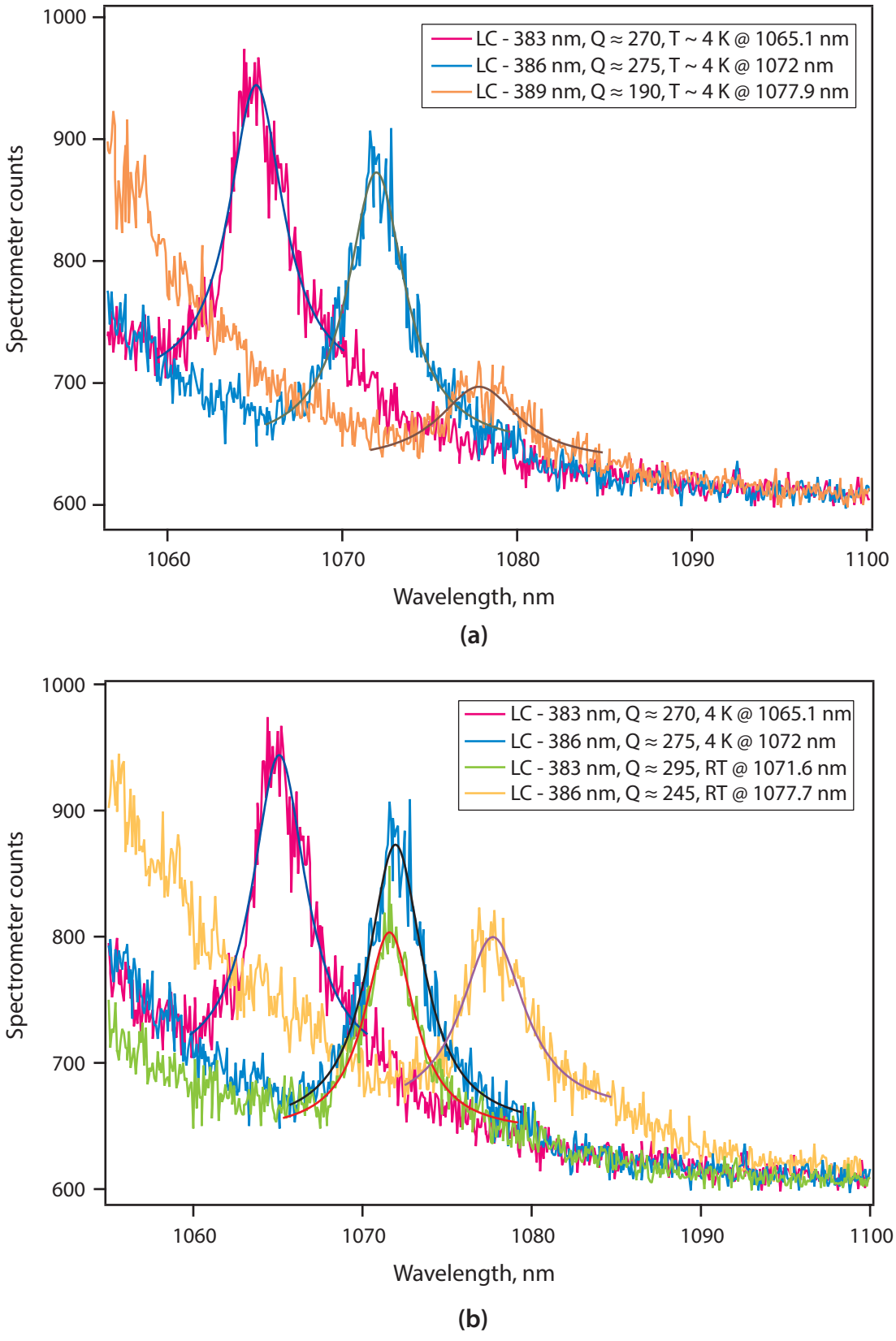

Figure 6.7: Low temperature characterisation of circular Bragg resonators (CBRs): (a) grating period dependence of fundamental CBR mode at 4K and (b) thermal shift in the cavity modes

overall Q values are consistent with the simulated Q-factor of ~ 250 obtained for the CBR devices. However, a trend of a drop in the Q values can be observed for the longer wavelengths. Our optical setup is not placed on a vibration isolating platform and the motorised stage holds the whole cryostat. So, the system suffers from vibrations and stage drifts which worsen for longer measurement times. We therefore speculate that the drop of measured Q values at longer wavelengths derives from factors such as the vibration noise and stage drift, combined with the need for longer exposure times at longer wavelengths.

After the room temperature measurements, we cooled down the sample mounted in the helium flow cryostat, to a stable temperature of ~ 4 K, and characterise the CBR devices. Figure 6.7a shows the CBR fundamental modes at low temperature around ^{31}P $D^0X \rightarrow D^0$ transitions. For lattice constants of 383 nm, 386 nm and 389 nm, the resonant modes appear at wavelengths 1065.1 nm, 1072 nm and 1077.9 nm, respectively. The quality factors for these resonant modes are extracted using the Lorentzian fits similar to the case of room temperature features and Q values of 270 ± 14, 275 ± 12 and 190 ± 27 are obtained for 1065.1 nm, 1072 nm and 1077.9 nm resonances. Comparing with room temperature Q values (Figure 6.6b), we observe that the low temperature quality factors is slightly decreased for the resonances at similar wavelengths. When the helium transfer arm is connected to the cryostat and the vacuum pump is running during low temperature measurements, we observe that significant vibrational noise is picked up by the system. The drift in the sample stage also increases due to the additional pressure from the transfer arm as the motorised stage has to manoeuvre the whole cryostat system (Figure 6.4). The sample drift led us to collect unwanted modes distributed on circular gratings close to the target mode of the central resonator. Thus, the efficiency of measurements drops at low temperatures and becomes even worse for longer exposure times. Another important feature observed in Figure 6.7a is the thermal shift of the CBR resonances for the same grating periods at low temperature, caused by the temperature dependence of the silicon refractive index. In Figure 6.7b, we compare the room and low temperature resonances for CBR devices with grating periods of 383 nm and 386 nm. We find that there is a consistent ~ 6 nm blueshift of resonant modes when we cool down the devices from room temperature to 4 K.

6.4 Optical characterisation of photonic crystal (PhC) cavities

According to their optical properties, both from literature and our simulations, the photonic crystal (PhC) cavities can provide very high quality resonance at small mode volumes as well as efficient outcoupling of photons from emitters embedded in cavities. Thus, PhC cavities are the ideal candidate for enhancing the total emission from embedded emitters. However, to the best of our knowledge, no experimental study has been carried out to investigate PhC cavities for enhancing the total emission from impurities emitting close to the band-edge of silicon. Few works carried out in this direction and wavelength range are aimed at enhancing or investigating phonon-assisted band-edge recombination[263, 309], silicon inter-band/TO-phonon-assisted transitions [150, 151], electron-hole droplet recombination[206, 310, 311] and copper isoelectronic centres [191] related emissions. In all these cases, the wavelength range of emissions/interest covers the range 1100 nm to 1250 nm and the optical properties of all realised PhC cavities are studied only through PL measurements. No optical characterisation of unloaded PhC cavities and systematic attempt for improving far-field radiation have been reported yet for such wavelength ranges. In this work, we attempt, for the first time, to realise PhC cavities with resonances below 1100 nm which can be used to enhance shallow impurity emissions such as ^{31}P $D^0X \rightarrow D^0$ transitions in silicon. We implement the fine-tuning and band-folding on L3 cavities in order to achieve high quality factors and better outcoupling of light. In this section, we discuss the resonant scattering characterisation of PhC cavities fabricated with the standard single layer resist process and of those fabricated with our novel multilayer resist process.

6.4.1 PhC cavities: fabricated with single layer resist

We begin our PhC cavity characterisation with devices fabricated with the single layer EBL resist process (discussed in the Section 5.4). These PhC devices have been designed for high quality factors ($\sim 1.5 \times 10^5$) and extraction efficiency ($\gtrsim 38\%$). Figure 6.8a and b show the schematic for the fine-tuned, far-field tailored L3 cavity design and the zoomed SEM image of a fabricated device, respectively. These devices were fabricated in our very first attempt to realise any photonic cavity; and we have tried to realise ideal design parameters within a limited range. This turns out to be a limiting

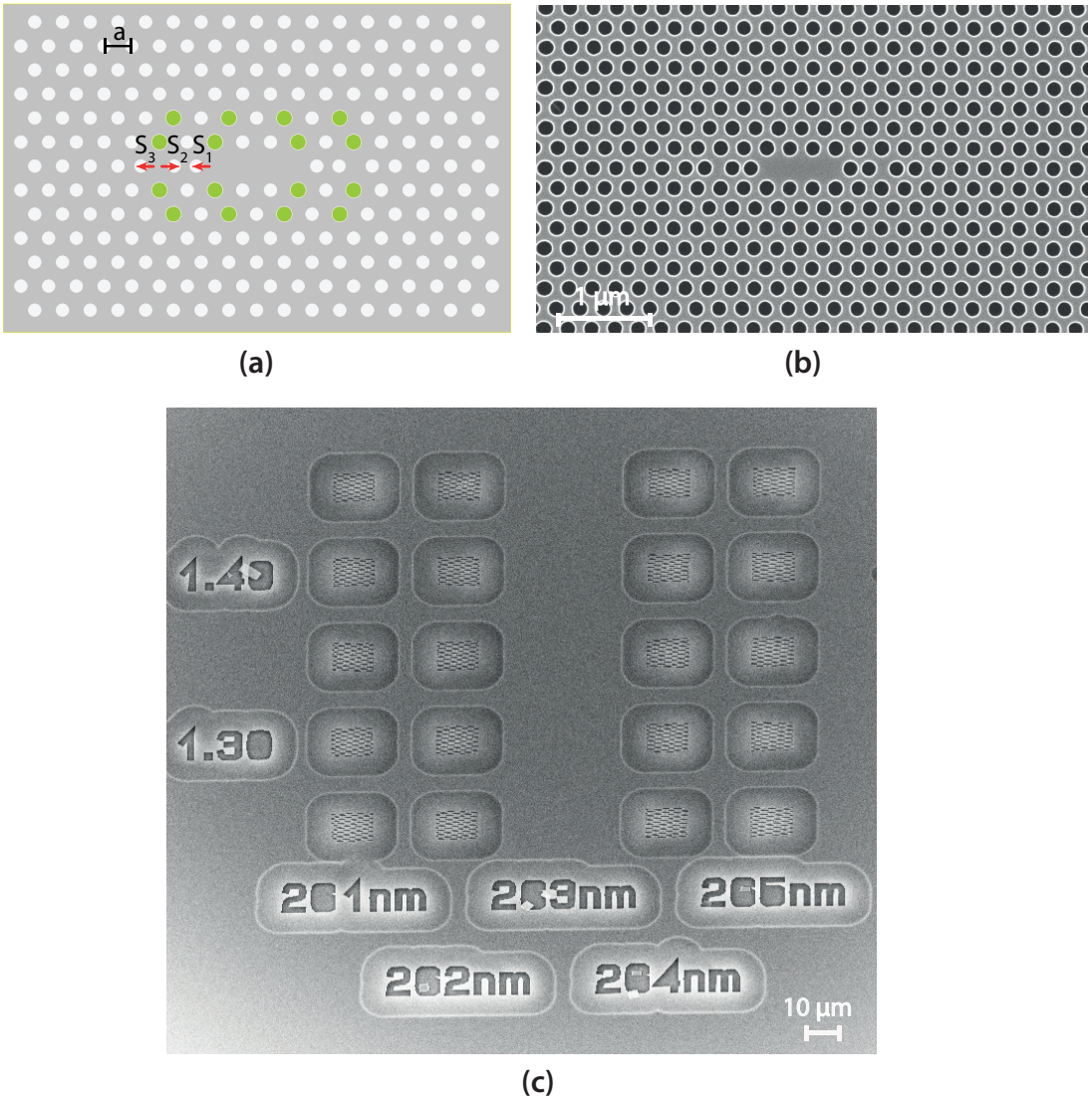

Figure 6.8: Fine-tuned, far-field tailored L3 PhC cavities: (a) A schematic of a Fine-tuned, far-field tailored L3 PhC cavity where the hole-size modulation is implemented with Design-1, (b) the SEM image of an example device, and (c) an array of devices fabricated with single layer resist process

factor in the case of practical implementation and finding cavities with desired performance. For example, we have varied the lattice constant of this batch of devices only over a range of 5 nm with a step size of 1 nm. In addition, the size of holes along the column of the device arrays is varied in order to adjust the resonant modes, as shown in Figure 6.8c. We have replicated such an array of PhC cavities many times to get several redundant devices for measuring. However, the small span and steps of lattice constant variation provides only a narrow lithographic tuning range and inefficient shift in resonance. Furthermore, in order to apply the band folding i.e., tailor the far-field radiation pattern, the radii of the selected holes have to be changed. We implement the

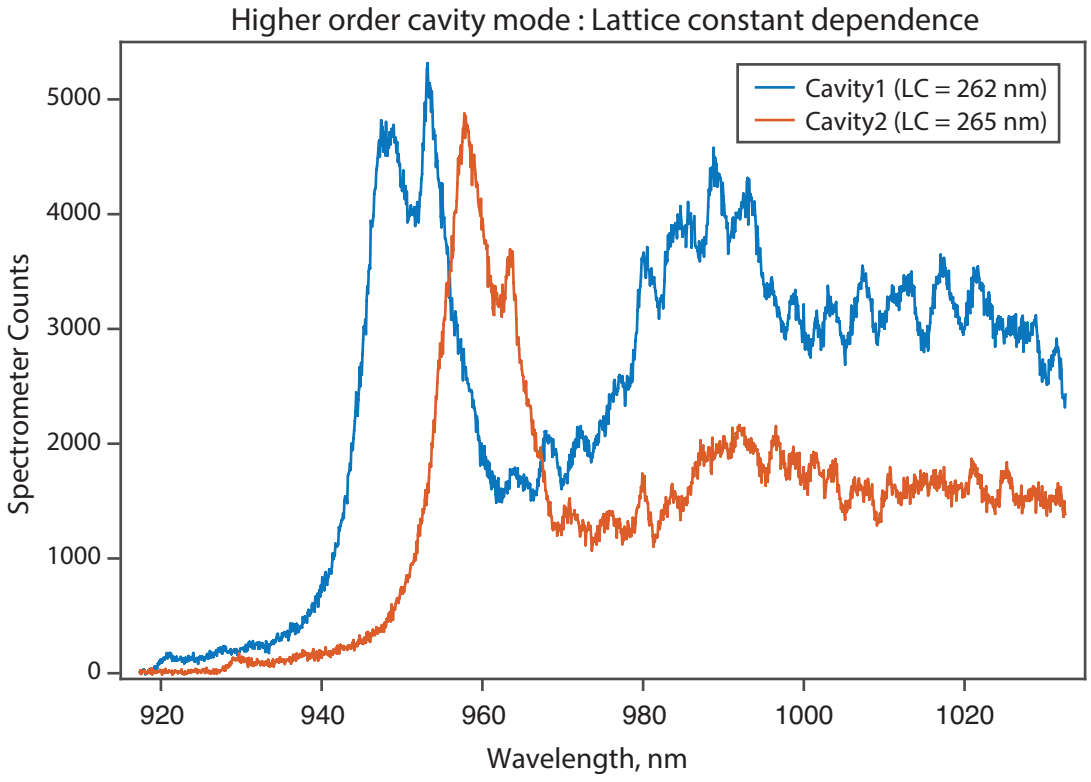

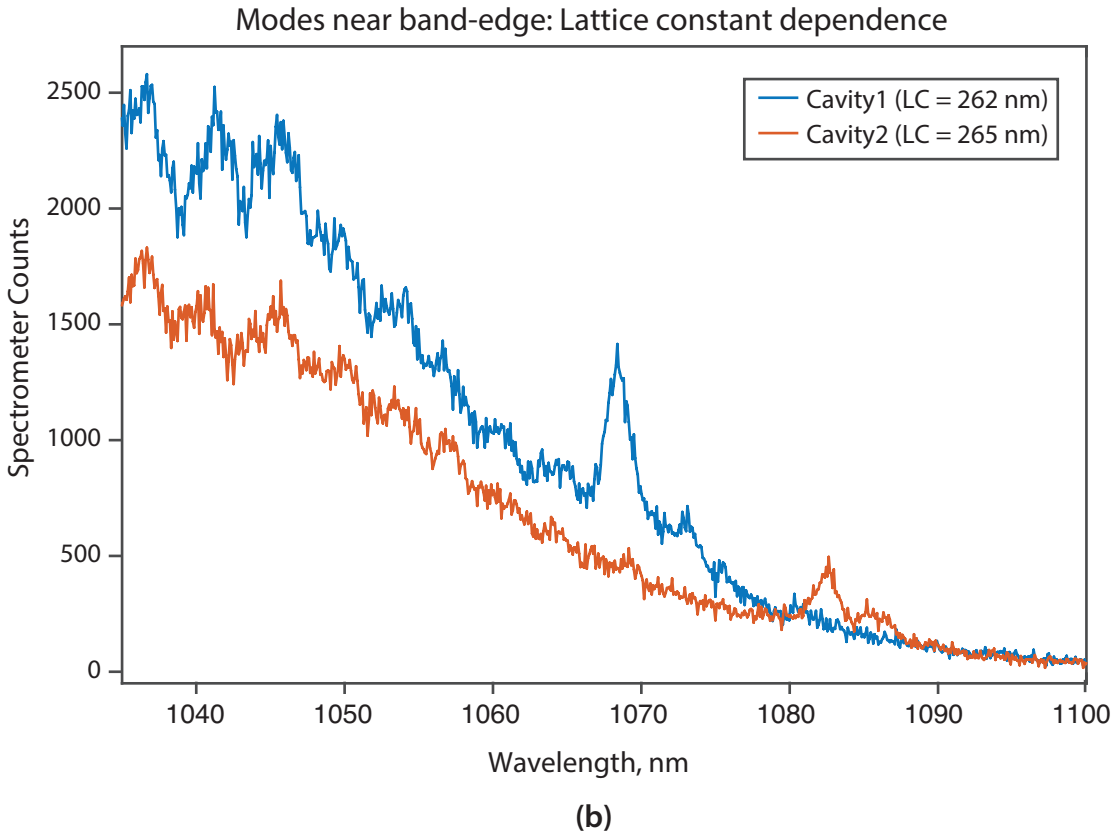

Figure 6.9: Resonant scattering characterisation of fine-tuned L3 PhC cavities: lattice constant dependence in (a) higher order modes and (b) modes near the band edge

band-folding by using the hole-size modulation scheme - Design-1 (Section 4.5.2) and a modulation amplitude, $\Delta r = 0.01a < 3$ nm.

Figure 6.9 summarises the resonant-scattering (RS) measurements carried out on PhC devices fabricated with the single layer EBL resist process. The RS measurements of the devices reveal interesting features around $940 - 970$ nm (Figure 6.9a) and $1060 - 1090$ nm (Figure 6.9b). However, the spectra contain significant background and show peaks that are broad compared to expected cavity modes, making it difficult to attribute the observed peaks to the cavities. So, we investigate the effect of lattice constant variation on the observed features to confirm their cavity related origin. We compare both the short and long wavelength peaks from two devices with different lattice constants - 262 nm and 265 nm, as shown in Figure 6.9. The comparison shows that there occurs a ~ 15 nm shift in the observed peaks both at short (Figure 6.9a) and long (Figure 6.9b) wavelengths with the change the lattice constant by 3 nm. We also investigate the position dependence of these features, as shown Figure 6.10, to ensure that the peaks arise from the cavities, not from any random scattered mode of the photonic crystal structure. To carry out the position dependence check, we select a cavity and carefully position it under the excitation/collection spot so that the detected signal obtains the maximum intensity. We attribute this maximum intensity position to the center or field maxima of the cavity and label the position with 'Offset $= 0$ μm' as shown in Figure 6.10. If the observed peaks in the detected signal do not originate from the cavity itself, the peak intensity should remain unchanged in case we move away a short distance from the cavity. Finally, we move the cavity away from the collection spot in several ~ 1 μm steps and measure the scattering signals at each step. The steps are taken along the length of the cavity and the measured signal after each step is recorded and labeled according to the position offset from the centre of the cavity. We find that the detected peaks at both short (Figure 6.10a) and long (Figure 6.10b) wavelengths show high position dependence. The peak intensity for both cases decreases rapidly at each step and completely disappears beyond 2 μm offset from the central position. As our collection spot size is around 3 μm, the cavity goes out of the collection range when moved beyond 2 μm from the central position. This correlation between the peak intensity and cavity position indicates that the peaks originate from cavity modes. However, the linewidths of the cavity modes near the silicon band-edge are in

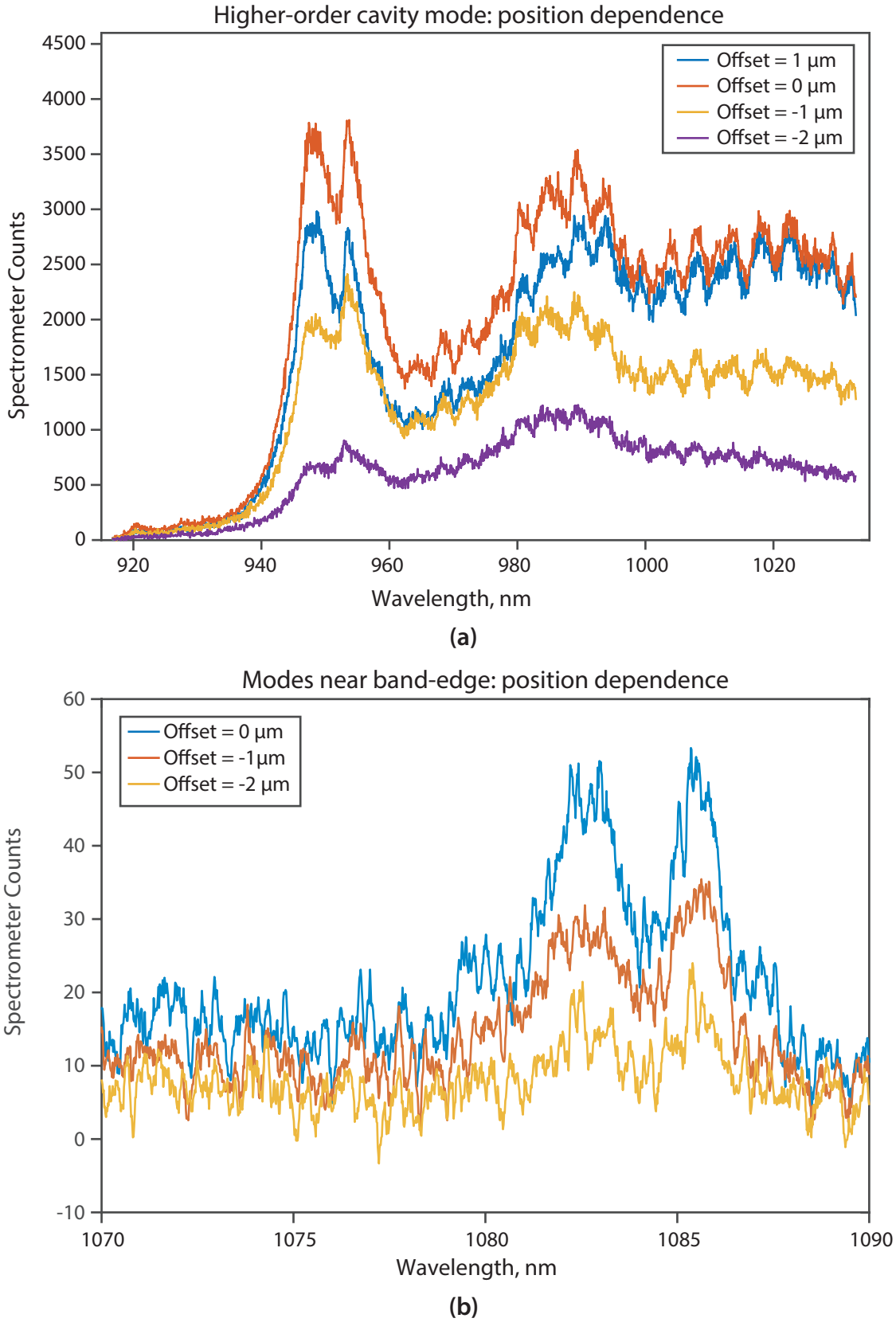

Figure 6.10: Position dependence of cavity modes observed in resonant scattering characterisation: position dependence in (a) higher order modes and (b) modes near the band edge

the order of nanometers which is significantly broader than the designed fundamental modes. One possibility is that the observed cavity modes near the silicon band-edge are not the high-Q fundamental modes and the fundamental mode appears outside our effective measurement window. Due to a limited lithographic tuning range, we could not verify this fact with the current batch of devices. From the SEM images, we did not find any noticeable deformation/irregularity in the hole profiles (Section 5.4) of these PhC cavities. Therefore, another rational reason for not seeing the high-Q mode can be an inefficient hole-size modulation for tailoring the far-field radiation. The high-Q modes usually appear at high grazing angles. So, it is difficult to collect high-Q modes with objectives of a moderate numerical aperture if the far-field is not effectively tailored. Moreover, small fabrication errors or structural imperfections (< 3 nm), which are difficult to identify under SEM, can be considered as a random modulation of hole sizes in the PhC structure. If the amplitude of the designed hole-size modulations is smaller or the same order of such structural errors in the photonic crystal pattern, then it would not be possible to achieve the expected cavity and outcoupling behaviour. Thus, we need further work on device fabrication and characterisation before obtaining the optimum fabrication parameters and desired cavity properties.

6.4.2 PhC cavities: fabricated with multilayer resists

The single layer EBL resist based process is expensive and the necessary resources were not available in the LCN cleanroom. An iterative fabrication and systematic evaluation of cavity devices is therefore difficult with the single resist process. For this reason,

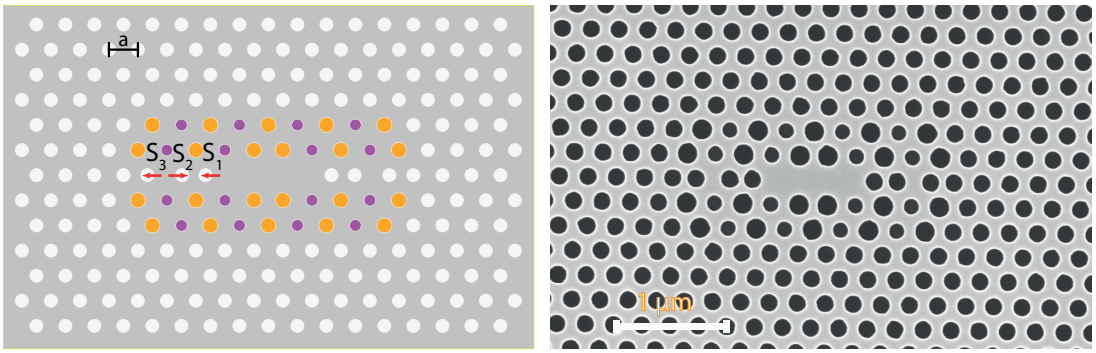

Figure 6.11: Larger hole-size modulation in L3 PhC cavities for enhanced outcoupling: (a) The schematic of far-field tailored L3 cavity with Design-2 and (b) SEM image of an example device fabricated with multilayer resist process

we developed a relatively inexpensive, multilayer resist process which is based on the available resources in our cleanroom (process details are discussed in Section 5.5). We also incorporate further changes in our design to boost the outcoupling of light while relaxing the fabrication constraints. For a strong and abrupt tailoring of the far-field, we increase the modulation of hole size and apply it to a larger number of holes around the cavity with the modulation scheme of Design-2 (as discussed in Section 4.6) [254, 255]. The schematic of far-field tailored L3 cavity with Design-2 is shown in Figure 6.11a. This time we implement a large range of lattice constant variation, from 240 nm to 335 nm, with a step size of 5 nm. Three different hole modulation values (modulation amplitude, $\Delta r = \pm 0.02a, \pm 0.03a$ and $\pm\, 0.04a$) are incorporated for each lattice constant to find out the most suitable practical outcoupling. By increasing the hole-size modulation for better outcoupling, we compromise Q values, but at this stage we prioritise collecting photons and detecting the resonances properly over achieving high quality factors. We fabricate an array of devices where we vary the lattice constant across the rows and the modulation amplitudes along the column. Thus, we get a 20×3 array of PhC cavities covering wide range of wavelengths and three levels of modulation. A zoomed SEM image of an L3 PhC cavity implemented with Design-2 and modulation amplitude, $\Delta r = \pm 0.04a$ is shown in Figure 6.11b as an example.

Clearly distinguishable peaks in RS measurements of our PhC devices are observed, showing the lattice constant and position dependence which imply that the observed features originate from the cavities. From all the measurements, optimum results in terms of intensity and linewidths are obtained for cavities with a modulation amplitude of $\Delta r = \pm 0.03a$ which agrees very well with the simulation results in Section 4.6. To summarise the characterisation results, we pick four devices starting from a lattice constant of 265 nm up to 280 nm with a step of 5 nm. The interesting and near band-edge features from the selected PhC cavities with the modulation amplitude of $\Delta r = \pm 0.03a$ are shown in Figure 6.12. Sharp cavity modes appears at around 1032 nm, 1056 nm, 1080 nm and 1104 nm for the selected PhC devices with ascending order of lattice constants. This shows a consistent $\sim$ 24 nm shift in the cavity mode for each 5 nm steps in the lattice constant. The cavity mode at 1080 nm (green circled peak in Figure 6.12) is very close to the silicon band edge/D^0X emission corresponding to the lattice constant 275 nm. Furthermore, it can be noticed that significantly extended

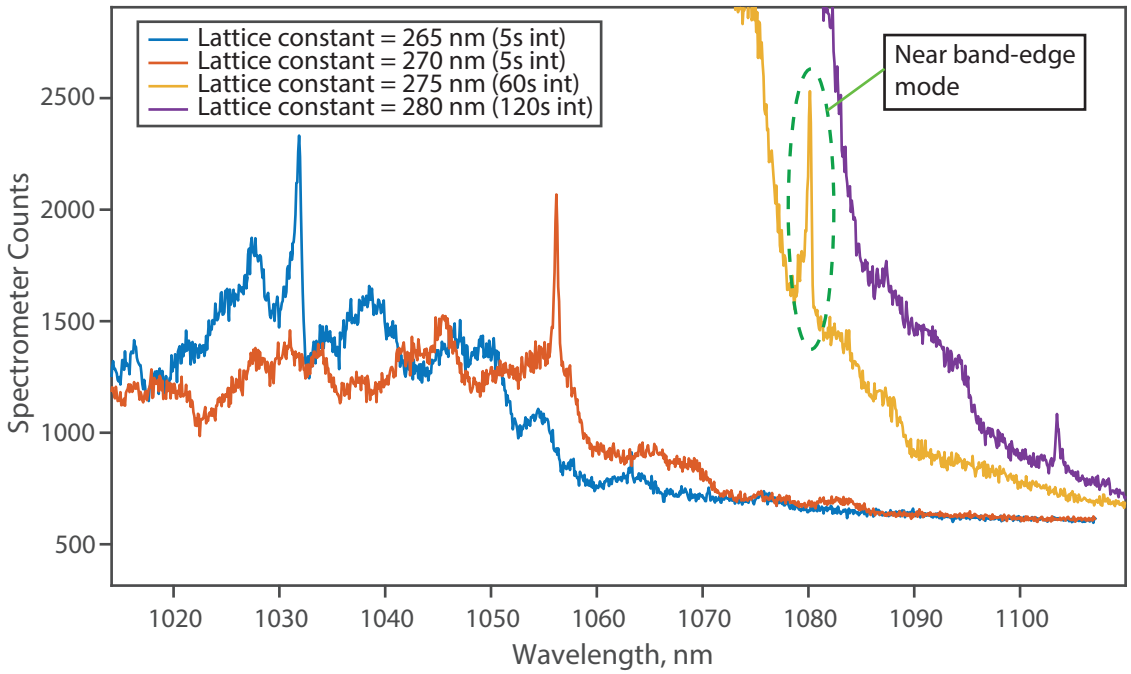

Figure 6.12: Resonant scattering characterisation of L3 cavities with with large hole-size modulation: Measured spectra for the PhC structures which are modified with Design-2 ($\Delta r = \pm 0.03a$) for highly directional outcoupling. Clear cavity modes with a consistent lattice constant dependence is observed. A near silicon band-edge cavity mode (green circled) is observed for the L3 PhC cavity with a lattice constant of 275 nm.

measurement times are required for cavity modes appearing at longer wavelengths as discussed in Section 6.2.

So, the strong far-field tailoring enables the detection of cavity modes with the existing setup. To gain confidence that the peaks observed (for example, in Figure 6.12) are the fundamental resonant modes, we simulate (see Figure 6.13) the bandstructure of the PhC device under consideration, using the MIT Photonic-Bands (MPB) package (free software for computing the band structures (dispersion relations) and electromagnetic modes of periodic dielectric structures [312]). The computed cavity modes for TE polarised light in the L3 cavity have also been included in the bandgap at their normalised frequency positions. Furthermore, the localised field intensity distributions for each mode is simulated using the FDTD method and provided beside the photonic band diagram in Figure 6.13. The fundamental localised (resonant) mode for the cavity appears just above the dielectric band and has the lowest frequency (longest wavelength) among all the cavity modes. It is also well separated from the higher order modes. The fundamental mode is the most interesting one as it experiences strongest confinement

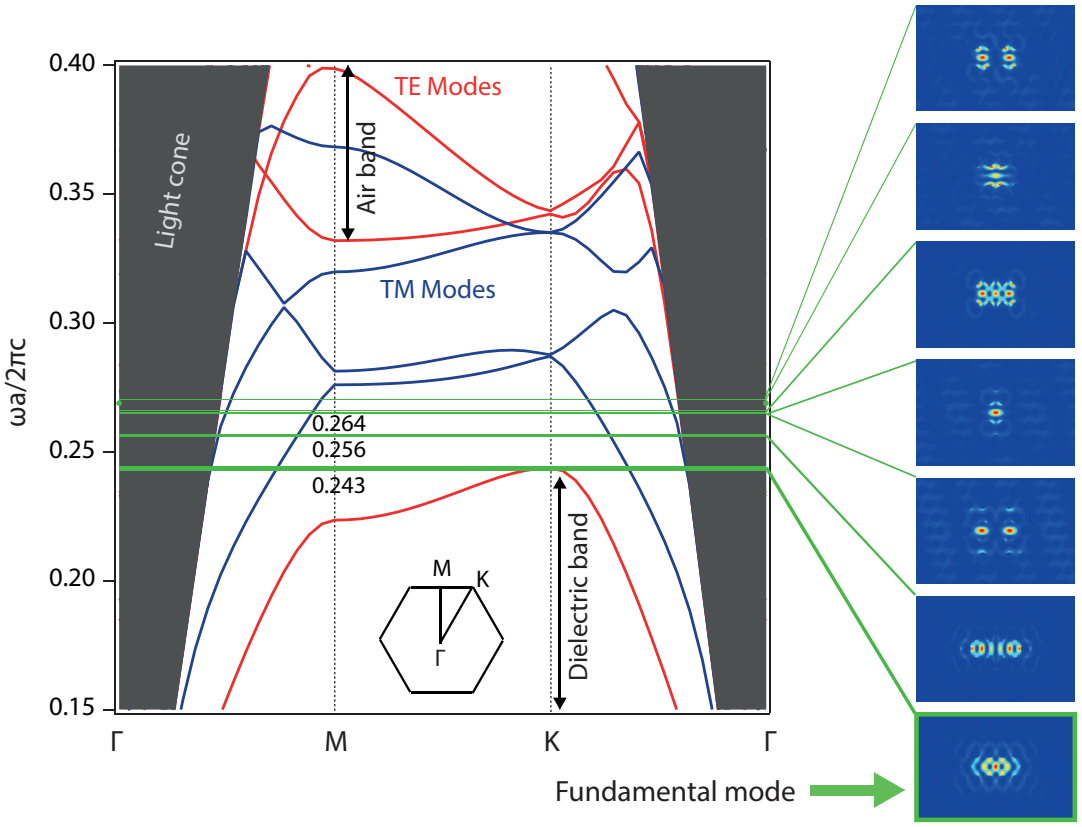

Figure 6.13: Simulated bandstructure and cavity modes of a far-field modulated and fine-tuned L3 PhC cavity

and provides the highest Q value. In the calculated band diagram, the fundamental or 0th order mode appears at a normalised frequency, $a/\lambda = 0.243$ and seems to overlap with the highest mode of the dielectric band (Figure 6.13). This overlapping is just an artefact of the simulation carried out with a limited mesh resolution. The next higher mode (1st order) appears at $a/\lambda = 0.256$. The other higher modes appearing at and above $a/\lambda = 0.264$ are not very well separated. So, it is difficult to distinguish and label these higher modes individually which also suggest that their overlap might occur in the measured spectrum.

Next, we analyse the measured cavity spectra and try to identify cavity modes from the observed features by comparing with the simulations. In Figure 6.14, the full resonant-scattering spectra from PhC devices under consideration have been plotted against the normalised frequencies (with dimensionless units) so that the characteristic properties of the photonic crystal structures become scale independent of the lattice constant values. The wavelength scales have also been provided on the plots in Figure 6.14 for clarity and depicting the lattice constant dependent shifts. Now,

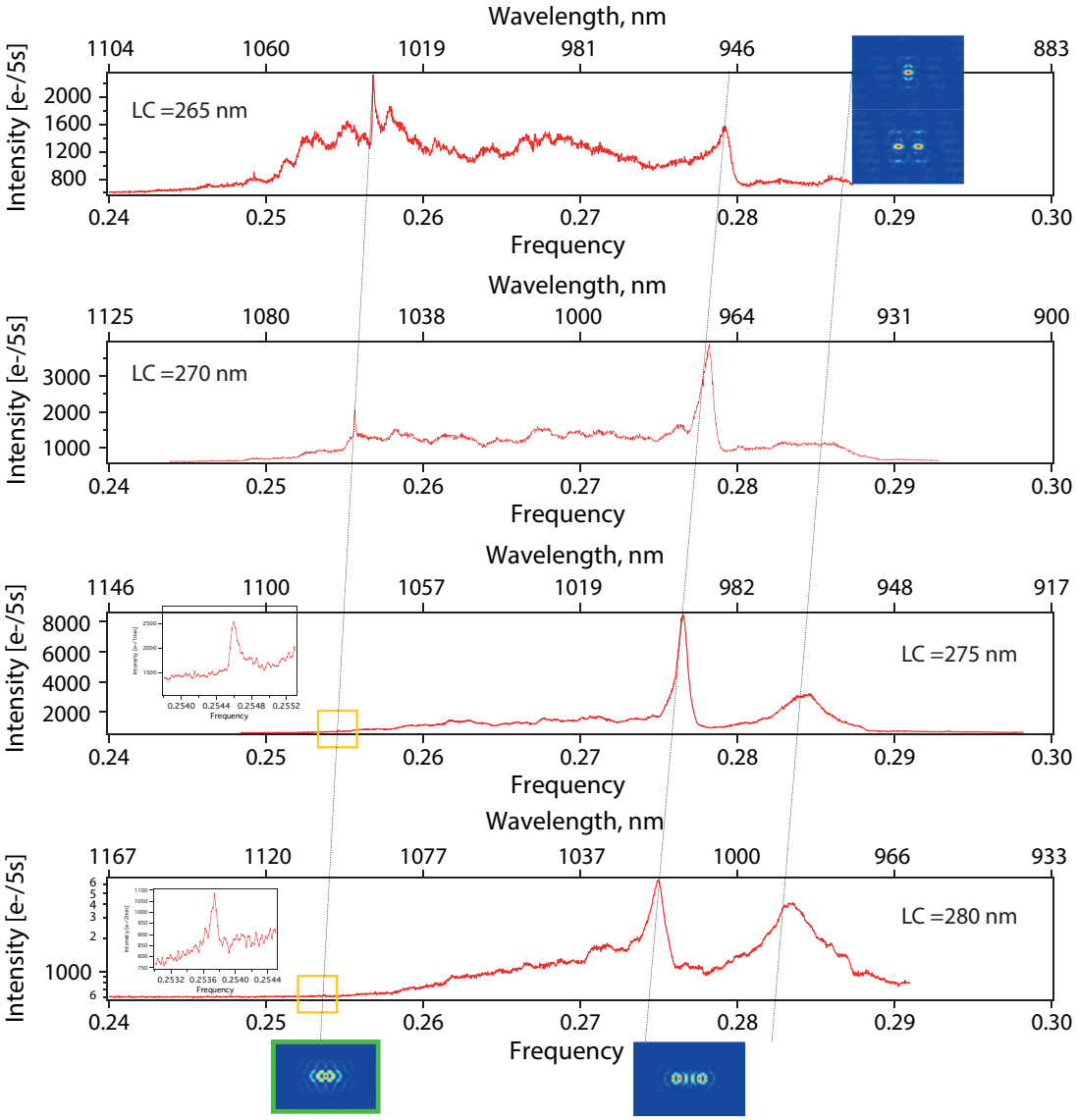

Figure 6.14: Comparison of simulated and measured cavity modes of a far-field modulated and fine-tuned L3 PhC cavity

we compare the spectra from the four cavities and find a mode that appears consistently at the lowest frequency, around $a/\lambda = 0.255$, for all the devices. Moreover, this mode provides apparently the narrowest linewidth and is the nearest one to the simulated fundamental cavity mode occurring at $a/\lambda = 0.243509$. Therefore, this mode around $a/\lambda = 0.255$ most closely resembles the 0th order mode and we assign it as the fundamental mode in Figure 6.14. Inspecting in the wavelength scale, we further find that the sharp peaks/modes observed earlier in Figure 6.12 are the fundamental cavity mode. The next two clear features sequentially appear around $a/\lambda = 0.275$ and $a/\lambda = 0.285$ in the measured spectra (Figure 6.14). We attribute these features to the

next higher modes found in the simulation (Figure 6.13). The simulated mode positions suggest that the feature appearing around $a/\lambda = 0.285$ is an overlap of the 2nd and 3rd order cavity modes. Similar to the fundamental mode, the higher order modes in the measured spectra are observed at larger frequencies than the corresponding simulated values. Finally, we haven't managed to see any distinguishable feature from the 4th order and/or other higher order modes. One possible reason for this is the small Q values of higher order modes. The efficiency of the excitation source (M1050D1 LED) at shorter wavelengths (higher frequencies) is also very poor ($< 10\%$ below 950 nm). In Figure 6.14, we can see that the signal intensity starts to deteriorate below 950 nm even though the detector efficiency is improving ($> 30\%$) in this region. Furthermore, the cross-polarisation setup can also play a role in suppressing some modes if the mode polarisation does not align favourably with the cross-polarisation configuration.

6.4.3 Low temperature characterisation and extraction of Q values

Here, we investigate the low temperature behaviour of our PhC devices and check the compatibility of our system for low temperature PhC cavity measurements. We pick the PhC cavity with a lattice constant (LC) of 270 nm for investigation, because the fundamental mode appears around 1056 nm (Figure 6.12) which is in a favourable range for both the excitation source and the detector. After positioning the selected PhC device, we cool down the system and characterise the cavity at low temperatures. Though the dissociation temperature of ^{31}P D^0X is around 40 K, any realistic experiment related to ^{31}P $D^0X \rightarrow D^0$ transitions is preferred around/below 10 K as the D^0X emission linewidth broadens with increasing temperature. So, we focus on the cavity behaviour around this temperature range and measure the cavity modes at 20 K, 10 K and 4 K. The fundamental modes measured at low temperatures are then plotted with the room temperature mode, as shown in Figure 6.15. Compared to room temperature, a blue shift of ~ 7 nm can be observed for the fundamental cavity modes measured at/below 20 K. The thermal shift in PhC cavity mode is consistent with the shift observed for the CBR devices in Section 6.3, suggesting that the thermal shift does not depend on the cavity design (i.e., mechanical deformation by the temperature change does not have the primary effect) and is rather due to the temperature dependence of the refractive index of the substrate. Below 20 K, no shift in the cavity mode is observed. This can

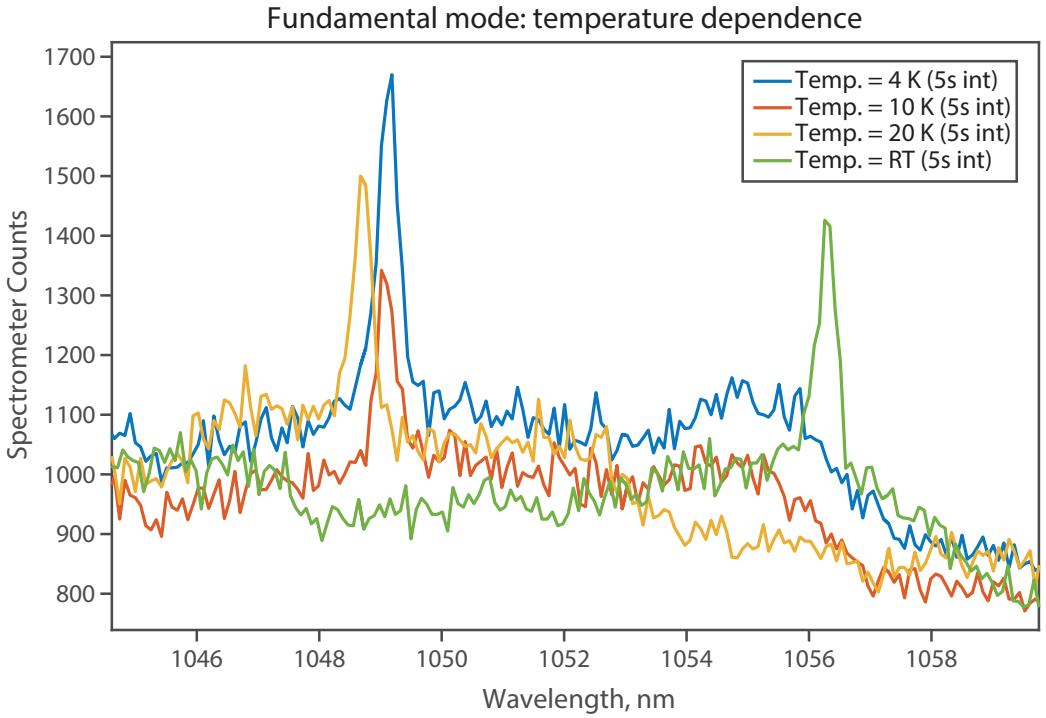

Figure 6.15: Thermal shift of L3 cavity mode

be attributed to charge carrier freeze out and a negligible change in the thermo-optical coefficient values in silicon below 30 K [313, 314] which in turn lead to an insignificant variation in the refractive index and cavity modes.

As discussed in Section 6.3), the vibrational noise and the drift in the sample stage start to affect the efficiency of the confocal system in the low temperature measurements. For PhC cavities this issue becomes even more serious as the cavities are smaller and their responses are highly position dependent. To investigate the effect of such noise during low temperature measurements, we characterise the cavity with different exposure times at 4 K and at room temperature. The quality factors are then extracted for each dataset. In Figure 6.16, the extracted quality factors at 4 K for exposure times of 10 s, 5 s and 1 s are presented along with a room temperature measurement outcome for an exposure period of 5 s. For the room temperature measurement, when the vacuum pump and the helium transfer arm are not connected, the extracted Q value is 2950 ± 200 (Figure 6.16a). This room temperature Q-value remains constant when the exposure time is changed. The calculated value of Q-factor for the cavity design under consideration (Fine-tuned L3 cavity with Design-2 hole-size modulation) is around 8500 (Section 4.6) which is almost three times larger than the experimental value. In

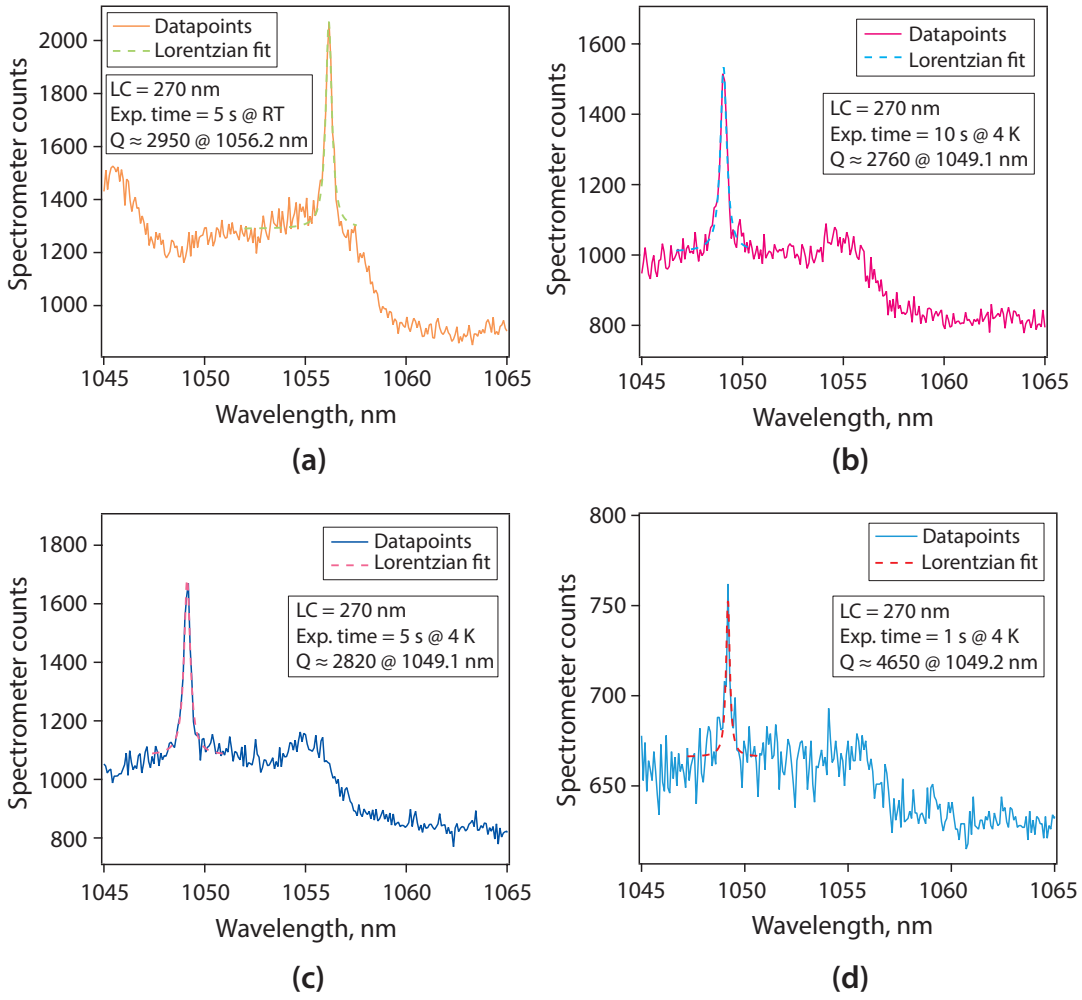

Figure 6.16: Measurement of L3 cavity mode at room and low temperatures

the case of measurements at 4 K, the extracted Q values are 2760 ± 170, 2820 ± 160 and 4650 ± 600 for the exposure time of 10 s, 5 s and 1 s, respectively (Figure 6.16b, c and d), which reveal that both the Q value (4650 ± 600) and the extraction error ($\sim 13\%$) increase at 4 K for a short exposure time (1 s). Our optical setup is affected by vibrational noise and stage/sample drift, which prohibit long exposure times and efficient extraction of Q values at low temperatures. Therefore, we could not fully verify/investigate the scope of this increase in Q value at low temperatures with the present measurement setup.

6.5 Improving Q values: cavities fabricated with multilayer resists

We observed that our hole-size modulated ($\Delta r = \pm 0.03a$) L3 PhC cavities can enhance the outcoupling sufficiently to detect and identify the fundamental resonances. However, the extracted quality factors are lower than the calculated design value ($Q_{calculated} \approx 8500$). Thus, we need to carefully investigate and address all the issues affecting the cavity performance in order to obtain the optimum device design and Q values. The most critical factors which affects the cavity performance or Q values are the material absorption, design issues and any physical deformation in the device structure. In this section, we address these issues to find an optimum cavity.

6.5.1 Effect of material absorption on quality factors of silicon PhC cavities

The intrinsic absorption of the substrate material is the most influential factor which can restrict the practical cavity performance. The qualify factor (Q) of a cavity, which is the figure of the performance, is the number of oscillations until the cavity system loses its electromagnetic energy down to $e^{-2\pi}$ or $\sim 0.2\%$. If the intrinsic absorption of the substrate material is high, the resonant electromagnetic mode inside cavity experiences fewer number of oscillations as it gets absorbed quickly. Thus, the absorption near the material bandgap intrinsically limits achieving high Q values.

Being an indirect bandgap semiconductor, silicon usually allows any photon capture through some phonon assisted optical transitions. At low temperatures, the formation of the free excitons also contribute to the total photon absorption process. Thus, the indirect optical absorption is a complex process which strongly depends on the density of phonons, energy of the captured photons and temperature [315–317]. The available experimental data on the temperature dependent absorption in silicon over a wide photon energy range is limited [316, 318]. This scarcity of experimental study arises mainly from the fact that the absorption coefficient values drop significantly at low temperatures for low photon energies ($\hbar\omega \leq 1.15$ eV) and the sensitivity of measuring apparatus also becomes limited [318]. Through a private communication with

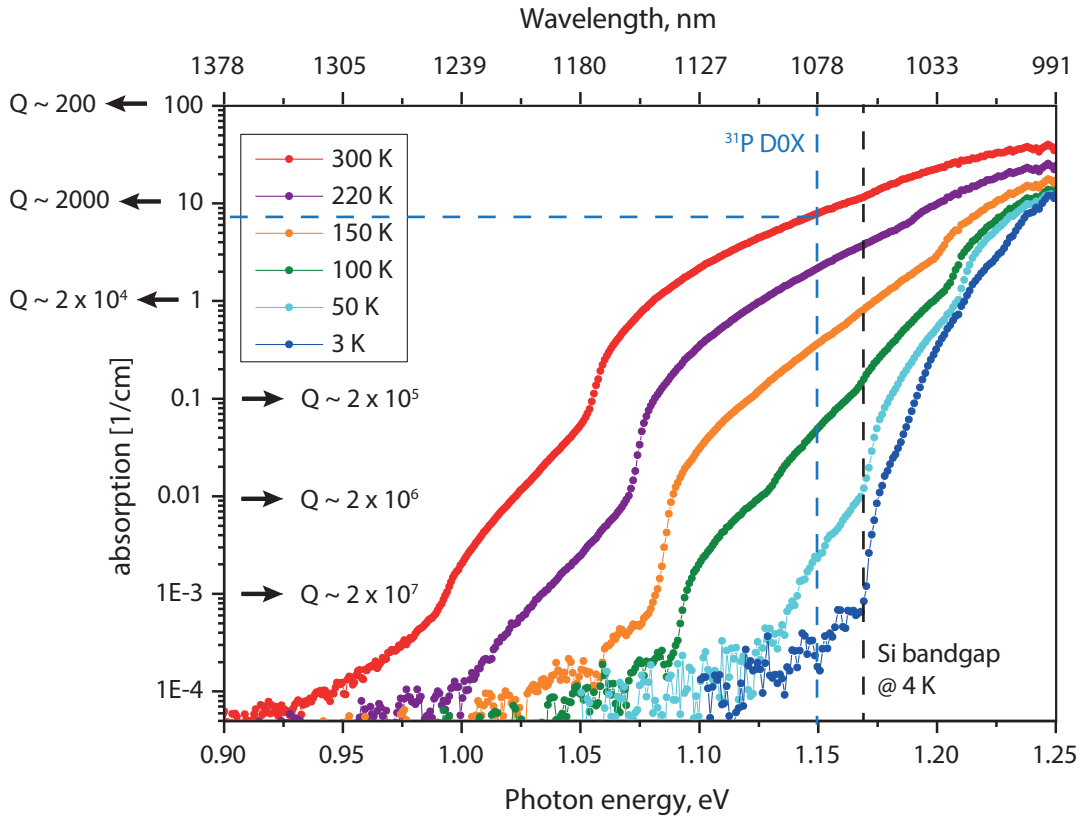

Figure 6.17: Material absorption and projected values of absorption limited Q for silicon PhC cavity at different temperatures. The absorption data is obtained by J. Komma in the group of R. Nawrodt at the Friedrich Schiller University, Jena

R. Nawrodt [1], we obtained high precision material absorption data for silicon over a sufficient range of photon energy and temperature for our work. The absorption data has not been published yet, however, they show remarkable agreement with theoretical estimation and previous experimental results [219, 316, 318]. The obtained absorption data is presented in Figure 6.17. From the absorption data, the Q values for our silicon PhC cavities can be estimated. The mode volume for the Fine-tuned L3 PhC cavity is around $0.7(\lambda/n)^3$ [264]. We approximate the Q value from the number of times a photon bounces back and forth (oscillate) inside the cavity confined space before getting absorbed by the substrate material. Thus, we have calculated Q values for ^{31}P D^{0}X emission (1078 nm) using mode volume ($V_{\text{mode}} \sim 0.7(\lambda/n)^3$) and absorption information. In Figure 6.17, Q values ($Q \sim \left(2\alpha_{\text{abs}}\sqrt[3]{V_{\text{mode}}}\right)^{-1}$) at 1078 nm have also been shown for varying absorption coefficients (α_{abs}). The projected Q values provide an idea about the achievable quality factors in silicon at ^{31}P D^{0}X emission

[1] Ronny Nawrodt, Friedrich Schiller University Jena, and his PhD student Julius Komma have carried out experiments to measure material absorption in silicon.

wavelength (1078 nm) for different temperatures. For example, the material absorption for silicon around 1078 nm is very high at room temperature. From literature, the room temperature absorption coefficient is found to be within $5-7$ cm^{-1} [319–322], which gives approximate Q values within $\sim 3000-4000$. Thus, high absorption sets an upper bound of only few thousands (~ 4000) for achievable Q values around ^{31}P D^{0}X emission wavelength (1078 nm) at room temperature. Therefore, even with a very efficient design and fabrication, it is not possible to attain high Q values at room temperature for silicon PhC cavities around 1078 nm. However, at sufficiently low temperatures (around liquid helium temperature), the phonon bath freezes out completely and the absorption coefficient values drop significantly ($\alpha_{\text{abs}} \leq 1 \times 10^{-3}$ cm^{-1}) below the silicon bandgap energy ($E_{\text{g,4K}} \approx 1.17$ eV) [315] and $\alpha_{\text{abs}} \approx 3 \times 10^{-4}$ cm^{-1} at 1078 nm, as observed in Figure 6.17. Thus, the absorption data suggest that, at low temperatures with an efficient design, it is possible to achieve very high Q values ($Q \sim 10^7$) around D^{0}X emission wavelengths. This is a sufficient upper bound for our goal as our PL measurement results suggest that Q values of few tens of thousand can in principle provide enough enhancement of ^{31}P D^{0}X emissions to access a single donor.

Our cavity characterisation results in the previous section (Figure 6.16a and d) indeed indicate a trend of significant increase in Q values around the liquid helium temperature. However, at room temperature, we find a discrepancy in the measured and estimated Q values. In our room temperature measurement, we have obtained Q value of ~ 2950 for a resonant wavelength of 1056.2 nm. But the projection of absorption limited Q at room temperature in Figure 6.17 suggests that the achievable value at 1056 nm would be ~ 2000. This discrepancy most probably arises from the combined effect of measurement uncertainties of the absorption coefficients [321] and our simplified estimation of absorption limited Q values using absorption coefficients of bulk silicon and the cavity mode volume at wavelength of interest. These give us approximate idea but not the exact parameter values for a cavity fabricated in a thin and suspended silicon membrane. So, it is not surprising that the calculated Q values in Figure 6.17 underestimates the attainable quality factors at room temperature.

6.5.2 Optimising hole-size modulation for tailored far-field

As already discussed, any tailored far-field radiation pattern comes with a price of a considerable reduction in the cavity quality factor. From a realisation point of view, it is more efficient to achieve a tailored far-field when the size modulation is applied to a larger number of holes. However, for the same amplitude of hole-size modulation, the reduction in Q is more severe when the modulation is applied to larger number of holes, as in the case of Design-2 (Section 4.6). For example, a strong band folding (i.e., efficient far-field radiation) can be obtained with Design-2 for the PhC cavities investigated in Section 6.4.2, however, the calculated Q value degrades by at least an order of magnitude compared to the initial batch of PhCs implemented with Design-1 (Section 6.4.1). Moreover, numerical simulations (Section 4.6) suggest that, for larger hole-size modulation amplitudes, Design-1 and Design-2 provide similar outcoupling efficiencies while the degradation of Q values is less severe in the case of Design-1. To investigate this experimentally, we reconsider our initial modulation scheme (Design-1, Section 6.4.1) where fewer holes are modulated (as shown in Figure 6.18a). But this time we increase the hole-size modulation amplitude ($\Delta r = 0.02a, 0.03a$ and $0.04a$) while realising PhC cavities with Design-1, compared to the initial attempt of $\Delta r = \pm 0.01a$ (Section 6.4.1).

This time, to implement the cavity devices with Design-1 (Figure 6.18a), we have utilised the multilayer resist process. As before, replicated arrays of PhC cavities have been fabricated where each array covers a range of lattice constants and hole-size modulation amplitudes ($\Delta r = 0.02a, 0.03a$ and $0.04a$). In this batch, the step size for lattice constant variation is reduced to a value of 3 nm, to minimise the gap between consecutive resonant modes. The SEM image of an example cavity with modulation $\Delta r = 0.03a$ is provided in Figure 6.18b. Next, we carry out resonant scattering measurements to characterise the fabricated cavities at room temperature. Similar to the case of Design-2 PhC cavities, the optimum cavity performance in terms of measured intensity and linewidths is obtained from Design-1 PhC cavities for a modulation amplitude of $\Delta r = 0.03a$. The near band-edge resonant modes from selected PhC cavities with the modulation amplitude of $\Delta r = 0.03a$ have been presented in Figure 6.18c. We maintain an exposure time of 120 s for near band-edge/D^0X transition wavelength measurements due to the low source and detection efficiency. For the room temperature configura-

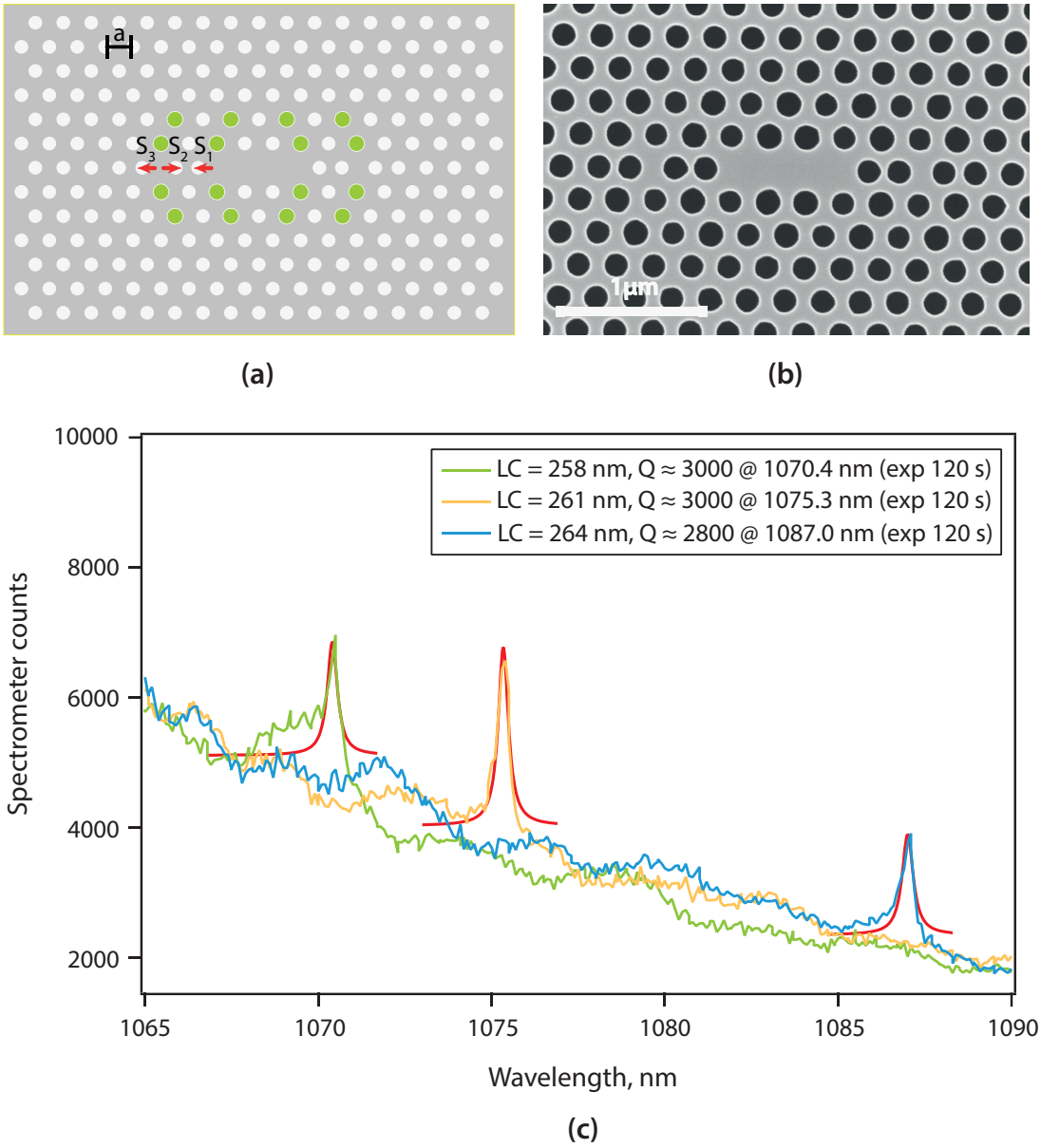

Figure 6.18: L3 PhC cavity with optimised far-field modulation: (a) the design schematic in which fewer number of holes have been modulated for tailoring far-field radiation pattern (labeled/designated as Design-1), (b) the SEM image of an example cavity with modulation $\Delta r = 0.03a$ and (c) Result of resonant scattering characterisation for L3 cavities with Design-1 and hole size modulation of $\Delta r = 0.03a$

tion, we have not observed any significant drift or vibration noise coupled to the system which permits a longer exposure time without significantly affecting the measurement outcome. Distinct fundamental modes appear around 1070.4 nm, 1075.3 nm and 1087 nm for lattice constants of 258 nm, 261 nm and 264 nm respectively, as shown in Figure 6.18c. The simulated quality factor found for Design-1 PhC cavities with the modulation amplitude of $\Delta r = 0.03a$ is around $25,000$. For the 300 g/mm grat-

ing used in our measurements, we get an effective resolution of approximately 100 pm around the ^{31}P $D^0X \rightarrow D^0$ transition wavelengths. Thus, we can measure quality factors efficiently up to a value of $\sim 10,000$ with our spectrometer system. However, at room temperature, we extract Q values around $3,000$, $3,000$ and $\sim 2,800$ for resonances at 1070.4 nm, 1075.3 nm and 1087 nm, respectively. We find the fitting errors/uncertainties are large ($\sim 10\%$) for these datasets and shows a tendency to worsen at longer wavelengths where detection is inefficient. From the characterisation result, two deviations from the expected cavity behaviour are observed. Firstly, the wavelength intervals between consecutive resonances are considerably different which should not be the case for any variation in lattice constant with a fixed step size (e.g., 3 nm in the present case). Secondly, we do not observe any noticeable and consistent rise in the Q values with increasing resonance wavelength. The material absorption decreases in silicon with increasing wavelength. So, if the PhC cavities are efficiently realised, a consistent increase in Q values is expected for resonances at longer wavelengths. This should be true even at room temperature where the maximum achievable Q values are seriously restricted around D^0X transition wavelengths due to high absorption. Thus, both of the observed discrepancies indicate that there exists some structural imperfections in our fabricated cavities. This indication of the structural imperfection becomes discernible if we carefully inspect the SEM image of the example cavity provided in Figure 6.18b. A careful inspection reveals that few of the holes suffer from a random imperfection and they have slightly deformed circular shapes. This deformation in the hole shapes is likely responsible for the unexpected behaviour observed in the measured cavities.

We found an unconventional and quick technique to spot devices with structural deformation and/or imperfect cavity mode. In our cross-polarisation setup, we use a high sensitivity, monochrome camera (WAT-910HX/RC) for surface inspection, focussing and cavity positioning before carrying out the resonant-scattering measurements. If the cross-polarisation (CP) configuration is implemented while imaging a PhC device with this monochrome camera, only the resonantly scattered light with favourable polarisations should be detected from the cavity region. So, in the camera image under the CP configuration, only a bright spot is expected from the cavity region within the PhC structure. However, in the case of PhC devices with structural imperfec-

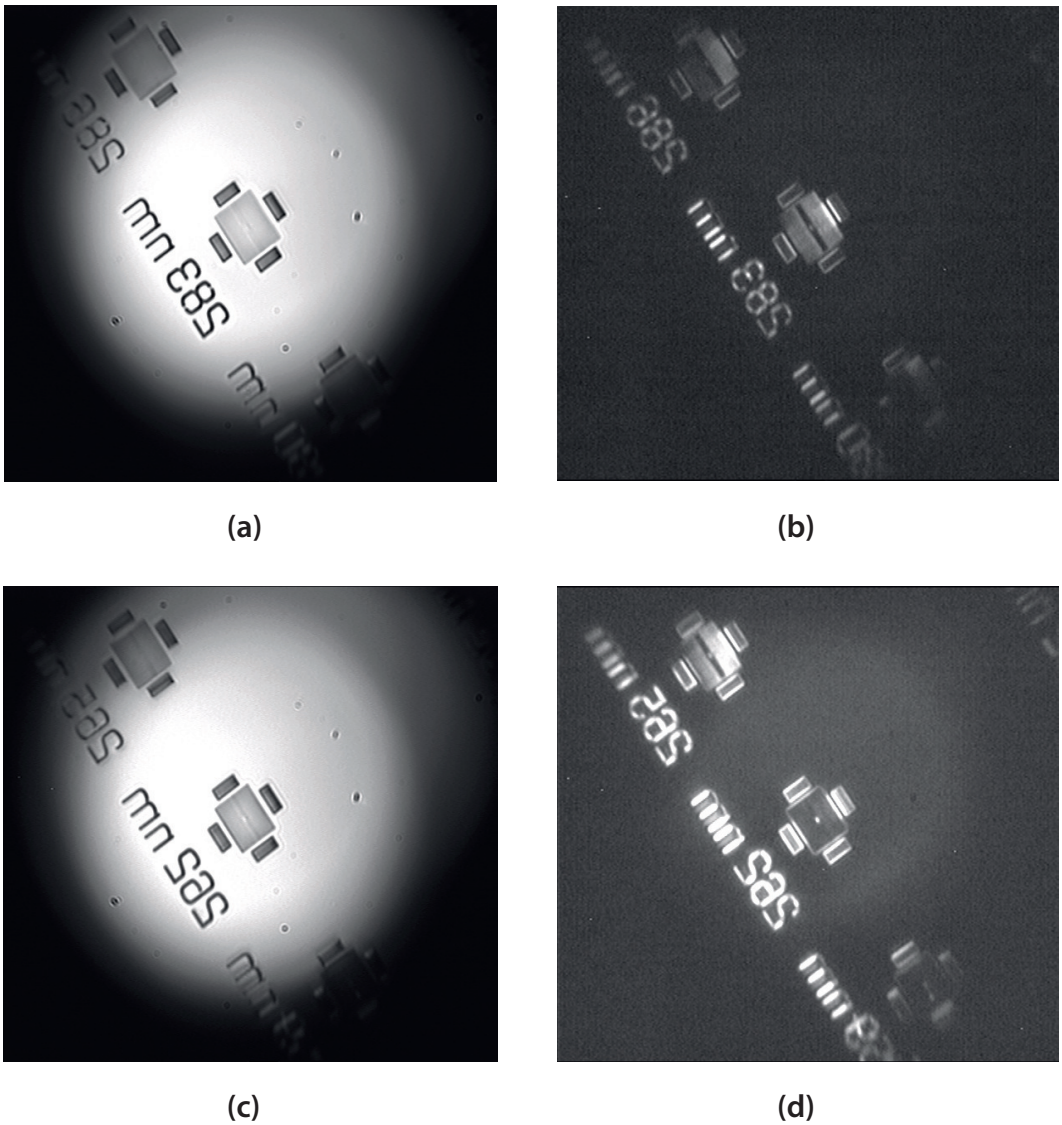

Figure 6.19: Cross-polarisation imaging for the detection of structural imperfection in L3 cavities: A device with structural imperfection has been imaged (a) without and (b) with cross-polarised configuration. Unwanted scattering from the non-cavity region of an imperfect device is captured in the cross-polarised image. A cavity with negligible structural deformation has also been imaged (c) without and (d) with cross-polarised configuration. For the second device, cross polarised image contains only a bright spot from the cavity region within the PhC structure.

tion, we observe strong deviation from this expected image. The random deformation in the PhC structure causes imperfect confinement/cavity modes and unwanted scattering from non-cavity region, which are captured in the camera image. In Figure 6.19, the camera images of cavities with and without noticeable structural deformation are shown for comparison. The cross-polarisation image of an imperfect device shows strong scattering from the non-cavity region of the PhC structure and rather weak response from the cavity itself, as shown in Figure 6.19b. On the other hand, in the case of

a reasonably efficient device, we observe bright cavity spot in very good contrast with the non-cavity PhC region, as in Figure 6.19d. Thus, the cross-polarisation imaging of the PhC devices provides a quick and convenient way to identify imperfect devices though it does not offer any quantitative measure of structural integrity. This quick technique has saved us a considerable amount of SEM imaging and measurement time.

Finally, our study in this section reveals that the structural integrity of our fabricated PhC cavities is a more critical issue for the device performance than the large hole-size modulation. Optimising the hole-size modulation alone does not help improving cavity quality factors when the structural imperfection is significant. So, we need to ensure both the optimum design and its reliable implementation in order to obtain the desired cavity performance.

6.5.3 Reducing fabrication errors

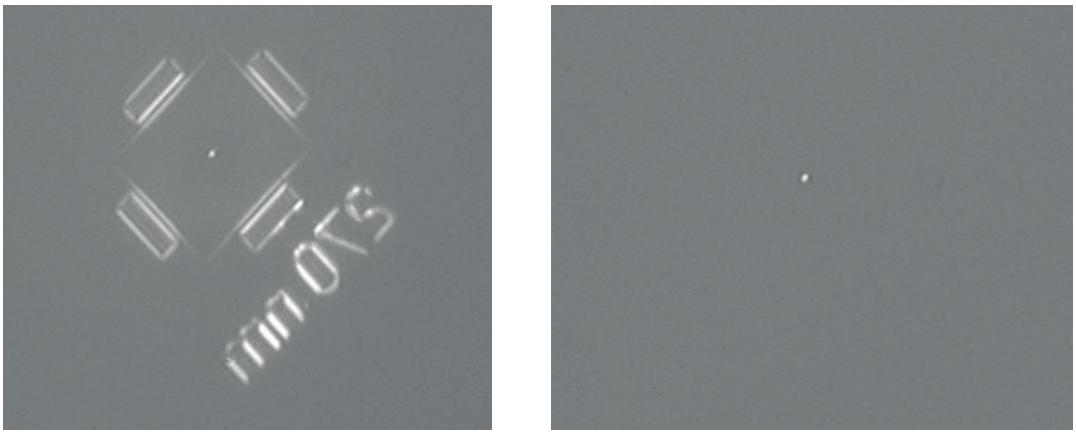

(a) (b)

Figure 6.20: Cross-polarisation image (CP) of cavity scattered light: (a) CP image of a PhC cavity fabricated with the revised EBL mask. The clean, bright spot from cavity scattering and strongly suppressed signals from non-cavity region indicate the structural integrity of the fabricated device. (b) The CP image after the implementation of the spatial filtering where only the cavity scattered light is allowed to pass. This spatially filtered signal is ultimately sent to the spectrometer through fiber coupling.

A single faulty step in a multistep fabrication process can cause significant deformation in the final product as the fault is carried and escalated by the following steps. When we started a careful investigation to find the faulty fabrication steps, a quite unexpected source of error has been identified. Some subtle incompatibility of the design file/mask with our EBL system software restricted the use of a special patterning fea-

ture of the system. This restriction in turn causes inefficient patterning of nanoscale features. The random patterning errors then get amplified in the following steps and appear as visible structural deformations in the fabricated PhC devices. So, we address the issue by changing the design files into ones compatible with our Raith EBL system (Section 5.5.4). The simple tweak in design file format significantly improve the patterning efficiency and no noticeable trace of structural deformation is observed in SEM and/or cross-polarisation images. A cross polarised image of an example PhC cavity is shown in Figure 6.20a where the bright spot from the cavity scattering and a suppressed background/non-cavity region indicate negligible structural deformation. The use of pinhole further filtered the collected signal and only allowed the resonantly scattered signal from the cavity to pass (Figure 6.20b).

We fabricated the cavities with Design-1 in a similar way to the previous batches, covering a range of lattice constants and replicated devices for redundancy. However, we only incorporate hole-modulation amplitudes of $\Delta r = 0.02a,\ 0.03a$ with Design-1 into the PhC devices for the far-field tailoring because the modulation amplitude of $\Delta r = 0.04a$ has not provided good result so far. We performed RS measurement on the new batch of PhC cavities at room temperature. Now, with an improved structural integrity, we find good results even from cavities with modulation of $\Delta r = 0.02a$. SEM and cross-polarisation images of an example cavity are shown in Figure 6.21a and b, respectively. The resonant modes around the D^0X transitions have been selected from the RS measurements of the PhC cavities (modulation, $\Delta r = 0.02a$) and presented in Figure 6.21c. Measurement times of 60 s and 120 s have been used in order to counteract the detection inefficiency and obtain comparable signal intensities. Fundamental cavity modes appear at 1070.4 nm, 1078.4 nm and 1084.8 nm for PhC lattice constants of 261 nm, 264 nm and 267 nm, respectively. The calculated quality factor for PhC cavities with Design-1 and modulation amplitude of $\Delta r = 0.02a$ is around 50,000; and the extracted values are $\sim 3,000$, $\sim 5,000$ and $\sim 6,300$ for resonances at 1070.4 nm, 1078.4 nm and 1084.8 nm, respectively with extraction errors around 10%. The results show that the wavelength spacing between consecutive resonances are more uniform than before - (8 nm and 6.4 nm) and that there a gradual rise in the quality factors for the fundamental modes with increasing wavelength. In the presence of material absorption, this is precisely the expected behaviour of efficiently realised silicon PhC

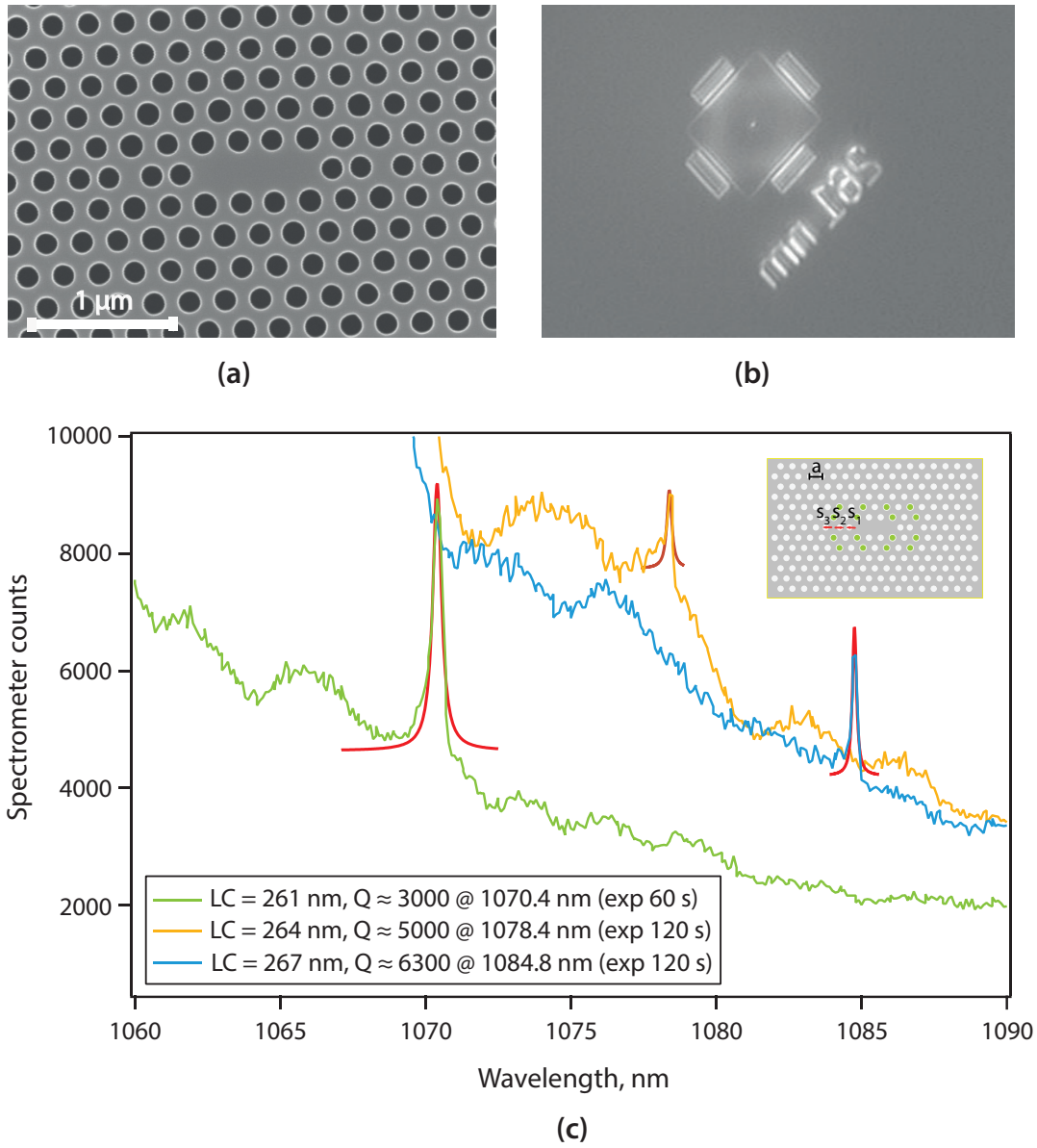

Figure 6.21: Characterisation of fine-tuned L3 PhC cavities with reduced fabrication error: (a) an SEM image of a cavity (LC = 261 nm) with reduced fabrication error. (b) The CP image of the same cavity which confirms the structural integrity of the device. (c) Result of resonant scattering characterisation for selected L3 cavities with Design-1 and hole size modulation of $\Delta r = 0.02a$

cavities with incremental lattice constants for resonances around ^{31}P D^{0}X transitions. A comparison of results from Figure 6.21 and Figure 6.18 shows that reducing fabrication error significantly lessen the discrepancy between the expected and measured behaviour of realised PhC cavities.

Once the optimum fabrication process and reasonable structural integrity have been realised, we test different design parameters on the L3 PhC cavity to check the consistency of our findings. Figure 6.22 shows an example of a single hole shifted PhC

cavity with modulation Design-1 ($\Delta r = 0.02a$) and its fundamental resonance. The calculated Q value for this cavity is around $\sim 29,000$. We implement this modified design to demonstrate the consistency of achievable Q values near D^0X transition wavelength. For the fabricated PhC cavity with lattice constant 262 nm (SEM and CP images are shown in Figure 6.22a and b), the fundamental cavity mode is detected at 1077 nm

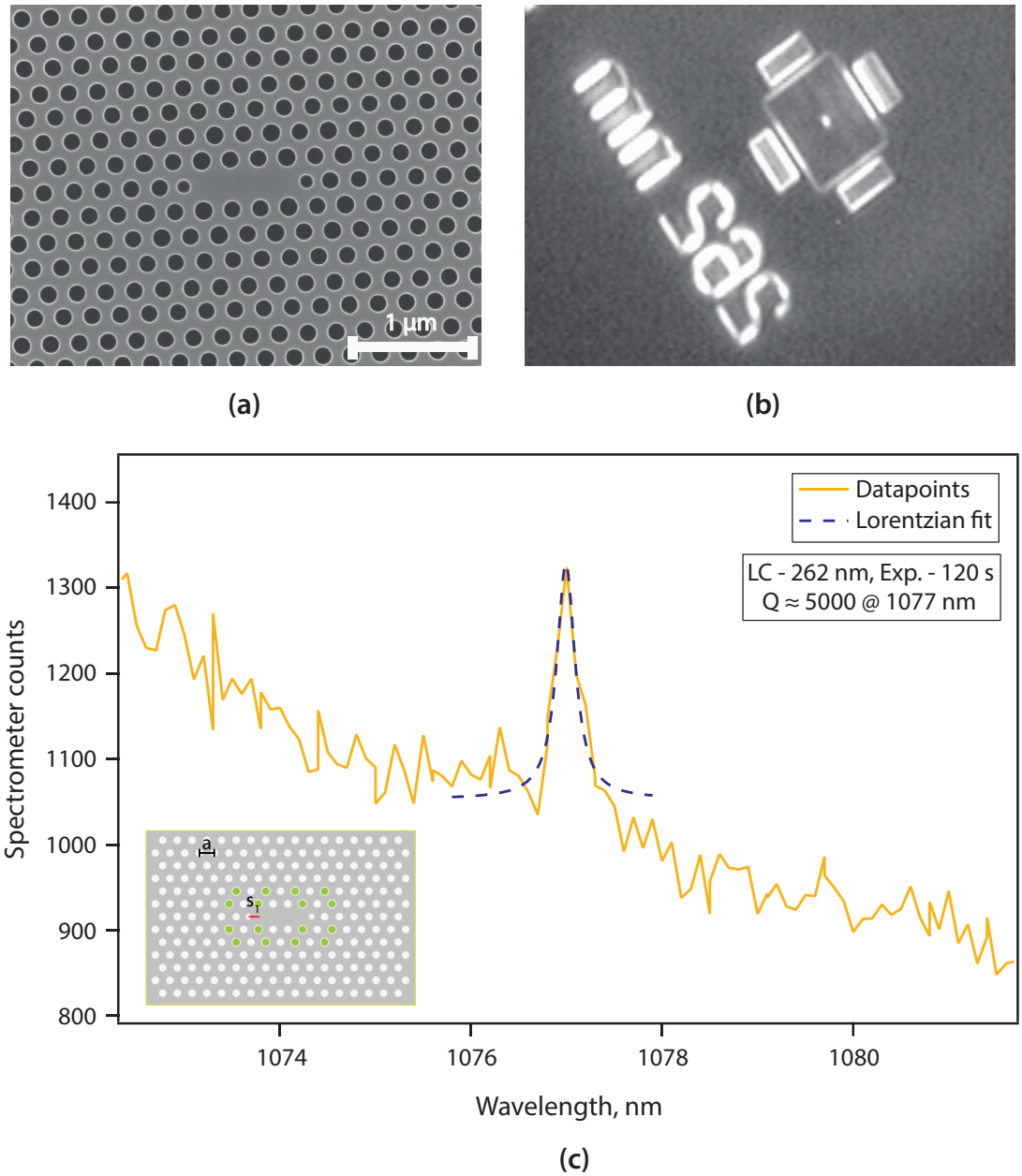

Figure 6.22: L3 PhC cavity with single hole shift and measured Q-value: (a) SEM image of a PhC cavity in which a single hole has been shifted for tuning the quality factor and $\Delta r = 0.02a$ with Design-1 has been implemented for far-field tailoring (b) cross-polarisation image of the cavity with lattice constant of 262 nm and (c) the result of the resonant-scattering measurement shows that the fundamental mode appears at a wavelength of 1077 nm with a quality factor of $\sim 5,000$.

through the RS measurement (Figure 6.22c). We extract a Q value of $\sim 5,000$ from the measured resonant mode. This result is reasonably consistent with that from the three hole shifted/fine-tuned cavity design both in terms of the position (1078.4 nm) and quality ($Q \sim 5,000$) of the resonance at near D^0X transition (Figure 6.21).

6.6 Cavities around D^0X transition wavelengths: summary of characterisation

In this chapter, we have characterised, for the very first time, silicon photonic structures/cavities designed and realised for enhancing ^{31}P D^0X emissions and photon collection. We carried out PL measurement on SiSILs which were fabricated in ^{31}P doped bulk silicon to improve the collection of ^{31}P D^0X emission. SiSILs are not capable of enhancing radiative emission, they can only improve the collection. A two-fold improvement in photon collection is obtained with this structures, but this does not provide the required enhancement to detect emissions from a single/few donors.

Silicon photonic cavities such as CBRs and PhC cavities can enhance both emission and collection of photons. We have developed a multilayer resist based fabrication recipe for realising silicon photonic cavities. Both CBR and PhC devices considered here are designed and implemented for enhanced collection of cavity scattered light. We have implemented the resonant-scattering (RS) measurement technique with a cross-polarisation setup for measuring the intrinsic quality factors of the fabricated photonic cavities. For CBR devices, we have extracted Q values of a few hundred both at room and low temperatures, limited by the cavity design. The calculated collection efficiency of such CBRs is around 40% for an NA of 0.65. Thus, a CBR, in principle, can enhance the total emission by two orders of magnitudes and permit detection of emission from few tens of donors. To obtain higher Q values, we have realised PhC cavities. The ^{31}P D^0X transition wavelengths in silicon are quite unfavourable for optical experiments due to the intrinsic absorption in silicon and the inefficiency of the excitation and detection resources. To minimise the detrimental effects of these constraints, we have implemented band-folding/far-field tailoring in PhC cavity designs. With an improved collection, we have optically characterised the fabricated PhC cavities through RS measurements. An intrinsic quality factor as high as $\sim 5,000$ has

been measured reliably around D^0X transition wavelengths (1078 nm) even at room temperature. However, the projection of absorption limited Q at room temperature in Figure 6.17 suggests that the achievable value at 1078 nm would be within $3000-4000$. We believe that the discrepancy between the calculated and measured Q values arises most probably from the combined effect of measurement uncertainties in the absorption coefficients [321] and our simplified estimation of Q values from absorption coefficients of bulk silicon and the cavity mode volume. Therefore, the calculated Q values in Figure 6.17 underestimates the measured quality factors at room temperature.

The maximum attainable Q values around D^0X transitions in silicon cavities at room temperature are fundamentally limited by the material absorption. This restriction is significantly lifted at low temperatures and in principle, very high Q values ($\sim 10^7$) can be obtained at wavelengths of our interest (Figure 6.17). In this work, we have not managed to characterise silicon cavities at low temperatures due to inefficient vibrational noise isolation from the measurement system. However, we have demonstrated Si PhC cavities, with sufficient Q values even at room temperature, required for accessing spins at single or few donors level. With an improved, noise-isolated measurement setup, we expect that the Si PhC cavity performance will only improve at low temperatures and allow us to access single donor spins.

Chapter 7

Summary and future works

7.1 Summary

The key focus of this work is to build a platform for enhancing the no-phonon emission from ^{31}P $D^0X \rightarrow D^0$ transitions in silicon, which has the potential to open the door for optical control over donor spins. The indirect bandgap nature of silicon results in very low radiative quantum efficiency, $QE \sim 10^{-4}$ for ^{31}P D^0X(NP) emissions [72]. To address this issue, we study photonic structures such as solid immersion lenses (SILs), circular Bragg resonators (CBRs) and photonic crystal (PhC) cavities, which can enhance no-phonon emission and/or its collection in silicon. Low temperature PL measurement of ^{31}P D^0Xs in Fz-Si reveals that we can detect D^0X(NP) emissions from around a thousand effective ^{31}P D^0X emitters inside the collection volume. This suggests that we need to enhance the total emission by at least three orders of magnitude in order to access a single donor. We have also investigated ion implantation in SOI samples for deterministic positioning of ^{31}P donors and optimised a post-implant thermal treatment recipe for damage repair and donor activation. An optimum ion dose window, necessary for observing ^{31}P D^0X(NP) emissions in silicon-on-insulator (SOI) substrates, has been identified which leads to a ~ 0.2 nm emission linewidth from ion implanted Fz-type SOI samples. Although the linewidth from implanted samples is broader than that of diffusion doped Fz-Si ones, there is still room for cavity mediated enhancement.

We have fabricated SiSILs using a Ne FIB milling tool. PL measurements have been carried out on SiSIL structures revealing that the use of SIL structures apparently increases the photon collection by around a factor of 2. With an optimised damage

repair step, photon collection can be further improved but SiSILs cannot enhance the emission rate. Thus, SILs are not by themselves useful for accessing a single or few donors. A low cost, bilayer resist based fabrication recipe has been optimised for realising photonic cavities, in which polymethyl methacrylate (PMMA) acts as soft EBL mask and CVD grown oxide layer as hard mask for dry etch. Using this bilayer resist process, we efficiently fabricate photonic cavities (CBRs and PhC cavities) designed for enhancing emission and extraction of photons from ^{31}P $D^0X \rightarrow D^0$ transitions. High-Q photonic cavities, in principle, can provide sufficient enhancement for detecting emission from single or few ^{31}P donors in silicon. However, to date, there has been no report of silicon photonic cavities in the literature which exhibit fundamental resonances around ^{31}P D^0X(NP) emission ($\sim$ 1078 nm) wavelengths. CBRs provide a design limited Q value of a few hundreds with cubic wavelength mode volume for resonances around 1078 nm. With an enhanced collection ($\eta_{\text{outcouple}} \sim 0.4$), such Q values can enable optical access to few tens of donors. Higher Q values are obtained with PhC cavities, though we had to carefully optimise the band folding/far-field radiation for reliably detecting the fundamental resonances. Room temperature optical characterisation of fabricated cavities unveils an absorption-limited Q of $\sim$ 5000 with $V_{\text{mode}} \sim 0.7(\lambda/n)^3$ at around 1078 nm. Implementation of the band folding in L3 PhC designs enhances the extraction significantly ($\eta_{\text{outcouple}} \approx 0.7$). The restriction of material absorption is significantly lifted at low temperatures and thus, higher Q values can be achieved. Such Si L3 PhC cavities are ideally capable of providing sufficient Purcell enhancement to optically detect single/few donor spins and play an important role in realising efficient spin-photon interfaces in Si systems.

We have just set the first stepping stone in the research for cavity-mediated enhancement of ^{31}P D^0X(NP) emission. So, in addition to the proof of principle demonstrations in this work, we have identified several critical challenges which have to be overcome before uncovering the full picture of the problem and availing the opportunities. First of all, the poor oscillator strength ($f_{\text{osc}} \sim 7.1 \times 10^{-6}$) and quantum efficiency $QE \sim 10^{-4}$ of ^{31}P D^0X(NP) emission impose a stringent requirement for a high Purcell enhancement ($F_{\text{P}} \gtrsim 100$) along with an improved outcoupling efficiency ($\eta_{\text{outcoupling}} > 0.1$). In practical cavity-emitter systems, achieving such a high Purcell enhancement is difficult due to non-ideal spatial matching and dipole alignment be-

tween an emitter and the cavity mode. Recently, a very large Purcell enhancement ($F_P \sim 650$) has been observed from coupling Er^{3+} emitters in yttrium orthosilicate (YSO) crystal to silicon PhC cavities [267]. This Er^{3+} 1.5 μm transition also have poor oscillator strength ($f_{osc} \sim 10^{-7}$) which is very similar to the case of ^{31}P D^0X emitters in silicon [71, 268]. However, the presence of strong non-radiative decay channel for ^{31}P D^0X emitters further complicate the issue of achieving high Purcell enhancements in silicon and it is not clear yet what would be the achievable upper limit for the radiative emission enhancement under consideration. Furthermore, due to the poor *QE* of ^{31}P D^0X(NP) emission, it is also not possible to optically locate single donors in the substrate prior to cavity fabrication. This makes deterministic positioning of ^{31}P emitters at the cavity field maxima challenging.

Second, a high quality (Fz-Si or isotopically purified ^{28}Si substrate) starting material and thin ($\sim$ 200 nm) SOI substrates are required for reducing inhomogeneous broadening and efficient cavity fabrication, respectively. These requirements pose significant restrictions for achieving a effective cavity-emitter system. Thus, ideally we would opt for an SOI substrate with a thin Fz-Si device layer on a thick BOX layer. However, such an SOI substrate fulfilling both material quality and thickness requirement is rare and expensive. We are still trying to extract some of those SOI wafers from the foundries. To demonstrate the proof of principle for ^{31}P D^0X(NP) emission from ion implanted SOI substrates, we have used commercially available SOI substrates with a 2 μm thick Fz-Si device layer. As already mentioned, such a thick device layer is not suitable for realising photonic cavities. We have attempted thinning the device layer through oxidation and subsequent HF etches. However, these thick SOI structures are formed with wafer bonding techniques and it turns out that thinning below $\sim$ 1 μm is not efficient for these bonded SOI substrates. Thus, we need to get thin, Fz-SOI wafers which would allow both ^{31}P D^0X(NP) emission and cavity fabrication in the top device layer.

Third, all the commercially available Fz-SOI wafers come with either intrinsic or high-resistivity ($\gtrsim$ 1 kΩ-cm) top silicon/device layer. Thus, for ^{31}P donor incorporation and deterministic positioning in the device layer of SOI substrates, we have utilised the ion implantation technique. Any ion implantation needs a subsequent thermal treatment for implant activation ad structural damage repair. We have attempted to

optimise a thermal treatment recipe, however, it turns out that damage repair and activation is are difficult in SOI structure. The recipe used in this work provides an activation efficiency of $\sim 1\%$. PL measurements reveal a ^{31}P D^0X(NP) emission linewidth of ~ 0.2 nm, which is double of the measurement limited linewidth from diffusion doped bulk Fz-Si sample and more than an order of magnitude broader than the actual ^{31}P D^0X(NP) emission linewidth (~ 5 pm) in bulk Fz-Si for moderate concentration of ^{31}P donors ($\sim 10^{15}$ cm^{-3}). This indicates the presence of a significant amount of structural damage/strain remaining in the thermally treated Fz-SOI sample. With a ~ 0.2 nm linewidth, implanted emitters can be effectively coupled to a cavity with $Q \lesssim 5000$. However, it will become an issue if coupling with higher Q cavities is necessary. So, further optimisation is required in post-implant treatment for more efficient activation and damage repair.

Fourth, the misalignment between the emitter dipole moment and the local cavity polarisation significantly degrades the attainable Purcell enhancement. An efficient way to address this issue is not available yet.

Fifth, we have not managed to find out the upper limit of achievable Q values for PhC cavities fabricated with our bilayer resist process. This is because our optical setup is not currently well suited for vibrational noise cancellation and carrying out high spatial-resolution measurements at low temperature. Therefore, we have only measured the absorption limited Q values for our cavities at room temperature. At sufficiently low temperatures, Q values are limited by structural imperfections. Thus, low temperature characterisation of fabricated devices would reveal if the bilayer resist process is suitable for obtaining very high Q PhC cavities.

Now, apart from few proposals [91, 107, 323, 324], no experimental research has been reported to date for the emission enhancement and optical read-out of ^{31}P donor spins in silicon. So, none of the issues discussed above has been carefully investigated/addressed before. Thus, addressing these challenges will be the milestones in our ultimate research goal of implementing an efficient ^{31}P emitter-cavity coupled system in silicon.

7.2 Future works

Acquiring Fz-SOI wafers with suitable dimensions ($\sim$ 200 nm device layer) for CBR/PhC cavity fabrication and building a efficient low temperature optical measurement setup are the next steps for the immediate future. As our wavelength range of interest (near the silicon band-edge) is unfavourable for optical experiments, any little improvement in the optics, detection and excitation systems is important. Incorporation of efficient detectors such as superconducting nanowire single photon detectors (SNSPDs) can relax the poor detection ($\sim$ 1% for Si CCDs) and strict cavity design issues around ^{31}P $D^0X \rightarrow D^0$ transition wavelengths since SNSPDs allow detection efficiencies up to 80% with dark count rates $\lesssim$ 10 Hz for such wavelengths. High stability, narrow linewidth tunable lasers can provide efficient excitation, filtering and cavity characterisation.

For deterministic positioning of ^{31}P donors at the cavity field maxima, scanning tunnelling microscope (STM) lithography can be utilised [52, 325]. As an alternative to ion implantation, the STM technique is non-invasive and can provide atomic level precision.

The potential of realising PhC cavities from bulk substrate [326, 327] should be explored in silicon. If realised efficiently, a PhC cavity from bulk silicon would significantly relax the requirements for thin Fz-SOI substrates, donor incorporation and deterministic positioning.

Thus, with suitable substrates (e.g., thin Fz-SOI wafers), deterministic ^{31}P donor positioning and an improved measurement system, practical cavity-mediated enhancements of ^{31}P D^0X(NP) emission should be obtained and once that goal is achieved, many more paths for interesting research will be opened!

Bibliography

[1] E Gibney. Physics: Quantum computer quest. *Nature*, 516(7529):24–26, December 2014. 1

[2] A Trabesinger. Quantum computing: towards reality. *Nature*, 543(7646):543S1a–S1, March 2017.

[3] M A Nielsen and I L Chuang. *Quantum computation and quantum information*. Cambridge University Press, 10th anniversary edition, 2010. 1, 2, 5

[4] T D Ladd, F Jelezko, R Laflamme, Y Nakamura, C Monroe, and J L O'Brien. Quantum computers. *Nature*, 464(7285):45–53, March 2010. 1, 2

[5] A Montanaro. Quantum algorithms: an overview. *npj Quantum Information*, 2(1):1, November 2016. 1

[6] R P Feynman. Simulating physics with computers. *International Journal of Theoretical Physics*, 21(6-7):467–488, June 1982. 1

[7] P W Shor. Polynomial-Time Algorithms for Prime Factorization and Discrete Logarithms on a Quantum Computer. *SIAM Journal on Computing*, 26(5):1484–1509, October 1997. 1

[8] L K Grover. Quantum Mechanics Helps in Searching for a Needle in a Haystack. *Physical Review Letters*, 79(2):325–328, July 1997. 1

[9] N Gisin and R Thew. Quantum communication. *Nature Photonics*, 1(3):165–171, March 2007. 1

[10] G Cariolaro. *Quantum Communications*. Signals and Communication Technology. Springer International Publishing, Cham, 2015.

[11] S-K Liao, W-Q Cai, W-Y Liu, L Zhang, Y Li, J-G Ren, J Yin, Q Shen, Y Cao, Z-P Li, F-Z Li, X-W Chen, L-H Sun, J-J Jia, J-C Wu, X-J Jiang, J-F Wang, Y-M Huang, Q Wang, Y-L Zhou, L Deng, T Xi, L Ma, T Hu, Q Zhang, Y-A Chen, N-L Liu, X-B Wang, Z-C Zhu, C-Y Lu, R Shu, C-Z Peng, J-Y Wang, and J-W Pan. Satellite-to-ground quantum key distribution. *Nature*, 549(7670):43–47, August 2017. 1, 2

[12] W Nawrocki. *Introduction to Quantum Metrology*. Springer International Publishing, 2015. 1

[13] V Giovannetti, S Lloyd, and L Maccone. Advances in quantum metrology. *Nature Photonics*, 5(4):222–229, April 2011. 1

[14] R van METER, K M ITOH, and T D Ladd. ARCHITECTURE-DEPENDENT EXECUTION TIME OF SHOR'S ALGORITHM. In *Proceedings of the International Symposium*, pages 183–188. WORLD SCIENTIFIC, November 2011. 1

[15] R van METER and C Horsman. A blueprint for building a quantum computer. *Communications of the ACM*, 56(10):84–93, October 2013. 1, 2

[16] A Kandala, A Mezzacapo, K Temme, M Takita, M Brink, J M Chow, and J M Gambetta. Hardware-efficient variational quantum eigensolver for small molecules and quantum magnets. *Nature*, 549(7671):242–246, September 2017. 1

[17] R Srivastava, I Choi, and T Cook. The Commercial Prospects for Quantum Computing . Technical report, EPSRC, December 2016. 1, 2

[18] V Dunjko, J M Taylor, and H J Briegel. Quantum-Enhanced Machine Learning. *Physical Review Letters*, 117(13):130501, September 2016. 1

[19] J Biamonte, P Wittek, N Pancotti, P Rebentrost, N Wiebe, and S Lloyd. Quantum machine learning. *Nature*, 549(7671):195–202, September 2017. 1

[20] A V Frolov. Can a quantum computer be applied for numerical weather prediction? *Russian Meteorology and Hydrology*, 42(9):545–553, October 2017. 2

[21] X-W Yao, H Wang, Z Liao, M-C Chen, J Pan, J Li, K Zhang, X Lin, Z Wang, Z Luo, W Zheng, J Li, M Zhao, X Peng, and D Suter. Quantum Image Processing and Its Application to Edge Detection: Theory and Experiment. *Physical Review X*, 7(3):433, September 2017. 2

[22] L C Comandar, M Lucamarini, B Fröhlich, J F Dynes, A W Sharpe, S W B Tam, Z L Yuan, R V Penty, and A J Shields. Quantum key distribution without detector vulnerabilities using optically seeded lasers. *Nature Photonics*, 10(5):312–316, April 2016. 2

[23] K-A Suominen. Physical Implementation of Large-Scale Quantum Computation. In *Handbook of Natural Computing*, pages 1493–1520. Springer Berlin Heidelberg, Berlin, Heidelberg, 2012. 2

[24] D Loss and D P DiVincenzo. Quantum computation with quantum dots. *Physical Review A*, 57(1):120–126, January 1998. 2

[25] D P DiVincenzo. The Physical Implementation of Quantum Computation. *Fortschritte der Physik*, 48(9-11):771–783, September 2000. 2, 5

[26] F A Zwanenburg, A S Dzurak, A Morello, M Y Simmons, L C L Hollenberg, G Klimeck, S Rogge, S N Coppersmith, and M A Eriksson. Silicon quantum electronics. *Reviews of Modern Physics*, 85(3):961–1019, July 2013. 3, 4, 6, 7

[27] J J L Morton, D R McCamey, M A Eriksson, and S A Lyon. Embracing the quantum limit in silicon computing. *Nature*, 479(7373):345–353, November 2011. 3, 4, 5

[28] C Lo and J Morton. Silicon's second act. *IEEE Spectrum*, 51(8):37–43, July 2014.

[29] J J Pla, K Y Tan, J P Dehollain, W H Lim, J J L Morton, F A Zwanenburg, D N

Jamieson, A S Dzurak, and A Morello. High-fidelity readout and control of a nuclear spin qubit in silicon. *Nature*, 496(7445):334–338, April 2013. 5, 10

[30] M Urdampilleta, A Chatterjee, C C Lo, T Kobayashi, J Mansir, S Barraud, A C Betz, S Rogge, M F Gonzalez-Zalba, and J J L Morton. Charge Dynamics and Spin Blockade in a Hybrid Double Quantum Dot in Silicon. *Physical Review X*, 5(3):031024, August 2015.

[31] M Veldhorst, J C C Hwang, C H Yang, A W Leenstra, B de Ronde, J P Dehollain, J T Muhonen, F E Hudson, K M Itoh, A Morello, and A S Dzurak. An addressable quantum dot qubit with fault-tolerant control-fidelity. *Nature Nanotechnology*, 9(12):981–985, December 2014. 5

[32] M Veldhorst, C H Yang, J C C Hwang, W Huang, J P Dehollain, J T Muhonen, S Simmons, A Laucht, F E Hudson, K M Itoh, A Morello, and A S Dzurak. A two-qubit logic gate in silicon. *Nature*, 526(7573):410–414, October 2015.

[33] E Kawakami, P Scarlino, D R Ward, F R Braakman, D E Savage, M G Lagally, Mark Friesen, S N Coppersmith, M A Eriksson, and L M K Vandersypen. Electrical control of a long-lived spin qubit in a Si/SiGe quantum dot. *Nature Nanotechnology*, 9(9):666–670, August 2014. 5

[34] L R Schreiber and H Bluhm. Quantum computation: Silicon comes back. *Nature Nanotechnology*, 9(12):966–968, December 2014. 5

[35] P Harvey-Collard, N T Jacobson, M Rudolph, J Dominguez, G A Ten Eyck, J R Wendt, T Pluym, J K Gamble, M P Lilly, M Pioro-Ladrière, and M S Carroll. Coherent coupling between a quantum dot and a donor in silicon. *Nature Communications*, 8(1):143, October 2017. 3

[36] J J Pla, K Y Tan, J P Dehollain, W H Lim, J J L Morton, D N Jamieson, A S Dzurak, and A Morello. A single-atom electron spin qubit in silicon. *Nature*, 489(7417):541–545, September 2012. 5

[37] A V Gusev and A D Bulanov. High-purity silicon isotopes 28Si, 29Si, and 30Si. *Inorganic Materials*, 44(13):1395–1408, November 2008. 5

[38] K M ITOH and H Watanabe. Isotope engineering of silicon and diamond for quantum computing and sensing applications. *MRS Communications*, 4(4):143–157, December 2014.

[39] N V Abrosimov, D G Aref'ev, P Becker, H Bettin, A D Bulanov, M F Churbanov, S V Filimonov, V A Gavva, O N Godisov, A V Gusev, T V Kotereva, D Nietzold, M Peters, A M Potapov, H J Pohl, A Pramann, H Riemann, P-T Scheel, R Stosch, S Wundrack, and S Zakel. A new generation of 99.999% enriched 28Si single crystals for the determination of Avogadro's constant. *Metrologia*, 54(4):599–609, July 2017. 5

[40] M Steger, K Saeedi, M L W Thewalt, S Simmons, H Riemann, N V Abrosimov, P Becker, and H J Pohl. Quantum information storage for over 180 s using donor spins in a 28Si "semiconductor vacuum". *Science*, 336(6086):1280–1283, June 2012. 5

[41] K Saeedi, S Simmons, J Z Salvail, P Dluhy, H Riemann, N V Abrosimov, P Becker, H-J Pohl, J J L Morton, and M L W Thewalt. Room-Temperature Quantum Bit Storage Exceeding 39 Minutes Using Ionized Donors in Silicon-28. *Science*, 342(6160):830–833, November 2013. 5

[42] E S Petersen, A M Tyryshkin, S Simmons, E Abe, S Tojo, K M Itoh, M L W Thewalt, and S A Lyon. Nuclear spin decoherence of neutral P31donors in silicon: Effect of environmental Si29nuclei. *Physical Review B*, 93(16):1311, April 2016.

[43] J T Muhonen, J P Dehollain, A Laucht, F E Hudson, R Kalra, T Sekiguchi, K M ITOH, D N Jamieson, J C McCallum, A S Dzurak, and A Morello. Storing quantum information for 30 seconds in a nanoelectronic device. *Nature Nanotechnology*, 9(12):986–991, October 2014. 5

[44] J P D Lorenzana. *High-fidelity microwave control of single-atom spin qubits in silicon*. PhD thesis, Electrical Engineering & Telecommunications, Faculty of Engineering, UNSW, 2014. 5

[45] J T Muhonen, A Laucht, S Simmons, J P Dehollain, R Kalra, F E Hudson, S Freer, K M Itoh, D N Jamieson, J C McCallum, A S Dzurak, and A Morello. Quantifying the quantum gate fidelity of single-atom spin qubits in silicon by randomized benchmarking. *Journal of Physics: Condensed Matter*, 27(15):154205, April 2015. 5

[46] G Tosi, F A Mohiyaddin, V Schmitt, S Tenberg, R Rahman, G Klimeck, and A Morello. Silicon quantum processor with robust long-distance qubit couplings. *Nature Communications*, 8(1):450, September 2017. 5

[47] D Culcer, Ł Cywiński, Q Li, X Hu, and S D Sarma. Quantum dot spin qubits in silicon: Multivalley physics. *Physical Review B*, 82(15):155312, October 2010. 5

[48] A M Tyryshkin, S Tojo, J J L Morton, H Riemann, N V Abrosimov, P Becker, H-J Pohl, T Schenkel, M L W Thewalt, K M ITOH, and S A Lyon. Electron spin coherence exceeding seconds in high-purity silicon. *Nature Materials*, 11(2):143–147, December 2011. 5, 10

[49] S R Schofield, N J Curson, M Y Simmons, F J Rueß, T Hallam, L Oberbeck, and R G Clark. Atomically Precise Placement of Single Dopants in Si. *Physical Review Letters*, 91(13):136104, September 2003. 6

[50] M Fuechsle, J A Miwa, S Mahapatra, H Ryu, S Lee, O Warschkow, L C L Hollenberg, G Klimeck, and M Y Simmons. A single-atom transistor. *Nature Nanotechnology*, 7(4):242–246, April 2012.

[51] S J Hile, M G House, E Peretz, J Verduijn, D Widmann, T Kobayashi, S Rogge, and M Y Simmons. Radio frequency reflectometry and charge sensing of a precision placed donor in silicon. *Applied Physics Letters*, 107(9):093504, August 2015.

[52] J R Petta. Atom-by-Atom Construction of a Quantum Device. *ACS Nano*, 11(3):2382–2386, February 2017. 6, 208

[53] P Y Yu and M Cardona. *Fundamentals of Semiconductors*. Graduate Texts in Physics. Springer Berlin Heidelberg, Berlin, Heidelberg, 2010. 6, 7, 8

[54] K S Ilkhchy. *Optical NMR Study of ^{31}P Donor Spins in Isotopically Enriched ^{28}Si*. PhD thesis, Simon Fraser Unniversity, July 2014. 6, 7, 8, 11, 12

[55] I Pelant and J Valenta. Luminescence of excitons. In *Luminescence Spectroscopy of Semiconductors*. Oxford University Press, Oxford, 2012. 7

[56] M A Lampert. Mobile and Immobile Effective-Mass-Particle Complexes in Nonmetallic Solids. *Physical Review Letters*, 1(12):450–453, December 1958. 7

[57] J R Haynes. Experimental Proof of the Existence of a New Electronic Complex in Silicon. *Physical Review Letters*, 4(7):361–363, April 1960. 7, 55

[58] G Feher. Electron Spin Resonance Experiments on Donors in Silicon. I. Electronic Structure of Donors by the Electron Nuclear Double Resonance Technique. *Physical Review*, 114(5):1219–1244, June 1959. 8

[59] A Yang. *Optical hyperpolarization and detection of electron and nuclear spins of phosphorus donors in highly enriched 28Si*. PhD thesis, May 2010. 8, 64, 104

[60] M Tajima. Determination of boron and phosphorus concentration in silicon by photoluminescence analysis. *Applied Physics Letters*, 32(11):719–721, 1978. 8, 53, 54, 58

[61] K Nishikawa and R Barrie. PHONON BROADENING OF IMPURITY SPECTRAL LINES: I. GENERAL THEORY. *Canadian Journal of Physics*, 41(7):1135–1173, July 1963. 8

[62] P Lodahl. Quantum-dot based photonic quantum networks. *Quantum Science and Technology*, 3(1):013001, January 2018. 9, 10

[63] M Atatüre, D Englund, N Vamivakas, S-Y Lee, and J Wrachtrup. Material platforms for spin-based photonic quantum technologies. *Nature Reviews Materials*, 491:421, April 2018. 9, 10

[64] L Gordon, J R Weber, J B Varley, A Janotti, D D Awschalom, and C G Van de Walle. Quantum computing with defects. *MRS Bulletin*, 38(10):802–807, October 2013. 10

[65] W B Gao, A Imamoglu, H Bernien, and R Hanson. Coherent manipulation, measurement and entanglement of individual solid-state spins using optical fields. *Nature Photonics*, 9(6):363–373, June 2015. 9, 11

[66] P Michler, editor. *Single Semiconductor Quantum Dots — Peter Michler — Springer*. Springer-Verlag, Berlin Heidelberg, 2009. 9, 10

[67] R W Kelsall, I W Hamley, and M Geoghegan, editors. *Nanoscale Science and Technology*. Kelsall/Nanoscale Science and Technology. John Wiley & Sons, Ltd, Chichester, UK, December 2005. 9, 10

[68] J N Becker and C Becher. Coherence Properties and Quantum Control of Silicon Vacancy Color Centers in Diamond. *physica status solidi (a)*, 214(11):1700586, September 2017. 9, 10

[69] D J Christle, P V Klimov, C F de las Casas, K Szász, V Ivády, V Jokubavicius, J Ul Hassan, M Syväjärvi, W F Koehl, T Ohshima, N T Son, E Janzén, Á Gali, and D D Awschalom. Isolated Spin Qubits in SiC with a High-Fidelity Infrared Spin-to-Photon Interface. *Physical Review X*, 7(2):021046, June 2017. 10

[70] T Zhong, J M Kindem, E Miyazono, and A Faraon. Nanophotonic coherent light–matter interfaces based on rare-earth-doped crystals. *Nature Communications*, 6(1):8206, September 2015. 10, 96, 106, 132

[71] P J Dean, W F Flood, and G Kaminsky. Absorption due to Bound Excitons in Silicon. *Physical Review*, 163(3):721–725, November 1967. 10, 103, 106, 206

[72] W Schmid. Auger lifetimes for excitons bound to neutral donors and acceptors in Si. *physica status solidi (b)*, 84(2):529–540, 1977. 103, 106, 204

[73] A Yang, M Steger, T Sekiguchi, M L W Thewalt, J W Ager, and E E Haller. Homogeneous linewidth of the ^{31}P bound exciton transition in silicon. *Applied Physics Letters*, 95(12):122113, September 2009. 10, 104

[74] M H Abobeih, J Cramer, M A Bakker, N Kalb, M Markham, D J Twitchen, and T H Taminiau. One-second coherence for a single electron spin coupled to a

multi-qubit nuclear-spin environment. *Nature Communications*, 9(1):29, June 2018. 10

[75] F C Waldermann, P Olivero, J Nunn, K Surmacz, Z Y Wang, D Jaksch, R A Taylor, I A Walmsley, M Draganski, P Reichart, A D Greentree, D N Jamieson, and S Prawer. Creating diamond color centers for quantum optical applications. *Diamond and Related Materials*, 16(11):1887–1895, November 2007.

[76] S Kilin, A Nizovtsev, J F Roch, F TREUSSART, J Wrachtrup, and F Jelezko. DIAMOND-BASED QUANTUM INFORMATION TECHNOLOGIES AT A NANOSCALE LEVEL. In *Proceedings of the International Conference on Nanomeeting 2007*, pages 3–13. WORLD SCIENTIFIC, November 2011. 10

[77] L J Rogers, K D Jahnke, T Teraji, L Marseglia, C Müller, B Naydenov, H Schauffert, C Kranz, J Isoya, L P McGuinness, and F Jelezko. Multiple intrinsically identical single-photon emitters in the solid state. *Nature Communications*, 5(1), August 2014. 10

[78] B Pingault, D-D Jarausch, C Hepp, L Klintberg, J N Becker, M Markham, C Becher, and M Atatüre. Coherent control of the silicon-vacancy spin in diamond. *Nature Communications*, 8:15579, May 2017. 10

[79] G W Morley, M Warner, A M Stoneham, P T Greenland, J van Tol, C W M Kay, and G Aeppli. The initialization and manipulation of quantum information stored in silicon by bismuth dopants. *Nature Materials*, 9(9):725–729, August 2010. 10

[80] Y Yamamoto, T D Ladd, D Press, S Clark, K Sanaka, C Santori, D Fattal, K M Fu, S Höfling, S Reitzenstein, and A Forchel. Optically controlled semiconductor spin qubits for quantum information processing. *Physica Scripta*, 2009(T137):014010, December 2009. 11

[81] K De Greve. *Towards Solid-State Quantum Repeaters*. Springer Theses. Springer International Publishing, Heidelberg, 2013.

[82] A Predojević and M W Mitchell, editors. *Engineering the Atom-Photon Interaction*. Nano-Optics and Nanophotonics. Springer International Publishing, Cham, 2015.

[83] M S Blok, N Kalb, A Reiserer, T H Taminiau, and R Hanson. Towards quantum networks of single spins: analysis of a quantum memory with an optical interface in diamond. *Faraday Discuss.*, September 2015. 11

[84] D Press, T D Ladd, B Zhang, and Y Yamamoto. Complete quantum control of a single quantum dot spin using ultrafast optical pulses. *Nature*, 456(7219):218–221, November 2008. 11, 12

[85] J Berezovsky, M H Mikkelsen, N G Stoltz, L A Coldren, and D D Awschalom. Picosecond coherent optical manipulation of a single electron spin in a quantum dot. *Science*, 320(5874):349–352, April 2008. 12

[86] L C Bassett, F J Heremans, D J Christle, C G Yale, G Burkard, B B Buckley, and D D Awschalom. Ultrafast optical control of orbital and spin dynamics in a solid-state defect. *Science*, 345(6202):1333–1337, September 2014.

[87] Y Chu, M Markham, D J Twitchen, and M D Lukin. All-optical control of a single electron spin in diamond. *Physical Review A*, 91(2):021801, February 2015. 11

[88] A Yang, M Steger, D Karaiskaj, M L W Thewalt, M Cardona, K M Itoh, H Riemann, N V Abrosimov, M F Churbanov, A V Gusev, A D Bulanov, A K Kaliteevskii, O N Godisov, P Becker, H J Pohl, J W Ager, and E E Haller. Optical Detection and Ionization of Donors in Specific Electronic and Nuclear Spin States. *Physical Review Letters*, 97(22):227401, November 2006. 11, 12, 58, 104

[89] A Yang, M Steger, T Sekiguchi, M L W Thewalt, T D Ladd, K M Itoh, H Riemann, N V Abrosimov, P Becker, and H J Pohl. Simultaneous Subsecond Hyperpolarization of the Nuclear and Electron Spins of Phosphorus in Silicon by Optical Pumping of Exciton Transitions. *Physical Review Letters*, 102(25):257401, June 2009. 58

[90] C C Lo, M Urdampilleta, P Ross, M F Gonzalez-Zalba, J Mansir, S A Lyon, M L W Thewalt, and J J L Morton. Hybrid optical–electrical detection of donor electron spins with bound excitons in silicon. *Nature Materials*, 14(5):490–494, March 2015. 12, 55, 60

[91] K-M C Fu, T D Ladd, C Santori, and Y Yamamoto. Optical detection of the spin state of a single nucleus in silicon. *Physical Review B*, 69(12):125306, March 2004. 12, 62, 89, 207

[92] M Steger, T Sekiguchi, A Yang, K Saeedi, M E Hayden, M L W Thewalt, K M Itoh, H Riemann, N V Abrosimov, P Becker, and H J Pohl. Optically-detected NMR of optically-hyperpolarized 31P neutral donors in 28Si. *Journal of Applied Physics*, 109(10):102411, May 2011. 12

[93] K-M C Fu, S M Clark, C Santori, C R Stanley, M C Holland, and Y Yamamoto. Ultrafast control of donor-bound electron spins with single detuned optical pulses. *Nature Physics*, 4(10):780–784, August 2008. 12

[94] S Iwamoto and Y Arakawa. Enhancement of Light Emission from Silicon by Utilizing Photonic Nanostructures. *IEICE Transactions on Electronics*, E95.C(2):206–212, 2012. 12, 41

[95] W D A M de Boer, D Timmerman, K Dohnalová, I N Yassievich, H Zhang, W J Buma, and T Gregorkiewicz. Red spectral shift and enhanced quantum efficiency in phonon-free photoluminescence from silicon nanocrystals. *Nature Nanotechnology*, 5(12):878–884, December 2010. 13

[96] A Irrera, P Artoni, F Iacona, E F Pecora, G Franzo, M Galli, B Fazio, S Boninelli, and F Priolo. Quantum confinement and electroluminescence in ultrathin silicon nanowires fabricated by a maskless etching technique. *Nanotechnology*, 23(7):075204, February 2012. 13, 14

[97] A Irrera, M J Lo Faro, C D'Andrea, A A Leonardi, P Artoni, B Fazio, R A Picca, N Cioffi, S Trusso, G Franzò, P Musumeci, F Priolo, and F Iacona. Light-emitting silicon nanowires obtained by metal-assisted chemical etching. *Semiconductor Science and Technology*, 32(4):043004, April 2017. 13, 14

[98] D Shiri, A Verma, C R Selvakumar, and M P Anantram. Reversible Modulation of Spontaneous Emission by Strain in Silicon Nanowires. *Scientific reports*, 2:461, June 2012. 13

[99] F Priolo, T Gregorkiewicz, M Galli, and T F Krauss. Silicon nanostructures for photonics and photovoltaics. *Nature Nanotechnology*, 9(1):19–32, January 2014.

[100] L Vivien and L Pavesi. *Handbook of Silicon Photonics*. Series in Optics and Optoelectronics. CRC Press, Taylor & Francis Group, April 2013. 13

[101] K Kůsová, I Pelant, and J Valenta. Bright trions in direct-bandgap silicon nanocrystals revealed by low-temperature single-nanocrystal spectroscopy. *Light: Science & Applications*, 4(10):e336, October 2015. 13, 14

[102] J Valenta, B Bruhn, and J Linnros. Coexistence of 1D and Quasi-0D Photoluminescence from Single Silicon Nanowires. *Nano Letters*, 11(7):3003–3009, July 2011. 13

[103] K Dohnalová, A N Poddubny, A A Prokofiev, W D de Boer, C P Umesh, J MJ Paulusse, H Zuilhof, and T Gregorkiewicz. Surface brightens up Si quantum dots: direct bandgap-like size-tunable emission. *Light: Science & Applications*, 2(1):e47, January 2013.

[104] S S Walavalkar, A P Homyk, C E Hofmann, M D Henry, C Shin, H A Atwater, and A Scherer. Size tunable visible and near-infrared photoluminescence from vertically etched silicon quantum dots. *Applied Physics Letters*, 98(15):153114, April 2011. 13

[105] S S Walavalkar, C E Hofmann, A P Homyk, M D Henry, H A Atwater, and A Scherer. Tunable Visible and Near-IR Emission from Sub-10 nm Etched Single-Crystal Si Nanopillars. *Nano Letters*, 10(11):4423–4428, November 2010. 13

[106] K Kůsová, P Hapala, J Valenta, P Jelínek, O Cibulka, L Ondič, and I Pelant. Direct Bandgap Silicon: Tensile-Strained Silicon Nanocrystals. *Advanced Materials Interfaces*, 1(2):n/a–n/a, April 2014. 14

[107] B Yan, R Rurali, and Á Gali. Ab Initio Study of Phosphorus Donors Acting as Quantum Bits in Silicon Nanowires. *Nano Letters*, 12(7):3460–3465, June 2012. 14, 207

[108] I F Crowe, N Papachristodoulou, M P Halsall, N P Hylton, O Hulko, A P Knights, P Yang, R M Gwilliam, M Shah, and A J Kenyon. Donor ionization in size controlled silicon nanocrystals: The transition from defect passivation to free electron generation. *Journal of Applied Physics*, 113(2):024304, January 2013. 14

[109] S M Mansfield and G S Kino. Solid immersion microscope. *Applied Physics Letters*, 57(24):2615–2616, December 1990. 16

[110] G S Kino. Applications and theory of the solid immersion lens. *Optoelectronics '99 - Integrated Optoelectronic Devices*, 3609:56–66, June 1999.

[111] C Matthiesen. *Coherent photons from a solid-state artificial atom*. PhD thesis, University of Cambridge, 2013. 16

[112] W L Barnes, G Björk, J M Gérard, P Jonsson, J A E Wasey, P T Worthing, and V Zwiller. Solid-state single photon sources: light collection strategies. *The European Physical Journal D - Atomic, Molecular, Optical and Plasma Physics*, 18(2):197–210, February 2002. 16

[113] V Zwiller, T Aichele, and O Benson. Quantum optics with single quantum dot devices. *New Journal of Physics*, 6(1):96–96, July 2004.

[114] K A Serrels, E Ramsay, P A Dalgarno, B Gerardot, J O'Connor, R H Hadfield, R Warburton, and D Reid. Solid immersion lens applications for nanophotonic devices. *Journal of Nanophotonics*, 2(1):021854–021854–29, January 2008.

[115] S Moehl, H Zhao, B D Don, S Wachter, and H Kalt. Solid immersion lens-enhanced nano-photoluminescence: Principle and applications. *Journal of Applied Physics*, 93(10):6265–6272, May 2003. 16

[116] E M Purcell. Spontaneous emission probabilities at radio frequencies. *Physical Review*, 69:681, 1946. 16, 19

[117] S Haroche and D Kleppner. Cavity Quantum Electrodynamics. In *Confined Electrons and Photons*, pages 849–855. Springer US, Boston, MA, 1995. 16, 17

[118] S Haroche and J-M Raimond. *Exploring the Quantum*. Oxford University Press, 2006. 16, 17

[119] K Semba. Entanglement Control of Superconducting Qubit Single Photon System. *NTT Technical Review*, 6, 2008. 17

[120] G Khitrova, H M Gibbs, M Kira, S W Koch, and A Scherer. Vacuum Rabi splitting in semiconductors. *Nature Physics*, 2(2):81–90, February 2006. 18, 19

[121] C Santori, D Fattal, and Y Yamamoto. *Single-photon Devices and Applications*. Wiley-VCH, 2010. 18

[122] J Wolters. *Integrated Quantum Hybrid Systems*. Pan Stanford, September 2015. 18, 19

[123] C Santori, D Fattal, J Vuckovic, G S Solomon, and Y Yamamoto. Indistinguishable photons from a single-photon device. *Nature*, 419(6903):594–597, September 2002. 19

[124] A Dousse, J Suffczyński, A Beveratos, O Krebs, A Lemaître, I Sagnes, J Bloch, P Voisin, and P Senellart. Ultrabright source of entangled photon pairs. *Nature*, 466(7303):217–220, July 2010. 19

[125] E M Purcell, H C Torrey, and R V Pound. Resonance Absorption by Nuclear Magnetic Moments in a Solid. *Physical Review*, 69(1-2):37–38, January 1946. 20

[126] J Joannopoulos, S Johnson, J Winn, and R Meade. *Photonic Crystals: Molding the Flow of Light*. Princeton University Press, second edition, 2008. 23, 24, 25, 26, 27, 28, 29, 31, 32, 35, 36, 37, 39, 42, 49

[127] C Kittel. *Introduction to solid state physics*. Wiley, Hoboken, NJ, 8th edition, 2005. 28

[128] U P Dharanipathy. *On the investigation of light-matter interactions in slab photonic crystal cavities*. PhD thesis, EPFL, 2014. 29

[129] C C Cheng, V Arbet-Engels, A Scherer, and E Yablonovitch. Nanofabricated three dimensional photonic crystals operating at optical wavelengths. *Physica Scripta*, 1996(T68):17–20, 1996. 29

[130] S Y Lin, J G Fleming, D L Hetherington, B K Smith, R Biswas, K M Ho, M M Sigalas, W Zubrzycki, S R Kurtz, and J Bur. A three-dimensional photonic crystal operating at infrared wavelengths. *Nature*, 394(6690):251–253, July 1998.

[131] Y A Vlasov, X-Z Bo, J C Sturm, and D J Norris. On-chip natural assembly of silicon photonic bandgap crystals. *Nature*, 414(6861):289–293, November 2001.

[132] S Takahashi, K Suzuki, M Okano, M Imada, T Nakamori, Y Ota, K Ishizaki, and S Noda. Direct creation of three-dimensional photonic crystals by a top-down approach. *Nature Materials*, 8(9):721–725, August 2009.

[133] R W Tjerkstra, L A Woldering, J M van den Broek, F Roozeboom, I D Setija, and W L Vos. Method to pattern etch masks in two inclined planes for three-dimensional nano- and microfabrication. *Journal of Vacuum Science & Technology B, Nanotechnology and Microelectronics: Materials, Processing, Measurement, and Phenomena*, 29(6):061604, December 2011.

[134] D A Grishina, C A M Harteveld, L A Woldering, and W L Vos. Method for making a single-step etch mask for 3D monolithic nanostructures. *Nanotechnology*, 26(50):505302, December 2015.

[135] K Ishizaki, K Suzuki, and S Noda. Fabrication of 3D Photonic Crystals toward Arbitrary Manipulation of Photons in Three Dimensions. *Photonics*, 3(2):36, June 2016. 29, 38

[136] S Arpiainen, K Vynck, J Dekker, M Kapulainen, W Khunsin, T Aalto, M Mulot, G K Oberlehrer, R Zentel, C M S Torres, D Cassagne, and J Ahopelto. Self-assembled three-dimensional inverted photonic crystals on a photonic chip. *physica status solidi (a)*, 214(9):1700039, September 2017. 29

[137] M-L Hsieh, P Kuang, J A Bur, S John, and S-Y Lin. Review on recent progress of three-dimensional optical photonic crystal. *AIP Conference Proceedings*, pages 204–209, February 2015. 29

[138] Christopher Kang. *Multiple-Hole Defects: Optimizing Light-Matter Interaction in Photonic Crystal Cavities*. PhD thesis, Vanderbilt University, 2011. 31

[139] M H Nguyen. *Two dimensional photonic crystal devices*. PhD thesis, Delft University of Technology, 2012. 36

[140] M Qi, E Lidorikis, P T Rakich, S G Johnson, J D Joannopoulos, E P Ippen, and H I Smith. A three-dimensional optical photonic crystal with designed point defects. *Nature*, 429(6991):538–542, June 2004. 38

[141] S A Rinne, F García-Santamaría, and P V Braun. Embedded cavities and waveguides in three-dimensional silicon photonic crystals. *Nature Photonics*, 2(1):52–56, December 2007.

[142] K Aoki, D Guimard, M Nishioka, M Nomura, S Iwamoto, and Y Arakawa. Coupling of quantum-dot light emission with a three-dimensional photonic-crystal nanocavity. *Nature Photonics*, 2(11):688–692, October 2008.

[143] A Tandaechanurat, S Ishida, D Guimard, M Nomura, S Iwamoto, and Y Arakawa. Lasing oscillation in a three-dimensional photonic crystal nanocavity with a complete bandgap. *Nature Photonics*, 5(2):91–94, December 2010.

[144] N Hauke, A Tandaechanurat, T Zabel, T Reichert, H Takagi, M Kaniber, S Iwamoto, D Bougeard, J J Finley, G Abstreiter, and Y Arakawa. A three-dimensional silicon photonic crystal nanocavity with enhanced emission from embedded germanium islands. *New Journal of Physics*, 14(8):083035, August 2012.

[145] S Iwamoto, S Takahashi, T Tajiri, and Y Arakawa. Semiconductor Three-Dimensional Photonic Crystals with Novel Layer-by-Layer Structures. *Photonics*, 3(2):34, June 2016. 38

[146] A Laucht. *Semiconductor quantum optics with tailored photonic nanostructures*. PhD thesis, Technical University of Munich, 2011. 39, 40

[147] A R A Chalcraft, S Lam, D O'Brien, T F Krauss, M Sahin, D Szymanski, D Sanvitto, R Oulton, M S Skolnick, A M Fox, D M Whittaker, H Y Liu, and M Hopkinson. Mode structure of the L3 photonic crystal cavity. *Applied Physics Letters*, 90(24):241117, June 2007. 40

[148] S L Portalupi, M Galli, C Reardon, T F Krauss, L O'Faolain, L C Andreani, and D Gerace. Planar photonic crystal cavities with far-field optimization for high coupling efficiency and quality factor. *Optics Express*, 18(15):16064–16073, July 2010. 40, 122

[149] Y Lai, S Pirotta, G Urbinati, D Gerace, M Minkov, V Savona, A Badolato, and M Galli. Genetically designed L3 photonic crystal nanocavities with measured quality factor exceeding one million. *Applied Physics Letters*, 104(24):–, 2014. 40, 43, 119, 122

[150] M Fujita, Y Tanaka, and S Noda. Light Emission From Silicon in Photonic Crystal Nanocavity. *Selected Topics in Quantum Electronics, IEEE Journal of*, 14(4):1090–1097, 2008. 40, 178

[151] N Hauke, T Zabel, K Müller, M Kaniber, A Laucht, D Bougeard, G Abstreiter, J J Finley, and Y Arakawa. Enhanced photoluminescence emission from two-dimensional silicon photonic crystal nanocavities. *New Journal of Physics*, 12(5):053005, 2010. 40, 178

[152] A David, C Weisbuch, and H Benisty. Optimization of Light-Diffracting Photonic-Crystals for High Extraction Efficiency LEDs. *Journal of Display Technology*, 3(2):133–148, June 2007. 42

[153] A R Knapitsch. *Photonic Crystals: Enhancing the Light Output of Scintillation Based Detectors*. PhD thesis, 2012. 42

[154] K Vahala, editor. *Optical Microcavities*, volume 5 of *Advanced Series in Applied Physics*. World Scientific Publishing Co. Pte. Ltd., 2004. 42, 49

[155] K Thyagarajan and A Ghatak. *Lasers: Fundamentals and Applications*. Graduate Texts in Physics. Springer US, Boston, MA, 2011. 42, 49

[156] P B Deotare, M W McCutcheon, I W Frank, M Khan, and M Lončar. High quality factor photonic crystal nanobeam cavities. *Applied Physics Letters*, 94(12):121106, March 2009. 43, 104, 116, 117, 118, 119

[157] H Sekoguchi, Y Takahashi, T Asano, and S Noda. Photonic crystal nanocavity with a Q-factor of ˜9 million. *Optics Express*, 22(1):916–924, January 2014. 43, 119

[158] W H Bragg and W L Bragg. The Reflection of X-rays by Crystals. *Proceedings of the Royal Society of London A: Mathematical, Physical and Engineering Sciences*, 88(605):428–438, July 1913. 43

[159] G P Agrawal. *Applications of Nonlinear Fiber Optics*. Academic Press, Elsevier, second edition, 2008.

[160] H P Myers. *Introductory Solid State Physics, Second Edition*. Taylor & Francis Ltd, second edition edition, 1997. 43

[161] H Wenzel, R Guther, A M Shams-Zadeh-Amiri, and P Bienstman. A Comparative Study of Higher Order Bragg Gratings: Coupled-Mode Theory Versus Mode Expansion Modeling. *Quantum Electronics, IEEE Journal of*, 42(1):64–70, January 2006. 44

[162] J Scheuer and A Yariv. Coupled-waves approach to the design and analysis of bragg and photonic crystal annular resonators. *Quantum Electronics, IEEE Journal of*, 39(12):1555–1562, December 2003. 45, 46, 47, 51

[163] J Scheuer and A Yariv. Circular photonic crystal resonators. *Physical Review E*, 70(3):036603, September 2004. 46, 47, 51

[164] X Sun and A Yariv. Surface-emitting circular DFB, disk-, and ring-Bragg resonator lasers with chirped gratings. II: nonuniform pumping and far-field patterns. *Optics Express*, 17(1):1–6, January 2009.

[165] X Sun and A Yariv. Surface-Emitting Circular Bragg Lasers – A Promising Next-Generation On-Chip Light Source for Optical Communications. In *Frontiers in Guided Wave Optics and Optoelectronics*. InTech, February 2010. 45, 46, 47, 48, 50, 51

[166] X Sun and A Yariv. Surface-emitting circular DFB, disk-, and ring-Bragg resonator lasers with chirped gratings: a unified theory and comparative study. *Optics Express*, 16(12):9155–9164, June 2008. 47, 48, 51, 52

[167] X Sun. *Supermode Si/III–V lasers and circular Bragg lasers*. PhD thesis, April 2010. 46, 47, 50, 51, 52

[168] J Scheuer, W M J Green, G A DeRose, and A Yariv. InGaAsP annular Bragg lasers: theory, applications, and modal properties. *Selected Topics in Quantum Electronics, IEEE Journal of*, 11(2):476–484, May 2005. 47

[169] X Sun, J Scheuer, and A Yariv. Optimal Design and Reduced Threshold in Vertically Emitting Circular Bragg Disk Resonator Lasers. *Selected Topics in Quantum Electronics, IEEE Journal of*, 13(2):359–366, April 2007.

[170] D Labilloy, H Benisty, C Weisbuch, T F Krauss, C J M Smith, R Houdré, and U Oesterle. High-finesse disk microcavity based on a circular Bragg reflector. *Applied Physics Letters*, 73(10):1314–1316, October 1998.

[171] A K Saha, M Uemukai, and T Suhara. InGaAs circular-grating-coupled surface emitting laser with focusing function fabricated by electron beam writing with circular scanning. *Optical Review*, 21(3):206–209, June 2014.

[172] J Gu, X Xi, J Ma, Z Yu, and X Sun. Parity–time-symmetric circular Bragg lasers: a proposal and analysis. *Scientific reports*, 6:37688, November 2016. 47

[173] A J Bay. *Optical integrated devices with circular-grating resonators*. PhD thesis, ETH, Zurich, 2006. 47, 49

[174] A Jebali, D Erni, S Gulde, R F Mahrt, and W Bächtold. Analytical calculation of the Q factor for circular-grating microcavities. *Journal of the Optical Society of America B*, 24(4):906–915, April 2007. 47, 49

[175] E Hecht. *Optics*. Pearson Education Limited, 5th edition edition, 2016. 48

[176] M Davanço, M T Rakher, D Schuh, A Badolato, and K Srinivasan. A circular dielectric grating for vertical extraction of single quantum dot emission. *Applied Physics Letters*, 99(4):041102, July 2011. 50, 51, 52, 96, 104, 105, 107, 108, 109

[177] S Ateş, L Sapienza, M Davanço, A Badolato, and K Srinivasan. Bright Single-Photon Emission From a Quantum Dot in a Circular Bragg Grating Microcavity. *Selected Topics in Quantum Electronics, IEEE Journal of*, 18(6):1711–1721, 2012. 52, 109

[178] L Sapienza, M Davanço, A Badolato, and K Srinivasan. Nanoscale optical positioning of single quantum dots for bright and pure single-photon emission. *Nature Communications*, 6:7833, July 2015. 50, 51, 52, 107, 108, 109

[179] W M J Green, J Scheuer, G DeRose, and A Yariv. Vertically emitting annular Bragg lasers using polymer epitaxial transfer. *Applied Physics Letters*, 85(17):3669–3671, October 2004. 50

[180] M Y Su and R P Mirin. Enhanced light extraction from circular Bragg grating coupled microcavities. *Applied Physics Letters*, 89(3):033105, July 2006. 51, 52

[181] D Taillaert, W Bogaerts, P Bienstman, T F Krauss, P Van Daele, I Moerman, S Verstuyft, K De Mesel, and R Baets. An out-of-plane grating coupler for efficient butt-coupling between compact planar waveguides and single-mode fibers. *Quantum Electronics, IEEE Journal of*, 38(7):949–955, July 2002. 51, 108

[182] J Qi, T Kaiser, A E Klein, M Steinert, T Pertsch, F Lederer, and C Rockstuhl. Enhancing resonances of optical nanoantennas by circular gratings. *Optics Express*, 23(11):14583–14595, June 2015. 51

[183] J Zheng, A C Liapis, E H Chen, C T Black, and D Englund. Chirped circular dielectric gratings for near-unity collection efficiency from quantum emitters in bulk diamond. *Optics Express*, 25(26):32420–32435, December 2017. 51

[184] I Pelant and J Valenta. *Luminescence Spectroscopy of Semiconductors*. Oxford University Press, Oxford, 2012. 53, 63

[185] S Binetti, A Le Donne, and A Sassella. Photoluminescence and infrared spectroscopy for the study of defects in silicon for photovoltaic applications. *Solar Energy Materials and Solar Cells*, 130:696–703, November 2014. 53

[186] A S Kaminskii, L I Kolesnik, B M Leiferov, and Y E Pokrovskii. Luminescence analysis of group III and V impurities in silicon. *Journal of Applied Spectroscopy*, 36(5):516–520, May 1982. 53, 58

[187] A Henry, J Svensson, E Janzén, and B Monemar. New photoluminescence lines in selenium-doped silicon. *Materials Science and Engineering: B*, 4(1-4):261–264, October 1989. 53

[188] X Zhang, M Kleverman, and J Olajos. A photoluminescence study of selenium-diffused silicon. *Semiconductor Science and Technology*, 14(12):1076–1079, December 1999. 53

[189] M Singh, E C Lightowlers, G Davies, C Jeynes, and K J Reeson. Isoelectronic bound exciton photoluminescence from a metastable defect in sulphur-doped silicon. *Materials Science and Engineering: B*, 4(1-4):303–307, October 1989. 54

[190] A Yang, M Steger, M L W Thewalt, M Cardona, H Riemann, N V Abrosimov, M F Churbanov, A V Gusev, A D Bulanov, I D Kovalev, A K Kaliteevskii, O N Godisov, P Becker, H J Pohl, J W Ager, and E E Haller. High resolution photoluminescence of sulphur- and copper-related isoelectronic bound excitons in highly enriched 28Si. *Physica B: Condensed Matter*, 401-402:593–596, December 2007.

[191] H Sumikura, E Kuramochi, H Taniyama, and M Notomi. Ultrafast spontaneous emission of copper-doped silicon enhanced by an optical nanocavity. *Scientific reports*, 4(1):5040, May 2014. 54, 55, 106, 178

[192] M Tajima, A Yusa, and T Abe. Characterization of Residual Impurities in Highly

Pure Si Crystals by Photoluminescence Technique. *Japanese Journal of Applied Physics*, 19(S1):631, January 1980. 54

[193] M L W Thewalt. Details of the structure of bound excitons and bound multiexciton complexes in Si. *Canadian Journal of Physics*, 55(17):1463–1480, September 1977.

[194] P Pichler. *Intrinsic Point Defects, Impurities, and Their Diffusion in Silicon*. Computational Microelectronics. Springer Vienna, Vienna, 2004. 54

[195] M Steger. *Transition-Metal Defects in Silicon*. Springer Theses. Springer Berlin Heidelberg, Berlin, Heidelberg, 2013. 54

[196] J Weber, R J Davis, H U Habermeier, W D Sawyer, and M Singh. Photoluminescence detection of impurities introduced in silicon by dry etching processes. *Applied Physics A*, 41(3):175–178, November 1986. 54

[197] I Broussell, V A Karasyuk, and M L W Thewalt. Photoluminescence method for detecting trace levels of iron in ultrapure silicon. *Applied Physics Letters*, 78(20):3070–3072, May 2001. 54

[198] M Tajima. Photoluminescence Analyses of Shallow Impurities in Silicon. *Japanese Journal of Applied Physics*, 16(12):2263–2264, December 1977. 54

[199] M Tajima. Correlation between Photoluminescence Spectra and Impurity Concentrations in Silicon. *Japanese Journal of Applied Physics*, 16(12):2265–2266, December 1977. 54

[200] H Nakayama, T Nishino, and Y Hamakawa. Analysis of the Exciton Luminescence of Silicon for Characterization of the Content of Impurities. *Japanese Journal of Applied Physics*, 19(3):501–511, March 1980. 54

[201] M Tajima and M Nomura. Photoluminescence Analysis of Impurities in Epitaxial Silicon Crystals. *Japanese Journal of Applied Physics*, 20(10):L697–L700, October 1981. 54

[202] S T Davey, J R Davis, K J Reeson, and P L F Hemment. Photoluminescence studies of silicon-on-insulator substrates formed by oxygen implantation. *Applied Physics Letters*, 52(6):465–467, February 1988. 55

[203] M Tajima, A Ogura, T Karasawa, and A Mizoguchi. Defect Analysis in Bonded and H + Split Silicon-on-Insulator Wafers by Photoluminescence Spectroscopy and Transmission Electron Microscopy. *Japanese Journal of Applied Physics*, 37(10B):L1199–L1201, 1998. 55

[204] M Tajima, Z Li, and R Shimidzu. Photoluminescence Mapping System Applicable to 300 mm Silicon-on-Insulator Wafers. *Japanese Journal of Applied Physics*, 41(Part 2, No. 12B):L1505–L1507, December 2002. 55

[205] H Sumikura, K Nishiguchi, Y Ono, A Fujiwara, and M Notomi. Bound exciton photoluminescence from ion-implanted phosphorus in thin silicon layers. *Optics Express*, 19(25):25255–25262, December 2011. 55, 58, 74, 76, 85, 95

[206] H Sumikura, E Kuramochi, H Taniyama, and M Notomi. Enhanced electron-hole droplet emission from surface-oxidized silicon photonic crystal nanocavities. *Optics Express*, 24(2):1072–1081, January 2016. 55, 63, 178

[207] M L W Thewalt. Excited states of donor bound excitons and bound multiexciton complexes in silicon. *Solid State Communications*, 21(10):937–939, March 1977. 58

[208] I Broussell, J A H Stotz, and M L W Thewalt. Method for shallow impurity characterization in ultrapure silicon using photoluminescence. *Journal of Applied Physics*, 92(10):5913–5916, November 2002. 58

[209] L Novotny and B Hecht. *Principles of Nano-Optics*. Cambridge University Press, Cambridge, second edition, 2012. 59

[210] M A Green and M J Keevers. Optical properties of intrinsic silicon at 300 K. *Progress in Photovoltaics: Research and Applications*, 3(3):189–192, January 1995. 59

[211] M Abramowitz, J C Long, and M W Davidson. **Interaction of Photons with Silicon**, July 2000.

[212] M A Green. Self-consistent optical parameters of intrinsic silicon at 300K including temperature coefficients. *Solar Energy Materials and Solar Cells*, 92(11):1305–1310, November 2008. 59

[213] S Meroli. Czochralski vs Float Zone: growing mono-crystalline silicon, 2012. 59, 69

[214] F Shimura, editor. *Oxygen in Silicon*, volume 42 of *Semiconductors and Semimetals*. Elsevier, 1994.

[215] F Shimura. ***Semiconductor silicon crystal technology*** . Academic Press, San Diego, 1989. 59, 69

[216] J Katsura, H Nakayama, T Nishino, and Y Hamakawa. Characterization of Thermally-Induced Defects in CZ–Si by Room-Temperature Photoluminescence. *Japanese Journal of Applied Physics*, 21(5R):712–715, May 1982. 61

[217] M Tajima, A Kanamori, S Kishino, and T Iizuka. Photoliminescence Analysis of 'New Donors' in Silicon. *Japanese Journal of Applied Physics*, 19(12):L755–L758, December 1980.

[218] A V Mudryi, A I Patuk, I A Shakin, A G Ulyashin, R Job, W R Fahrner, A Fedotov, A Mazanik, and N Drozdov. Impurities and defects in multicrystalline silicon for solar cells: low-temperature photoluminescence investigations. *Solar Energy Materials and Solar Cells*, 72(1-4):503–508, April 2002. 61

[219] M P Ross. *Bound exciton-assisted spin-to-charge conversion of donors in silicon*. PhD thesis, University College London, July 2017. 63, 192

[220] Y H Chen and S A Lyon. Photoluminescence and diffusivity of free excitons in doped silicon. *IEEE Journal of Quantum Electronics*, 25(5):1053–1055, May 1989. 63

[221] M Tajima, S Ibuka, and S Arai. Condensate luminescence under ultraviolet excitation: application to the study of ultrathin SOI layers. *Materials Science and Engineering: B*, 91-92:10–15, April 2002. 63

[222] S Franssila. *Introduction to Microfabrication*. John Wiley & Sons, Ltd, Chichester, UK, September 2010. 65, 68, 80, 137, 138

[223] S A Campbell. *Fabrication Engineering at the Micro- and Nanoscale*. Oxford University Press, fourth edition edition, November 2012. 65, 66, 148

[224] J F Ziegler. SRIM - The Stopping and Range of Ions in Matter. 2013. 67, 68

[225] J F Ziegler, J P Biersack, and M D Ziegler. *SRIM, the stopping and range of ions in matter*. SRIM Co., 2008. 68

[226] D N Jamieson, W I L Lawrie, S G Robson, A M Jakob, B C Johnson, and J C McCallum. Deterministic doping. *Materials Science in Semiconductor Processing*, 62:23–30, May 2017. 68

[227] J van Donkelaar, C Yang, A D C Alves, J C McCallum, C Hougaard, B C Johnson, F E Hudson, A S Dzurak, A Morello, D Spemann, and D N Jamieson. Single atom devices by ion implantation. *Journal of Physics: Condensed Matter*, 27(15):154204, April 2015.

[228] S Freer, S Simmons, A Laucht, J T Muhonen, J P Dehollain, R Kalra, F A Mohiyaddin, F E Hudson, K M ITOH, J C McCallum, D N Jamieson, A S Dzurak, and A Morello. A single-atom quantum memory in silicon. *Quantum Science and Technology*, 2(1):015009, March 2017. 68

[229] J R Liefting, J S Custer, and F W Saris. Time evolution of dislocation formation in ion implanted silicon. *Materials Science and Engineering: B*, 25(1):60–67, June 1994. 69

[230] K S Jones, S Prussin, and E R Weber. A systematic analysis of defects in ion-implanted silicon. *Applied Physics A*, 45(1):1–34, January 1988.

[231] R J Schreutelkamp, J S Custer, J R Liefting, W X Lu, and F W Saris. Pre-amorphization damage in ion-implanted silicon. *Materials Science Reports*, 6(7-8):275–366, August 1991.

[232] M Tamura. Damage formation and annealing of ion implantation in Si. *Materials Science Reports*, 6(4-5):141–214, April 1991. 69

[233] R C Newman. Defects in silicon. *Reports on Progress in Physics*, 45(10):1163–1210, October 1982. 69

[234] L Antos, J Gyulai, N Q Khanh, and L Frey. End-of-range disorder influenced by inherent oxygen in silicon. *Nuclear Instruments and Methods in Physics Research Section B: Beam Interactions with Materials and Atoms*, 71(4):399–405, September 1992. 69, 70

[235] T Sands, J Washburn, E Myers, and D K Sadana. On the origins of structural defects in BF 2+-implanted and rapid-thermally-annealed silicon: Conditions for defect-free regrowth. *Nuclear Instruments and Methods in Physics Research Section B: Beam Interactions with Materials and Atoms*, 7-8:337–341, March 1985. 70

[236] J Pelleg and B M Ditchek. Diffusion of P in a novel three-dimensional device based on Si–TaSi2 eutectic. *Journal of Applied Physics*, 73(2):699–706, June 1998. 70

[237] D J Fisher, editor. *Diffusion in Silicon*. 10 Years of Research. Scitec Publications, 1998.

[238] Y H Lee, A Pogany, H B Harrison, and J S Williams. Rapid thermal annealing of phosphorus implanted silicon. *IAEA*, November 1985. 70

[239] N Yu, K B Ma, C Kirschbaum, K Varahramyan, and W K Chu. Enhancement of electrical activation of ion-implanted phosphorus in Si(100) through two-step thermal annealing. *Applied Physics Letters*, 63(8):1125–1127, August 1993. 71

[240] A R Chelyadinskii and H I H Taher. Diffusion of ion-implanted phosphorus in silicon. *physica status solidi (a)*, 142(2):331–338, April 1994.

[241] T E Seidel, D J Lischner, C S Pai, R V Knoell, D M Maher, and D C Jacobson. A review of rapid thermal annealing (RTA) of B, BF 2 and As ions implanted into silicon. *Nuclear Instruments and Methods in Physics Research Section B: Beam Interactions with Materials and Atoms*, 7-8:251–260, March 1985. 71

[242] C Christofides. Annealing kinetics of defects of ion-implanted and furnace-annealed silicon layers: thermodynamic approach. *Semiconductor Science and Technology*, 7(11):1283–1294, November 1992. 72

[243] H Boo, J-H Lee, M G Kang, K Lee, S Kim, H C Hwang, W J Hwang, H O Kang, S Park, S J Tark, and D Kim. Effect of High-Temperature Annealing on Ion-Implanted Silicon Solar Cells. *International Journal of Photoenergy*, 2012(12):1–6, 2012. 72

[244] M Tamura. Secondary defects in phosphorus-implanted silicon. *Applied Physics Letters*, 23(12):651, 1973. 76

[245] T Schenkel, A Persaud, S J Park, J Nilsson, J Bokor, J A Liddle, R Keller, D H Schneider, D W Cheng, and D E Humphries. Solid state quantum computer development in silicon with single ion implantation. *Journal of Applied Physics*, 94(11):7017–7024, November 2003. 76

[246] S PARK. Processing issues in top–down approaches to quantum computer development in silicon. *Microelectronic Engineering*, 73-74:695–700, June 2004. 76

[247] M Bruel, B Aspar, and A-J Auberton-Hervé. Smart-Cut: A New Silicon On Insulator Material Technology Based on Hydrogen Implantation and Wafer Bonding*1. *Japanese Journal of Applied Physics*, 36(3S):1636–1641, March 1997. 77

[248] L Yingxue, Z Zhikuan, N Weihua, X Zhang, and W Yangyuan. SOI wafer achieved by smart-cut process. In *Fifth International Conference on Solid-State and Integrated Circuit Technology-ICSICT'98*, pages 761–764. IEEE, October 1998. 77

[249] S J Fonash. An Overview of Dry Etching Damage and Contamination Effects. *Journal of The Electrochemical Society*, 137(12):3885–3892, December 1990. 84

[250] B M Arora, R Pinto, and R S Babu. Reactive ion-etching-induced damage in silicon using SF6 gas mixtures. *Journal of Vacuum Science & Technology B: Microelectronics Processing and Phenomena*, June 1998. 84

[251] H Norström, H O Blom, M Ostling, A N Larsen, J Keinonen, and S Berg. Silicon surface damage caused by reactive ion etching in fluorocarbon gas mixtures containing hydrogen. *Journal of Vacuum Science & Technology B: Microelectronics and Nanometer Structures Processing, Measurement, and Phenomena*, June 1998. 84

[252] B J Villis, G Matmon, P T Greenland, D Li, M Erfani, X Yu, B N Murdin, A J Fisher, and G Aeppli. Electrical Detection of Impurity Orbital Transitions in Silicon Field Effect Transistors. *Manuscript in preparation*. 85, 86

[253] A Faraon, C Santori, Z Huang, V M Acosta, and R G Beausoleil. Coupling of Nitrogen-Vacancy Centers to Photonic Crystal Cavities in Monocrystalline Diamond. *Physical Review Letters*, 109(3):033604, July 2012. 96, 106, 132

[254] N-V-Q Tran, S Combrié, and A De Rossi. Directive emission from high-Q photonic crystal cavities through band folding. *Physical Review B*, 79(4):041101, 01 2009. 96, 105, 122, 184

[255] N-V-Q Tran, S Combrié, P Colman, A De Rossi, and T Mei. Vertical high emission in photonic crystal nanocavities by band-folding design. *Physical Review B*, 82(7):075120, 08 2010. 96, 105, 122, 123, 184

[256] K S Yee. Numerical solution of initial boundary value problems involving maxwell's equations in isotropic media. *IEEE Transactions on Antennas and Propagation*, 14(3):302–307, May 1966. 97, 98, 99

[257] University of Texas at El Paso. *Electromagnetic Analysis Using Finite-Difference Time-Domain*, 2016. 97, 101

[258] A H W Choi. *Handbook of Optical Microcavities*. Pan Stanford, 2014.

[259] D M Sullivan. *Electromagnetic Simulation Using the FDTD Method*. IEEE Press, John Wiley & Sons, Inc., second edition edition, 2013. 97

[260] A Taflove and S C Hagness. *Computational Electrodynamics: The Finite-Difference Time-Domain Method*. Artech House, third edition, 2004. 100

[261] L C Andreani, G Panzarini, and J-M Gerard. Strong-coupling regime for quantum boxes in pillar microcavities: Theory. *Physical Review B*, 60(19):13276–13279, November 1999. 103

[262] P Michler, editor. *Single Semiconductor Quantum Dots*. NanoScience and Technology. Springer Berlin Heidelberg, Berlin, Heidelberg, 2009. 103

[263] S Nakayama, S Ishida, S Iwamoto, and Y Arakawa. Effect of cavity mode volume on photoluminescence from silicon photonic crystal nanocavities. *Applied Physics Letters*, 98(17):171102, 2011. 104, 178

[264] Y Akahane, T Asano, B-S Song, and S Noda. Fine-tuned high-Q photonic-crystal nanocavity. *Optics Express*, 13(4):1202–1214, 2005. 104, 120, 121, 192

[265] R Lo Savio, M Miritello, A Shakoor, P Cardile, K Welna, L C Andreani, D Gerace, T F Krauss, L O Faolain, F Priolo, and M Galli. Enhanced 1.54 μm emission in Y-Er disilicate thin films on silicon photonic crystal cavities. *Optics Express*, 21(8):10278–10288, 2013 2013. 106

[266] F Liu, A J Brash, J O'Hara, L M P P Martins, C L Phillips, R J Coles, B Royall, E Clarke, C Bentham, N Prtljaga, I E Itskevich, L R Wilson, M S Skolnick, and A M Fox. High Purcell factor generation of indistinguishable on-chip single photons. *Nature Nanotechnology*, 7:1, July 2018. 106

[267] A M Dibos, M Raha, C M Phenicie, and J D Thompson. Atomic Source of Single Photons in the Telecom Band. *Physical Review Letters*, 120(24):243601, June 2018. 106, 206

[268] E Miyazono, T Zhong, I Craiciu, J M Kindem, and A Faraon. Coupling of erbium dopants to yttrium orthosilicate photonic crystal cavities for on-chip optical quantum memories. *Applied Physics Letters*, 108(1):011111, January 2016. 106, 132, 206

[269] M L W Thewalt, A Yang, M Steger, D Karaiskaj, M Cardona, H Riemann, N V Abrosimov, A V Gusev, A D Bulanov, I D Kovalev, A K Kaliteevskii, O N Godisov, P Becker, H J Pohl, E E Haller, J W Ager, and K M Itoh. Direct observation of the donor nuclear spin in a near-gap bound exciton transition: 31P in highly enriched 28Si. *Journal of Applied Physics*, 101(8):081724, April 2007. 106

[270] https://www.lumerical.com/tcad-products/fdtd/. 109, 118

[271] Murray W McCutcheon and M Lončar. Design of a silicon nitride photonic crystal nanocavity with a Quality factor of one million for coupling to a diamond nanocrystal. *Optics Express*, 16(23):19136–19145, November 2008. 116, 117, 118, 119

[272] T Tetsumoto, H Kumazaki, K Furusawa, N Sekine, and T Tanabe. Design, Fabrication, and Characterization of a High Q Silica Nanobeam Cavity With Orthogonal Resonant Modes. *Photonics Journal, IEEE*, 9(5):1–9, October 2017. 116

[273] J S Foresi, P R Villeneuve, J Ferrera, E R Thoen, G Steinmeyer, S Fan, J D Joannopoulos, L C Kimerling, H I Smith, and E P Ippen. Photonic-bandgap microcavities in optical waveguides. *Nature*, 390(6656):143–145, November 1997. 116

[274] T M Babinec, J T Choy, K J M Smith, M Khan, and M Lončar. Design and focused ion beam fabrication of single crystal diamond nanobeam cavities. *Journal of Vacuum Science & Technology B*, 29(1):010601, January 2011. 117, 119

[275] P Seidler, K Lister, U Drechsler, J Hofrichter, and T Stöferle. Slotted photonic crystal nanobeam cavity with an ultrahigh quality factor-to-mode volume ratio. *Optics Express*, 21(26):32468–32483, December 2013. 119

[276] Y Akahane, T Asano, B-S Song, and S Noda. High-Q photonic nanocavity in a two-dimensional photonic crystal. *Nature*, 425(6961):944–947, October 2003. 120, 121

[277] P Scholz, C Gallrapp, U Kerst, T Lundquist, and C Boit. Optimizing focused ion beam created solid immersion lenses in bulk silicon using design of experiments. *Microelectronics Reliability*, 50(9-11):1441–1445, September 2010. 134, 140

[278] P Scholz, N Herfurth, M Sadowski, T Lundquist, U Kerst, and C Boit. Efficient and flexible Focused Ion Beam micromachining of Solid Immersion Lenses in various bulk semiconductor materials – An adaptive calibration algorithm. *Microelectronics Reliability*, 54(9-10):1794–1797, September 2014. 134

[279] N Yao, editor. *Focused Ion Beam Systems: Basics and Applications*. Cambridge University Press, 2007. 134

[280] I Utke, P Hoffmann, and J Melngailis. Gas-assisted focused electron beam and ion beam processing and fabrication. *Journal of Vacuum Science & Technology B*, 26(4):1197–1276, July 2008. 134

[281] P Rai-Choudhury. *Handbook of Microlithography, Micromachining, and Microfabrication. Volume 1: Microlithography*. SPIE PRESS, 1997. 135, 136

[282] ZEISS GeminiSEM Family: Your Field Emission SEMs for the Highest Demands in Imaging and Analytics from Any Sample . Technical report, 2017. 135

[283] H H Gatzen, V Saile, and J Leuthold. *Micro and Nano Fabrication: Tools and Processes*. Springer Berlin Heidelberg, Berlin, Heidelberg, 2015. 136, 137, 138, 148

[284] Maria Stepanova and Steven Dew, editors. *Nanofabrication*. Springer Vienna, Vienna, 2012. 136

[285] G Calusine, A Politi, and D D Awschalom. Silicon carbide photonic crystal cavities with integrated color centers. *Applied Physics Letters*, 105(1):011123, July 2014. 138

[286] K Nojiri. *Dry Etching Technology for Semiconductors*. Springer International Publishing, Cham, 2015. 139

[287] M V Kotlyar, N Tripathi, R Wilson, L O'Faolain, M V Kotlyar, N Tripathi, R Wilson, and T F Krauss. Fabrication of photonic crystals using a spin-coated hydrogen silsesquioxane hard mask. *Journal of Vacuum Science & Technology B*, 24(1):336–339, January 2006. 147, 150, 164

[288] Stefano Cabrini and Satoshi Kawata. *Nanofabrication Handbook*. CRC Press, February 2012. 148

[289] A Malinin, T Majamaa, and A Hovinen. Anisotropic Si reactive ion etching in fluorinated plasma. *Microelectronic Engineering*, 43-44:641–645, August 1998. 150

[290] H Jansen, H Gardeniers, M de Boer, M Elwenspoek, and J Fluitman. A survey on the reactive ion etching of silicon in microtechnology. *Journal of Micromechanics and Microengineering*, 6(1):14–28, March 1996. 150

[291] E Gogolides, S Grigoropoulos, and A G Nassiopoulos. Highly anisotropic room-temperature sub-half-micron Si reactive ion etching using fluorine only containing gases. *Microelectronic Engineering*, 27(1-4):449–452, February 1995. 150

[292] S Grigoropoulos, E Gogolides, A D Tserepi, and A G Nassiopoulos. Highly anisotropic silicon reactive ion etching for nanofabrication using mixtures of SF6/CHF3 gases. *Journal of Vacuum Science & Technology B*, 15(3):640–645, May 1997. 150, 151

[293] Dow Corning Corporation. *XR-1541 E-Beam resist data sheet*, 2008. 152, 153

[294] K R Williams and R S Muller. Etch rates for micromachining processing. *Journal of Microelectromechanical Systems*, 5(4):256–269, 1996. 153

[295] K R Williams, K Gupta, and M Wasilik. Etch rates for micromachining processing-part II. *Journal of Microelectromechanical Systems*, 12(6):761–778, December 2003. 153

[296] W-C Wang, J N Ho, and P Reinhall. Deep reactive ion etching of silicon using an aluminum etching mask. In *ASDAM'02 (4th International Conference on Advanced Semiconductor Devices and Microsystems)*, pages 31–34. IEEE, 2002. 153

[297] Raith GmbH. *NanoSuite Software Reference Manual* , 6.0 edition, July 2012. 160

[298] T D Happ, A Markard, M Kamp, A Forchel, S Anand, J L Gentner, and N Bouadma. Nanofabrication of two-dimensional photonic crystal mirrors for 1.5 μm short cavity lasers. *Journal of Vacuum Science & Technology B*, 19(6):2775–2778, November 2001. 164

[299] F Pommereau, L Legouézigou, S Hubert, S Sainson, J P Chandouineau, S Fabre, G H Duan, B Lombardet, R Ferrini, and R Houdré. Fabrication of low loss two-dimensional InP photonic crystals by inductively coupled plasma etching. *Journal of Applied Physics*, 95(5):2242–2245, March 2004. 164

[300] M Mulot, S Anand, R Ferrini, B Wild, R Houdré, J Moosburger, and A Forchel. Fabrication of two-dimensional InP-based photonic crystals by chlorine based chemically assisted ion beam etching. *Journal of Vacuum Science & Technology B: Microelectronics and Nanometer Structures*, 22(2):707, March 2004. 164

[301] R Wüest, P Strasser, F Robin, D Erni, and H Jäckel. Fabrication of a hard mask for InP based photonic crystals: Increasing the plasma-etch selectivity of poly(methyl methacrylate) versus SiO2 and SiNx. *Journal of Vacuum Science & Technology B*, 23(6):3197–3201, November 2005. 164

[302] A Chen, S-J Chua, B Wang, and E A Fitzgerald. Fabrication of Two-Dimensional Photonic Crystals in AlGaInP/GaInP Membranes by Inductively Coupled Plasma Etching. January 2006. 164

[303] Ivan Prieto, J Herranz, L Wewior, Y González, B Alén, L González, and P A Postigo. High quality factor GaAs-based photonic crystal microcavities by epitaxial re-growth. *Optics Express*, 21(25):31615–31622, December 2013. 164

[304] V Zwiller and G Björk. Improved light extraction from emitters in high refractive index materials using solid immersion lenses. *Journal of Applied Physics*, 92(2):660–665, July 2002. 167

[305] M W McCutcheon, G W Rieger, I W Cheung, J F Young, D Dalacu, S Frédérick, P J Poole, G C Aers, and R L Williams. Resonant scattering and second-harmonic spectroscopy of planar photonic crystal microcavities. *Applied Physics Letters*, 87(22):221110, November 2005. 168, 169

[306] K Rivoire, A Faraon, and J Vuckovic. Gallium phosphide photonic crystal nanocavities in the visible. *Applied Physics Letters*, 93(6):063103, 2008.

[307] M Galli, S L Portalupi, M Belotti, L C Andreani, L O'Faolain, and T F Krauss. Light scattering and Fano resonances in high-Q photonic crystal nanocavities. *Applied Physics Letters*, 94(7):071101, February 2009.

[308] W C Stumpf, T Asano, T Kojima, M Fujita, Y Tanaka, and S Noda. Reflectance measurement of two-dimensional photonic crystal nanocavities with embedded quantum dots. *Physical Review B*, 82(7):075119, August 2010. 168, 169

[309] S Iwamoto, Y Arakawa, and A Gomyo. Observation of enhanced photoluminescence from silicon photonic crystal nanocavity at room temperature. *Applied Physics Letters*, 91(21):211104, 2007. 178

[310] H Sumikura, E Kuramochi, H Taniyama, and M Notomi. Purcell enhancement of fast-dephasing spontaneous emission from electron-hole droplets in high-Q silicon photonic crystal nanocavities. *Physical Review B*, 94(19):195314, November 2016. 178

[311] T Ihara, Y Takahashi, S Noda, and Y Kanemitsu. Enhanced radiative recombination rate for electron-hole droplets in a silicon photonic crystal nanocavity. *Physical Review B*, 96(3):035303, July 2017. 178

[312] J D Joannopoulos and S G Johnson. Block-iterative frequency-domain methods for Maxwell's equations in a planewave basis. *Optics Express*, 8(3):173–190, January 2001. 185

[313] N Cherroret, A Chakravarty, and A Kar. Temperature-dependent refractive index of semiconductors. *Journal of Materials Science*, 43(6):1795–1801, January 2008. 189

[314] B J Frey, D B Leviton, and T J Madison. Temperature-dependent refractive index of silicon and germanium. In Eli Atad-Ettedgui, Joseph Antebi, and Dietrich Lemke, editors, *SPIE Astronomical Telescopes + Instrumentation*, page 62732J. SPIE, July 2006. 189

[315] W Bludau, A Onton, and W Heinke. Temperature dependence of the band gap of silicon. *Journal of Applied Physics*, 45(4):1846–1848, 1974. 191, 193

[316] K Rajkanan, R Singh, and J Shewchun. Absorption coefficient of silicon for solar cell calculations. *Solid-State Electronics*, 22(9):793–795, September 1979. 191, 192

[317] J Noffsinger, E Kioupakis, C G Van de Walle, S G Louie, and M L Cohen. Phonon-Assisted Optical Absorption in Silicon from First Principles. *Physical Review Letters*, 108(16):167402, April 2012. 191

[318] G G Macfarlane, T P McLean, J E Quarrington, and V Roberts. Fine Structure in the Absorption-Edge Spectrum of Si. *Physical Review*, 111(5):1245–1254, September 1958. 191, 192

[319] W C Dash and R Newman. Intrinsic Optical Absorption in Single-Crystal Germanium and Silicon at 77°K and 300°K. *Physical Review*, 99(4):1151–1155, August 1955. 193

[320] M Saritaş and H D McKell. Absorption coefficient of Si in the wavelength region between 0.80–1.16 μm. *Journal of Applied Physics*, 61(10):4923–4925, 1987.

[321] C Schinke, P C Peest, J Schmidt, R Brendel, K Bothe, M R Vogt, I Kröger, S Winter, A Schirmacher, S Lim, H T Nguyen, and D Macdonald. Uncertainty analysis for the coefficient of band-to-band absorption of crystalline silicon. *AIP Advances*, 5(6):067168, June 2015. 193, 203

[322] Julius Karl Komma. *Optische Eigenschaften von Substratmaterialien für zukünftige kryogene Gravitationswellendetektoren*. PhD thesis, Friedrich-Schiller-Universität Jena, June 2016. 193

[323] M Abanto, L Davidovich, B Koiller, and R L de Matos Filho. Quantum computation with doped silicon cavities. *Physical Review B*, 81(8):085325, 02 2010. 207

[324] K J Morse, R J S Abraham, A DeAbreu, C Bowness, T S Richards, H Riemann, N V Abrosimov, P Becker, H-J Pohl, M L W Thewalt, and S Simmons. A photonic platform for donor spin qubits in silicon. *Science Advances*, 3(7):e1700930, July 2017. 207

[325] S P Cooil, F Mazzola, H W Klemm, G Peschel, Y R Niu, A A Zakharov, M Y Simmons, T Schmidt, D A Evans, J A Miwa, and J W Wells. In Situ Patterning of Ultrasharp Dopant Profiles in Silicon. *ACS Nano*, 11(2):1683–1688, February 2017. 208

[326] M J Burek, Y Chu, M S Z Liddy, P Patel, J Rochman, S Meesala, W Hong, Q Quan, M D Lukin, and M Lončar. High quality-factor optical nanocavities in bulk single-crystal diamond. *Nature Communications*, 5:5718, December 2014. 208

[327] N H Wan, S Mouradian, and D Englund. Two-dimensional photonic crystal slab nanocavities on bulk single-crystal diamond. *Applied Physics Letters*, 112(14):141102, April 2018. 208